UNIVERSITÀ DEGLI STUDI DI MESSINA

Dipartimento Scienze Matematiche e Informatiche,
Scienze Fisiche e Scienze della Terra
Dottorato di Ricerca in Fisica
XXX Ciclo

Newly-Designed Spongy TiO₂ Layers by Modified Sputtering Methods for Hybrid PhotoVoltaics
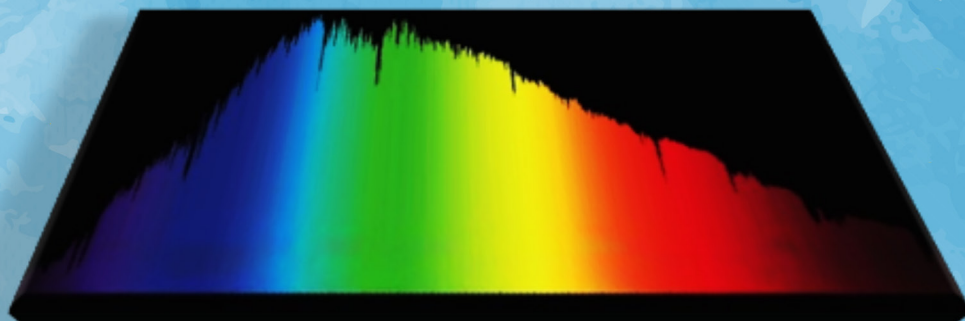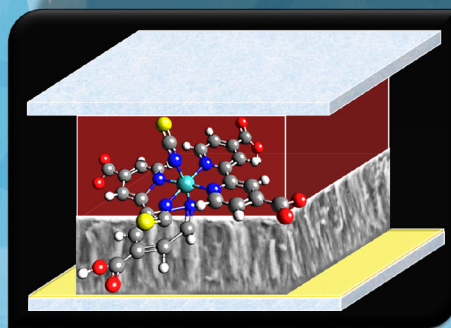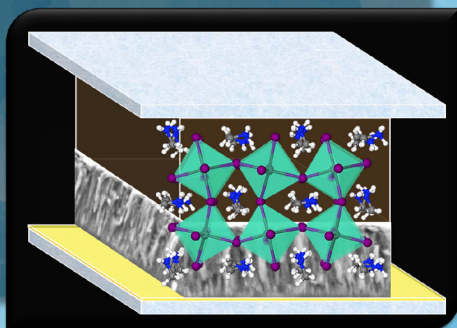

Salvatore Sanzaro

UNIVERSITÀ DEGLI STUDI DI MESSINA

**Dipartimento Scienze Matematiche e Informatiche,
Scienze Fisiche e Scienze della Terra
Dottorato di Ricerca in Fisica
XXX Ciclo (FIS/01)**

Salvatore Sanzaro

Newly-Designed Spongy TiO$_2$ Layers by Modified Sputtering Methods for Hybrid PhotoVoltaics

Supervisors	*Coordinator*
Prof. Fortunato Neri	**Prof. Lorenzo Torrisi**
Dr. Alessandra Alberti	

2014-2017

"*Nothing is created, nothing is destroyed, everything is transformed.*"

Antoine Laurent Lavoisier, *Traité Élémentaire de Chimie*, 1789.

*   *   *

"*One can never know with perfect accuracy both of those two important factors which determine the movement of one of the smallest particles - its position and its velocity. It is impossible to determine accurately both the position and the direction and speed of a particle at the same instant.*"

Werner Karl Heisenberg, *Die Physik der Atomkerne*, 1952.

*   *   *

"*There's Plenty of Room at the Bottom.*"

Richard Phillips Feynman, *An Invitation to Enter a New Field of Physics*, 1959.

Index

Extended Abstract

The ability to build up cheap multifunctional devices envisages the possibility of a large dissemination of new technologies to improve the quality of life, worldwide. Among the requirements to hit the target of multi-functionality, multi scale-porosity is an increasingly strategic property for inorganic materials to provide simultaneous sensitivity to light, liquids, gases, complex molecules or hybrid counterparts. The control of porosity mainly in terms of size (from meso to nano) and arrangement (random vs. ordered, monodimensional vs. hierarchical) is thus a key cornerstone for the actual design and fabrication of functional devices. In order to join and simultaneously cover different fields, new material architectures with transversal empowering are required.

Porous TiO_2 is currently applied for energy, health and environment purposes. Among the others, TiO_2–based 1D nanostructures are especially appealing since they usually expose large active facets with good mechanical and surface-related performances, and high electrical conductivity. All those properties enrich 1D-TiO_2 architectures to be efficiently used as scaffold for Dye and Perovskites Solar Cells, anodes for Li batteries, electrodes for water splitting devices, materials for biosensors detecting DNA or glucose, scaffold for gas sensing or photo-catalysis.

Framed in this context, the main purpose of the Ph.D. thesis was designing new low-dimensional TiO_2-structures through a high-throughput method which is up-scalable, contaminant-free, implementable on low cost substrates and eco-compatible in terms of waste reduction and material saving. The process is described in details and the produced materials investigated from different point of views, comprising structure, optical behavior, interface engineering, surfaces functionalization, electrical response under illumination. A plethora of techniques some of which recently developed, are used to disentangle the different properties.

The newly-conceived material, we called *gig-lox TiO₂*, was integrated as scaffold in hybrid technologies for solar energy conversion into electricity by exploiting approaches beyond-silicon: namely, Dye Sensitized Solar Cells (DSC) and Perovskite Solar Cells (PSC). DSCs compete with silicon for Integrated Building Photovoltaics and flexible/wearable

devices; whilst PSCs are attractive for two-level tandem with silicon solar cells that prospects efficiency improvement over 30%.

There is a general consensus, supported by the explosion of publications in the field during the last 8 years, that Hybrid Solar Cell technologies can breathe new life by their capillary distribution in a complementary way to silicon solar panels and plants already installed all over the world, at price competitively low ($\leq 0.5\$/Wp$).

To open up new opportunities for high–performance and high-throughput hybrid solar cells, the outcome of the Ph.D thesis is: 1) a new strategy enabling sputtering-based method to grow spongy-TiO₂ architectures with fine control over porosity in the meso- to nano-scale; 2) providing proofs-of-concept on the material use in DSC and PSC devices; 3) demonstrating the transversal empowering of the material through its application in gas sensing devices.

We conclude that our *gig-lox TiO₂* material opens a reliable perspective to integrate different functionalities on a shared platform for multipurpose devices.

The Ph.D. thesis is organized in four chapters.

The first chapter is an overview on renewable energies solutions and perspectives to counteract the climate change, with special focus on the clean energy provided by the sun. In the context of the photovoltaic devices, DSC and PSC technologies, comprising their operation principles, are described as viable solutions beyond-silicon.

In the second chapter, we provide a detailed description of the newly conceived *gig-lox* process used for the deposition of spongy TiO₂ layers. *Gig-lox* stems for Grazing Incidence sputtering Geometry coupled with Local OXidation. The several effects of the deposition parameters are described and exploited to the intent of properly building-up the multi-scale porosity and its solid-state frame. The properties of the *gig-lox TiO₂* layers are also investigated from different perspectives: morphology, lattice structure and optical behaviour in comparison to reference layers deposited by standard parallel plate sputtering methods.

Shortly following, chapter three is the proof-of concept of the mainstays of the new material. It contains the description of the TiO₂ functionalization by photoactive molecules (N-719) in different solvents (CH_3CH_2OH and CH_3CN) via a detailed characterization on the dye infiltration, chemisorption and on the collection of the photo-generated electrons. The chapter also describes the coverage of the spongy-TiO₂ layers with perovskites, *i.e.* MAPbI₃,

supported by morphological, structural and optical descriptions. Finally, we report on DSC and PSC prototypal devices wherein the spongy-TiO$_2$ is integrated as scaffold.

Chapter two and three represent the core of the Ph.D. thesis.

The fourth final chapter complements the others to explore alternative materials and applications for future devices. It contains: 1) TiO$_2$ flowers grown by a chemical approach (AA-MOCVD) as a possible alternative to the *gig-lox* method; 2) the application of *gig-lox TiO$_2$* layers for gas sensing; 3) the growth of ZnO:Al (AZO) by low-temperature reactive co-sputtering as a valid alternative to commercial transparent conductive oxides (TCO) for solar cells. The chapter aims at further elucidating the transversal empowering of nanostructures and at prospecting their easy integration with Aluminum doped Zinc-Oxide (AZO) layers in a shared deposition chamber potentially on any kind of substrate. This strategy would positively impact on the costs of the photo-anode.

Chapter 1

State of the art and perspectives on Photovoltaics

The fast development of the society through the industrialization of the productive activities and the improvement of the living standards brought exponentially increasing rate of climate change via pollution overflow and temperature rise.[1,2,3] Greenhouse gases, especially carbon dioxide (CO_2) emissions, concurrently increases (see **Figure 1.1(a)**), causing progressive global warming as depicted in **Figure 1.1(b)**.[4,5,6]
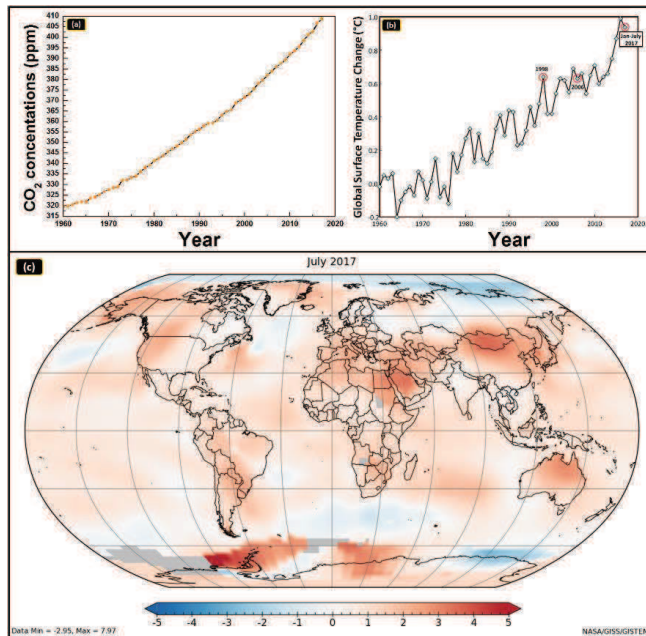
Figure 1.1: Trends from 1960 to 2017 of **(a)** Atmospheric concentrations of CO_2 (font: NOAA-ESRL Global Monitoring, CO_2-Earth)[5] and **(b)** global surface temperature (font: NASA Global Surface Temperature data).[6] **(c)** July 2017 blended land and sea surface temperature anomalies in °C (Font: NASA).[6]

Predictive models[5,7] indicate that the temperature could further increase by 2.0°C-5.4°C in ~100 years at the Earth's surface if actions are not seriously taken (**Figure 1.1(c)**). Such climate changes are already causing droughts, floods, sea level rise, glacier melting, and severe damages in agriculture and natural ecosystems; thereby the mounting consensus on the need to reduce the overall emissions by switching many traditional energy sources to

renewable energy. Sun, water, bio-energy or wind powers were all sources used in early human societies and nowadays provide hope to our Earth for a better future. In all those fields, several strategies have been explored and / or even already exploited based on the use / implementation / tailoring of highly performing nano-materials.
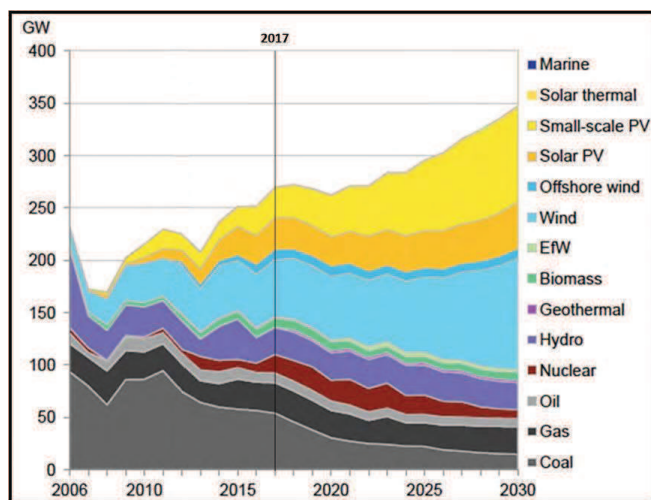
Figure 1.2: current world scenario on the renewable energy production and its projection to 2030.[8]

Figure 1.2 depicts the current scenario on the renewable energy production and its projection to 2030. Photovoltaics has been getting off the ground to satisfy the 25% world's energy in the 2050 at a rate, which overcomes the expectation. The reason is related to the new emerging technologies having solicited the curiosity of scientist and industrial actors: hybrid photovoltaics among the others.

1.1. *The sun as renewable energy source*

Renewable energy sources can be defined as "energy obtained from the continuous or repetitive currents on energy recurring in the natural environment"[9] or as "energy flows which are replenished at the same rate as they are used".[10] All the earth's renewable energy sources somehow originate from solar radiation as depicted in **Figure 1.3(a)**. This radiation is perceived as white light since it spans over a wide spectrum of wavelengths, from the short-wave infrared to ultraviolet (see **Figure 1.3(b)**). Such radiation plays a major role in generating electricity either indirectly or directly by means of the photovoltaic (PV) effect.

It is well known that PV-based technologies are the simplest to be designed and

installed;[11] however they are still not sufficiently cheap to be largely distributed. The advantages lie in the fact that PV is an environmentally friendly, non-pollutant and low-maintenance energy source. Solar photovoltaics, in combination with concentrating solar power technologies, is being used by developers and utilities to produce electricity on a massive scale to power cities and small towns.
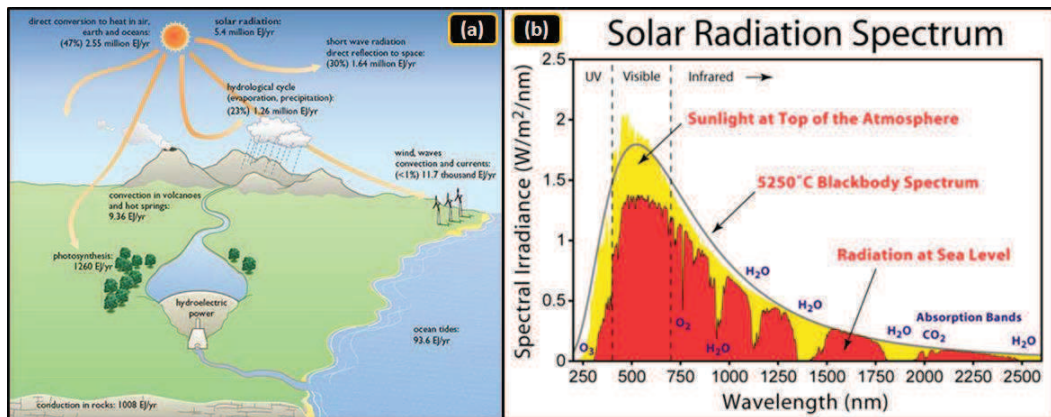
Figure 1.3: (a) Various forms of renewable energy depend primarily on incoming solar radiation.[12] **(b)** Solar radiation spectrum.

1.2. *Overview on photovoltaic technologies*

PV materials and devices convert sunlight into electrical energy. A single PV device is known as a cell. An individual PV cell is usually small (~cm²), typically producing around 1 W of power. To boost the power output of PV cells, they are connected together in chains to form larger units known as modules or panels. Modules can be used individually, or several can be connected to form arrays. One or more arrays is then connected to the electrical grid as part of a complete PV system.

The active material in a PV cell is a semiconductor. It is physically connected to other boundary materials (heavily doped semiconductors or metals) to generate internal electric fields during sun illumination and to extract carriers towards external grids and loadings. Different materials and interfaces are indeed involved in the operation of a solar cell with different roles, each of them requiring research and optimization steps.

There are varieties of semiconductor materials used in solar cells. Traditional solar cells are made from *silicon*, are usually flat-plate, and generally are high efficiency solutions. They are representing approximately 90% of the modules sold today.[13] It is also the second

most abundant material on Earth (after oxygen) and the most common semiconductor used in computer chips. Second-generation solar cells are called *thin-film solar cells* because they are made from amorphous silicon or non-silicon materials such as cadmium telluride (CdTe) and copper indium gallium diselenide (CIGS). Both materials can be deposited either directly onto the front or back of the module surface. Thin film solar cells use semiconductor layers only a few micrometers thick to save raw materials and consequently money. Because of their flexibility, thin film solar cells can be applied as rooftop shingles and building facades.

Third-generation solar cells are being made from a variety of new materials beyond silicon, and include organic and hybrid solar cells.
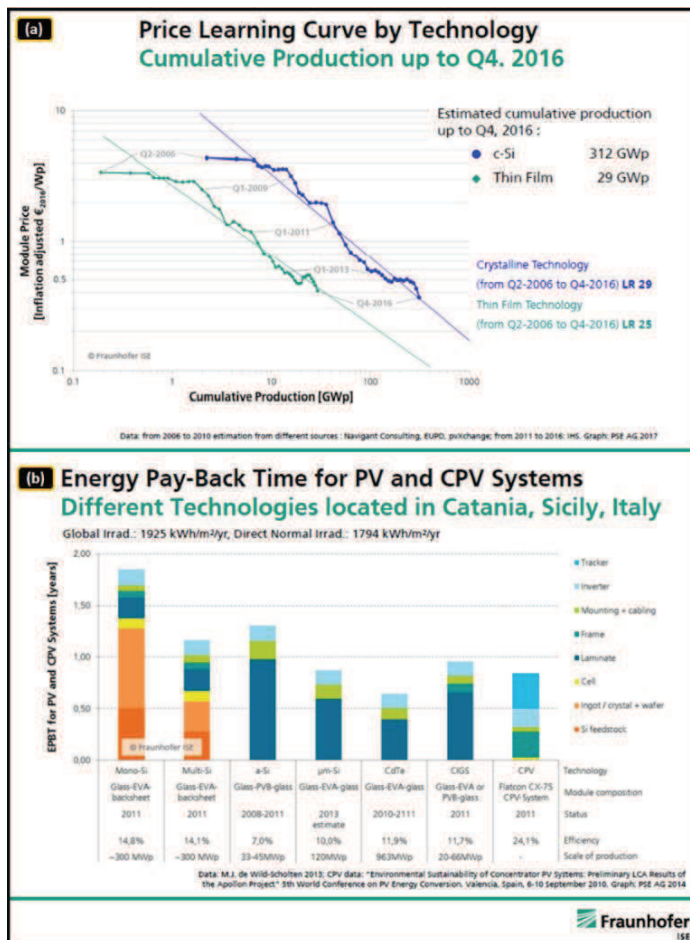
Figure 1.4: (a) Module Price as a function of the cumulative production for crystalline and thin-film technologies updated at 2017; **(b)** Overview of the different photovoltaic technologies located in Catania, Sicily, Italy (Font: Fraunhofer Institute for Solar Energy Systems) and the related pay-back time.[14]

Figure 1.4 reports the recent price and pay-back time of some technologies. The graphs highlight the driving force residing in the cost reduction and the weight in price of the different parts in a single technology.
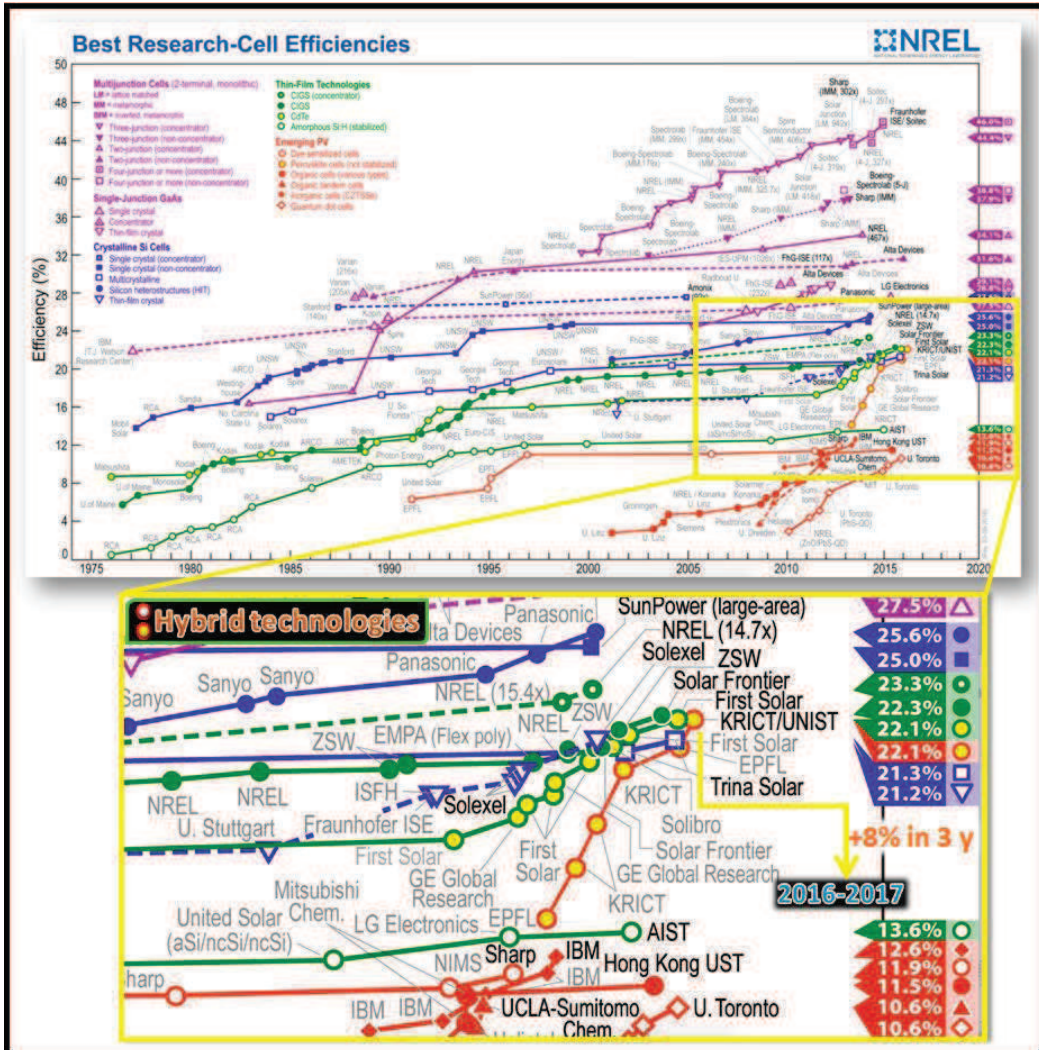
Figure 1.5: Efficiency trend of all photovoltaic technologies from 1975-2017 (font: NREL).[15]

Besides the costs, the power conversion efficiency (η) becomes a further main parameter. The efficiency of a cell is the amount of electrical power coming out of a cell divided by the energy from sunlight coming in. The amount of electricity produced from PV cells depends on the light harvesting capability of the absorbing material, on the light intensity and (usually) by the photon capture angle. Multiple other factors play roles in

limiting the efficiency of a PV system being related to the active material (charge recombination, material instability, sunlight loss), or independent from that (current loss trough the external grid, working temperature).

As reported in the official National Renewable Energy Laboratory (NREL) chart[15] (**Figure 1.5),** the highest efficiency is nowadays registered in multijunction solar cells (46%). At the same time, the efficiency gained through the last few years by hybrid solar cells technologies cannot slip through unnoticed. Dye Sensitized (DSC) and, more recently, Perovskite Sensitized (PSC) solar cells have been emerging as viable solutions, in alternative or combined in tandem to other well assessed technologies (*e.g.* those Si-based). The driving force partially resides in the easy, low cost and versatile manufacturing of those technologies, the hopes raised by the fast improvement of their efficiency even under cloudy and artificial light conditions (i.e. for in-door use). For pure DSCs, the efficiency record currently is 13.6%,[15] while for the PSCs it flies even higher. In fact, in the last 3 years the efficiency value raised by 8% to get to 22.1% in 2016.[16]

Despite the linked story of the two hybrid PV technologies (see details in the next paragraph), their efficiency trend experienced a cut-off in the 2014-2015 (see zoom in Figure 1.5) as the research hardly invested in the comprehension of the light harvesting and transport in photoactive perovskite layers[17,18] to find out applicative technological improvement (involving materials and layout) for new records.

1.3. *Hybrid Solar Cells*

Hybrid solar cells bring together organic and inorganic materials.[19] The inorganic main components are usually oxides of transition metals while the organic-containing counterpart spans from dye molecules to thin films or thick layers .[20,21]

In the literature, hybrid solar cells are manufactured using different concepts which exploit the solid/liquid state (DSCs)[22,23] or the fully solid state (PSCs).[24,25,26,27,28,29,30,31,32,33,34]

DSCs have been receiving increasing interest in the research as well as in the industrial framework at a level that a number of manufacturers have begun investing in this sector, driven by the prospected short payback period, by the simple manufacturing processes. Another value-added consists of applying the technology in Building Integrated

Photovoltaics (BIPV), which Si-based solar cells do not offer, thanks to the transparency of the cells and to the photovoltaic conversion yield not sensibly affected by the photon incident angle. The esthetic of those cells is not negligible and offers a real fascinating range of colors. Nowadays, the BIPV is one of the fastest growing segments of the PV industry. In the standard scheme of the photo-anode of a DSC, proposed by M. Grätzel (**Figure 1.6)**, the father of this technology,[22,23] a mesoporous thin film of nano-sized TiO_2 crystals (nano-paste) is deposited on a transparent conductive oxide (TCO) and sensitized by a photoactive dye.[35]

Figure 1.6: the famous inventors of highly performing Hybrid Sola Cells technologies. From left to right: M. Grätzel (EPFL, Lausanne, Switzerland), T. Miyasaka (Toin Univeristy of Yokohama, Japan), H. J. Snaith (Oxford University, UK).

Perovskites are a large class of materials well known for many years, but their first incorporation into a solar cell was only recently reported by T. Miyasaka et al. in 2009 from the Toin University of Yokohama in Japan.[24] He has the huge merit of having substituted the photo-active dye with a film of hybrid perovskite to finely cover a mesoporous TiO_2 scaffold. This change has been still producing conveniences and allowing the cell efficiency to aim high. Starting from that date, an increasing emphasis have been dedicated to this new technology that provided Prof. Tsutomu Miyasaka with the title of PSC's father **(Figure 1.6).** This is a really unique event in the history of photovoltaics which has created a lot of excitement all over the academic and industrial world.

After the first power conversion efficiency generated (3.8%), Park et al. improved the record to 6.5% PCE.[36] A breakthrough came in 2012, when Henry Snaith **(Figure 1.6).** and

Mike Lee from the University of Oxford realized that a PSC architecture does not necessarily require a scaffold to work. This allowed to launch a layered PSC structure, with the perovskite layer sandwiched between the electron and the hole transporting materials.[37,38] The idea was supported by the experiment in which a perovskite-covered TiO_2 architecture was replaced by an inert scaffold.[39] Further trials in replacing the mesoporous TiO_2 with Al_2O_3 resulted in increased open-circuit voltage and a relative improvement by 3–5% in efficiency.[40] All those pioneering experiments were then closely followed by the clear demonstration that the perovskite is a bipolar conductive material, able to transport both electrons and holes.[41,42,43,44]

In 2013, planar and sensitized architectures experienced a number of developments. Burschka et al. reported, for the sensitized architecture, efficiency exceeding 15% using a two-step solution processing to deposit the perovskite active layer,[45] Malinkiewicz et al. and Liu et al. showed the possibility to fabricate planar solar cells by thermal co-evaporation, achieving ∼12% and ∼15% efficiency in p-i-n and an n-i-p architectures, respectively.[46,47,48] Inverted configuration were also successfully applied by Docampo et al.[49]

The story on material and device improvements (comprising a plethora of combination or mixture of cations and anions, 2D perovskites and tandem materials) is still running fast.

1.3.1. *Dye-Sensitized Solar Cells (DSC)*

In the late 1960s, it was discovered that sun-irradiated organic dyes, placed in electrochemical cells, can generate electricity[50] in a way similar to what occurs in photosynthesis. The phenomenon was studied at the University of California at Berkeley with chlorophyll extracted from spinach (bio-mimetic or bionic approach).[51] On the basis of such experiments, the dye-sensitization solar cell basic principle was demonstrated and discussed in 1972.[52] Starting from those pioneering experiments, the instability of the dye solar cell and the low power conversion efficiency (mainly linked to the small light harvesting probability) were identified as a highly limiting drawbacks; consequently, the idea was not further expanded in the next years.[53].

Many years after, Michael Grätzel[23] revived that idea on the basis of the intuition that the surface availability for efficient photovoltaics effects needed to be increased. Thereby, the use of a mesoporous scaffold with surface to volume ratio multiplied by a factor of 10000.

DSCs were, at the end, a real breakthrough since they represented the first PV device based on a three-dimensional junction.

However, to turn this discovery into market with real dissemination perspectives, efficiency and stability have been requested to survive over the years. Today, there are companies like G2E and EXEGER that have major DSC production outputs growing every year. The production volume for G2E is approximately 30000 m^2/year; a new factory with an output of 200000 m^2 per year is being built in Switzerland, and the company is planning to increase to 1000000 m^2/year.[54] Therefore, through this production, the power being delivered by DSCs is about megawatts, even hundreds of megawatts. Another important DSC application is to capture and convert diffuse light or ambient daylight. EXEGER, in Sweden, is producing DSCs for use as ambient light-harvesting devices in e-Book readers or other portable electronic devices. They are at the top of the efficiency and also they are making 200000-300000 m^2/year.[54] The research in this field is expanding since there is still room for technological improvements.

1.3.1.1. *DSCs architecture*

In the original design of Grätzel and O'Regan,[22] the cell has three primary parts. A transparent conductive oxide (TCO) made of fluoride-doped tin dioxide (SnO_2:F or FTO) is deposited on a substrate, typically a glass. On the conductive substrate, a compact and thin (tens of nanometers) TiO_2 layer is deposited, followed by a mesoporous thick (several microns) layer of the same oxide. They are the blocking and the scaffold layers, respectively. The TiO_2 scaffold is adjusted by a process of sintering at temperature of 450-500°C needed to release the residual solvent (being the scaffold conventionally made of chemically sintered commercial nanopastes) and to merge the grains at their interfaces. At those temperatures, the TiO_2 scaffold is made of anatase grains and absorbs a fraction of the solar photons in the UV range above the energy gap of the material (E_g = 3.2 eV).[55] The photoanode is then immersed in a mixture of a photosensitive ruthenium-polypyridine dye[55] and a solvent. After soaking the film in the dye solution, a number of dye molecules are left covalently bonded to the surface of the TiO_2.

Then, a separate electrode (cathode) is made with a thin layer of the iodide electrolyte (I^-/I_3^-) spread over a conductive sheet, typically platinum metal. The two electrodes are

then joined and sealed together to prevent the electrolyte from leaking. The construction is simple enough that there are hobby kits available to hand-construct them.[56] Although they use a number of advanced materials, these are inexpensive compared to the silicon needed for normal cells because they require no expensive manufacturing steps. In **Figure 1.7** is reported the standard DSC architecture.
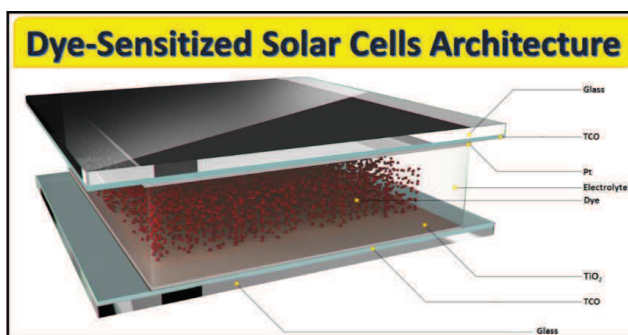
Figure 1.7: Standard Dye-Sensitized Solar Cells architecture.

1.3.1.2. *Mechanism of DSCs operation*

In the operation scheme, the dye is the active material for light harvesting. Upon absorption of photons, dye molecules are excited from the highest occupied molecular orbitals (HOMO) to the lowest unoccupied molecular orbital (LUMO) states as shown schematically in **Figure 1.8**. Equation 1 represents this process. Due to the convenient LUMO position with respect to the Conduction Band (CB) of the TiO₂ scaffold, the photo-generated electron has a driving force to be injected into the CB. Once it occurs, the dye molecule remains in the oxidized state. (Equation 2). The injected electron is transported through the TiO₂ porous layers and then extracted from a load (Equation 3). Electrolytes containing I^-/I_3^- redox couples are used as an electron mediator between the TiO₂ photoelectrode and the counter electrode (C.E.). Through them, the oxidized dye molecules are regenerated by receiving electrons from the I^- ion redox mediator that get oxidized to I_3^-. Equation 4 represents this process. The I_3^- substitutes the internally donated electron with that from the external load and reduced back to I^- ion, (Equation 5). The movement of electrons in the conduction band of the wide bandgap nanostructured semiconductor is accompanied by the diffusion of charge-compensating cations in the electrolyte layer close to the TiO₂ surface.[57]

$S + h\nu \rightarrow S^*$ (1) Excitation process

$S^* + TiO_2 \rightarrow S^+ + e^-_{(TiO2)}$ (2) Injection process

$e^-_{(TiO2)} + C.E. \rightarrow TiO_2 + e^-_{(C.E.)} + electrical\ energy$ (3) Energy generation

$S^+ + \frac{3}{2} I^- \rightarrow S + \frac{1}{2} I^-_3$ (4) Regeneration of dye

$\frac{1}{2} I^-_3 + e^-_{(C.E.)} \rightarrow \frac{3}{2} I^- + C.E.$ (5) e⁻ Recapture reaction
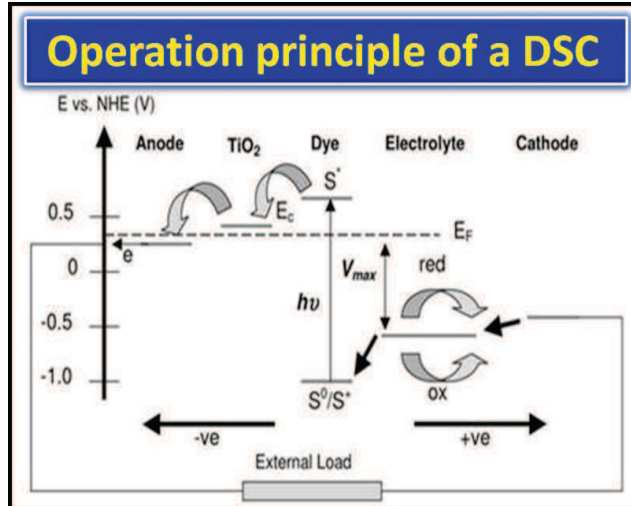
Figure 1.8: Photovoltaic mechanism of DSC.

1.3.2. *Perovskite Solar Cells (PSC)*

Hybrid lead iodide perovskites are revolutionizing views and perspectives in all fields that can take advantage from their high electrical performances[58,59] and wide absorption capabilities (IR-UV),[58] thereby attracting interest in photonics and also, more recently, in microelectronics. Among others, the most intensively investigated perovskite for PV conversion has the cation methylammonium (MA⁺) as organic moiety, with overall stoichiometry $CH_3NH_3PbI_3$ (MAPbI₃).[24,60,61,62,63,64,65,66,67,68] MAPbI₃ is cheap to produce and simple to manufacture for PSC.

The easy preparation procedure and the competitive electrical properties have been pushing forward a rapid development of solar cells based on perovskite-like materials.[24,69,70,71] In particular, diffusion lengths of several microns, the wide absorption range and the bandgap tunability made them widely studied from many point of views.[72,73,74,75,76,77,78] In the material architecture, the mutual relationship between the

inorganic cage and the organic cations represents a main point in disclosing the fundamentals of its behavior.

In its original architecture, a PSC resembles a DSC provided the dye is substituted with a perovskite coverage for light-harvesting.[79,80] In a recent interview, Michael Grätzel has declared:[54] "…..It is true that these cells are very efficient and can compete with silicon and other thin-film technologies on a laboratory scale, but there are concerns…..Having said this, the other main reason for concern has been the long-term device stability, long-term light soaking at 60°C holding the cells at their maximum power point and in addition performing the damp heat test at 85°C for 1000 h. So, we still have, I think, a pretty long testing period in front of us. My guess is that perhaps in 5 years we will have mature systems that can be put on the market." Those limitations have pushed more than 10 000 researchers working in this field worldwide.

It is true that the intrinsically low structural stability of the MAPbI₃ layers risks to retard its wide-range applications in low cost/high yield device technologies.[81] To this end, a large effort is still needed for the deep comprehension of the instability sources in relationship with boundary materials[82] and operation conditions, including temperature,[83] illumination (e.g UV),[84] and external agents.[84,85,86,87] As a main origin of MAPbI₃ degradation, the proton exchange between the organic (MA⁺) and the inorganic (I⁻) moieties of the lattice cage is an intrinsic thermodynamically activated process[88,89] that occurs even in vacuum conditions.[24,90] Proton exchange with the consequent release of volatile species is further promoted by mediators (catalysts) such as water molecules[88,91] or oxygen;[87] thereby humid air is widely regarded as responsible for degradation and indeed requires mitigation actions.[92,93] Although the overall scenario is less obscure than years ago, the back-reaction of perovskites to the starting byproducts (PbI₂, MAI) needs to be further elucidated especially in proximity of the operation temperature. During the device exposure to heat sources (*e.g.* under the sun), in fact, the effective temperature of the active layer can rise above 60°C.[85,93] This is not ineffective, since a polymorphic transition from a tetragonal to a cubic lattice is expected around 54°C in MAPbI₃ layers.[83,90,94,95,96]. The perovskite engineering, mainly focusing on composition, is nowadays prospecting some solutions, although MAPbI₃-based PSC's performances remains the best published in the literature.[16]

1.3.2.1. *PSCs architecture*

Perovskite solar cells work efficiently in a number of different architectures depending either on the role of the perovskite material in the carrier transport or on the nature of the top and bottom electrodes. Thereby, PSC devices can be divided into "sensitized", where the perovskite acts mainly as a light absorber whilst charge transport occurs into the scaffold; or thin film "layered", where electron and hole transport mostly occurs in the bulk of the perovskite itself. In the first scheme, similarly to DSCs, the perovskite material covers a charge-conducting mesoporous scaffold (most commonly made of TiO₂). The photo-generated electrons are transferred from the perovskite layer to the mesoporous sensitized layer through which they are transported to the electrode and extracted into the circuit. The thin film layered architecture, instead, is based on the bipolar transport capability of the perovskite materials.[97] After light absorption and the subsequent charge-generation, indeed, both negative and positive carriers flay away along a mean free path of microns to reach the electron and the hole extractors.
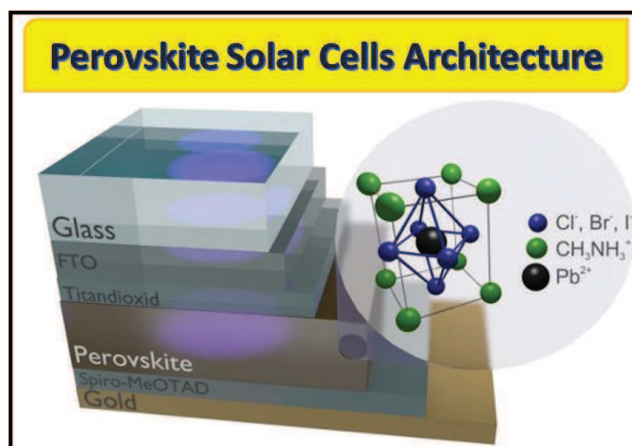
Figure 1.9: Standard Perovskite Solar Cells Architecture.

Figure 1.9 shows a layered PSC architecture wherein the hole-transporting layer (Spiro-OMeTAD) is buried under the perovskite instead of covering it, in a configuration therefore called inverted.

More recently, some researchers also successfully demonstrated the possibility of fabricating flexible devices with perovskites,[49,82,98] a technological solution for energy demand on flexible (e.g. wearable, portable).

1.3.2.2. *Mechanism of PSCs operation*
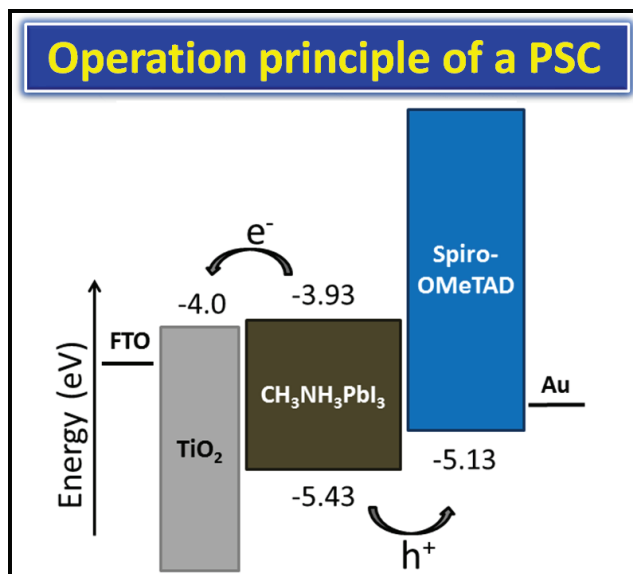
Figure 1.10: Operation principle of PSC.

Independently of the shape (thin film or scaffold), the TiO_2 material behaves as an electron-transporting layer. This depends on the CB position of the perovskite with respect to the CB position in the TiO_2, as shown in **Figure 1.10.** Their mutual relationship introduces a driving force for the photo-generated electrons to be extracted at the TiO_2 side. Depending on the choice of the structure, the extension of the exchanging interfaces changes, and this has an impact on the device hysteresis, usually less pronounced in mesoporous architectures. The interfaces and the related behavior play a main role in the operation of the cell, and thus they pose interesting issues to be faced by the scientific community from different perspectives. The concomitantly generated holes is injected into the valence band of the spiro-OMeTAD layer and, through it, carried away towards the lead. The operation principle of a PSC is illustrated in Figure 1.10.

1.4. *Titanium dioxide as a main actor in DSC and PSC*

Titanium dioxide (TiO_2), since its discovering for water photolysis by Fujishima and Honda in 1972,[99] has progressively raised the interest and consequently used in many fields such as for photocatalytic degradation of pollutants,[100,101,102] photocatalytic CO_2 reduction

into energy fuels,[103,104,105,106] water splitting,[107,108,109] solar cells,[110,111] supercapacitors,[112,113] biomedical devices,[114,115,116] and lithium-ion batteries.[117,118,119]

In the photovoltaic field, recent advances were linked to the application of porous TiO₂ in hybrid solar cell architecture with the efficiencies that consequently went up strikingly rapidly[54] thanks to the new ideas of M. Grätzel (DSC)[22,23] and T. Miyasaka (PSC).[24,25,26]

In order to rise the efficiency of DSCs, efforts are being made to optimize various components,[54,120,121] *e.g.* anode, cathode and redox couple. Many main processes occurring in DSCs, such as light harvesting, electron injection, back-electron transfer are primarily dependent on the anode scaffold. Similar concerns have been raised on PSC, comprising the stability and durability of materials and devices.

The most diffused and versatile way to generate scaffolds with nano-TiO₂ architectures is by chemical approaches. They offer a large plethora of fascinating hierarchical and mesoporous structures[122,123,124] with high infiltration capability.

On the other hand, standard physical growth methods have an intrinsic tendency to form compact layers[125] or, based on the Thornton's approach,[126,127] can generate a porosity (not necessarily interconnected) in the nanoscale. Several attempts were done in the literature in order to increase the TiO₂ layer porosity above the Thornton limit by using sputtering or evaporation approaches which generated cauliflower,[128] penniform[129] or zig-zag[125] structures. Some other attempts were done by sputtering in GLancing Angle Deposition (GLAD)[130] to deposit Ti nanostructures[131,132,133,134,135,136,137] which requires ex-situ oxidation for TiO₂ reaction; or by using array of template materials (e.g. polystyrene nano-spheres) to exploit their shadowing effect during TiO₂ growth.[138] They however lack of process simplification (*e.g.* external oxidation, need of templating layers or seeds), in countertrend with the need of high production throughput, or do not provide clear evidences on the applicative valence spanning through different technologies.

Additionally, to assure compatibility with DSC and PSC technologies, the TiO₂ engineering has to face another main critical issue which is the uncomplete pore filling of the scaffold.[139] This relates not only to the infiltration capability of the hole transporting material (the electrolyte in DSC, the spiro-OMeTAD in PSC), but it is also related to the homogeneous distribution of the photo-active material (dye or perovskite) through the layer thickness and to its proper linking to the scaffold (chemisorption). The dye molecules, in fact, need to get to the deep portion of the scaffold and chemically bind to its internal surfaces

with convenient geometries; also, the perovskite needs to deeply infiltrate the scaffold establishing stable, defect-free and tightly linked interfaces to efficiently exchange carriers.

In this framework, the thesis illustrates the empowering offered by newly-designed spongy TiO$_2$ layers deposited by a reactive sputtering method based on the combination between a Grazing-Incidence Geometry and the Local OXidation of the sputtered species (hereby called gig-lox). The growth process produces spongy layers and is conceived to be compatible with the use of any kind of substrate. It is up-scalable as needed for high production throughput. The spongy TiO$_2$ gig-lox layer offers as main empowering a bimodal porosity, with a finely interconnected matrix of pores of convenient size for dye and perovskite infiltration / anchoring. The gig-lox scaffold is integrated in DSC and PSC structures to investigate its behaviour and mainstays. In the last part of the thesis, the use of gig-lox layers for gas sensing is also explored to extend their applicative strength in view of the realization of platforms shared by different functionalities in smart devices.

Aims:

➢ development of a new sputtering deposition method for porous oxides growth;

➢ spongy TiO$_2$ engineering;

➢ exploitation of the TiO$_2$ sponge for molecules and hybrid materials infiltration to form active blends;

➢ optimization of electron injection and collection by the engineered photoactive blend;

➢ spongy TiO$_2$ integration as scaffold in DSC and PSC technologies to compete with consolidated approaches;

➢ sequential sputtering deposition of ZnO:Al as alternative TCO and spongy TiO$_2$ layers

In addition:

➢ exploring alternative chemical deposition methods to deposit porous TiO$_2$ layers;

➢ spongy TiO$_2$ structure exploitation in the gas sensing field.

Chapter 2

Spongy TiO₂ layers deposited by reactive sputtering: standard and new methods

Sputtering deposition is a widely applied method in the research field as well as in the industrial panorama to deposit thin and thick layers, potentially on any kind of substrate. The technique is based on accelerated ions, usually Ar^+, impacting on a source material (the target). The bombardment results in a vapor of atoms and ions (and electrons) escaping the target due to a momentum transfer. Hence, this technique is part of the class of Physical Vapor Deposition (PVD) methods which includes, among the others, Thermal Evaporation Deposition (TED), Electron Beam Physical Vapor Deposition (EBPVD) and Pulsed Laser Deposition (PLD). The most common approach to grow thin films by sputtering is based on the use of a magnetron source, in which a magnet increases the path of the electrons close to the target with a consequent enhancement of the gas ionization. The target can be powered in different ways, ranging from dc for conductive targets, DC pulsed or RF for nonconductive targets.

Although sputtering is a physical process, adding chemistry to deposit oxides or nitrides is feasible through the insertion into the plasma of a reactive gas, in what is called reactive sputtering. As a counterpart, the undesirable reaction of the reactive gas with the target material results in a non-linear behavior of the deposition parameters as a function of the reactive gas flow that can drastically reduce the sputtering rate. To counteract this phenomenon, the fluxes of the various species in the deposition chamber should be tailored in a proper way. Equally important is the deposition rate on the substrate, different from the sputtering rate, mainly related to the gas pressure and composition (once fixed the sputtering power) in the chamber.

The combination of the sputtering conditions (sputtering rate, voltage applied, working pressure etc.) influences the growth mode and rate of the desired film, as well as its microstructure mainly via the fluxes and charge state of the species , the reaction path, the energy per particle and the trajectory.[140]

Sputtering is intrinsically devoted to grow compact layers and to conformally cover morphological features on the growing front. For that, it is a widely consolidated technique in the industries for coatings as well as for layered devices production.

To enlarge the field of application taking advantage from the high throughput, reproducibility and up-scalability of the sputtering method, the advent of new idea for reliable sputtering solutions is highly hoped specially to grow materials with high porosity levels. This would open the field to non-conventional applications (*e.g.* for energy, sensing, photo-cleaning) which require the materials to expose extended surfaces in a small volume. Currently, materials of extreme interest are mainly oxides.

A first attempt in this direction was done by Thornton with his semi-empirical model.[126,127] The Thornton's model defines a range of deposition parameters such that the layer structure can be qualitatively tuned from dense to nano-porous, depending on the deposition temperature and on the gas pressure in the chamber. The method is general and not necessarily applies to reactive sputtering. On the basis of this model, the deposition temperature needs to be taken as low as possible to reduce surface diffusion of the deposited ad-atoms, and the Ar pressure likely high enough to induce a porosity. As a drawback of the method, the pore size cannot be largely tuned and the pore accessibility to introduce materials from outside (gas, liquid or others) is limited. Some complex strategies have been explored, comprising the use of seed layers from an extra step preceding deposition or the ex-situ oxidation of a sputtered metallic layer.

In this chapter, we describe a new not-tricky sputtering method (called *gig-lox*) which fully takes place *in situ* and the related mainstays to deposit spongy TiO₂ layers with a double-scale porosity. It is based on reactive sputtering in oxygen.

We move from a standard parallel plate approach (ppg, section 2.1.) to introduce our modified deposition method that will be immediately after expanded in section 2.2. The new method is tailored on the need to grow nanostructured TiO₂ layers with extended pores accessibility to species of different size and nature, namely photo-actives dyes/materials, liquids and gas molecules, to provide the oxide with transversal empowering. This represents the focus of the thesis.

Gig-lox TiO₂ layers are indeed investigated from different perspectives (section 2.3), comprising morphology, lattice structure and optical parameters. Where needed, gig-lox properties are compared to those of standardly deposited TiO₂ layers (ppg).

2.1. *Sputtering by a method based on Standard Parallel Plate Geometry (ppg)*

The simplest and common geometry encountered in a sputtering chamber consists of two electrodes in Parallel Plates Geometry (ppg) being held at different electrical potential. One electrode is called cathode and is negatively charged; the other is the anode, biased at positive potential. They work generating a glow discharge.

The glow discharge owes its name to the luminous glow of the plasma. When a sufficiently strong electric field is established in a gaseous medium, atoms and molecules will be ionized by accelerated free electrons colliding with atoms. This occurs as they gain sufficient energy to cause ionization of neutral gas atoms, and a chain reaction starts creating more and more free charges. The luminous glow is produced by a process of excited atoms decay.

Once the glow discharge is established, the potential drops rapidly close to the cathode, varying slightly through the plasma column, and changes again close to the anode. Consequently, the electric field is strong in proximity of the cathode (Cathode Sheath region, CSR) and partially at the anode side (Anode Zone, AZ). The electric field in the system is therefore restricted to sheaths adjacent to each of the two electrodes.
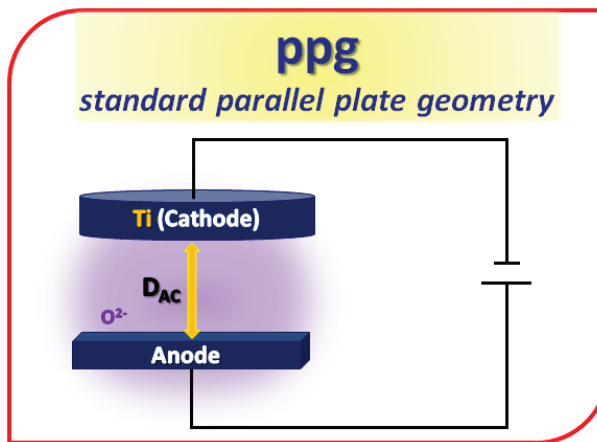
Figure 2.1: Schematic representing a standard parallel plate geometry (ppg) for reactive sputtering deposition.

Figure 2.1 depicts a ppg reactive chamber for the deposition of Ti-oxides from a Ti target in presence of oxygen species.

In the thesis, for the deposition of TiO₂ reference layers, we used a ppg chamber equipped with a 6-inch circular Ti target. The process was carried out in Oxygen ambient by

applying a constant power of 600W (1.24 A, 498V, power loading 4.9 W/cm^2). An O$_2$/Ar flow rate ratio as low as of 5/45 sccm was set which gives rise to a growth rate of 3.7 nm/min and guarantees the needed layer stoichiometry. The large content of argon was chosen to enter the Thornton's chart (**Figure 2.2**)[126]) in a compromise with other constraints (further increasing the value would reduce the deposition rate and affect the layer composition). The deposition processes were carried out at a pressure of 9.0 µbar (7 mTorr - see working region in Figure 2.2) with an anode–cathode distance of 10 cm. In the chamber, a uniform plasma (pink color), linked to the presence of oxygen species, was established between the plates. With this approach, the deposited layers gain an overall porosity close to ~30% volume.
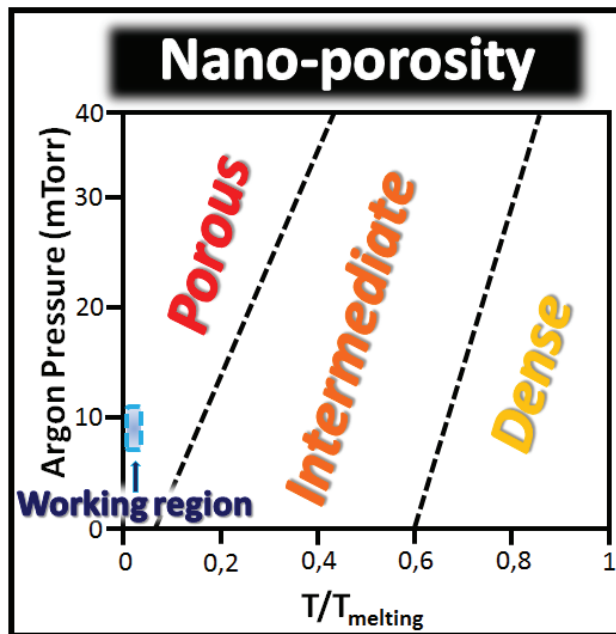
Figure 2.2: Schematic representing the nano-porosity expected on the basis of the Thornton's model. T$_{melting}$ anatase = 1843°C. The working regions refers to ppg and gig-lox processes (from bottom to top, respectively) as described in the text.

2.2. *Sputtering by a new method based on Grazing Incidence Geometry coupled by Local Oxidation (gig-lox)*

The idea of newly-designed TiO$_2$ layers was realised on the basis of the customized equipment sketched in **Figure 2.3(a)**. The source is a 2-inch pure Ti target.
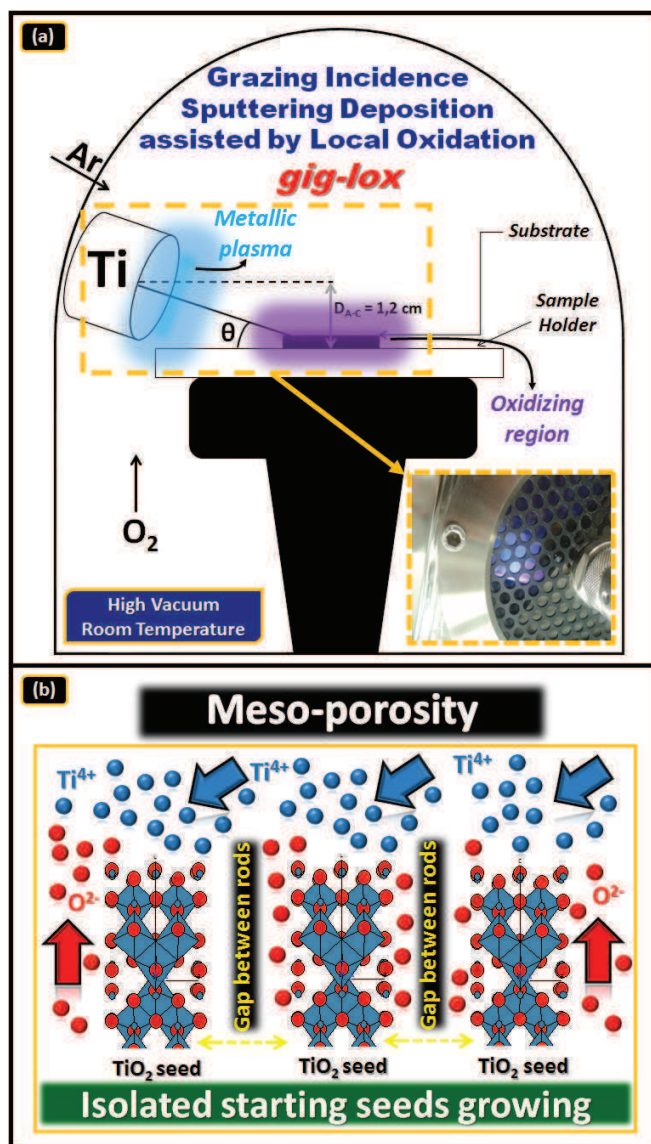
Figure 2.3: **(a)** Customized Sputtering system, which allows working in a separately-charged- regime of the plasma (note that the Ar and O₂ sources are separated); this is combined with shadowing effects. θ is the inclination angle of the source. The inset is a picture of the double plasma (**blue** = metallic and **violet** = oxidizing) established inside the chamber. **(b)** Schematic of the **meso-porosity** achieved by a combination of flux shadowing plus local oxidation. The seeds are formed in-situ at the early stages of the deposition process. The **nano-porosity** is inside the rods and originates from tailoring the Ar pressure in the proper Thornton's regime (Figure 2.2).

We exploited a combined strategy to provide the material with a double-range-porosity during growth. It is fully carried out in the deposition chamber (in-situ) and does not require any template/seed layer or any ex-situ oxidation step. A nano-porosity was

settled by applying Thornton's conditions[126] as indicated in Figure 2.2 (see working region). To add a porosity in the meso-range (tens of nanometers) we exploited a twofold idea: 1) a Ti off-axis source at inclination angle θ (**Figure 2.3(b)**) and 2) the oxidizing zone confined at the sample surface, far from the cathode sheath region. Local oxidation allows a bottom-up growing process of oxidised rods.

For what said, a main parameter is the inclination angle θ (see **Figure 2.3(a)**). An optimum inclination angle of 12.1° was identified in our setup as a compromise between the shadowing effect by the starting TiO₂ seeds (this define the lower limit in θ) and the verticalization of the Ti flux occurring by increasing θ, that has a tendency to progressively close the pores by proceeding the deposition.
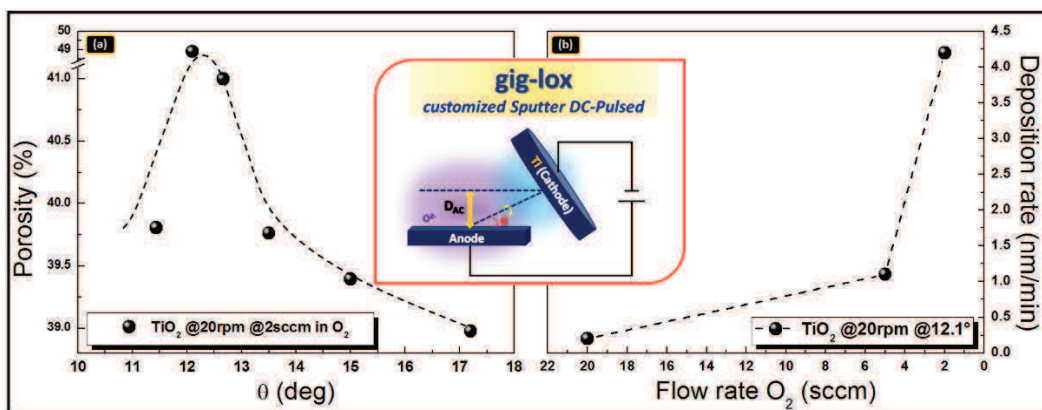
Figure 2.4: **(a)** TiO₂ layer porosity as a function of the inclination angle (θ) of the Ti source with respect to the sample position.; **(b)** TiO₂ deposition rate as a function of the O₂ flow rate at inclination angle of. 12.1°. All data collected at 20 rpm on as deposited samples. The layer thickness is ~800nm.

Besides the off-axis source, the other peculiarity of the equipment resides in the oxygen inlet, being independent from the Ar inlet, and placed in close proximity of the substrate. This configuration, in appropriate conditions which mainly depends on the oxygen flow-rate, allows confining the oxidation at the growing front. As a matter of fact, abounding with the oxygen flow rate reduces the deposition rate due to oxidizing species reaching the target. The data are shown in **Figure 2.4(b)** taken at fixed rotation speed of 20 rpm and inclination angle of 12.1°. They depict an inverse trend of the deposition rate with the O₂ flow rate, being it maximum at 2 sccm (standard cubic centimeters per minute). This value was chosen and fixed for the next surveys.

Effects on porosity and grain size were also recorded by rotating the substrate under the source during deposition, depending on the rotation speed. The grain population and diameter distribution are shown in **Figure 2.5(a)**. Working in static condition was *a priori* excluded due to a lack of thickness uniformity over the sample surface.
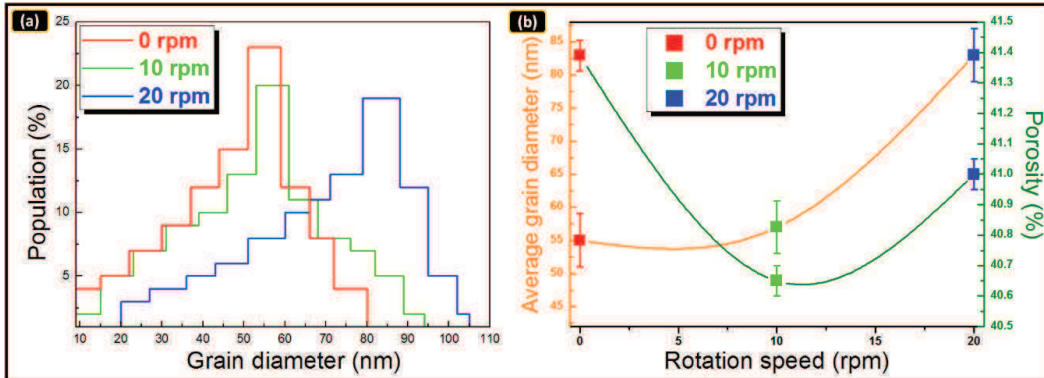
Figure 2.5. – (a) TiO₂ grain diameter distribution as measured by SEM analyses; **(b)** average grain diameter and layer porosity of the TiO₂ layer as a function of the rotation speed. Data taken at Inclination angle 12.7°.

Our results define the use of 20 rpm as a compromise value to frame grain size and porosity in a proper way (see **Figure 2.5(b)**). In **Table 2.1** we show porosity data as a function of: 1) the incident angle applied to the Ti target and 2) the rotation speed applied to the anode.

Table 2.1: Porosity measurements as a function of the different angles applied to the Ti target and as a function of the rotation speed.

TiO₂ gig-lox	
Theta (degree) @20 rpm	**Porosity (%) ±1**
11.4	39.8
12.1	48.9
12.7	41.0
13.5	39.7
15.0	39.4
17.2	39.0
Rotation speed (rpm) @12.7	**Porosity (%) ±1**
0	41.4
10	40.6
20	41.0

In addition, we also explored: the anode-cathode distance in order to optimize the deposition rate; the flow rate of both carrier gas (Ar) and reactive gas (O$_2$); the power applied to the cathodes. All the depositions were done at room temperature to be compatible with any kind of substrate and device.

In our optimized multi-parameters gig-lox process, the Ar flow-rate was settled at 69 sccm, corresponding to a deposition pressure of 14.0 µbar (10.5 mTorr). The O$_2$ flow rate was 2 sccm, at a power of 140 W, a current of 475 mA and a voltage of 295 V, all tuned in order to get stoichiometric TiO$_2$ layers. The corresponding growth rate was 4.25 nm/min, the power loading was 6.9 W/cm^2, the anode-cathode distance was set at 1.2 cm and, during deposition, the substrate was kept rotating at 20 rpm under the beam. Under these working conditions, a double regime is settled up into the deposition chamber (see Figure 2.3(a)): a blue plasma (metallic) in proximity of the source, and an oxidizing region confined at the sample surface (violet color). This allowed reducing charging effects and working under stable conditions, at relatively high deposition rate (limited/avoided target oxidation). As a main empowering, a bottom-up growth process is established by local oxidation of the landing Ti species. The maximum porosity we have got amounts to ~49-50% volume.
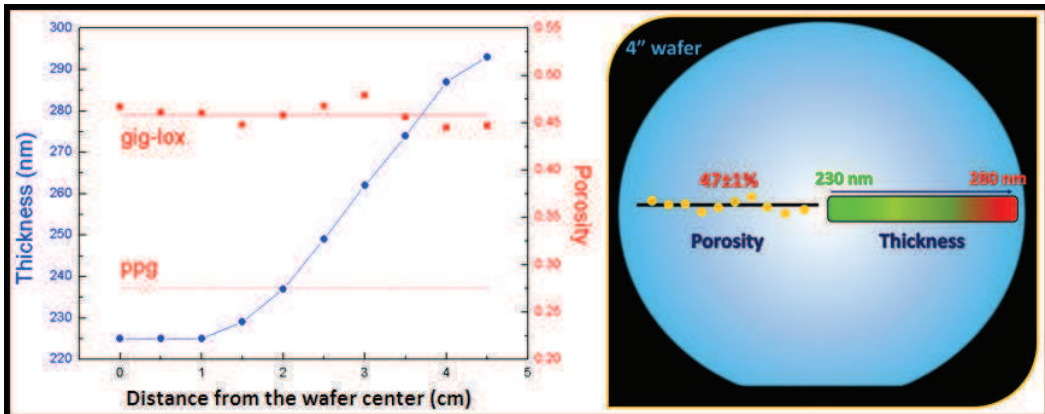
Figure 2.6: Test of thickness uniformity in a TiO$_2$ gig-lox layer deposited on a 4-inch oxidized Si wafer. The plot additionally shows the comparison between gig-lox and ppg layer porosity as a function of the distance from the wafer center. Note that the source in the gig-lox chamber was just 2 inches in diameter.

The up-scalability of the process was tested on a 4-inch Si wafer and the results are shown in **Figure 2.6**. They represent a success in terms of porosity uniformity and an encouraging starting point in terms of thickness uniformity (30% of variation) with a

limitation, in this respect, due to the use of a 2-inch Ti target. Increasing the target size can increase the thickness uniformity.

2.3. *TiO₂ layers grown by ppg and gig-lox processes*

TiO₂ layers have been deposited on corning glass slices or Transparent Conductive Oxides (TCO), depending on the experiment, by using the standard parallel plate geometry in a Kenotec–made Magnetron DC-reactive sputtering or by exploiting the customized grazing incidence geometry in a Kenosistec–made Magnetron DC-pulsed equipment.

In both working geometries, each deposition process is preceded by a pre-sputtering step to clean up the surface of the Titanium target and to eventually remove residual thin oxide layer. With our best process, porous TiO₂ layers were deposited at room temperature with thickness in the range from 150 nm to 1000 nm. The effect of post-deposition thermal treatments was also explored where needed, namely at 200°C for 30 minutes, 450°C 1h, 500°C 30 seconds or 500°C 5 min, using a mixture of 78%N₂:22%O₂ (dry air).

The parameters used for the optimized TiO₂ gig-lox and ppg depositions are collected in **Table 2.2**. The differences in some values, such as the power, are due to the different set-up of the chambers, being DC or DC pulsed. In all, the parameters compensate to have comparable growth conditions in the two geometries (ppg and gig-lox), such as deposition rate and ad-atoms energy (mainly a combination of temperature, power loading and A-C distance). In both cases, the listed parameters allowed rising to maximum the layer porosity.

Table 2.2: Parameters used for the optimized TiO₂ deposition in the two geometries.

Deposition parameters	gig-lox	ppg
Vacuum Pre-Deposition (μbar)	2.0×10^{-4}	1.2×10^{-5}
Working Pressure (μbar)	13.0	9.0
Flow rate Ar (sccm)	69.0	45.0
Flow rate O₂ (sccm)	2.0	5.0
Ti Power (W)	140	620
Ti Voltage (V)	295 - 298	498 - 501
Ti Current (A)	0.472 - 0.475	1.24 - 1.26
Ti Diameter (inch)	2.0	5.0
Power Loading (W/cm²)	6.9	4.9
Anode-Cathode Distance (cm)	1.2	10
Deposition Temperature (°C)	25	160
Deposition Rate (nm/min)	4.2	3.7

2.3.1. *Morphological Analyses of gig-lox layers*

The morphology of the Ti-oxide layers was explored by Field Emission-Scanning Electron Microscopy (FE-SEM) and Coherent X-Ray Diffraction Imaging (CXDI).

2.3.1.1. *Scanning Electron Microscopy analyses*

FE-SEM analyses were performed in plan-view and cross section configurations.
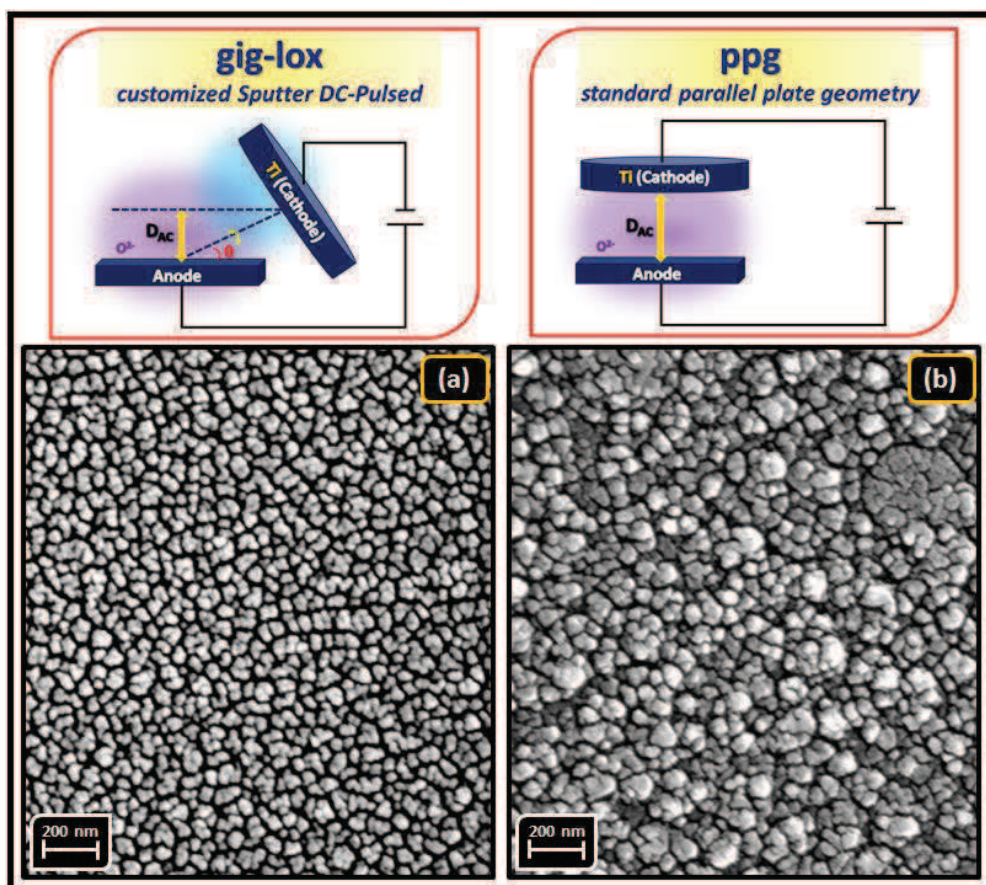
Figure 2.7. FE-SEM images in plan-view of as prepared TiO₂ samples (**a**) in gig-lox and (**b**) in ppg configurations. In the gig-lox layer, the grains size distribution is more uniform than in the ppg material. In this top-view, the grains are smaller in the gig-lox layer.

To avoid charging effects, Au nanograins (~5 nm in diameter) were sputtered on the sample surface or section (in some cases they are visible on the sample surface). The as deposited gig-lox layer (**Figure 2.7(a)**) is characterized by an array of grains, whose

diameter is in the range of ~60-90 nm (Figure 2.5(a)). A network of voids surrounds the TiO$_2$ grains. For the composition of the starting material see the XPS section (Figure 2.18).

As a counterpart, the as deposited ppg layer, shown in **Figure 2.7(b)**, is made of grains with larger size (~50-150 nm) often aggregated in form of cauliflowers (see also Figure 2.14).
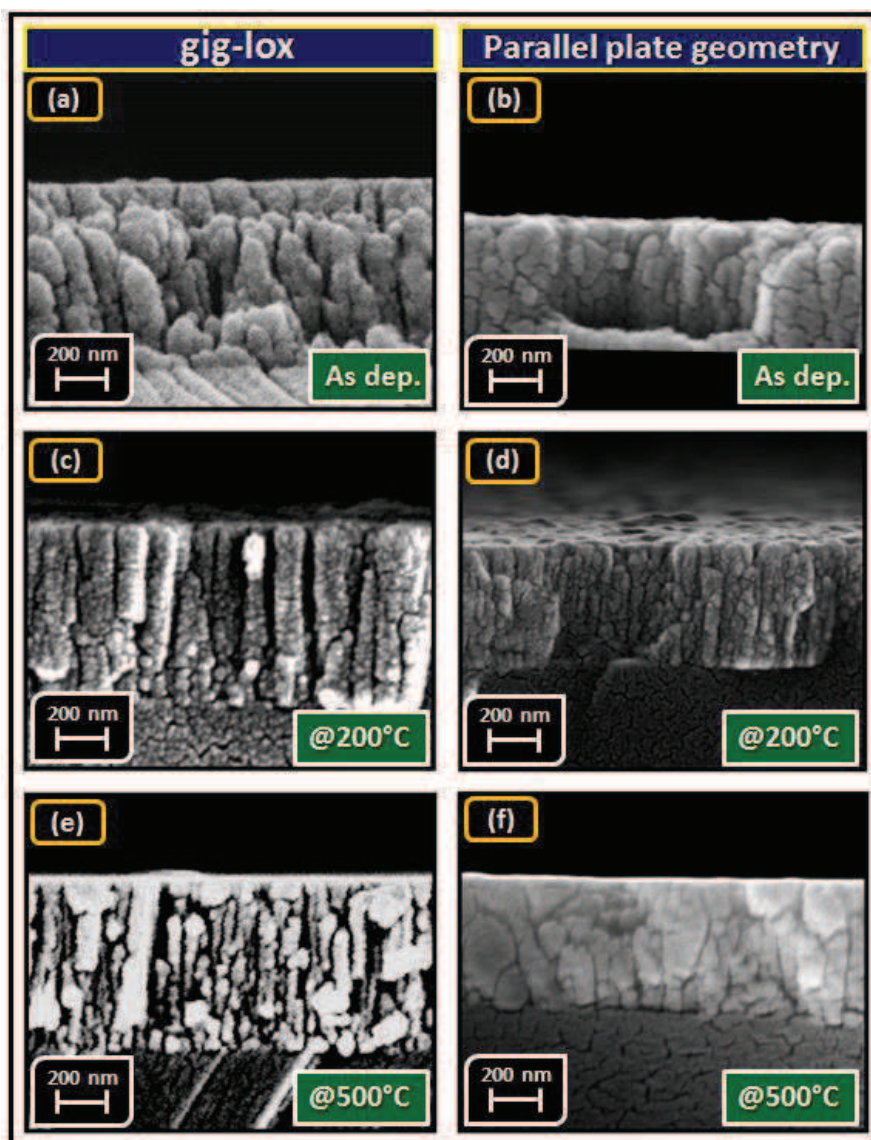
Figure 2.8: Cross-section FE-SEM images of TiO$_2$ layers deposited (**a**) in gig-lox (~800 nm) and (**b**) in ppg (~500 nm) configurations. Layers after thermal treatment: at 200°C 30 min in (**c**) gig-lox, (**d**) ppg; at 500°C 30s in (**e**) gig-lox, (**f**) ppg. The annealings were done in air. Notice how the gig-lox layer, differently from the reference, retains its porosity in depth even after treatment at 500°C.

Figure 2.8(a) visualizes a rods forest established through the section of the as deposited gig-lox layer, with rod diameter in the range of ~80-90 nm, in agreement with its plan-view (Figure 2.7(a)). The rods are separated by ~10-50 nm large voids extending through the whole thickness (being ~800 nm). This represents the meso-porosity of the layer. The ppg layer appears, instead, more compact (see **Figure 2.8(b)**), similarly to what reported in the literature,[128,141,142,143,144] Accordingly, after thermal treatments, grain coalescence causes a shrinkage of the pores in the ppg layer (especially at the surface: see **Figure 2.8(d,f)**). This effect is more pronounced after annealing at 500°C. On the opposite, the gig-lox layer retains its porosity through the whole thickness with the rod forest architecture still preserved (see **Figure 2.8(c,e)**).

2.3.1.2. *Coherent X-Ray Diffraction Imaging analyses*

To enter the 3D architecture of the TiO₂ gig-lox layers, we imaged representative samples using a non-conventional tomographic Coherent X-ray Diffraction Imaging (3D-CXDI) based on synchrotron radiation.[145,146] The investigation was done during the one-month stage at the European Synchrotron Radiation Facilities (ESRF) in Grenoble with the supervision of Dr. Federico Zontone. The technique provides detailed information via the electronic density distribution established through the material on the basis of its local structure (a combination of morphology and stoichiometry). This represents a powerful tool for visualizing the outer and the inner structures of micro particles with a resolution of a few tens of nanometers.[147,148] CXDI is a lens-less imaging technique where the electron density distribution of an isolated object in real space is retrieved by an iterative algorithm that phases an oversampled speckle pattern recorded in reciprocal space in the far field. (more detail in Appendix).[145,149,150]

The CXDI technique has been applied on isolated particles of TiO₂ annealed at 500°C and deposited on Si₃N₄ membranes upon gently scratching the sample, originally deposited on glass substrates at the sputtering chamber. The resulting dimensions of those fragments are in the range 2-6 μm. The reconstructed 3D electron density distributions are scaled in grey level values. With this method, specific sections (**Figure 2.9(a)**), integrated morphology (**Figure 2.9(b)**), or 3D reconstructions can be analyzed and evaluated. Additionally, a porosity parameter P (0 < P < 1) can be extracted from the 3D reconstructions as average

value, scaled to the bulk density, according to the formula:[151]

$$P\ (\%) = \left[\ 1\ - \left(\frac{\rho_{sample}}{\rho_{bulk}}\right)\ \right] \times 100\ , \qquad (6)$$

where ρ_{sample} and ρ_{bulk} are the sample and the bulk electronic densities, respectively. It is simply intuitive that $\rho_{sample} < \rho_{bulk}$ in a porous layer.
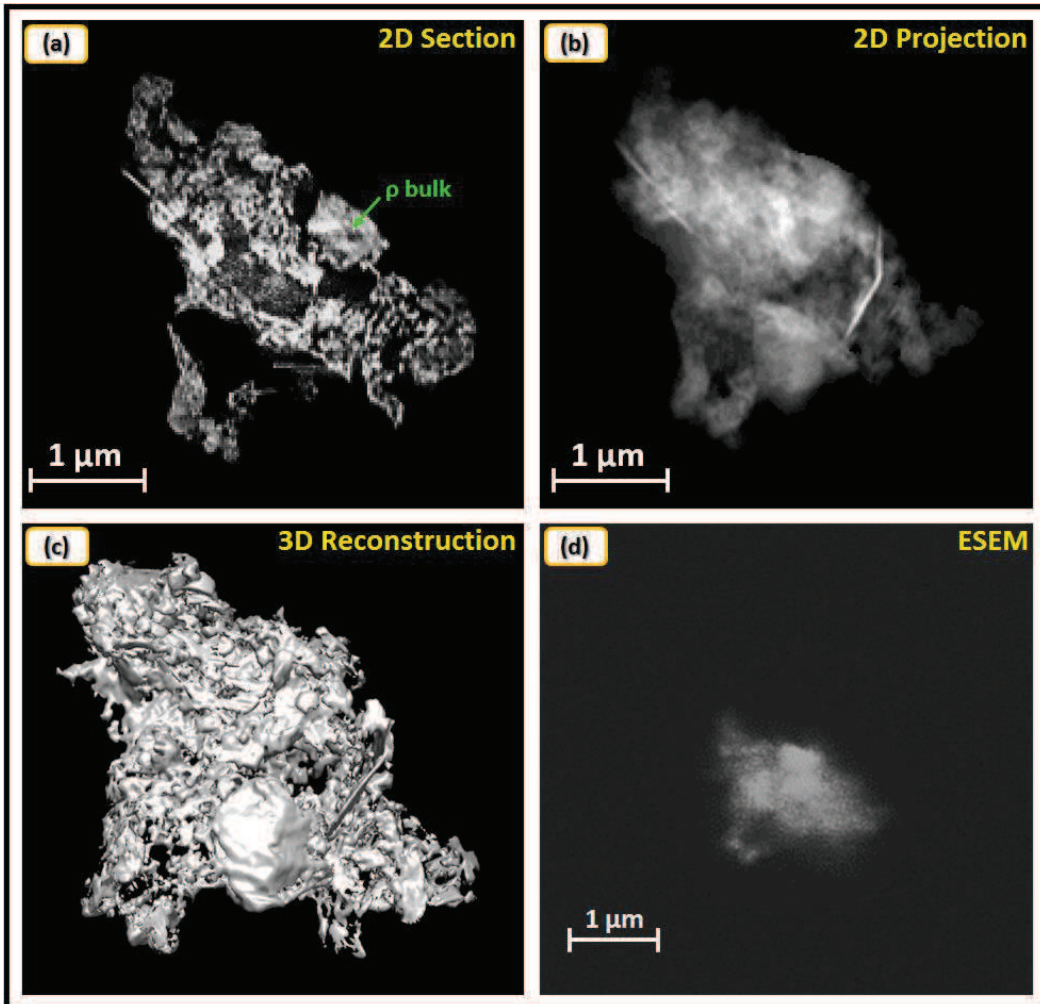
Figure 2.9: **(a)** Central slice used to obtain the ρ bulk (2D section), **(b)** volume representation used to obtain the average ρ sample (2D projection) and **(c)** 3D architecture (3D reconstruction) of the TiO₂ gig-lox layer obtained by CXDI analysis. **(d)** ESEM image used as benchmark of the CXDI reconstruction.

The sample and bulk intensity are estimated by histogramming the grey levels in the averaged slice (2D Projection, Figure 2.9(b)) and in the dense region of the slice (or 2D Section, Figure 2.9(a)), respectively. It was found that, in the area shown in Figure 2.8(a), the

grey level histograms have a quite narrow Gaussian distribution with a nearly constant average value over the region. We assume this value to be representative of the bulk electronic density of the TiO₂ gig-lox sample. We found the average value of the porosity to be P (%) = 46%±5, a value comparable to the one obtained from Ellipsometry measurements (see paragraph: Optical analysis).

Using the Chimera[152] software, we traced to the 3D architecture of the gig-lox fragment by merging the 2D slices (see **Figure 2.9(c)**). The image of the same fragment in **Figure 2.9(d),** acquired by ESEM (Environmental Scanning Electron Microscopy), shows a morphology in agreement with that provided by CXDI. The tomographic imaging offered by CDXI allows analyzing single slides and average or local parameters, such as the local morphology and the surface to volume ratio. As representative of the gig-lox TiO₂, we extracted a surface to volume ratio in favor of the surface, being 0.06 nm^{-1} in the case under investigation. The value well accounts for rods having radius ~30 nm, in full agreement with what shown by SEM analyses, following a calculation for cylindrically shaped rods:

$$\frac{S}{V} = \frac{2\pi rL}{\pi r^2 L} = \frac{2}{r} = 0.06 \, nm^{-1} \rightarrow r = 33 \, \text{nm} \qquad (7)$$

As expected on the basis of the resolution, the technique represents a viable tool to specifically investigate the meso-porosity of the layer we introduced through the grazing plus local oxidation processes. To disclose the nano component and its relationship with the meso-porosity, other tools will be applied (EEP and TEM).

The meso-porosity of the gig-lox TiO₂ layer represents a mainstay introduced by the method that was properly exploited for surface functionalization through dyes or perovskite coatings for the light harvesting in the PV field (Chapter 3), or for gas infiltration in the gas sensing field (Chapter 4).

2.3.1.3. *Enviromental Ellipsometric Porosimetry analyses*

Environmental Ellipsometric Porosimetry (EEP) is used to address the layer porosity in the nano-scale and to gain insight on the pore size distribution. Although the technique is based on optical analyses, we leave here the paragraph to complement the porosity issues from CDXI analyses. The measurements were performed at the Institut Matériaux Microélectronique Nanosciences de Provence (IM2NP) Aix-Marseille Université, Marseille, France by Prof. David Grosso and Dr. Thomas Bottein.

This technique measures the changes of the refractive index during adsorption and capillary condensation of isopropanol into the pores of the material. The volume fraction of adsorbed isopropanol is deduced from the Bruggeman Effective Medium Approximation (BEMA) which compares the refractive index of the empty film (void + TiO_2) with that of the film full of isopropanol (isopropanol + TiO_2).[153] In this calculation, the fraction of TiO_2 remains fixed and the fraction of void (porosity) is considered to be equal to the fraction of isopropanol. We are here assuming (as will be demonstrated by TEM analyses) that the totality of the voids is accessible to the alcohol. The analysis was performed using a refractive index of 2.65 for the as deposited sample, supposing a mixture of anatase and rutile in the local ordering of the amorphous phase; for the samples annealed at 500°C sample, being purely anatase (see Micro-Raman and XRD sections), we used a refractive index of 2.53
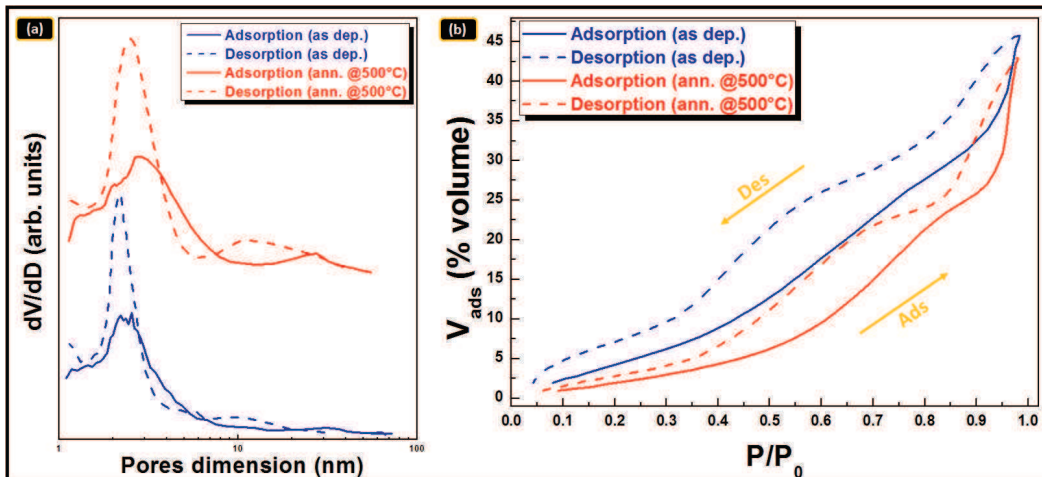
Figure 2.10: (a) Pore size distribution deduced from the Kelvin law for cylindrical interconnected pores for TiO_2 gig-lox in as deposited and after annealing at 500°C conditions. **(b)** Volume of adsorbed gas as a function of P/P_0 for TiO_2 gig-lox in as deposited and after annealing at 500°C conditions.

Based on the TEM images in Figure 2.16(c), pure cylindrical pores will be used for the calculation of pore size distribution (pore aspect ratio = 10). Pore size distribution (in term of diameter) is given in adsorption and in desorption operation mode. In adsorption, the average pore diameter is probed while in desorption average diameter of the interconnection between pores is determined. It is important to note, in **Figure 2.10(a,b)**, that the plot dV/dD gives the distribution of pore size diameter as a function of the number of pores.[153] In fact, large pores will be less visible on this graph even if they can represent a

large volume of the total porosity, because the number of large pores will be lower than the number of small pores for the same contribution in term of volume.

The pore size distribution in Figure 2.10(a) highlights some main points: 1) the bimodal distribution of the pores; 2) the persistence of small-size pores even after the thermal treatment at 500°C; 3) a slight enlargement of the distribution after annealing and a small shift of the maximum rightwards that accounts for a slight increase of the average pore size (further discussed in the next paragraphs). Those small changes are mainly related to the thermal contraction of TiO₂ occurring during crystallization into Anatase layer (a further contribution of pore sintering is not excluded).

In order to get a good vision over the pore distribution in term of volumetric percentage, it is preferable to consider the plot of V_{ads} as a function of P/P_o.[153]

2.3.1.4. *Standard Spectroscopic Ellipsometry analysis*

An average evaluation of the layer porosity was also done by measuring the refractive index (n) of the materials at $\lambda = 550$ nm (photon energy = 2.25 eV) to explore how eventually the overall porosity depends on the grown thickness. The refractive index was converted to layer porosity (%volume) following the formula given in the inset of **Figure 2.11(b)**.[154,155] Also here we used $n_{anatase}$=2.53 for fully crystallized samples and n_{film} = 2.65 for not complete crystallization (a mixture of anatase and rutile local lattice arrangement). The analyse were done using a A. Woollam VASE ellipsometer and a method both reported in Appendix.

To the purpose, gig-lox layers were grown in a range of thicknesses from 350 to 1000nm, at fixed growth parameters. As representative of the others, the data collected over a 350nm-thick gig-lox layer before and after annealing at 500°C are represented in **Figure 2.11.** Figure 2.11(a) shows how a porous layer differs from a compact layer in terms of refractive index, at a fixed lattice structure (anatase). Figure 2.11(b) reports the porosity data vs. thickness.

From this plot, we conclude that: 1) the porosity is not sensibly dependent on the layer thickness in the explored range (see schematic inside Figure 2.11(b)); 2) the porosity could only slightly reduce after annealing at 500°C. Those properties represent main empowering introduced by our method of growth. On the other hand, TiO₂ layers deposited in the Thornton regime by conventional ppg methods, compared to our grazing procedure, have a

tendency to close the pores for long deposition times (large thickness) and/or by annealing the sample.
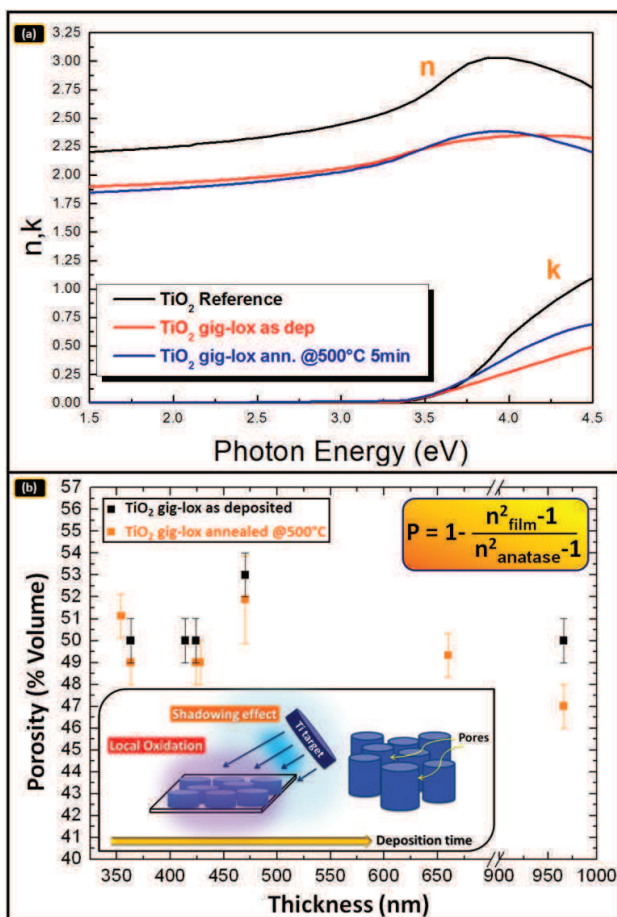
Figure 2.11: Optical analysis performed by SE measurements of TiO₂ gig-lox layer: **(a)** refractive index (n) and extinction coefficient (k) of a porous 350nm-thick layer before and after annealing at and 500°C in air (40%RH) in comparison with a compact TiO₂ anatase reference material: in all cases, n and k are systematically lower than in the reference. **(b)** layer porosity before and after annealing at 500°C as a function of the TiO₂ layer thickness (at fixed deposition parameters) calculated using n at photon energy of 2.25 eV ($\lambda = 550$ nm). In the inset: a sketch on the structural engineering that preserves the layer porosity over prolonged deposition times.

In **Table 2.3** we show a comparison of porosity data in the optimised gig-lox and ppg layers (see table 2.2) of similar thickness. It emerges that as deposited ppg sample is less porous than the gig-lox one and it becomes much more compact when subjected to annealing at 500°C. In contrast, the porosity in the gig-lox sample is pretty unaffected by the thermal treatment (50.8% vs. 48.9%); its refractive index is rather reduced according to the

structural arrangement of TiO_2 in the anatase lattice[65] (Figure 2.13(d) and Table 2.3. See also XRD analysis).

Table 2.3: Refractive index and layer porosity in an 800nm-thick layer calculated by Ellipsometric data fitting.

	gig-lox		ppg	
	As deposited	Annealed @500°C	As deposited	Annealed @500°C
Refractive index @550 nm	1.99	1.94	2.22	2.30
Porosity (%)	50.8	48.9	34	≤21

2.3.2. *Structural Analyses of gig-lox layers*

The crystallographic properties of the gig-lox TiO_2 samples were afforded by a cross-correlation of several techniques: Micro-Raman Spectroscopy, X-Ray Diffraction (XRD) and Transmission Electron Microscopy (TEM).

2.3.2.1. *Micro Raman analyses @532 nm*

Micro-Raman analyses were done on the gig-lox TiO_2 layer in the range 200–1000cm⁻¹ applying a resonant wavelength, tuned on the absorption band of the dye (namely 532 nm).

Following Leon et al,[156] the use of a resonant wavelength in presence of a nanostructured film represents a strategic configuration (called Surface Enhanced Resonant Raman Spectroscopy, namely SERRS) which allows reducing the laser intensity during analyses, thus limiting heating effects. The probed depth is the entire thickness since the penetration depth estimated by the formula[155]

$$d_p = \frac{2.3\lambda}{\theta\pi\alpha} \qquad (8)$$

is 1.34 μm. (λ = laser wavelength (532.0 nm), θ= incidence angle (90°), α = absorption index (3.24×10^{-4})).

Figure 2.12 shows the spectra related to the gig-lox TiO_2 layer after deposition and after thermal treatment at 500°C for 5 minutes in air. Before annealing, the material is mostly amorphous since the peaks are broad due to the average mixture of anatase and rutile (short range ordering). After thermal treatment at 500°C, the TiO_2 structure gains a long-range order in the anatase atomic arrangement[65] (see below the XRD analysis). As a matter of fact, in the spectrum, typical vibrational modes of the anatase phase are found at 399 cm⁻¹ (B_{1g}), 522 cm⁻¹ (B_{1g}, A_{1g}) and at 630 cm⁻¹ (E_g).
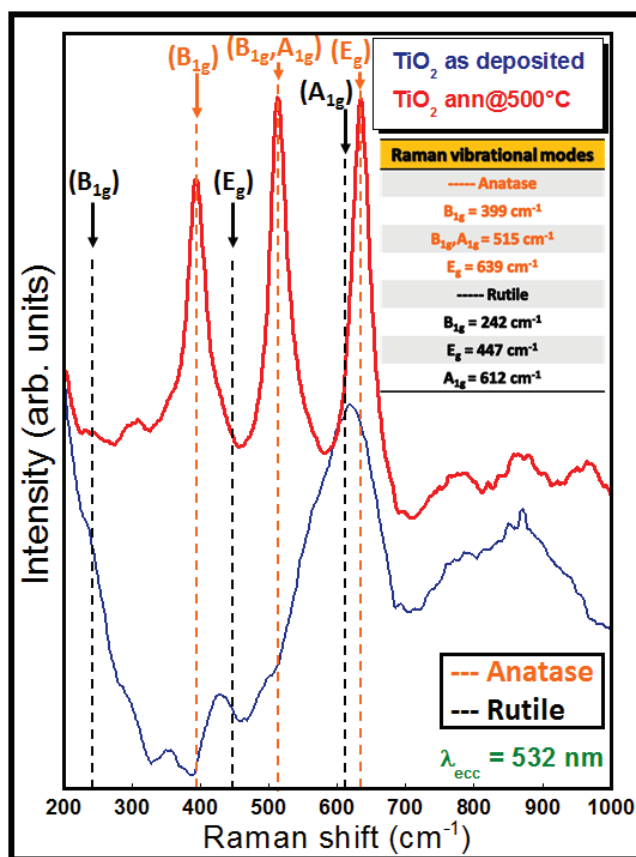
Figure 2.12: Micro-Raman spectra of — TiO₂ as deposited and — TiO₂ annealed @500°C shown in the range 200 – 1000 cm⁻¹.

2.3.2.2. *X-Ray Diffraction analyses*

X-Ray diffraction analyses have confirmed that a structural adjustment can be triggered by a thermal treatment. This is progressively gained by raising the temperature from 200°C to 500°C. **Figure 2.13(a)** shows the progressive nano-structuring of the TiO₂ gig-lox layer in the anatase form vs. different annealing conditions. This structural improvement has effect on the optical bandgap (see next paragraphs) but is ineffective at the side of the layer porosity (Figure 2.16).

Figure 2.13(b) compares the final structures of the gig-lox to that of the ppg layer after a thermal treatment at 500°C,[157,158]. The Full Width at Half Maximum (FWHM) of the diffraction peaks was used to calculate the size of the anatase domains. In particular, in the gig-lox layer FWHM values of 0.41° and 0.49° were measured for the (101) and (004) planes,

respectively; in the ppg layer, instead, the FWHM for the same set of peaks is 0.52° and 0.44°. The domain size was thus calculated by the Scherrer's formula,[159] being in average ~18±1 nm for the gig-lox layer and ~17±1 nm for ppg layer (see **Table 2.4**). Both values settle around a size expected for anatase nanostructures to be more stable than the rutile counterpart.[160] Please remember that the grain size evaluated by X-ray diffraction accounts for small un-defective domains coherently diffracting the incident beam. They are not required to match the grains given by morphological analyses (*e.g.* by FE-SEM).
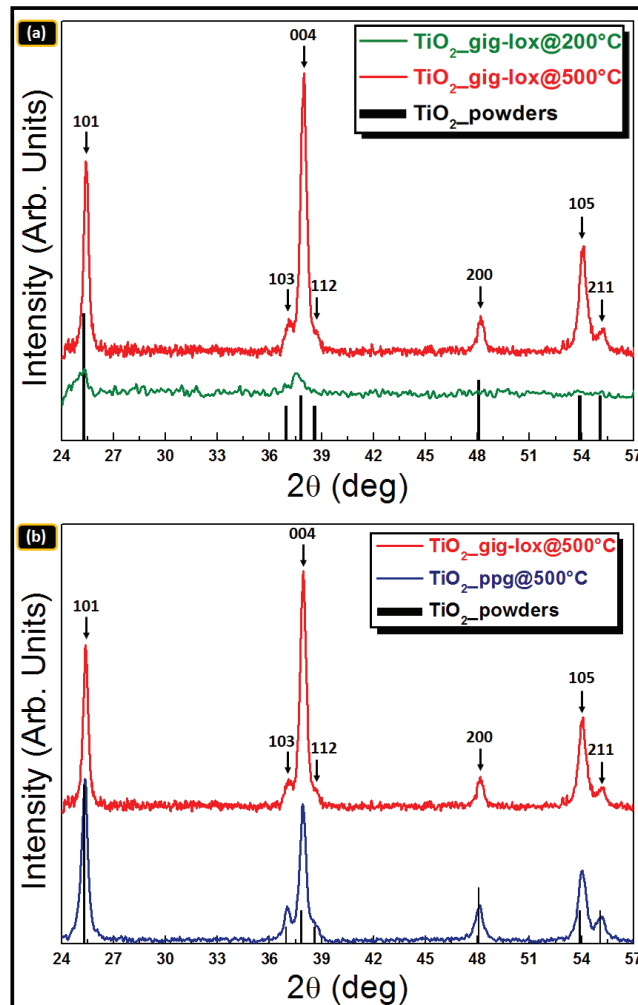
Figure 2.13: **(a)** Diffraction patterns of the TiO₂ gig-lox layer after annealing at — 200°C and — 500°C. With respect to the as deposited material, the nano-grains have gained a partial degree of order at 200°C with their consequent cooperative participation to some diffraction peaks. A full rearrangement of the meso-crystals in anatase is gained at 500°C. **(b)** Symmetric XRD patterns (2θ-ω) of TiO₂ layers deposited in — gig-lox and in — ppg configuration after thermal treatment at 500°C. Both patterns refer to anatase.

Table 2.4: XRD data for the TiO₂ anatase peaks in both deposition geometries.

		gig-lox			ppg		
XRD geometry	hkl	2θ (deg)	FWHM (deg)	Grain Size (nm)	2θ (deg)	FWHM (deg)	Grain Size (nm)
Simmetric diffraction - (2θ-ω)	(101)	25.38	0.41	19.9	25.28	0.52	15.7
Simmetric diffraction - (2θ-ω)	(004)	37.94	0.49	17.2	37.88	0.44	19.1
REFERENCE		2θ$_{(101)}$ = 25,28°					
		2θ$_{(004)}$ = 37,80°					

The statistical distributions of the (004) and the (101) planes (the most intense ones in the diffraction patterns) in the gig-lox layer spanned along the polar (φ) and the azimuthal (χ) coordinates are shown by stereographic projection in **Figure 2.14**.
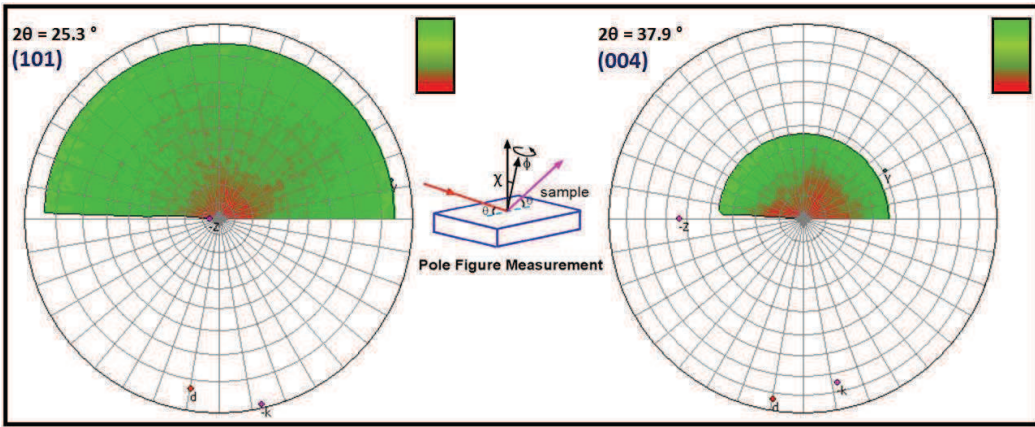
Figure 2.14: Polar figure analyses around the (101) and (004) poles as acquired in the TiO₂ gig-lox sample.

The diffraction data, in all, highlights a general predominance of the (004) growth planes. A similar tendency was found in ppg layers (see also Figure 2.13). Despite this similarity, the gig-lox layer has a larger abundance of domains exposing (004) planes at the sample surface. This was disclosed by measuring the texturing coefficient J as it follows:

$$J = \frac{I_{hkl}}{I_{hkl}^*}\Big/\sum_{hkl}(I_{hkl}/I_{hkl}^*), \qquad (9)$$

which has been calculated for all the detected crystallographic planes[161] and reported in **Table 2.5**. I_{hkl}^* is the expected intensity of peaks in a reference powder.

Most of the works in the literature on 1D-nano-structured TiO₂ materials report the (101) as preferential growth planes;[105,138,162,163,164,165] in some other cases (220)[128] or (004)[138,142,164,165,166] planes were claimed as preferentially selected during the growth process. The different findings must be rationalized in the framework of the specific growth conditions/methods used, namely the anode-cathode distance, the oxygen concentration

during deposition, the power loading, etc. The comparison of literature data elucidates that ad-atoms with high mobility are created under low pressure and/or high potential and/or high deposition temperature,[167] and this favours the exposure of (101) surfaces. This phenomenon is more pronounced in gig-lox layers, with respect to layers grown by conventional ppg, likely due to the peculiar growth procedure, which involves meso-pores and shadowing effects, which will be further elucidated in the next paragraph.

Table 2.5: Texturing coefficient extracted by the TiO₂ anatase peaks, in both deposition geometries. The texturing coefficients is calculated on the basis of the formula[159] reported in the table, where I^*_{hkl} is the expected intensity in a reference powder.

Planes	I*	gig-lox			ppg		
		I	I/I*	J	I	I/I*	J
(101)	100.00	976.20	9.76	0.066	975.20	9.75	0.083
(103)	10.00	166.50	16.65	0.113	215.80	21.58	0.183
(004)	20.00	1420.60	71.03	0.482	825.40	41.27	0.350
(112)	10.00	108.80	10.88	0.074	100.60	10.06	0.085
(200)	35.00	192.00	5.49	0.037	219.20	6.26	0.053
(105)	20.00	544.40	27.22	0.185	427.60	21.38	0.181
(211)	20.00	124.70	6.24	0.042	152.80	7.64	0.065
		$\sum(I/I^*) =$	147.26		$\sum(I/I^*) =$	117.94	

TiO₂ Texturing Coefficient $\quad J = \dfrac{I_{hkl}}{I^*_{hkl}} / \sum_{hkl} (I_{hkl}/I^*_{hkl})$

2.3.2.3. *Transmission Electron Microscopy analyses*

To go deeper into the origin of the preferential orientation of our gig-lox layer along the [001] direction, a complementary study on the structure was performed by Transmission Electron Microscopy. The meso-porosity of the layer is visible in **Figure 2.15(a)** with the pores giving a bright contrast. The dark field image in **Figure 2.15(b)**, collected by selecting a small portion of the (004) planes (**Figure 2.15(c)**), highlights a rod structure made of vertically stacked grains, with a nano-porosity established between them. The grains are laterally faceted as shown in **Figure 2.15(d,e)**, with the facets exposing (101) planes.

Similar architectures made of stacked faceted grains were reported elsewhere[168,169] for TiO₂ synthesized by sol-gel procedures. In those cases, it was proposed that the self-assembling of nanostructures into branched rods is based on a surface free energy gain (thermodynamics) combined with kinetic factors. In particular, the self-assembling of TiO₂ nano-grains along the [001] growth axis is argued to originate from the inherent anisotropy (tetragonal unit cell) and the centro-symmetry (body-centered lattice) of the TiO₂ anatase

lattice. This promotes equi-directional linear development of the nanocrystal lattice mainly along the high-symmetry c-axis.
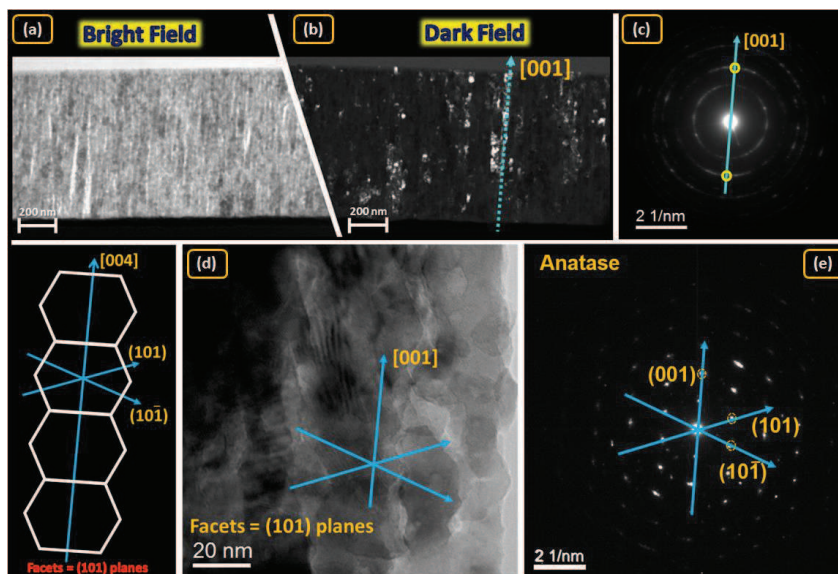
Figure 2.15: TEM analyses of the TiO₂ gig-lox layer after annealing at 500°C: **(a)** bright field image showing the meso-porous structure (the pores give a bright contrast); **(b)** dark field image originating from the region circled in **(c)**, highlighting single grains stacked within the rods (the bright objects); **(d)** detail of a rod with the related SAED in **(e)**. Left panel: a representative schematic of a TiO₂ rod made of stacked grains with facets along (101) and (10-1) planes, with growth axis along the [001] direction, according to XRD data in Figure 2.13. The preservation of this fine structure denotes that the annealing has a conservative effect on the porosity.

In our opinion, the assembly procedure in gig-lox TiO₂ layers resembles a bottom-up growth process in which the chains of atoms (TiO₆ blocks) are mostly pushed upwards during growth while are limited to expand laterally by the grazing configuration of the source. This produces separated rods with meso-pores extending through the whole thickness, as shown in **Figure 2.16(a).** The ppg layer is, instead, made of grains mostly in touch and is compact especially at the bottom half part (**Figure 2.16(b))**. The uppermost part has a typical cauliflower morphology as often reported in the literature.[128] This cauliflower structure remarks the possibility for the TiO₆-based chains to laterally expand out of the main c-axis along the equivalent transversal [101] and [011] directions, similarly to what reported in refs [169,170,171]. Differently from the case of grazing incidence (gig-lox), this lateral growth is made possible by the flux of species (roughly) vertically impinging on the growing front. A high surface roughness (~20 nm) is finally produced in ppg TiO₂ layers in correspondence of the boundaries between adjacent grains.

The given arguments on the two growths mode collaterally explain the texturing along the [001] direction observed by XRD analyses, and its predominance in gig-lox layers.

Figure 2.16(c) summarizes the mainstays of the proposed innovative structure by the aid of a TEM image, taken in a very thin region of the section. The image additionally envisages a role of the structure on the optical response of the material that will be expanded in the next paragraphs.
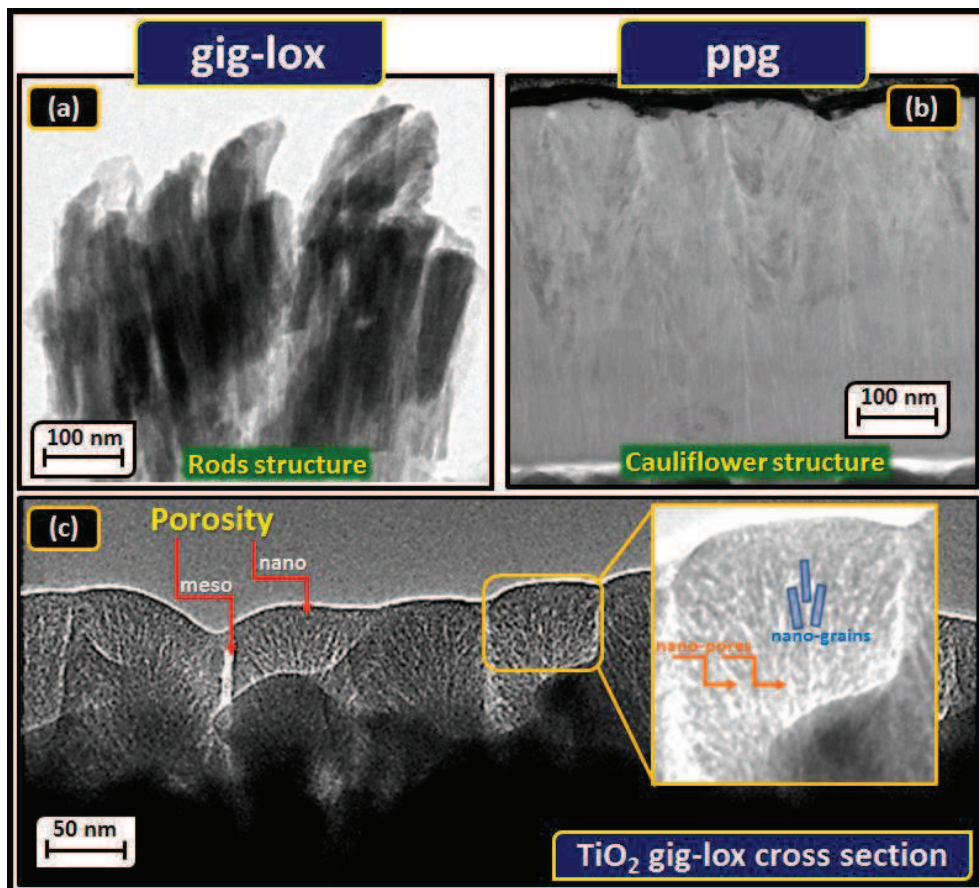
Figure 2.16: TEM images of as deposited TiO₂ layers: **(a)** gig-lox rods and **(b)** cross section ppg grains having a cauliflower structure. The double-scale porosity (nano and meso) of the gig-lox layer is traced. **(c)** TEM cross section of the gig-lox layer showing the material arrangement by nano-grains in a matrix of interconnected nano-pores (zoom in the yellow region).

2.3.3. *Optical response*

The optical response of the layers was evaluated by measuring the layer transmittance and absorbance. As representative of the others, we show the data on ~800 nm-thick gig-lox layers annealed at 500°C in **Figure 2.17(a)**.
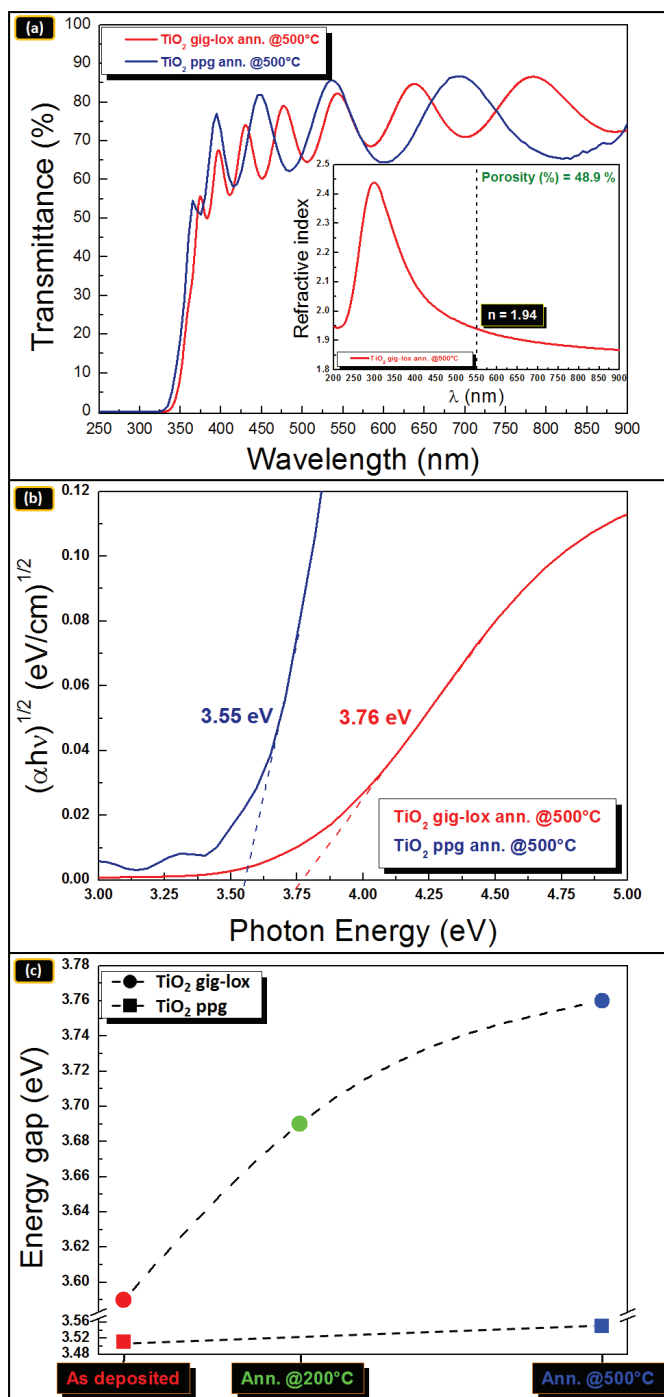
Figure 2.17: Optical analysis performed by SE measurements of TiO₂ gig-lox and ppg layers: **(a)** Transmittance and (inset) gig-lox refractive index; **(b)** Tauc's plot of the layers annealed at 500°C; **(c)** band gap measured by the Tauc's plot.

The transmittance of the gig-lox layer settles to an average value of ~80% above the wavelength of band gap, similarly to what found in the annealed ppg layer (thickness ~550 nm). The comparison for the two layers (Figure 2.17(a)), immediately highlights a different bandgap in the two materials impacting on the onset of the transmittance curve. As a matter of fact, **Figure 2.17(b)** shows two different bandgaps extracted by the related Tauc's plots.

In both kind of materials, the annealing causes an increase of the bandgap (see **Figure 2.17(c)**) with respect to the as deposited values. This is explained by a lattice ordering which is definitely settled at 500°C, in agreement with the XRD and Raman data. Accordingly, the changes in the extinction coefficient k are reported in Figure 2.11(a). The bandgap value measured in the gig-lox TiO_2 layer after annealing is 3.7 eV. Although this is more than what expected in an anatase bulk layer (3.1-3.3 eV), it is not surprising that nanostructure TiO_2 exhibit a higher bandgap due to the low dimensionality of the system, as reported in ref [172]. The superior nanostructuring level of the gig-lox layer with respect to the ppg accounts for the higher band gaps values shown in Figure 2.15(c).

2.3.4. *Surface properties*

The X-Ray Photoelectron Spectroscopy (XPS) technique provides surface analyses to elucidate the chemical bonding established between titanium and oxygen atoms in the two kinds of TiO_2 layers. The investigation was carried out after thermal treatment at 500°C to reset and to level the surface conditions. The binding energy (BE) scale was calibrated by centering the C 1s signal, due to the adventitious/hydrocarbon carbon, at 284.7 eV. The titanium contribution (**Figure 2.18(a)**) shows the typical spin-orbit doublet with the Ti $2p_{3/2}$ component centered at 458.50 eV and Ti $2p_{1/2}$ component centered at 464.30 eV. The O 1s signal (**Figure 2.18(b)**) shows a main component at 530.05 eV (O 1s) attributed to TiO_2 and a shoulder, that is composed by two bands at 531.2 eV (-O-H, due to Ti–OH groups)[173] and at 532.20 eV (-O-C=O, due to carbonate species from C adventitious). The Ti:O atomic ratio is ~1:2.2. The not perfect accordance with the oxide stoichiometric value is likely related to the presence of the hydroxyl/carbonate groups on the surface. On the other hand, in the same regions (see **Figure 2.18(c,d)**), the ppg layer shows similar contributions (slightly shifted in BE but inside the instrumental error, ±0.2) in the gig-lox layer. The difference relies on the larger abundance of –O-H and -O-C=O groups present on the TiO_2 ppg

surface. In **Table 2.6** the values in BE and relative atomic percentage upon deconvolutions of the O 1s band for both samples are listed.

The finding of hydroxyl groups decorating the TiO₂ surface is expected to have an impact on the hydrophilicity/hydrophobicity of the material, as further investigated in Chapter 4.
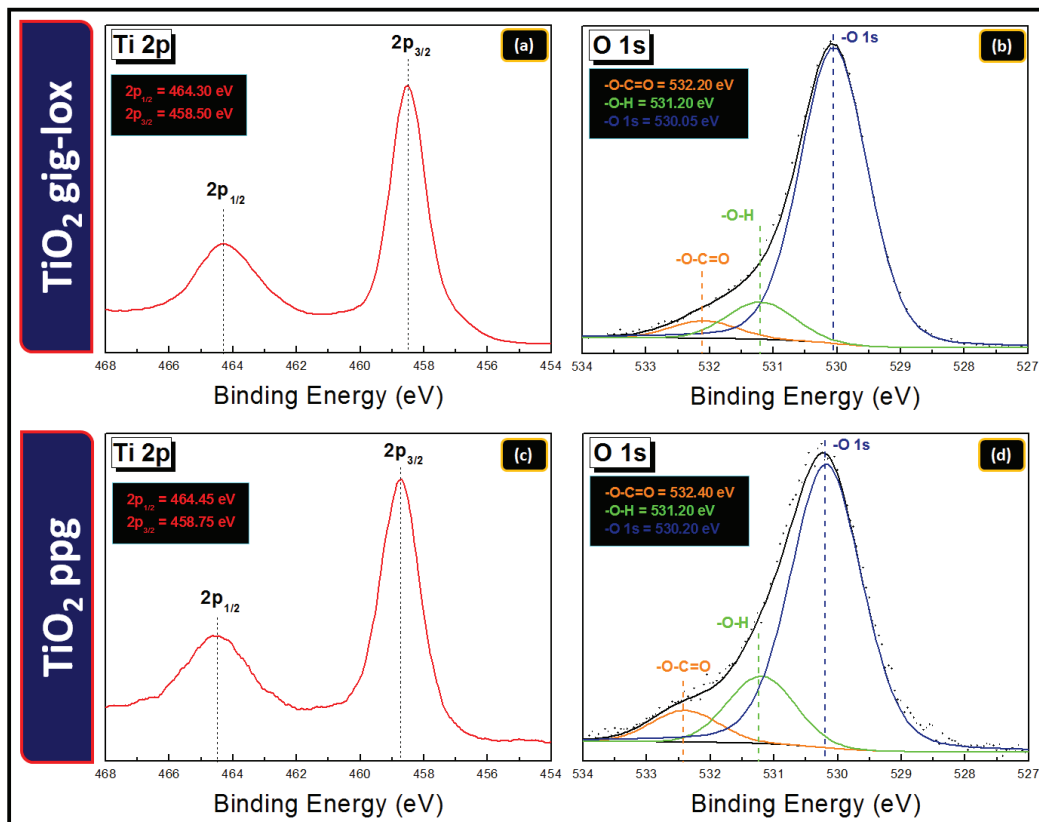
Figure 2.18: HR-XPS spectra of TiO₂ gig-lox and ppg layer annealed at 500°C in **(a,c)** Titanium and **(b,d)** The Ti:O atomic ratio is affected by the presence of some –O-H and -O-C=O groups on the TiO₂ surface.

Table 2.6: Contributions of TiO₂ gig-lox and ppg layer in the O 1s region.

O 1s region	gig-lox		ppg	
	BE (eV)	Relative at (%) ±0.2	BE (eV)	Relative at (%) ±0.2
-O-C=O	532.10	4.6	532.40	7.3
-O-H	531.20	9.8	531.20	15.6
-O 1s	530.05	85.6	530.20	77.1

Chapter 3

Gig-lox TiO₂ as a scaffold for hybrid solar cells

We here briefly recall some main points on hybrid solar cells technologies and on the related need of using porous TiO₂ scaffolds.

Among the possible applications that can take advantage from the use of TiO₂ nanostructures having multi-scale-porosity, DSCs (Dye Solar Cells)[174,175] have been pushed to a high level of maturity and, nowadays, represent an interesting alternative to semiconductors technologies.[22,176] As a matter of fact, the light-to-current conversion efficiency was rapidly raised up to 13.6%[177] in optimised DSC architectures. More recently, prof. Tsutomu Miyasaka first initiated the idea of replacing the dye with hybrid Perovskites (PSC) materials[24,45,61,62,178] as sensitizer, and this innovation allowed getting efficiency values as high as 22.1%.[63,64] In the standard scheme of the photoanode of a DSC[23] or a PSC,[24] a mesoporous thin film of nanosized TiO₂ crystals is deposited on a Transparent Conductive Oxide (TCO), annealed for grains sintering and anatase crystallization (typically at 500°C), and subsequently imbued with a photoactive dye[35,179,180,181,182] or infiltrated with perovskite.[24] In both cases, mesoporous TiO₂ in the anatase polymorphism has emerged as a main choice for the cell scaffold.[22,62,63,161]

In this chapter, we apply gig-lox TiO₂ scaffolds in photoanodes of DSC and PSC architectures for investigation purposes. Solar cells are also realised to provide the reader with proofs-of- concept on the mainstays of this new material.

3.1. *Dye-Sensitized Solar Cells*

The spongy TiO₂ gig-lox scaffold offers as mainstay for DSCs its bimodal porosity further empowered by the finely interconnected pore matrix and by the pore size, comparable with typical dye size (see chapter 2 for the morphological details). We demonstrate that this allows standard N-719 molecules deeply and copiously entering the layer (dye loading) and establishing a multiple-branch anchoring on the pore walls

(chemisorption). To this purpose, the effect of the solvent, used to dissolve the dye, is also evaluated using CH_3CN (acetonitrile) or CH_3CH_2OH (ethanol) to vary polarity, dipole momentum (μ), permittivity constant (ε), pKa, Gutmann of acceptor/donor number[183] (see **Table 3.1**) in the interaction of the dye with the inner TiO₂ surfaces. As a combination of all the advantages offered by the spongy gig-lox architecture in the dye chemisorption, an incremental density of photo-generated electrons injected into the gig-lox scaffold by 4 orders of magnitude with respect to the intrinsic carrier level after 1 sun illumination is recorded. The experiment measures the overall capability of the dye-TiO₂ blend to effectively harvest photons and to drive the photo-generated electrons towards an external load.

The complete solar cells, having the TiO₂-dye blend as photoanode, exhibit performances comparable to reference cells containing a standard commercial TiO₂ nano-array as scaffold, thus testifying that our gig-lox deposition method can definitely compete with chemical routes.

Table 3.1: Solvents properties used to dissolve N-719 for TiO₂ functionalization.

Properties	CH_3CN	CH_3CH_2OH	H_2O
Polarity	37.0	24.0	80.0
μ	3.5	1.7	1.9
pKa	25.0	16.0	15.7
ε	38.8	28.0	81.0
AN Gutmann	19.3	37.1	54.8
DN Gutmann	14.1	20.0	18.0

3.1.1. *Dye chemisorption into the gig-lox scaffold*

We exploited the peculiar nano-structuring of the optimised gig-lox layer[65,154] and the high overall porosity (~50% volume[65,184]) to fabricate DSC's photoanodes. To this intent, TiO₂ layers were sensitized with di-tetrabutylammonium cis-bis (isothiocyanato) bis (2,2-bipyridyl-4,4-dicarboxylato) ruthenium(II) (N-719, Aldrich) by immersion into Ethanol or Acetonitrile solutions with the Ru-complex using a concentration in the range of 2×10^{-5} - 2×10^{-4} M for 18h at room temperature in dark conditions. The sensitized layers were withdrawn from the solution, rinsed in pure Ethanol/Acetonitrile to remove any physisorbed dye and dried under flux

of nitrogen. In Appendix, you can find the full procedure to build up complete DSCs.

3.1.1.1. *Micro-Raman analyses @532 nm*

Micro-Raman analyses at high wavenumbers describe some aspects of the interaction between the dye and its scaffold after dye loading. For the analyses, we applied the same condition as in Chapter 2.
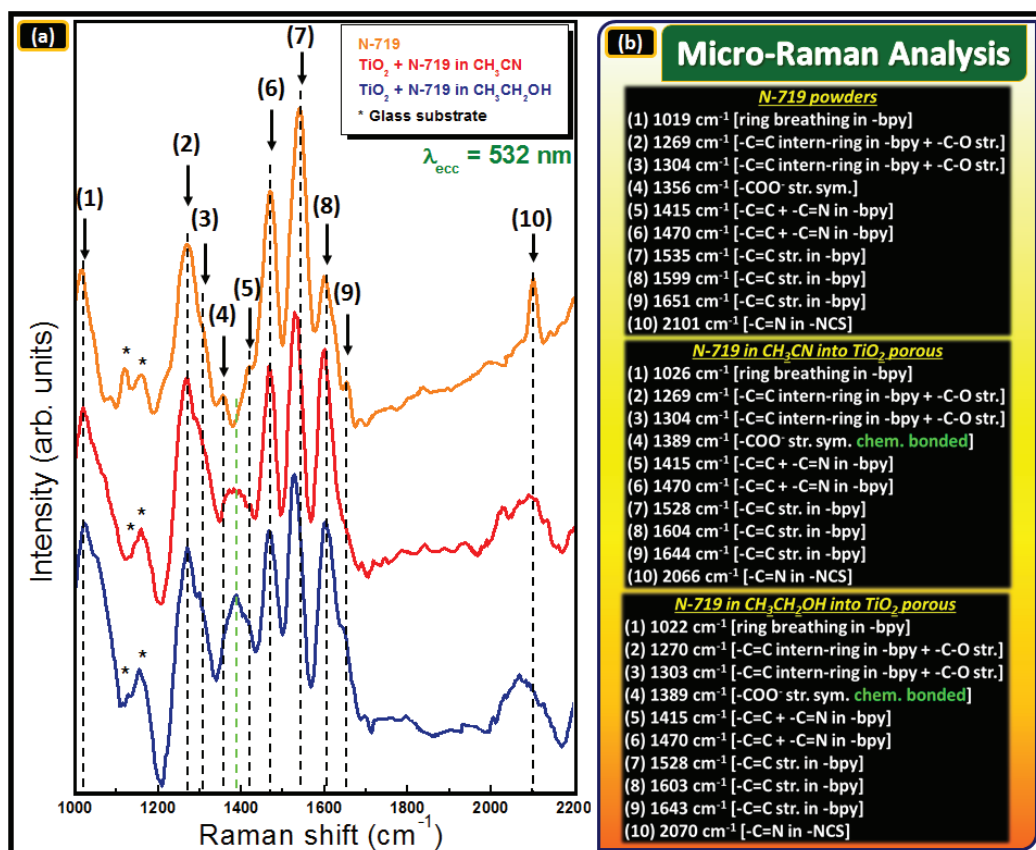
Figure 3.1: Micro-Raman spectra of **(a)** — N-719; TiO₂ functionalized with N-719 in — CH₃CN or — CH₃CH₂OH; **(b)** list of the Raman vibrational modes in the N-719 powder or infiltrated into the TiO₂ layer (the scaffold).

Figure 3.1(a) shows the micro-Raman spectra of the TiO₂ layer annealed at 500°C and subsequently functionalized with N-719 diluted in CH₃CN or in CH₃CH₂OH compared to the N-719 reference powders. The periphery of the N-719 complex (see molecular structure in the inset of **Figure 3.1(b)**) is made of two carboxylic acids, two carboxylates (at the TBA⁺ side) and two thiocyanate groups. In the reference spectrum, we consistently observe the

typical vibrational modes related to -COO⁻, -NCS and also of the bipyridine groups in the range 1000-2200 cm⁻¹ (see in Figure 3.1(b) the complete list) as markers of the molecular structure. In the spectrum, the contribution of $\nu(C=O)$ vibrations (1720 cm⁻¹) is weak probably due to some electronic noise and/or fluorescence phenomena.[185]

The main information we extract from the spectrum of the functionalized TiO₂ sample is related to the contribution from the $\nu_{sym}(COO^-)$ mode (peak n°4 in Figure 3.1(a)). With respect to the reference, wherein the $\nu_{sym}(COO^-)$ mode originates from the TBA-related groups (two per molecule), this contribution is red-shifted (1389 cm⁻¹), larger and relatively more intense (*e.g.* compared to the -C=N signal coming from the bpy ring). This represents a first indication of the dye chemisorption[186] into the surfaces of the porous TiO₂ layer distributed over the whole thickness. The other contributions in the spectra, which are sufficiently intense due to surface enhanced effects, are mostly preserved after anchoring, excepts for the thiocyanate groups. The $\nu(-NCS)$ band is, in fact, broader and blu-shifted (at 2066 cm⁻¹) compared to the reference spectrum of the pure dye (peak n°10 in Figure 3.1(a)), implying that the -NCS ligands feels the TiO₂ surface proximity.[156,186] Unfortunately, the Raman data do not allow disentangling the role of the solvent in the molecular anchoring, as shown in Figure 3.1(a), and therefore this aspect was explored by other techniques.

3.1.1.2. *ATR-FTIR analysis*

To have further and complementary information on the anchoring mechanism, being the pre-requisite to rationalize the charge transfer, we applied the Attenuated Total Reflectance - Fourier Transform Infra-Red technique (ATR-FTIR). The penetration depth is here 1.32 μm according to the formula[187]

$$d_p = \frac{\lambda}{2\pi(n_1^2 sen^2\theta - n_2^2)^{0.5}} \qquad (10)$$

where λ is the wavelength of light (2.2 μm), θ is the angle of incidence (48°), and n_1 and n_2 are the refractive indices of the Internal Reflection Elements (IRE = diamond 2.42) and the TiO₂ gig-lox sample (1.84), respectively. We have especially focused on the range 1200-2200 cm⁻¹ of: 1) the N-719 dye (powders), 2) the TiO₂ meso-porous layer annealed at 500°C (baseline) and 3,4) the N-719 -functionalised meso-porous TiO₂ layer (annealed at 500°C) using CH₃CN or CH₃CH₂OH as solvent. Special focus was addressed towards the two carboxylic acids, the two carboxylates and the two thiocyanate groups representing the main

actors for the anchoring.[188,189,190,191,192]

Figure 3.2(a) shows the ATR-FTIR spectra in low wavenumber region (1200-1900 cm^{-1}) of the four samples. The first finding is represented by the difference, in intensity and shape, between the spectra of TiO₂ without and with N-719. More in detail, the spectrum of the TiO₂ layer shows, in the 1300-1700 cm^{-1} range, the typical vibrational modes of C-O and H₂O adsorbed on the TiO₂ surface; whilst, after chemical treatment with the dye-complex, those bands are modified (Figure 3.2(a)) gaining a certain similarity with those of pure N-719: the differences are ascribable to the dye-TiO₂ surface interaction. We use as internal standard the vibrational mode of the bipyridine at 1547 cm^{-1}. On that basis, upon infiltration/binding, significant variation at the bands of the carboxylate (symmetric and asymmetric) and carboxylic acid groups are recorded in comparison with the reference spectrum (the dye). In detail, the bands related to the COOH groups, namely ν(C-O) and ν(C=O) at 1227 cm^{-1} (n°1 in Figure 3.2(a)) and 1703 cm^{-1} (n°7 in Figure 3.2(a)), respectively, are modified as follows: the ν(C-O) overlaps with the Ti-O lattice contribution; the ν(C=O) band is reduced, and this is compatible with a phenomenon of carboxylate deprotonation which would imply a tendency of the dye-complex to be covalently bonded on the TiO₂ surfaces. Note that this information on the behaviour of the C=O groups after anchoring complements with the Raman information, wherein the C=O peak was not detected likely due to fluorescence effects.

The anchoring geometry of the dye on the TiO₂ surface is argument of debate and likely it depends on the specific surfaces exposed. Several research groups,[156,190,191,193,194] have used as an empirical criterion the difference in the vibrational stretching of the carboxylate groups in N-719 ($\Delta\nu = \nu_{as}(COO^-) - \nu_{ss}(COO^-)$) located in the infrared region ("as" stems for asymmetric stretching; "ss" stems for symmetric stretching; see table in Figure 3.2(b)). This approach applies in comparing the isolated state ($\Delta\nu_{salt}$) and the adsorbed state ($\Delta\nu_{ads}$) of the dye[195] and gives rise to three possible scenaria: 1) $\Delta\nu_{salt} < \Delta\nu_{ads}$ = unidentate (easter linkage); 2) $\Delta\nu_{salt} > \Delta\nu_{ads}$ = bidentate chelate or bridge; 3) $\Delta\nu_{salt} >> \Delta\nu_{ads}$ = chelate ("salt" stands for neat/solid state, namely the isolated molecules; "ads" stands for adsorbed state, namely the adsorbed molecules). We explored all those possibilities, also taking into account the high surface availability to the molecular anchoring due to the high surface to volume ratio offered by the gig-lox layer (50% porosity, S/V = 0.06 nm^{-1}: see chapter 2).[65]

We have thus measured a $\Delta\nu_{salt}$ = 246 cm^{-1} and $\Delta\nu_{ads}$ = 227 cm^{-1}. These results lead us to argue that the N-719 molecules have established a bidentate linkage, being chelate or bridge-type ($\Delta\nu_{salt}>\Delta\nu_{ads}$), to the TiO₂ surfaces (see schematic in Figure 3.2(a)). Theoretical studies[189,196] have highlighted that the bidentate chelation links are unstable, thus leaving higher the probability of being formed bridging coordinations in our samples. Besides that, there is a trace of non-reacted -COOH groups testified by the shoulder at 1713 cm^{-1} (-C=O group, marker n°7 in Figure 3.2(a)) ascribable to not anchored carboxylic acid. A certain amount of TBA$^+$ is recorded on the functionalized sample on the basis of peak n°4 in Figure 3.2(a). No clear differences by using the two solvents can be still discriminated (see Figure 3.2(a)).
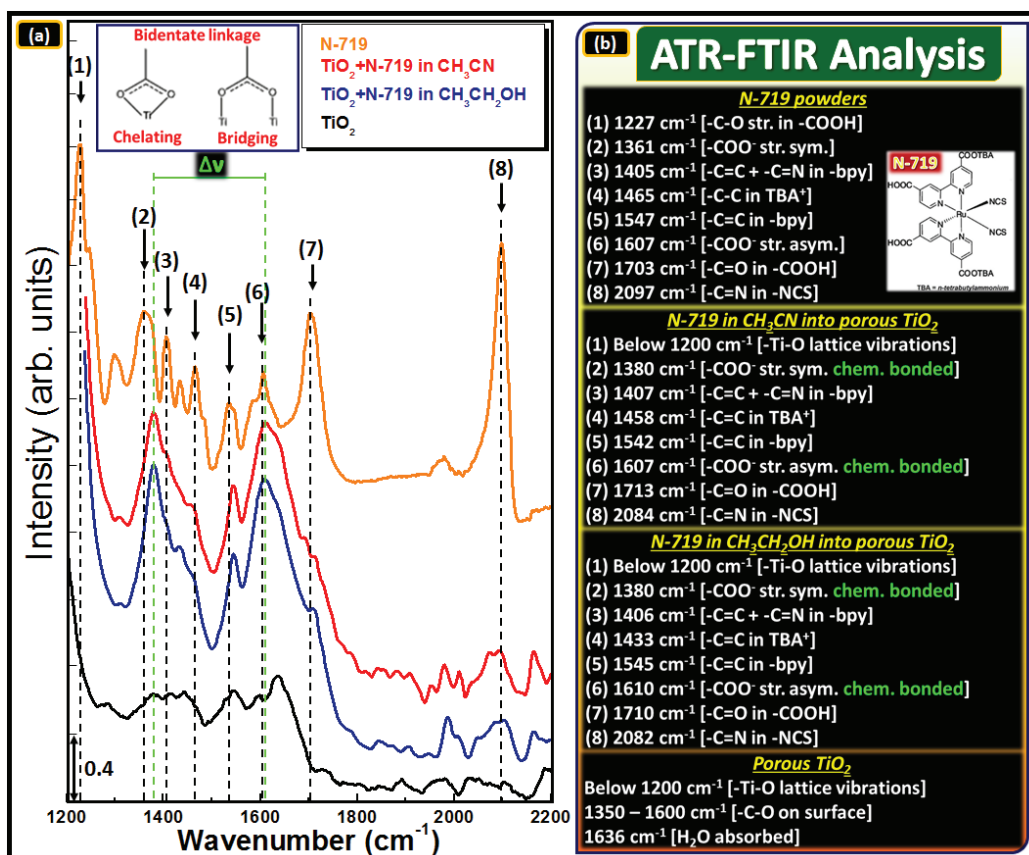
Figure 3.2: ATR-FTIR absorbance spectra of **(a)** — TiO₂ annealed @500°C without N-719, — TiO₂ annealed @500°C with N-719 in — CH₃CH₂OH or in — CH₃CN and — N-719 powders; **(b)** list of the Infra-Red vibrational modes in the N-719 powder and in the molecules infiltrated into the TiO₂ layer (the scaffold).

A further important marker on the molecular interaction with the TiO$_2$ surface is represented by the ν(NCS) band which is measured, in the not-anchored molecules, at 2097 cm^{-1}. Instead, in the chemisorbed molecules it contributes at 2084 cm^{-1}: the band is weak and slightly blue-shifted with respect to the reference powders. This means that, after dye loading, a close relationship between the –NCS groups and the TiO$_2$ surfaces is established, with a consequent modification of the dipole momentum of the ligand (see peak n°9 in Figure 3.2(a) and **Figure 3.2(b)**). That finding is in agreement with the Micro-Raman data (Figure 3.1(a) and related comments). The implication, weighted on the use of the different solvents, will be disclosed below by photocurrent measurements.

3.1.1.3. *X-Ray Photoelectron Spectroscopy analyses*

To go deeper inside the anchoring mode of the dye on the TiO$_2$ surfaces and to discriminate between the solvents, we have performed XPS analyses in N-719 sensitised TiO$_2$ gig-lox layers using CH$_3$CN or CH$_3$CH$_2$OH to dissolve the dye, in comparison with the N-719 powder (reference). All HR-XPS spectra reported in **Figures 3.3(a-f)** were calibrated using the C adventitious peak (-C-C/-C-H) at 284.70 eV.

The C 1s and Ru 3d HR-spectra of the three samples are shown in **Figures 3.3(a)**, **(b)** and **(c)**. The spectra reveal, for the C contributions, four peaks upon deconvolution *i.e.* -COOH, -COO$^-$, -C-N and -C-C/-C-H. In the same region, the Ru contributes with typical 3d$_{3/2}$ and 3d$_{5/2}$ components of the spin-orbit coupling, being the first one hidden under the major C 1s peak at a distance of 4.2 eV from the Ru 3d$_{5/2}$, instead located at 280.55 eV (in the N-719 powders).[197] It was taken into account in the overall deconvolution procedure.

A main information resides in the broad peak located at around 288.5 eV which originates from a combination of two contributions due to carboxylate (-COO$^-$) and carboxylic acid (-COOH) carbons. Regarding the detailed position of the -COOH/-COO$^-$ groups and Ru 3d$_{5/2}$ peak, we found that they shift toward higher binding energies as the dye is on the TiO$_2$ surface. This phenomenon is in agreement with the shift of the Ti 2p peaks shown in the **Figure 3.4,** there explainable by a change in the surface dipole (change the work function)[198,199] and/or by a change in the Fermi level position in the band gap, which shifts all the core levels of TiO$_2$[200,201] to higher energies. The latter is owing to the anchoring of the dye molecules through the COO$^-$ groups on the surfaces and thus confirms what

discussed by Infra-Red and Raman spectroscopies.
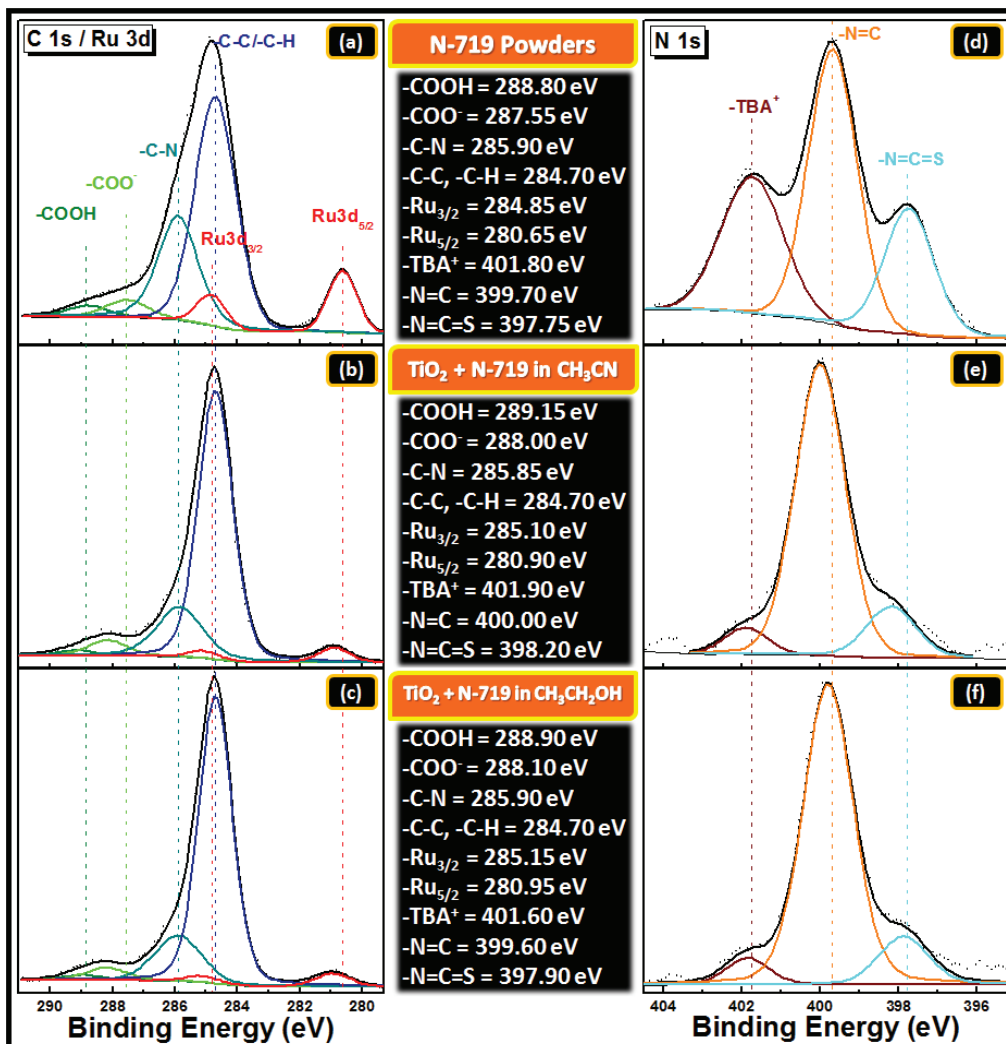
Figure 3.3: HR-XPS spectra in the C 1s/ Ru 3d region of **(a)** N-719 powders, N-719 in **(b)** CH₃CN and **(c)** CH₃CH₂OH -treated dye-TiO₂ gig-lox layers. HR-XPS spectra in the N 1s region of **(d)** N-719 powders, N-719 in **(e)** CH₃CN and **(f)** CH₃CH₂OH - treated dye-TiO₂ gig-lox layers.

In addition, we found that there are relatively more carboxylate groups in the TiO₂ gig-lox sample functionalized with N-719 in CH₃CN than in the other one sensitized in CH₃CH₂OH: namely the COO⁻/COOH ratio is 3.5 vs. 2.3 in the two solvents, respectively, being instead 1.6 in the reference powder (see **Table 3.2**). According to this finding, it is expected that acetonitrile molecules act on the dye deprotonation more than ethanol molecules. This is consistent with what reported by Azab et al[202] on the basis of the Proton-Solvent

Interaction; namely, since acetonitrile is a weak basic solvent, the H^+ ion becomes less stabilized with consequent increase of the activity coefficient of the protons (high pK_a value). The action of the CH_3CN at the dye periphery, in particular on the -COOH deprotonation, finally impacts on a higher probability of chemisorption via the carboxylate groups in the sample treated in acetonitrile than in the other treated in ethanol.[203,204,205,206,207]
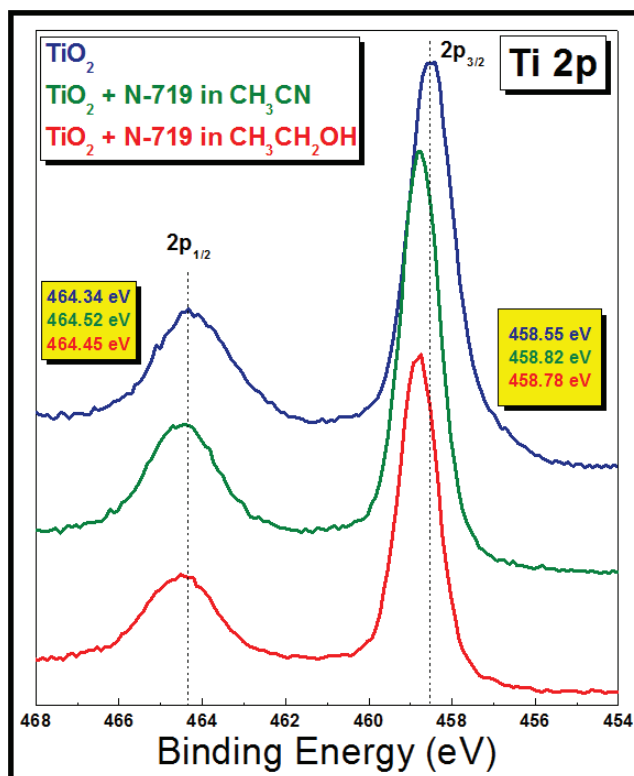
Figure 3.4: HR-XPS spectra of — TiO₂ gig-lox annealed at 500°C, TiO₂ gig-lox annealed at 500°C sensitized with N-719 in — CH₃CN or — in CH₃CH₂OH.

Table 3.2: Ratio between the area of C and oxidized C peaks, area of carboxylate and carboxylic acid groups and average FWHM from the deconvolution.

Samples	Area C/Cox	Area COO⁻/COOH	Average FWHM
N-719 Powders	10.9	1.6 ± 0.2	1.56 ± 0.01
TiO₂ + N-719 in CH₃CN	12.9	3.5 ± 0.2	1.58 ± 0.01
TiO₂ + N-719 in CH₃CH₂OH	15.0	2.3 ± 0.2	1.57 ± 0.01

Figures 3.3(d), **(e)** and **(f)** represent the HR-XPS spectra taken in the N 1s region of the reference powder and of the two differently functionalized gig-lox surfaces. All spectra

were deconvoluted by three peaks: the peak at lowest binding energy corresponds to the nitrogen contribution in the –NCS group, the middle peak represents the nitrogen in the bipyridine ligands and the peak at highest binding energy corresponds to the nitrogen in the TBA$^+$ group (tetra-butyl ammonium - the counterions to the –COO$^-$ group). More in detail, we found that the intensity of TBA after dye adsorption is reduced, but not totally lost (Figures 3.3(d-f)), in agreement with Micro-Raman and ATR-FTIR analyses. Moreover, we found that the contributions in the powders and in the TiO₂ functionalized with the dye dissolved in ethanol have slightly different positions; instead, for the TiO₂ sensitized in acetonitrile the peaks are clearly shifted to higher binding energy and increased in Full Width at Half Maximum (FWHM). This difference likely reflects an overall stronger interaction of the dye with the TiO₂ surfaces as CH₃CN is used as solvent. In addition, we notice that the relative atomic percentage of the -NCS peak is higher in the sample treated in acetonitrile, as shown in **Table 3.3**.

According to all those findings, we argue that, when the dye is dissolved in CH₃CN, the molecular structure of the N-719 is more preserved and more inclined to interact with the TiO₂ surfaces rather than when CH₃CH₂OH is used as solvent due to a different interaction of the solvent molecules with the dye during anchoring. In particular, using acetonitrile as solvent increases the probability of surface anchoring via -COO$^-$ and –NCS groups.

Table 3.3. Relative atomic percentages in the C 1s and N 1s regions, following the deconvolution procedure shown in Figure 3.3(a-f).

XPS Contributions		Relative atomic percentage (%) ±0.1		
		N-719 Powders	**TiO₂ + N-719 in CH₃CN**	**TiO₂ + N-719 in CH₃CH₂OH**
C 1s	-COOH	3.2	1.5	1.8
	-COO⁻	5.1	5.7	4.5
	-C-N	30.2	19.8	17.2
	-C-C, -C-H	61.5	73.0	76.5
N 1s	-TBA⁺	29.2	6.0	6.3
	-N=C	47.5	79.3	80.7
	-N=C=S	23.3	14.7	13.0

3.1.2. *Dye loading into the gig-lox scaffold*

3.1.2.1. *UV-VIS Optical Absorption Spectroscopy analyses*

We estimated the density of the infiltrated N-719 molecules ($D_{[N-719]}$) using the Lambert-Beer law:

$$D_{[N-719]} = \left[\frac{A}{\varepsilon \times b}\right] \times N_A \qquad (11)$$

where A is the absorbance, ε is the molar absorption coefficient, b is the light path and the N_A is the Avogadro's number.[208] In our case, the molar absorption coefficient is $\sim 1.4 \times 10^4$ $M^{-1}cm^{-1}$[23] (see **Table 3.4**). The data are represented in **Figure 3.5(a)** as a function of the annealing temperature done before sensitization and also of the solvent used to dissolve the dye. From the comparison, it emerges that the gig-lox layer annealed at 500°C accommodates the largest amount of molecules, likely due to the crystallographic improvement of the surface exposed by the TiO₂ rods edges with respect to the starting material, comprising: a) the faceting of the external surfaces (see Figure 2.15) and b) a likely increased reactivity of the anatase surfaces in comparison to less ordered surfaces.[23,35,209,210] Note that a value of $\sim 1 \times 10^{20}$ molecules/cm³ is consistent with a complete pore filling as calculated by taking into account the full volume of the pores and the N-719 size (the volume occupied by each molecule was ~ 3.8 nm³).[65] On the other hand, a lower infiltration capability is offered by the ppg layer in the sample pre-treated at 200°C due to the more compact overall structure (see Figure 2.8(d)); moreover, grain coalescence definitively obstruct the dye infiltration in the sample pre-treated at 500°C.

Table 3.4: Molecular density evaluated by UV-Vis measurements and estimated by the Lambert-Beer's law.

Deposition Geometry	Grazing angle (deg)	Annealing Temperature (°C)	Thickness (nm)	Solvent	Concentration (mM)	Net Absorbance	$D_{[N719]}$ (Molecules/cm³)
TiO₂ ppg + N-719	-	200	500±15	CH_3CH_2OH	0.02	0.027	3.25×10^{19}
		500		CH_3CH_2OH	0.02	~ 0	~ 0
TiO₂ gig-lox + N-719	12.7	200	800±10	CH_3CH_2OH	0.02	0.098	7.38×10^{19}
		500		CH_3CH_2OH	0.02	0.128	9.63×10^{19}
	12.1	500	400±10	CH_3CH_2OH	0.2	0.175	1.88×10^{20}
		500		CH_3CN	0.2	0.184	1.99×10^{20}

At fixed temperature of gig-lox pre-treatment (500°C), the density of infiltrated molecules is dependent on: 1) the N-719 concentration (from 0.02 mM to 0.2 mM); 2) the

solvent polarity and the other properties reported in Table 2.1 (CH₃CH₂OH vs. CH₃CN). The change of dye loading with thickness is apparent since the two set of scaffolds (800 nm and 400 nm thick) were grown using different grazing angles (see Figure 2.4(a)). The values are reported in Table 3.1. The comparison highlights the convenience of using acetonitrile also in view of optimising the dye loading with impact on the generated/collected photocurrent (section 2.1.5).
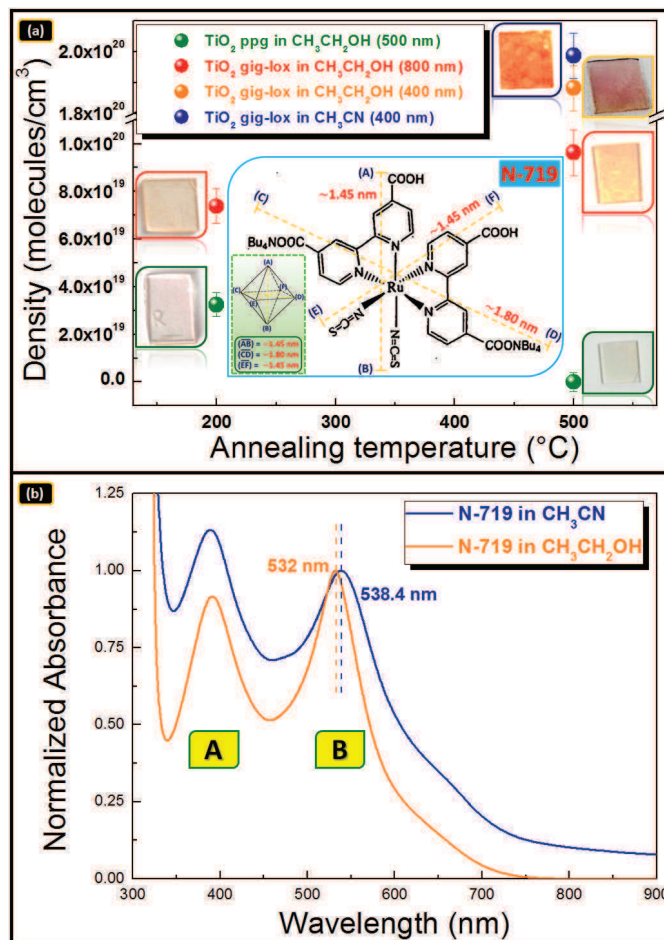
Figure 3.5: (a) Density of molecules infiltrated into the differently pre-treated TiO₂ layers (gig-lox vs. ppg). Insets: photos of functionalized TiO₂ glasses with the colour depending on the molecular density; N-719 molecule structure and dimensions. **(b)** UV-Vis absorption spectra of N-719 in both solvents, CH₃CN and CH₃CH₂OH, normalized to the band at 532 nm.

To explore if the solvent has a further role on the optical response of the dye, we performed UV-VIS optical absorption spectroscopy analyses. The absorption spectra are shown in **Figure 3.5(b)**.

In the visible region, the spectra of Ru(II)-complexes containing polypyridyl ligands are dominated by bands arising from metal-to-ligand charge-transfer (MLCT) transitions, in which an electron is promoted from a ruthenium dπ orbital (HOMO, Highest Occupied Molecular Orbital) to the π system of the polypyridyl ligand (LUMO, Lowest Unoccupied Molecular Orbital). The bands in the UV are instead due to intra-ligand transitions (ILCT, π - > π*).[211] It is important to emphasize, that the thiocyanate and carboxylic groups contributions to the HOMOs and LUMOs, respectively, are believed to have an important role in the regeneration and electron injection performance of dye sensitized TiO₂ solar cells. Then, the preservation of the molecular structure of the N-719 is fundamental, not only for the chemisorption of the dye molecules into TiO₂ layer, but also to increase the electron injection and then to improve the performances of the DSC.

In the spectra reported in Figure 3.5(b), we observe a solvatochromic shift,[156,212] namely a slight red shift on the band named A (MLCT little bit influenced of ILCT) and a blue shift on the band named B (MLCT) when the dye is dissolved in ethanol. The first shift from 389 to 391 nm (red shift) is expected to have resulted from a slightly increased delocalization of p-electrons in the sample treated in CH_3CH_2OH. The second larger shift from 532 nm to 538.4 nm (blue shift) can have a twofold explanation. One is ascribable to an increase of the Gutmann acceptor number (AN),[183] being AN = 37.1 in ethanol while AN = 19.3 in acetonitrile. On the other hand, amine complex transitions usually exhibit a red shift of the absorption band energies with increasing Gutmann donor number (DN) of the solvent (in ethanol DN = 20.0 and in acetonitrile DN = 14.1). This correlation has been ascribed to H-bonding of the solvent with the amine groups.[183,213] A second effect is the different protonation state of the carboxylic groups of the dye in the different solutions, owing to the solvent polarity, as observed in ref 212. This is in agreement with what observed in our data (Figure 3.5(a)), because the polarity of CH_3CN (37.0) is higher than that of CH_3CH_2OH (24.0).[214]

3.1.2.2. *SEM/TEM/EDX analyses*

The high infiltration/chemisorption capability of the gig-lox scaffold by N-719 molecules was further elucidated by combining FE-SEM and TEM+EDX analyses. The data set is shown in **Figure 3.6**.
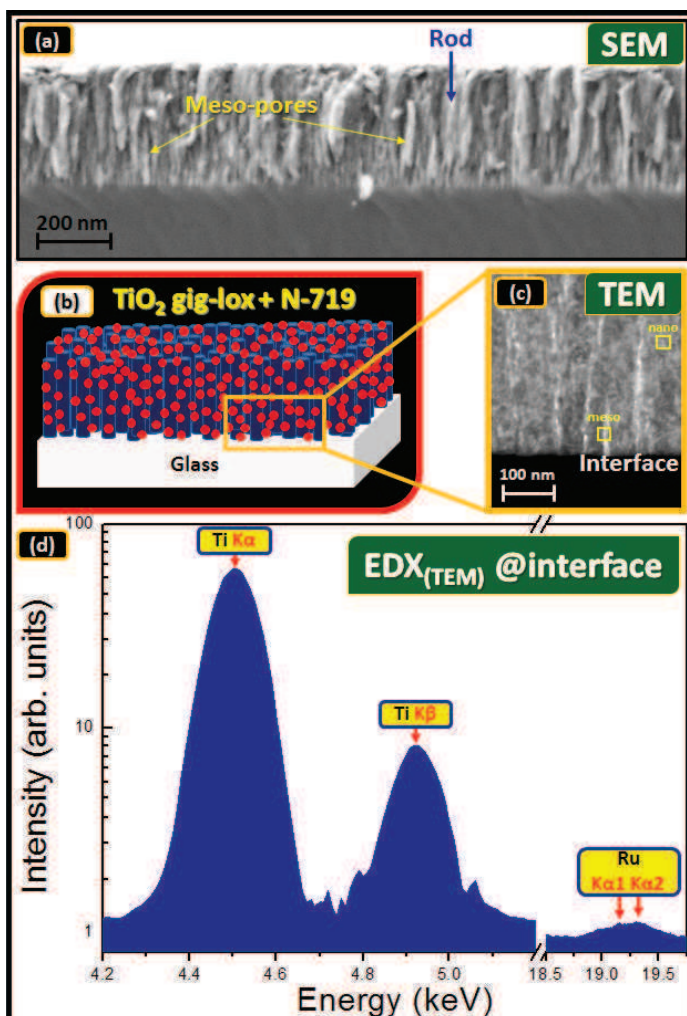
Figure 3.6: (a) FE-SEM image, **(b)** schematic of the sensitised gig-lox layer, **(c)** TEM image of TiO₂ gig-lox layer and **(d)** EDX spectra (beam diameter: 20 nm) of the N-719 -sensitised TiO₂ taken at the interface with the glass substrate to show the extent of the dye infiltration capability which exploits the interconnected array of nano-pores shown in (c).

The FE-SEM image in **Figure 3.6(a)** shows the already discussed (chapter 1) forest-like array of rods structures[215,216] with some details to reinforce or complete the landscape on the strengths of the material, namely: 1) the layer uniformity with flat surface and interface; 2) a good adhesion with the substrate; 3) uniform rods diameter along the layer, 20-30 nm, with intercalating meso-pores of similar size[65]); 4) uniform rods diameter through the layer thickness (∼400 nm); 5) interconnected nano-pore array (better given in Figure 3.6(c): pore size in the 3-5 nm range).

Figure 3.6(b) schematically represents the material. Another main peculiarity and strength of the gig-lox TiO$_2$ scaffold is in the TEM image of **Figure 3.6(c)**. It consists of an inner nanostructuration of the single rod with pores being nano-sized with dimension comparable to the N-719 steric hindrance (3.8 nm^3).[65] This not only allows a multiplicative effect on the surface exposed to the molecular functionalization (high surface to volume ratio) but also potentially makes possible a multi-branch (hereafter called octopus) configuration of the dye as a sufficient number of anchoring groups are available. The pore size, in fact, allows not co-planar ligands to simultaneously link to the TiO$_2$ surfaces exposed by the pore walls in a three-dimensional arrangement. According to the ATR-FTIR and XPS results, this octopus anchoring geometry is more likely to occur using acetonitrile as solvent through -COO$^-$ bidentate linking groups and likely via additional -NCS groups.[192,217]

According to this scenario, EDX data, taken using a 20nm-diameter e-beam probe at the TEM and shown in Figure 3.6(c), demonstrate that the interconnected nano-pore array allows a pervasive and deep infiltration of the dye molecules, as testified by the presence of Ruthenium at the bottom-side of the layer. We notice that the relative amount of Ru and Ti in the spectrum, once considered the layer porosity and the steric hindrance of the dye molecules, accounts for the presence of ~9×10^{19}-2×10^{20} molecules/cm^3, consistently to what measured through the Lambert-Beer approach using UV-Vis data (1-2×10^{20} molecules/cm^3).

This high, deep infiltration and the multi-branch chemical bonding preannounce positive results on light harvesting and charge injection.

3.1.3.   *Stability of the anchored dye using a highly polar solvent (H₂O)*

To test the strength of the dye linking to the TiO$_2$ inner surfaces, we dipped the sensitised scaffold in pure H$_2$O (solvent with polarity = 80, see Table 3.1 for the other properties) for 1 week and under 1 sun illumination produced by a solar simulator (SS). The irradiation time was 2 hours. This condition wants to mimic the operation of the photoanode, with special regards to the UV irradiation, in the adverse environmental conditions established by a solvent with polarity higher than that of the other solvents used for surface functionalization.
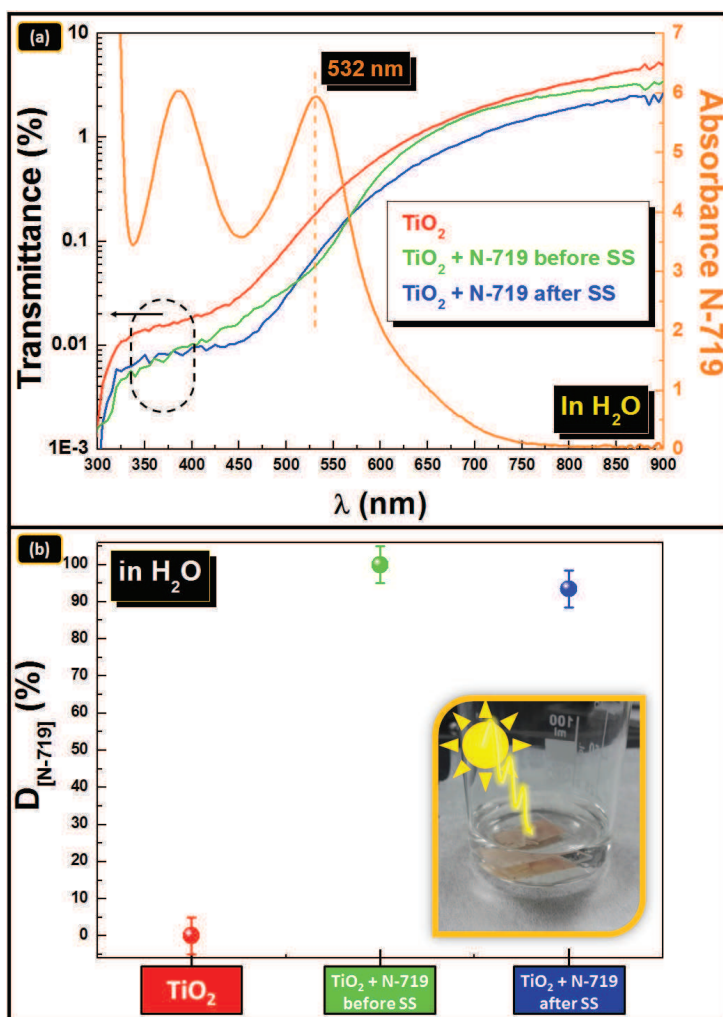
Figure 3.7: Stability test of the photoactive dye molecules infiltrated and anchored into the gig-lox TiO₂ layer; **(a)** Transmittance measurements of — TiO₂ without dye, — TiO₂ with N-719 before and — after solar simulator treatment. We reported also the absorbance spectrum of — N-719 with its Q-bands. **(b)** Density of infiltrated molecules before and after dipping in water for 1 week and the SS applied for 2 h. 100% stems for 1×10^{20} N-719/cm³.

Figure 3.7(a) shows the transmittance (T) of the TiO₂ sample without dye compared to that of the TiO₂ functionalised with N-719 before and after SS treatment. We focus on the variation of the layer absorbance (-log(T)) at 532 nm wherein a Q-band of N-719 is located. We found that, after treatment with SS (see **Figure 3.7(b)**), the sensitized sample has a slightly decreased (6.5%) density of molecules. Nevertheless, this discrepancy is sufficiently small to be included into the error bars or (at most) attributed to an exiguous loss of molecules (*e.g.* a portion in stacking). The conclusions on the resistance of the dye loading to

the prolonged deep and SS is also corroborated by the comparison of the transmittance data in the whole range wherein the N719 molecules absorbs (Figure 3.7(a)).

3.1.4. *Photocurrent measurements*

The combined effect of light harvesting and carrier injection into the TiO_2 scaffold was evaluated by photocurrent measurements done by a simplified method (also viewed as a crude form of device) that allowed disentangling the bare effects related to the dye/TiO_2 blend (light harvesting, carrier injection and collection) from many other parasitic/additional effects occurring in a complete device. We collected V-I curves in dark conditions and under illumination (1sun or 22%sun) by using a Four Point-Probe (FPP) configuration. FPP represents a powerful technique since it provides a direct evaluation of the electrical response of the Dye/TiO_2 blend under illumination without any other contributions as instead often occurs for indirect measurements. Additionally, it allows skipping the contact resistance contribution due to the tip-sample interaction, thus baring the neat resistance offered by the gig-lox TiO_2 layer to the current flow. We are aware that the method applied to a porous material can provide overestimated values of the material resistivity; nonetheless, the fact that the method can be successfully applied (as it is our case) implies that a percolation path can be arranged such to allow measuring the potential drop from the front-side of the sample; and it consequently demonstrates that the TiO_2 nanorods and nanograins are finely reciprocally interconnected. In this respect, the relative comparison between the data depicts a reliable scenario of the material behaviour before and after sun exposure, in the limit of heating and charging effects that will be discussed in more details.

Representative V-I data are shown in **Figure 3.8(a)** for a layer thickness of 350-400 nm. Similar results are found up to ~500 nm. The relative decrement of resistance values with respect to that in dark condition is a measure of the surplus of carrier injected into the TiO_2 layer from the dye (the scattering time is invariant since merely a function of the layer structure). This surplus of injected carriers was maximised by using CH_3CN as solvent (**Figure 3.8(b)**), being a factor of 10^4 with respect to the intrinsic carrier level. The value was measured under blowing to preserve the dye. Be aware that this incremental gain in the layer conductivity, with respect to the behaviour in dark, could even represent an

underestimation of the real injected carriers because of eventual trapping effects and also due to the percolative path which intrinsically reduces the layer conductivity in porous materials with respect to compact layers. The huge increase of carriers in the conduction band of the gig-lox TiO₂ is the proof of all the advantages offered by a combination of material and proper functionalization, both in terms of carriers injection and collection efficiency.
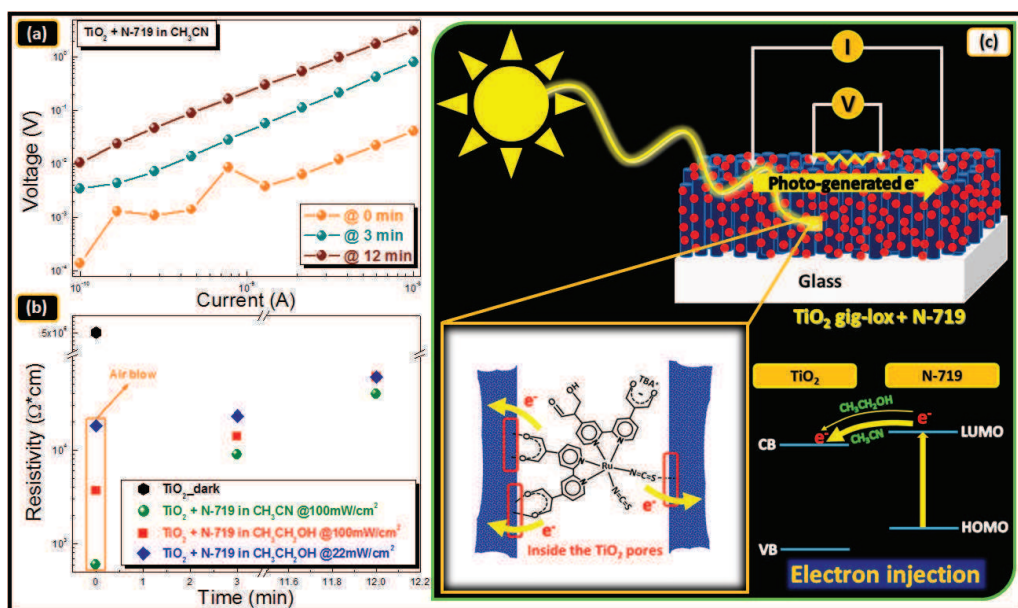
Figure 3.8: Photocurrent measurements of TiO₂ samples functionalized with N-719. **(a)** V-I current collected at the internal tips of the four-point probe (sketched in (c)) as a function of the time (0 stems for the first I-V curve). **(b)** The extracted resistivity from the slope of the curves in (a) taking into account the layer thickness (R=resistivity/thickness); the first values were taken under local blowing to avoid heating under the sun, and to thus disclose the maximum effect of charge injection and collection. The time stands for the waiting time before a further measurement is done. Note: the effect of the solvent on the starting values and the resistivity increase in subsequent measurements due to heating, dye damaging, charging effects. **(c)** Schematic of the basic principle of the analysis method, wherein the potential drop taken on the front side between the internal tips accounts for the layer resistivity that depends on the carriers flowing the TiO₂ layers through percolation paths. During illumination photo-generated carries cut-down by 2-4 order of magnitude the layer resistivity. It is also represented how an octopus dye configuration, established inside the pores thanks to a molecular steric hindrance similar to the pore dimension, is one the candidates that rises the collected photo-current as CH₃CN is used as solvent.

As a matter of fact, the overresponse by 1 order of magnitude in the TiO₂ functionalised in CH₃CN with respect to the analogous sample functionalised in CH₃CH₂OH (same concentration of the two solutions, namely 0.2 mM, same layer thickness, same TiO₂ structure) was explained by some cooperative factors. As first, the raised probability of the dye to establish an octopus configuration inside the pores by exploiting COO⁻ and –NCS ligands; this rises the injection probability. Secondly, a positive effect on the molecule integrity during the sensitization process in solution. An additional positive effect is on the

absorption range expected on the basis of the reduced HOMO-LUMO gap in CH_3CN vs. CH_3CH_2OH (30 meV)-treated N-719 dye, that can account for a larger IPCE.[218]

In the experiment, we have discriminated the impact of the sample heating by the sun exposure. In this respect, we observe that, as the blowing on the sample is stopped, the layer resistance progressively increases if recorded from time to time. This is likely due to a partial damaging/detachment of the dye and to charging of the functionalised surfaces. Consistently with the role of heating, the relative increase of resistance after stop blowing is a function of the sun exposure in terms of power density, being higher under 1 sun exposure with respect to the case of 22% ($22mW/cm^2$). The starting resistance value can be partially or totally recovered by a second air blow (see **Figure 3.9**), giving a feedback on the predominance of charging on permanent dye damaging. The experiment justifies the first resistance data (fresh sample) taken during air blowing as representative to describe the transport behaviour.
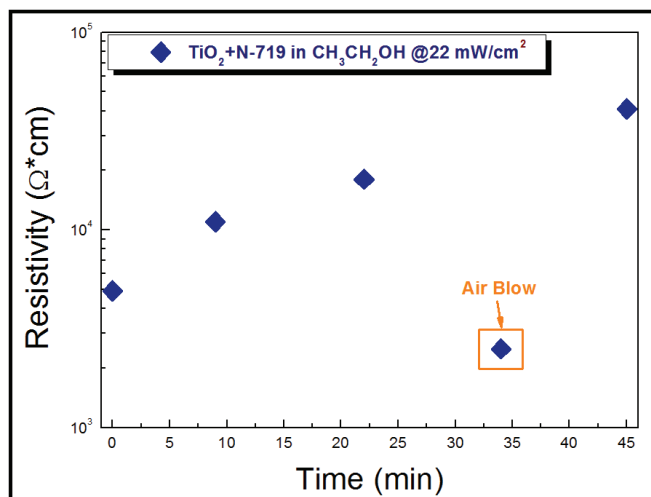
Figure 3.9: Photocurrent data of TiO₂ functionalized with N-719 molecules ($1.01\sim10^{20}$ molecules/cm³) in CH_3CH_2OH @$22mW/cm^2$. Where not written, the data are collected without air blow.

3.1.5. *Prototype Dye Solar Cell*

As a first proof of concept to endorse the gig-lox performances, we employed the described gig-lox scaffold in the architecture of Dye Sensitized Solar Cell. For the photoanode, a gig-lox TiO₂ layer $\sim$1µm thick was deposited on a F-doped SnO₂ substrate (FTO), (for details see Appendix). The dye loading was done using a solution containing CH_3CN/tert-buthanol (1/1vol.) because this mixture represents a choice to further increase

the dye deprotonation and then the number of molecules anchored. The use of this combined solution is also encountered in the literature. [65,182]
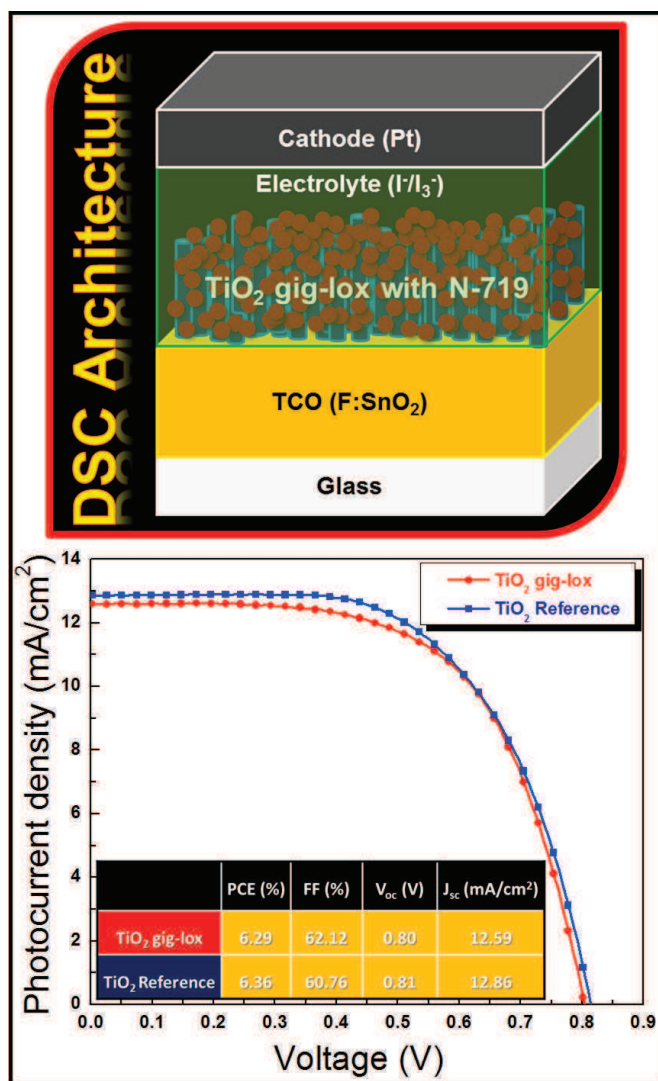
Figure 3.10: I–V curves of DSCs. Devices (~1μm-thick) based on gig-lox TiO₂ layers compared to a reference made by commercial TiO₂ pastes (Dyesol 18NR-T) under 1.0 sun illumination. The Cells parameters are listed in the table.

The photocurrent-voltage curve is shown in **Figure 3.10** in comparison to that of a reference cell wherein a scaffold of the same thickness is used exploiting a conventional (commercialised by Dyesol) array of nanograins. The two device architectures are identical (details in Appendix) and apply a standard (commercial) FTO (F:SnO₂) layer as TCO.

Photo-conversion efficiencies of 6.3% were measured for the gig-lox layers. The parameters on the reference cells are similar. The result, although it does not outperform existing devices in the literature that apply higher sensitized volumes (10 times scaffolds thickness) and different dyes to get records, needs to be framed in relationship to the scaled thickness of the scaffold and to the low molar absorption coefficient of the N-719 dye.[124,182] In the panorama of the recent literature, viable solutions to increase the efficiency facing on the light harvesting capability of the dye (new molecular engineering) or on the electrolyte performances (new electrolytes or gel with carrier mobility, stability) have been explored to further increase the cell efficiency and durability.[218]

Besides them, our issue represents the first demonstration that a sputtered TiO₂ layer can aspire to compete with chemically prepared ones. Our approach affords the advantages of an easy integration of the material on large-area-technologies (up-scalability) and encourages further investigations towards new records in the field of hybrid flexible solar cells, comprised perovskites-based solutions wherein thinner scaffold (typically around 300 nm) are required.

3.2. *Perovskite Solar Cells*

A second proof of concept to endorse the gig-lox performances was provided by integrating the optimised TiO_2 gig-lox layers as scaffold in Perovskite Solar Cells, using a solution processed $CH_3NH_3PbI_3$ material. The scaffold is that used for DSCs, except for the thickness which was scaled down for this application.

3.2.1. *Perovskite synthesis and properties*

TiO_2 gig-lox layers, annealed at 500°C 30s in air, were further treated by UV-O_3 for 10 minutes to clean the surface and avoid the presence of contaminants. The treated layers were infiltrated with perovskite materials (at the Toin University of Yokohama – Prof. Tsutomu Miyasaka) by solution processing, via a Cl-assisted one step deposition, and spin coating [65,219] both performed in a dry room with monitored humidity < 20%. Namely, a 40 wt% solution of $PbCl_2$ and methyl ammonium (MA) iodide (MAI) (ratio 1:3) in dimethyl formamide (DMF) was prepared at 70°C under stirring for 1 h. The solution was spin coated on the gig-lox TiO_2 at 1200 rpm for 30 seconds; after that, the rotational speed was increased to 2000 rpm for 6 seconds and subsequently to 4500 rpm for 24 seconds. During the spin coating, 1 mL of toluene was dripped onto the substrate as solvent treatment to form a homogenous film. The substrates were then placed on a hot plate, which was raised up to 90°C for 40 minutes, up to 100°C for 10 minutes and finally to 110°C for 10 minutes to complete the evaporation of the solvent.

Figure 3.11 figures out a resulting blend of perovskite and TiO_2 gig-lox nanorods. The samples were stored in vial under a dry nitrogen atmosphere immediately after preparation to avoid triggering any degradation before the analyses.

The fresh perovskite has a brown color as shown in Figure 3.11. It has the MAPbI₃ stoichiometry with I4-mcm tetragonal structure consistently with the diffraction pattern shown in **Figure 3.12**. According to this finding, the residual content of reaction products, such as PbI_2, is negligible. In the diffraction pattern, contributions from the TiO_2 scaffolds are also visible.
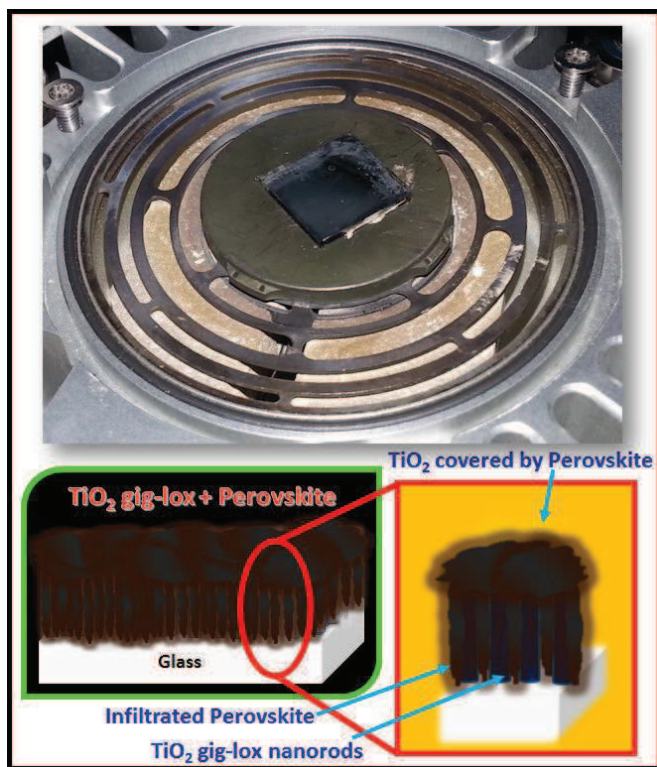
Figure 3.11: Perovskite deposited by spin-coating process. The sketch represent the complete infiltration and coverage of the TiO₂ gig-lox layer by the perovskite.
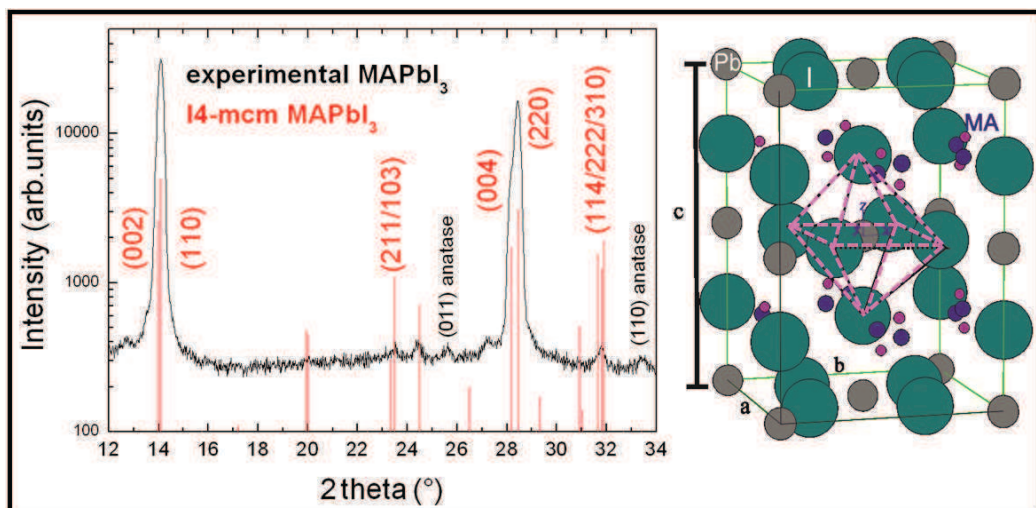
Figure 3.12: XRD pattern of the TiO₂/MAPbI₃ blend and the tetragonal lattice structure of the perovskite at room temperature.

As often encountered in the literature,[83,88,220,221], the layer is highly textured preferentially exposing (001)/(110) planes as growth planes.. This preferentiality causes the peaks at $2\theta = 14.1°$ and at $2\theta = 28.4°$ to be dominant over all the other expected peaks. They are generated by the same family of crystallographic planes and are replica for multiple $d_{spacing}$ (002/110 vs. 004/220, respectively). Following our previous works,[221,222], chlorine atoms do not take part in the perovskite lattice architecture; rather they have a role at the interface with the TiO_2 substrate to trigger the texturing of the large MAPbI₃ grains that provides the layer with a high degree of spatial uniformity.

The absorption behavior of the MAPbI₃ layer is shown in **Figure 3.13** to highlight its wide-range interaction with the solar spectrum. The figure reports the penetration depth (*x*) of the radiation at different wavelengths with cutoff at the bandgap: around this value the photons are able to enter 250 nm of material and to be absorbed therein. This implies that solar cells can be made just employing thin layers of such perovskite material to absorb a wide spectrum of photons. For silicon, several hundred microns are needed; for DSCs tens of microns are employed.
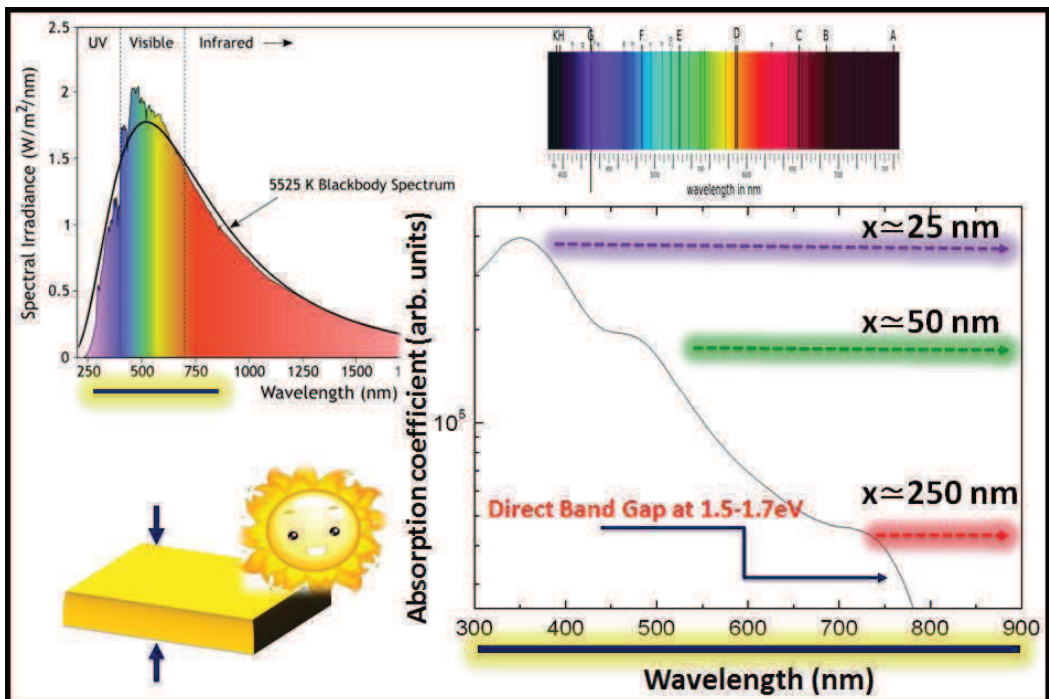
Figure 3.13: absorption coefficient of the perovskite layer determined by spectroscopic ellipsometry analyses, compared to the solar spectrum. *X* represents the penetration depth of the radiation into a MAPbI₃ layer.

3.2.2. *Perovskite loading*

The surface morphology of the TiO_2/$MAPbI_3$ blend was explored by FE-SEM imaging. Representative results are shown in **Figure 3.14**. The gig-lox layer used is 150-200 nm-thick. The surface of the sample is made of $MAPbI_3$ grains having size 1-5µm, or even more than that. The flatness and large size of the $MAPbI_3$ grains are mutually correlated and associated to the texturing of the material along the preferential crystallographic orientations found by XRD analyses, as effects of the growth procedure in presence of Cl species.[221] The inset visualizes a grain boundary network that makes the $MAPbI_3$ grains closely interconnected. The TiO_2 nanorods are not visible in top-view thus envisaging that the TiO_2/$MAPbI_3$ is closed by a cap of perovskite. We thus expect a complete filling of the TiO_2 pores under the cap, with the overall scenario depicted by the sketch in figure 3.14.
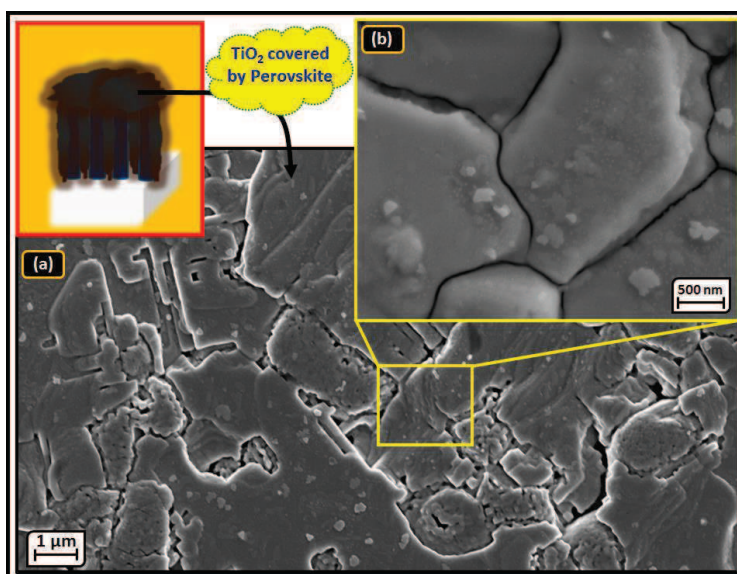
Figure 3.14: FE-SEM images of fresh $MAPbI_3$ (a) at low and (b) at high magnification. The sketch represents the complete pore filling of the gig-lox rods capped by a layer of pure perovskite.

The extent of perovskite infiltration into the gig-lox scaffold was evaluated by Scanning TEM (STEM) and EDX analyses. STEM is very sensitive to species with high atomic number (Z), and thus gives evidence (mainly) of the spatial distribution of the Pb atoms. In this respect, **Figure 3.15** shown Pb atoms atomically distributed through the layer or aggregated in nanometer spheres giving a bright contrast in the images. This results from the (mainly) vacuum-induced degradation,[219,221] of the starting perovskite layer. Perovskite degradation

occurs by creation and loss of volatile species,[219,221] and this causes iodine leaving the sample likely in form of HI. The consequent huge volume contraction[61] with respect to the initial perovskite distribution is responsible for the spatial discontinuity of residual Pb species observed in Figure 3.15. Nonetheless, the integral amount of Pb atoms, compared to the Ti counterpart (see EDX results in Figure 3.15), accounts for a starting complete pore filling inside the TiO_2 scaffold.
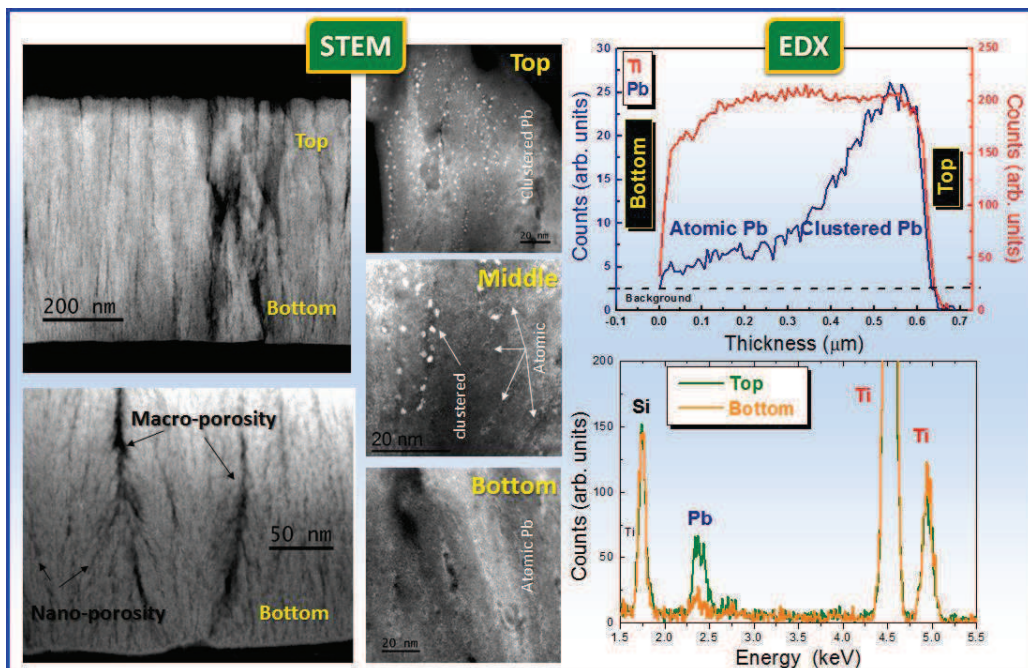
Figure 3.15: STEM and EDX analyses on the TiO_2 gig-lox layer after $CH_3NH_3PbI_3$ infiltration**.** In the STEM images, the Pb nano-aggregates (white Z-contrast) result from the perovskite degradation under high vacuum conditions[219] and are used as markers of the original distribution of the perovskite layer. Notice how the Pb aggregates nicely stack into the pores; also follow the Pb atomic distribution into the bottom part of the layer. Here the Pb/Ti atomic ratio is ~1/10, close to what expected by combining their atomic density in the starting $CH_3NH_3PbI_3$ (~$3Pb/1nm^3$) and in the TiO_2 layer with the gig-lox porosity ($CH_3NH_3PbI_3/TiO_2$ ~40% in volume) in a regime of complete pore filling.

Although the information on the continuity of the perovskite coverage over the TiO_2 rods is lost, the distribution and location of the Pb agglomerates account for the capability of the perovskite to deeply enter the structure (Pb distribution used as marker). As a matter of fact, in the STEM view of the top region of the sample, the Pb nano-agglomerates are vertically stacked into the TiO_2 pores. A different scenario is encountered in the bottom part of the layer wherein the Pb is atomically distributed (not aggregated) through the TiO_2 layer even entering into the nano-pores, as further supported by EDX profiling. The coexistence of

atomic and clustered Pb is found in the middle part of the layer.

The results indeed indicate that the perovskite enters the TiO_2 scaffold with a diffusion profile. This reinforces the fact that, scaling the gig-lox layer thickness to a value of 150-200 nm represents a strategy to get a uniform distribution of the infiltrated perovskite. This reduction of the layer thickness also positively combines with the high absorption coefficient offered by the perovskite materials (Figure 3.13)[24,45,60] (the dye, instead, having a relatively low absorption coefficient, forces the TiO_2 thickness to be more properly around 10 μm to increase the density of light absorbers).

3.2.3. *Stability of the Perovskite-TiO₂ blend*

In the experiment designed to test the stability of the hybrid Perovskite-TiO_2 blend under heating, the sample was forced to isothermal annealing in the range of 90- 135°C in controlled atmosphere, as schematically depicted in **Figure 3.16**. This was done as stress test to mimic prolonged operation conditions of the materials. The maximum temperature the cell would really experience under the sun stays around 60°C.
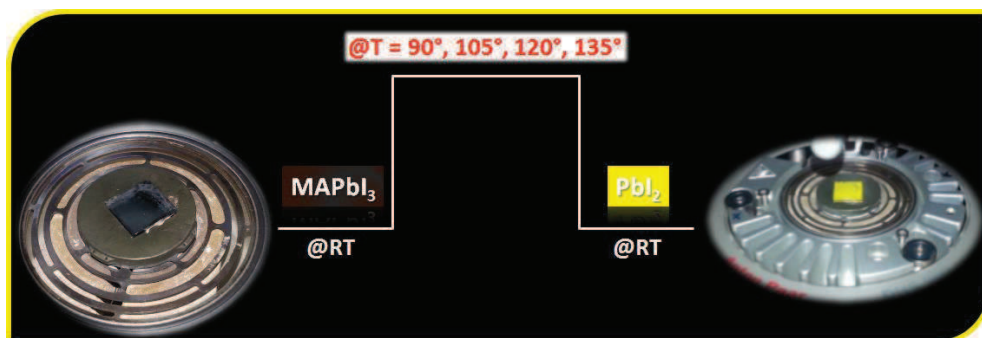
Figure 3.16: schematic representing the thermal stress test experienced by the gig-lox TiO_2/MAPbI₃ blend to mimic its operation under the sun. The two photo are taken before and after prolonged thermal stress.

The diffraction pattern of the blend is collected vs. time during each isothermal heating path, while the diffraction chamber is kept at 55±5% HR (relative humidity), *i.e.* intentionally under the threshold of hydrate phase formation[223,224]. A fresh sample was used for each temperature.

As a general behavior, it was observed that the isothermal annealing promotes, during time, a transition from fully MAPbI₃ to fully PbI₂ with a rate proportional to the applied temperature. Consistently, the color of the sample changed from brown to yellow as shown

in figure 3.16. In the diffraction pattern, the decrease of the MAPbI₃ peak at 2θ=14.00° (unique (002) planes in the cubic arrangement) accompanied by the simultaneous increase of the PbI₂ peak at 2θ = 12.6° ((003) planes of the 9R hexagonal structure) have suggested a relationship between those two materials (**Figure 3.17(a)**). The same decreasing trend is observed for the (004) MAPbI₃ peak at 2θ ~ 28.23°, which is crystallographically linked to the peak at 2θ ~ 14.00° (the same family of planes); moreover no other peaks related to the perovskite layer emerged in the diffraction pattern during annealing. On the basis of these findings, we can conclude that the perovskite layer is progressively changing in PbI₂ without any reorientation of the grains.[219] We measured the (110/002) MAPbI₃ peak area and used this parameter as marker for the degradation.
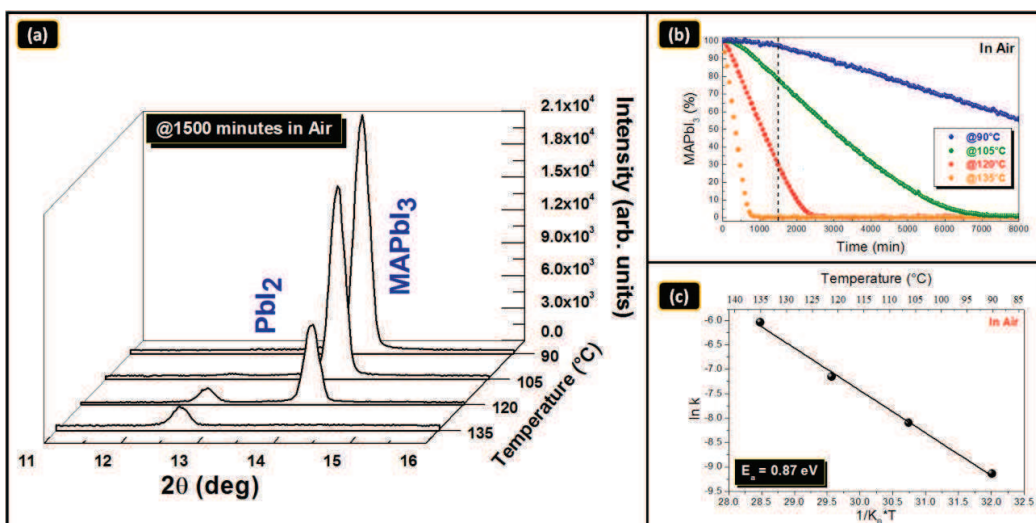
Figure 3.17: (a) XRD patterns collected after at 1500 minutes annealing in air at different temperature; **(b)** kinetic analysis and fitting of the degradation curves of blend samples annealed at four different temperatures (90°C, 105°C, 120°C and 135°C) in air; **(c)** Arrhenius plot of the kinetic constant and activation energy extracted in air condition. All data are collected in dark conditions.

In the procedure of quantitative data analyses, we assume, on the basis of what experimentally observed, that: 1) the degradation of the material occurs without re-orientation of the original crystal lattice and 2) the degree of the texturing is maintained during the degradation reaction. The MAPbI₃ percentage was obtained by applying the following equation:[225]

$$y = [MAPbI_3 \%] = \left[\left(\frac{A_0}{A_i(t)} \right) \times 100 \right] \qquad (12)$$

to the data in **Figure 3.17(b)**, where A_0 is the area of the (002) peak at t = 0 and A_i is the corresponding area at t = t_i. In air conditions, therefore in the presence of moisture, the degradation curves follow the behavior shown in **Figure 3.17(c)**. For all the temperatures analyzed, the rate of the degradation is constant and thus the curves follow zero order kinetics.

The kinetic constant k was indeed extracted by the degradation curves using the following relationship:

$$y = [MAPbI_3 \%] = [k(T) \times t] \qquad (13)$$

As expected, $k(T)$ is a monotonically decreasing function of the annealing temperature. The kinetic constant obtained by the fitting procedure was used in an Arrhenius plot to extract the activation energy (E_a) describing the degradation process of the layer using the following equation:

$$k(T) = k_0 e^{-\frac{E_a}{K_B T}} \qquad (14)$$

where K_B is the Boltzmann constant. The value obtained for degradation reaction of the MAPbI₃ in air ambient is ~0.87 eV. We emphasize the predictive role of the Arrhenius-type plot in terms of degradation times at temperature more similar to the working temperature (*e.g.* 60°C). We can also reason on the mechanism of perovskite degradation. In fact, zero order reactions (that proceed by constant rates) are usually catalytic reactions occurring in the presence of an excess of reagent, like in heterogeneous catalysis, biological reactions catalyzed by enzymes. In all these cases, the presence of an external factor (*e.g.* catalyst) promotes the reaction until all the reactant is converted into the product. On this basis, we attribute the zero order degradation process, observed during isothermal annealing in air, to the catalytic action of water molecules present as moisture.[91]

At the beginning of the transition, indeed, the amount of the perovskite material is so high that the transformation rate is independent of the perovskite concentration because water molecules have enough methylammonium molecules disposable to react with (see Figure 3.17(b) and related fitting curves). In this case the rate is constant because it depends only on the concentration of the catalyst that is constant during the reaction process (by definition, a catalyst is reformed after catalytic action). When the amount of the MAPbI₃ is low enough and the amount of the MA⁺ groups indeed becomes comparable with the amount of available water molecules, the MA⁺ cations become the limiting reagent so that the rate

does not depend only from the amount of the catalyst but also from the amount of residual MA+. Thereby, the degradation curve at the end of the transition is expected to bend as shown in Figure 3.17(b) (105°C).

Although the stress test prospects a degradation of the blend over more than 6 days at constant temperature of 90°C, we rather remind that 1) the real operation temperature will stay under this threshold; 2) the photoanode is constantly kept at the stress temperature under the sun operating cycles; 3) the photoanode is not protected and thus directly exposed to external agents such as water to exaggerate and study the effect of water molecules.
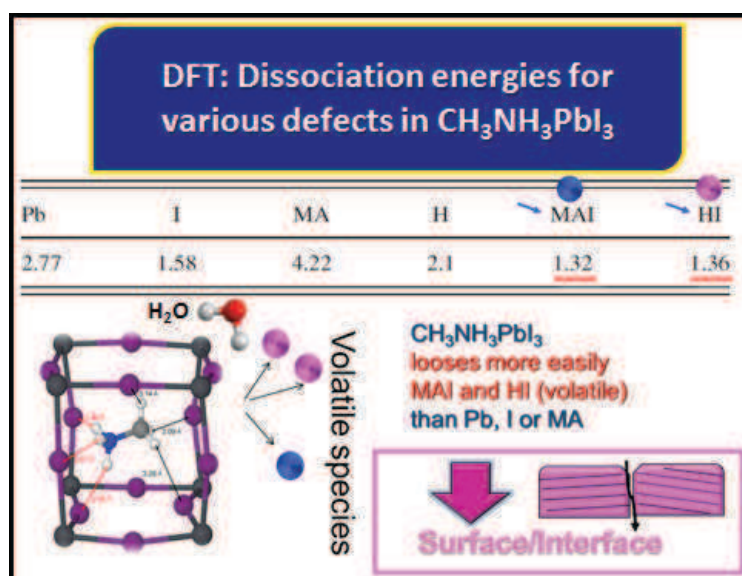
Figure 3.18: dissociation energies for defect formation into the perovskite lattice and related schematic indicating that the presence of water molecules act reducing the barrier for defect generation, especially at the grains boundaries

Our results accounts for the action of water as catalyst which reduces the activation energy for defects formation inside the perovskite layer compared to the predicted values.[88,219,221,226,227] The presence of grain boundaries in the layer can further promote the disaggregation of the cage via the action of water molecules diffusing through those pipelines. The scenario is depicted in **Figure 3.18**.

3.2.4. *Prototype Perovskite Solar Cell*

To tailor the device architecture, our findings definitely authorized to scale the gig-lox layer thickness to 150 nm and to use it in a blend with solution processed MAPbI₃ in a

complete pore filling arrangement. The related cell performances are shown in **Figure 3.19**. The cell architecture was that used by Prof. T. Miyasaka and co-workers (meso-structure).

The solar cell based on the gig-lox TiO₂ scaffold exhibited a photo conversion efficiency of 11.7%. Compared to a device fabricated using commercially available colloidal TiO₂ grains (commercialised by Dyesol), which reached 10.5% efficiency, it is even better. The I-V curves do not show hysteresis.

	PCE (%)	FF (%)	V$_{oc}$ (V)	J$_{sc}$ (mA/cm²)
TiO₂ gig-lox	11.70	67	0.97	18.06
TiO₂ Reference	10.51	67	1.00	15.51
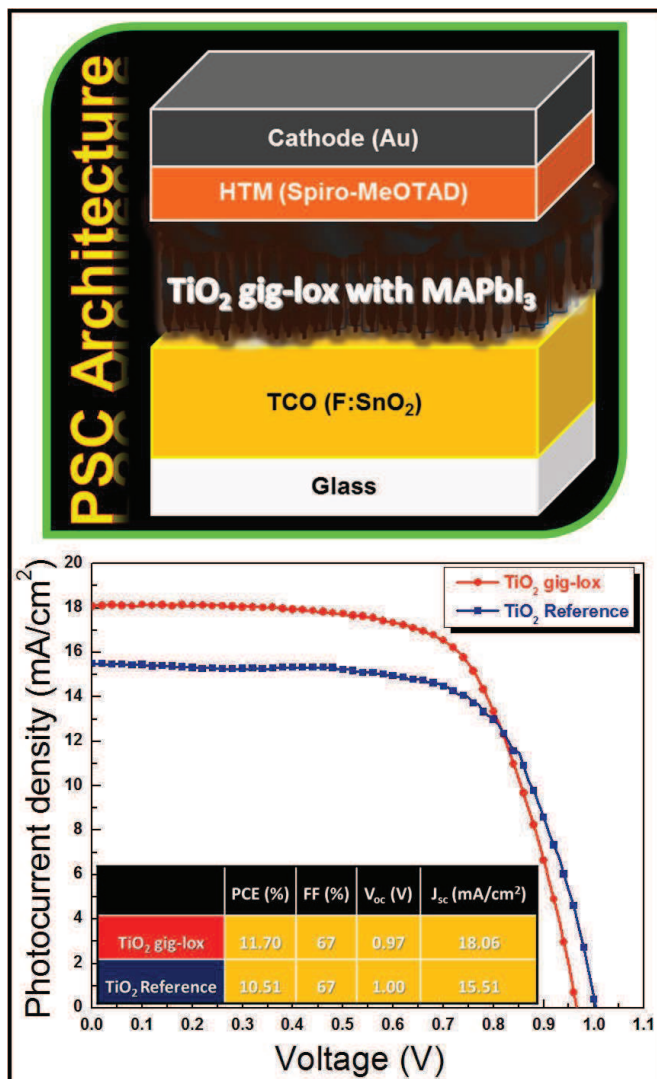
Figure 3.19: I–V curves of Perovskite Solar Cells. Devices based on gig-lox TiO₂ layers (~150 nm-thick) under 1.0 sun illumination (both are reverse curves). The cell architecture is also schematically drawn.

The enhanced photovoltaic performances of the gig-lox TiO$_2$ are mainly ascribed to the higher photocurrent density related to the fine grain morphology of the scaffold. In fact, the gig-lox TiO$_2$ layer is characterized by small interconnected grains, as seen in Chapter 2 in the XRD section and in Figure 2.14. An additional value-added for the benefit of the device performances is given by the capillary pervasive infiltration of the perovskite into the multi-scale-pores of the gig-lox structure (Figure 2.14); this leads to a more extended TiO$_2$-perovskite interface that rises the electrons injection efficiency. Although this value does not represent a record,[43] it states the potentialities of the material and encourages further optimizations of the TiO$_2$-perovskite blend and of the overall cell architecture.

Chapter 4

Alternative materials and applications for future devices

The chapter explores different perspective on 1) novel porous TiO₂ nanostructures grown by a chemical method in alternative to gig-lox; 2) the application of gig-lox layers in a field different from photovoltaic, namely for gas sensing; 3) the growth of ZnO:Al (AZO) by low-temperature reactive co-sputtering as a valid alternative to commercial TCO for solar cells. Specifically, The chapter aims at further elucidating the transversal empowering of nanostructures and at prospecting their easy integration with AZO in a shared deposition chamber by low-cost up-scalable processes potentially on any kind of substrate.

4.1. *TiO₂ micro-flowers deposited by AA-MOCVD*

This section is dedicated to my activity at the LMGP (Laboratoire des Matériaux et du Génie Physique, Grenoble) during a 3-months stage under the supervision of Dr. David Muñoz-Rojas and Dr. Carmen Jiménez. My aim was to be able to produce TiO₂ nanostructures with a technique potentially competitive with respect to the gig-lox method. This technique called AA-MOCVD (Aerosol Assisted Metal-Organic Chemical Vapor Deposition) is an assessed technique with capability to grow intriguing nanostructures with high surface to volume ratio. I followed the path signed in the host lab to reproduce micro-flowers structures using a new deposition chamber.

4.1.1. *AA-MOCVD set-up*

The AA-MOCVD experimental set-up (see **Figure 4.1(a)**) is made of two main chambers: the aerosol formation chamber (see **Figure 4.1(b)**) and the deposition chamber (see **Figure 4.1(c)**). In the first one, a precursor solution is loaded. Beneath, a piezoelectric plate vibrates (appropriate power and frequency values are settled) to create the aerosol from the solution. The aerosol flows through the vertical tubes and gets to the deposition chamber where the sample is located. The sample is heated through a heating plate in contact

with it. The deposition process is based on the aerosol carrying the precursor molecules towards the heated substrate, wherein the reaction occurs.
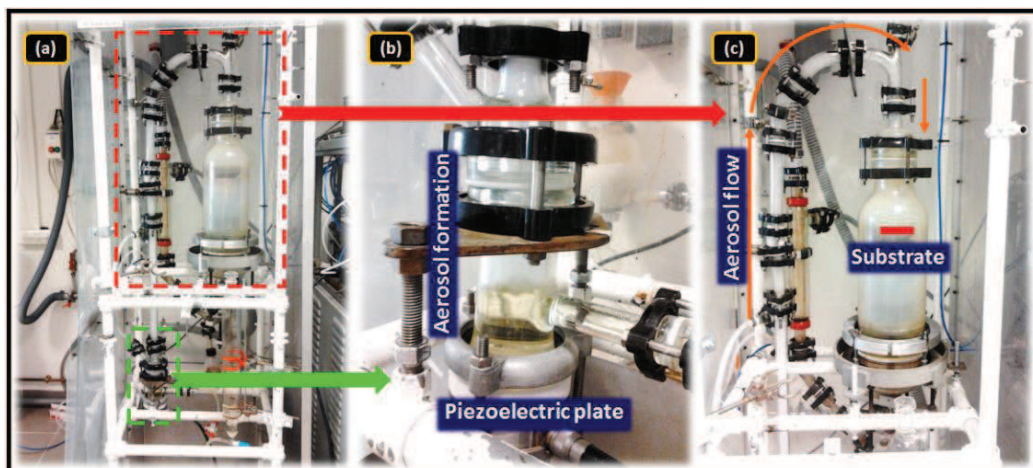
Figure 4.1: (a) AA-MOCVD experimental set-up, **(b)** aerosol formation chamber using a piezoelectric plate and **(c)** deposition chamber.

4.1.2. *TiO₂ synthesis*

In the solution, titanium (IV)-oxide bis-acetylacetonate ($C_{10}H_{14}O_5Ti$) and 1-butanol ($CH_3CH_2CH_2CH_2OH$) were used as precursor and as solvent, respectively. The concentration of the solution was kept at 0.03 M (standard conditions). This solution was made under continuous magnetic stirring for 2h at 60°C. The AA-MOCVD depositions is based on two steps, namely aerosol generation and aerosol transportation to the substrate. The deposition process is piloted by several parameters as reported in **Table 4.1**.

Table 4.1: AA-MOCVD deposition parameters used for the best process of TiO₂ Micro-flowers.

AA-MOCVD parameters	
Piezoelectric Frequency (arb. units)	3.3
Piezoelectric Power (arb. units)	6.3
Concentration (M)	0.03
Pressure (bar)	0.5
Bottom Air (L/min)	5.0
Top Air (L/min)	2.0
Deposition Temperature (°C)	354°C
Nominal Temperature (°C)	490°C
Deposition time (min)	60
Volume consumed (mL)	180.0
Desolution Feeding Rate (mL/min)	3.00
Thickness (nm)	200-300

The most important parameter for the micro-flowers growth is the desolution feeding rate (DFR) of the aerosol (analogous to the sputtering rate). This latter can be controlled and tuned through accurate control on the piezoelectric parameters: deposition time and substrate temperature, instead, impact on the deposition rate.
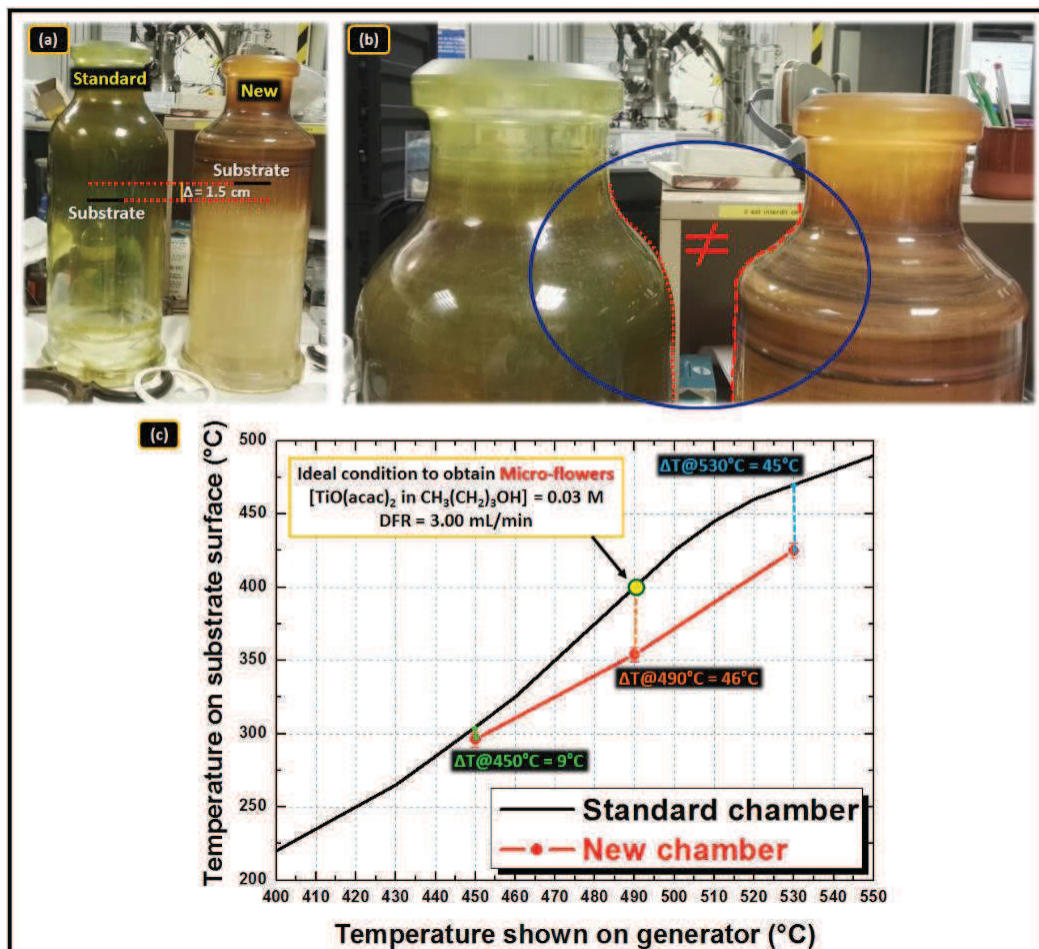
Figure 4.2: Comparison between the standard and new chamber wherein is shown **(a)** the different substrate deposition and **(b)** the different chamber neck curvature. **(c)** Plot of the temperature calibration in both chambers.

To this purpose, a new deposition chamber was used. This was different from the standard chamber used at LMGP mainly for the sample holder position (see **Figure 4.2(a)** for details) and for the chamber neck curvature (see **Figure 4.2(b)**). Differences in the substrates temperature were also found through the experiments (**Figure 4.2(c)**). These changes are expected to impact on the flux (kinetics) of the reacting species and on the

reaction path (thermodynamics + kinetics) on the substrate, with repercussions on shape and density of the deposited materials.

With an appropriate setting of the all parameters, optimized condition can yield to nanostructures such as micro-flowers.[137] They are fascinating and promising nano-architectures, and were considered as a possible chemical counterpart of our gig-lox material. Thereby, an explorative investigation on the growth of micro-flowers with the new deposition chamber was initiated through my stage at LMGP. The kind of material was identified by the density and size of the micro-structures. The density was given by the percentage of area (area fraction) covered by the flowers on the substrate. This was calculated selecting an area (100 μm^2) on the FE-SEM images in plan-view (see paragraph 4.1.3.1). The size of the flowers was described by their diameter, considering a sphere including each structure. The surface to volume ratio, the other main parameter, were qualitatively evaluated by SEM images or by applying innovative analytical techniques such as CDXI.

4.1.3. *TiO₂ nanostructures characterizations*

The structural properties of the TiO₂ deposited by AA-MOCVD on Si and glass substrates were investigated using different spectroscopic and microscopic techniques.

4.1.3.1. *FE-SEM analyses*

Morphological analyses were performed on the deposited layers by FE-SEM images in plan-view to complement the deposition step and give a recursive feedback to progressively and appropriately change the micro-flowers growth procedure.

Firstly, we performed the TiO₂ depositions at different substrate temperatures (in the 340-410°C range) and, then, tuning the deposition feeding rate (in the range 2.7-3.3). The two parameters are expected to impact on the deposition rate through a combination of incoming flux plus reaction and desorption paths at the substrate side. The data are shown in **Figure 4.3(a)**. In **Figure 4.3(b)** we consistently show the integrated deposited volume to take into account both the size and density of the deposited flowers. The substrate used was silicon. The flowers are deposited over an underlayer of TiO₂, concomitantly deposited during the process, whose thickness is in the range 200-300 nm.
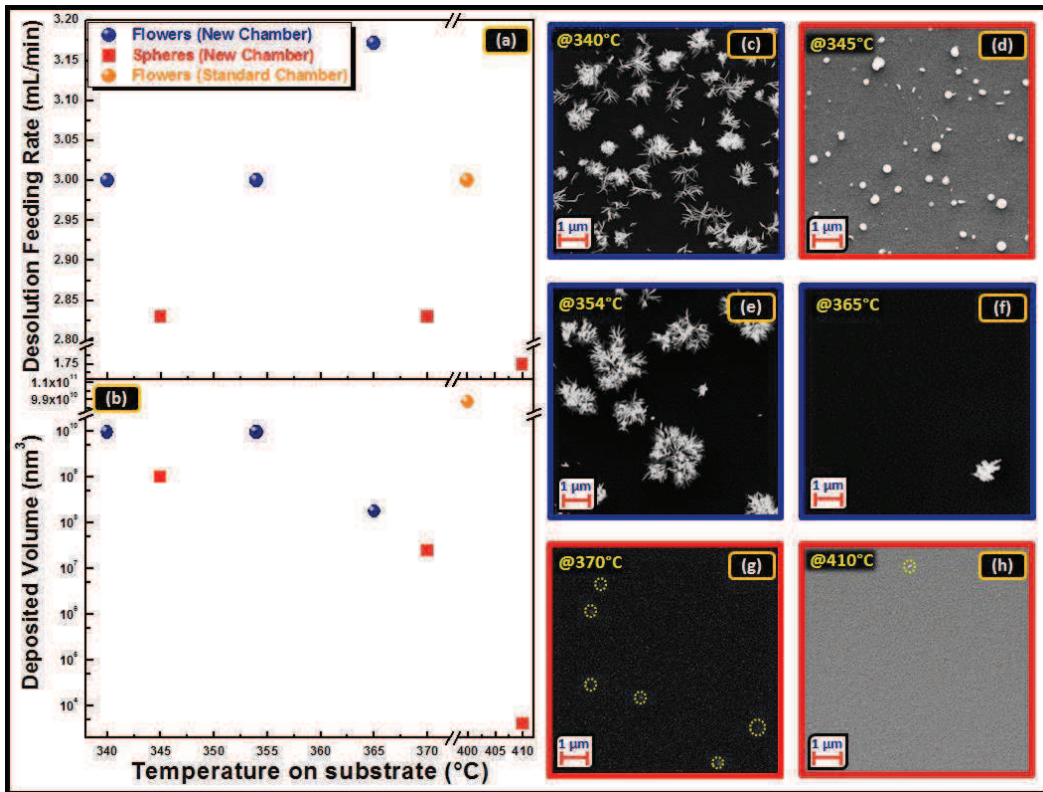
Figure 4.3: (a) Desolution feeding rate and **(b)** deposited volume of TiO₂ micro-structures as a function of the temperature measured on substrate. FE-SEM images in plan-view of TiO₂ deposited at **(c)** 340°C, **(d)** 345°C, **(e)** 354°C, **(f)** 365°C, **(g)** 370°C and **(h)** 410°C.

The FE-SEM images in **Figure 4.3(c-h)** and the data listed in **table 4.2** reveal that flowers are formed in a narrow range of temperatures, namely between 340-354 °C, with a surface density relatively high but not enough to cover the whole sample surface. The size of the flowers was found to increase as a function of the temperature in that range, although the limited extent of the process window does not allow further investigations. In the two cases explored, the DFR stays around 3.00 mL/min. It was verified that, moving from this, DFR value affects the morphology of the deposited material even invalidating the micro-flowers formation. In this respect, see the data taken at a DFR of 2.83 mL/min at temperatures of 345°C and 370°C. The related SEM images show sphere-like particles with density and size reducing with increasing temperature. The findings demonstrate that, in the competition between reaction, desorption and surface diffusion, the flux of species (the precursor) impinging on the sample surface and the substrate temperature play a major role.

We also argue that a low flux of species cannot be compensated by reducing the temperature to generate flowers, suggesting that high surface diffusion and/or sufficient energy are needed to make the precursor to properly react in form of flowers. On the other hand, overcoming the DRF threshold leaves opens the possibility to form flowers on the sample surface but using reduced surface density and size, as represented by the data taken at deposition temperature of 365°C. It could be convenient using a DFR of 3.33 mL/min at a temperature of 354°C to increase the flowers density. To converge towards a detailed description of the process of micro-flowers nucleation and growth, other experiments are needed.

Table 4.2 lists all the parameters used and the best conditions (at 354°C, see complete list of parameters in Table 4.1) to get micro-flowers with relatively high surface density and size (among those explored). The reference sample was, instead, deposited in the standard chamber at 400°C, C = 0.03 M and DFR = 3.00 mL/min in 1h, and it is characterized by micro-flowers having density of 0.12 /μm² and average size ~2.5 μm.

Table 4.2: Data on all samples deposited at different temperatures in the new chamber (340°C-410°C) compared to the data on the reference sample deposited in the standard chamber at 400°C.

Samples	Nominal Temperature (°C)	Deposition Temperature (°C)	Des. Feed. Rate (mL/min)	Particles' Number	Density (particles/μm²)	Average size (nm)	Deposited Volume (nm³)
1	480	340	3.00	54 flowers	0.54	~700	9.69×10^9
2	485	345	2.83	71 spheres	0.71	~300	1.00×10^9
3	490	354	3.00	14 flowers	0.14	~1100	9.75×10^9
4	500	365	3.17	1 flower	0.01	~700	1.79×10^8
5	505	370	2.83	6 spheres	0.06	~200	2.51×10^7
6	530	410	1.75	1 sphere	0.01	~20	4.19×10^3
Reference	490	400	3.00	12 flowers	0.12	~2500	9.81×10^{10}

The comparative morphological analysis is shown in **Figure 4.4**. In our sample, a higher density (0.14 flowers/μm²) but a lower average size of flowers (~1.1 μm) is achieved. In all, the deposited volume is higher in the reference due to the large size of the flowers.

As a prospective conclusion on the path to improve the use of the new chamber, we envisage to push forward the DFR if the need is keeping low the substrate temperature (~354°C); or to increase the substrate temperature toward 410°C provided the DFR is kept around 3mL/min. This would also allow disentangling the role of the geometry of the deposition chamber.
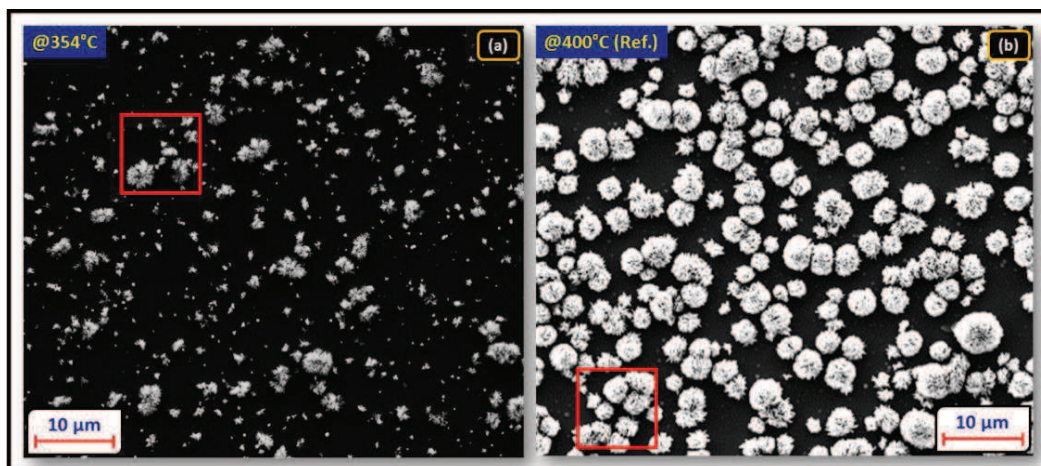
Figure 4.4: FE-SEM images to compare **(a)** our TiO$_2$ micro-flowers deposited at 354°C with **(b)** the reference sample deposited in standard conditions at 400°C. In both cases, an area of 100μm^2 was used to calculate the density and the average size of the flowers.

4.1.3.2. *CXDI analyses*

To look into the 3D architecture of the TiO$_2$ micro-flowers, we imaged representative samples using tomographic Coherent X-ray Diffraction Imaging (3D-CXDI) based on synchrotron radiation.[145,146]

As done for TiO$_2$ gig-lox (see Chapter 2) and using the same approach, we deposited on Si$_3$N$_4$ membranes upon gently scratching the sample. We performed porosity calculation and the 3D reconstruction of the scratched fragment from the best sample (sample n°3 in Table 5.2). Specific sections (**Figure 4.5(a)**), integrated morphology (**Figure 4.5(b)**) or 3D reconstructions are analyzed and evaluated.

To estimate the porosity we use the formula[151] reported in Chapter 2 and then we measure the sample and bulk density by histogramming the grey levels in the averaged slice (2D Projection) and in the central slice (or 2D Section), respectively. We found the average value of the porosity to be P (%) = 61±5%. Differently from the gig-lox case wherein a forest of nanorods was analyzed, the value describes the porosity inside a single flower. Moreover, using Chimera software also in this case as done for TiO$_2$ gig-lox (see Chapter 2), we extracted a surface to volume ratio. This latter in the TiO$_2$ micro-flowers is less in favor of the surface than in the TiO$_2$ gig-lox layer, being 0.04 nm^{-1} This represents that the TiO$_2$ micro-flowers expose relatively less surface likely due to its open structure.
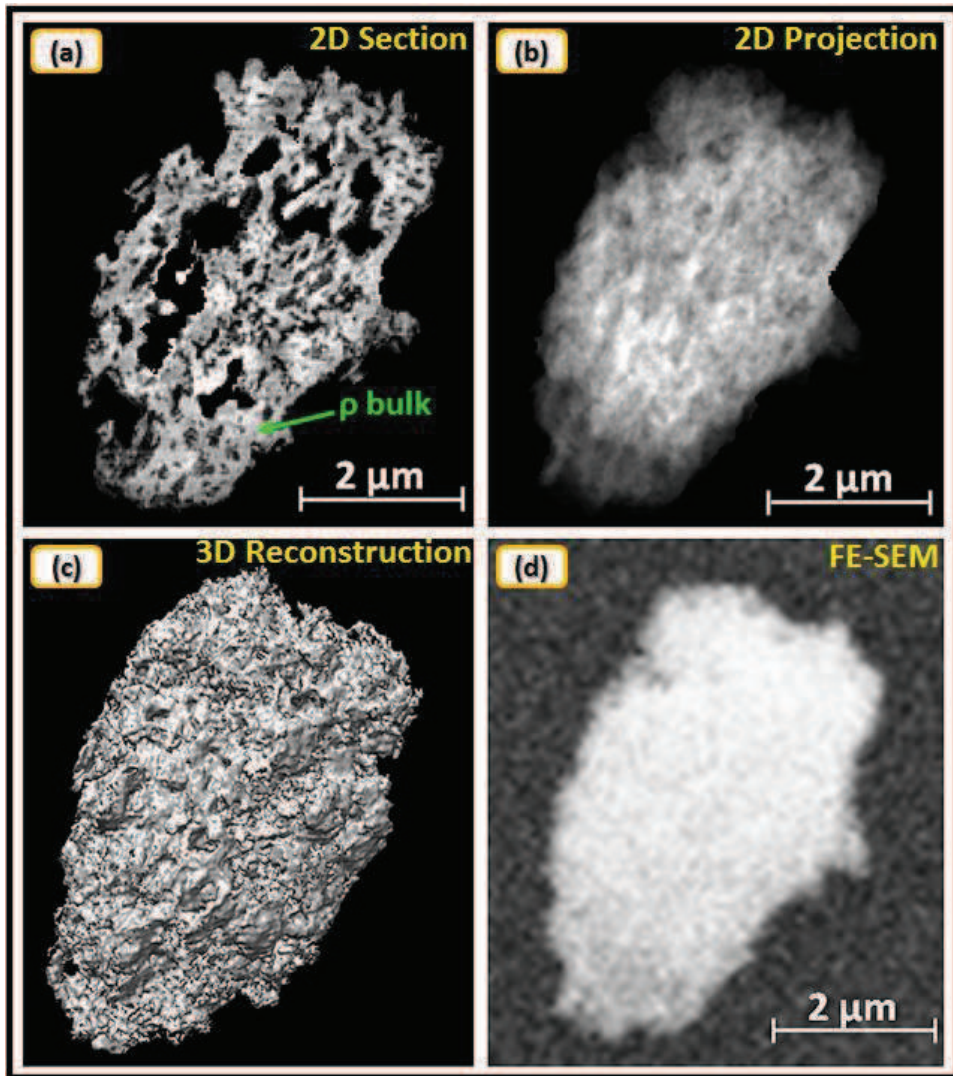
Figure 4.5: (a) Central slice used to obtain the ρ bulk (2D section), **(b)** volume representation used to obtain the average ρ sample (2D projection) and **(c)** 3D architecture (3D reconstruction) of the TiO₂ micro-flowers obtained by CXDI analysis. **(d)** FE-SEM image used as benchmark of the CXDI reconstruction. The sample was deposited at 354°C in the new chamber (best sample).

4.1.3.3. *Micro-Raman analyses @532 nm*

Micro-Raman Spectroscopy analyses were performed using a wavelength of 532 nm to investigate the lattice arrangement inside the flowers. Here we report the results on the sample deposited at 354°C.
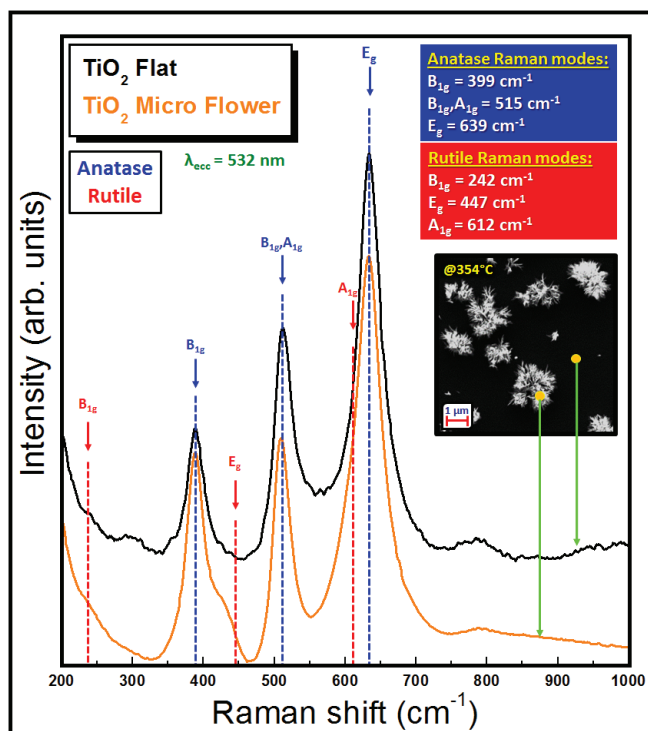
Figure 4.6: Micro-Raman spectra taken at 532 nm on a micro-flower in the TiO₂ sample deposited at 354°C in the new chamber and on a flat region of the same sample. Beam size = 1×1 μm².

Figure 4.6 shows the spectra of an as deposited TiO₂ sample in two different regions, namely on micro-flower and on a flat region (underlayer), in the range 200-1000 cm⁻¹. In both regions, the sample exhibits a long-range order in the anatase atomic arrangement.[65] As a matter of fact, in the spectra, typical vibrational modes of the anatase phase are found at 399 cm⁻¹ (B_{1g}), 515 cm⁻¹ (B_{1g}, A_{1g}) and at 639 cm⁻¹ (E_g). The lattice arrangement is gained owing to the deposition temperature, being in the range for anatase nucleation in nanostructures.[172,228] On the opposite, the gig-lox layers are deposited at room temperature, with a process consequently compatible with the use of any kind of substrate (*e.g.* plastics).

4.1.3.4. *TEM analyses*

To deepen the knowledge on the micro-flowers structure and to complement SEM Raman information, we performed Transmission Electron Microscopy on the sample deposited at T = 354°C.
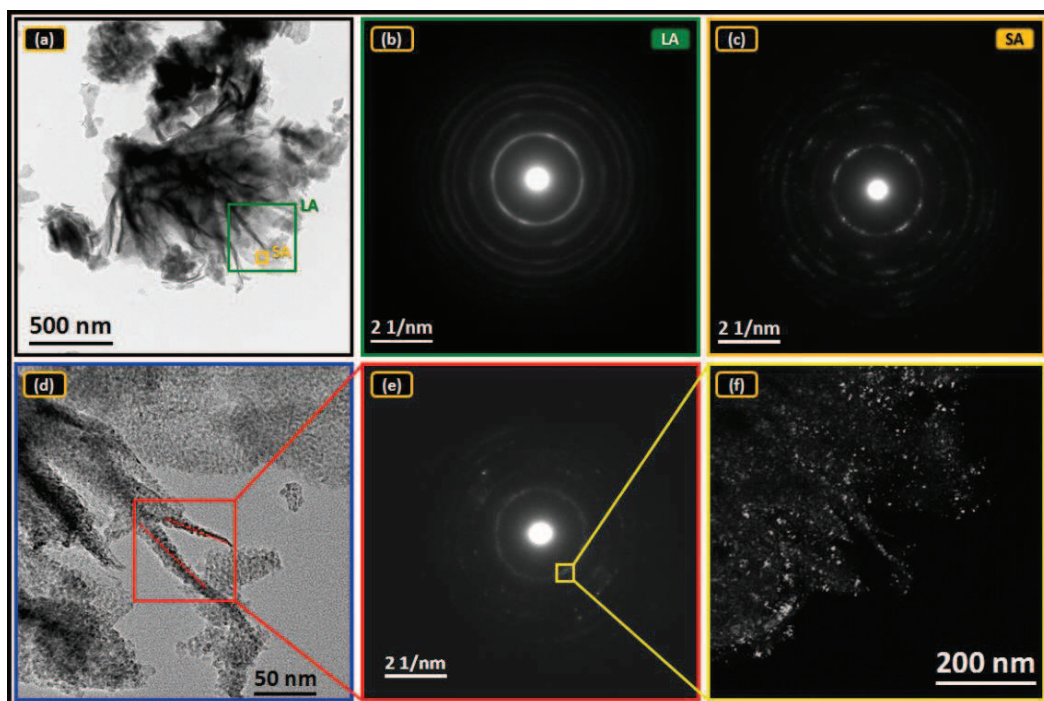
Figure 4.7: plan-view TEM images of as deposited TiO₂ micro-flowers **(a)** scratched on grid. The large area (LA) and the small area (SA) wherein the SAED (Selected Area Electron Diffraction) shown in **(b)** and **(c)** are collected, are also indicated. **(d)** High magnification in bright field of a portion of image (a), **(e)** its SAED and **(f)** dark field image originating from the region circled in (e).

Figure 4.7(a) shows the TEM image in plan-view of the TiO₂ micro-flowers scratched on a C-covered Cu-grid, wherein we can observe the petals of the structure. Their orientation is spread out towards different directions. The electron diffraction patterns (SAED) collected over a large (LA) and small (SA) area of the sample (**Figures 4.7(b,c)**) testify the anatase lattice structure of the flowers (first ring correspond to a lattice spacing of 3.51 Å). The result is in agreement with the micro-Raman data (see Figure 4.6).

In **Figure 4.7(d)** is reported a portion of the sample shown in figure 4.7(a), viewed in high magnification that elucidate the fine structure of the petals. Their nanostructuration accounts for the petals to bend in a wavy shape, making thus possible the peculiar shape of the flowers. The correspond SAED of the region circled in the Figure 4.7(d) is reported in **Figure 4.7(e)** in which we selected a specific spot and performed the analysis in dark filed (see **Figure 4.7(f)**). The findings do not indicate a preferential crystallographic orientation in the micro-flowers structure, and this can be put in relationship with the bending of the

petals which produces a randomization of the nano-grains configurations. In the dark-field image, the fine grain structure of the petals can be better appreciated.

4.1.3.5. *Optical properties*

The optical behaviour of the TiO₂ micro-flowers were investigated by UV-VIS transmission/absorption spectroscopy, with special regards to evaluate the scattering capability of the flowers. The material is, in a certain measure, transparent with total transmittance T% ~70%.

Light scattering was evaluated by means of the haze factor through the formula[229]

$$Haze\ Factor\ (\%) = \frac{T_{diffuse}}{T_{total}} \times 100 \qquad (15)$$

where $T_{diffuse}$ is the diffuse transmittance and T_{total} is the total transmittance. Diffuse transmittance was measured by the scattered light fraction out of the integrating sphere.

Figure 4.8 shows the Haze factor and the Tauc's plot of the best micro-flowers compared to the best gig-lox samples. The Tauc plot of TiO₂ micro-flowers gives an optical gap (3.57 eV) lower than that found in the gig-lox layer (3.76 eV). This is partially due to the lower degree of nanostructuration of the flowers compared to the gig-lox forest of rods, but it is also due to the presence of the unstructured layer under the flowers.[135] The discrepancy with the bulk value (3.3 eV) is in agreement with what reported in ref [172].
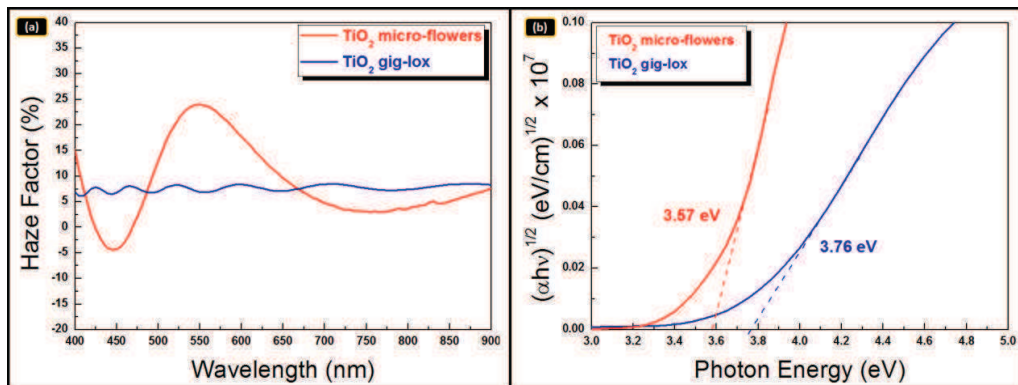
Figure 4.8: (a) Haze Factor comparison between the — TiO₂ micro-flowers and — TiO₂ gig-lox layer. **(b)** The corresponds Tauc plot.

4.1.3.6. *Contact Angle and perspective*

The wettability of the films was evaluated by contact angle (CA) measurements done using a water droplet. The property relies to the evaluation of the impregnation attitude of the layer for surface functionalization in a solvent.

In **Figure 4.9** is reported the CA trend as a function of the time exposure under solar siñlator (SS) at 1.5 W/cm^2 of the sample. Sun exposure was done to promote the photo-activity of TiO$_2$ through surface modification induced by UV absorption.

The data show the hydrophobic-hydrophilic transition of the TiO$_2$ layer.[230] The CA of the as deposited TiO$_2$ micro-flowers in dark condition is 133.7$\pm$2°, thus disclosing the hydrophobicity of the starting material.
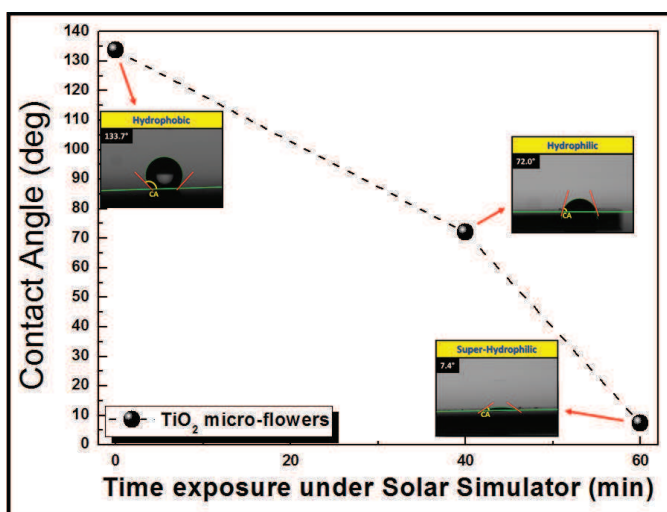
Figure 4.9: Contact Angle measurements of as deposited TiO$_2$ micro-flowers obtained by AA-MOCVD in dark and after exposure under solar simulator at 1.5 W/cm^2 to observe the hydrophobic-hydrophilic transition.

When the as deposited samples are exposed to solar simulator, their surface transformed from hydrophobic to hydrophilic (CA = (72$\pm$2)°) after 40 minutes of irradiation at 1.5 sun or super-hydrophilic (CA = (7.4$\pm$2)°) after 1h, as shown in Figure 4.9. This remarkable surface wettability transition can be tuned reversibly. In fact, after the SS-irradiated films were placed in the dark for three weeks, their hydrophobicity was gained back. When the film is irradiated, the photo-generated holes in TiO$_2$ by UV absorption[231] react with oxygens in the lattice to form, especially at the surface, oxygen vacancies. Water molecules from the ambient kinetically coordinate with them. This enhances the surface

hydrophilicity greatly. Thanks to the rough surface of flowers, the water droplet fills the grooves along the micro-flowers and replace the trapped air. When dark is reestablished, after hydroxyl groups have decorated the surface, an energetically metastable state is settled, and the adsorbed hydroxyl groups can gradually be replaced by atmospheric oxygen during time.[232] Thereby, the surface evolves back to its original state, and the surface wettability converts from super-hydrophilic to hydrophobic again. This result indicates that the surface structure strongly affects the wetting behavior.[233,234]

It was verified with a similar experiment that the gig-lox TiO_2 layer behaves as a hydrophobic material in dark condition. Consistently, a CA of 100.5° is measured. The hydrophilicity of the gig-lox layer can be partially recovered by a thermal treatment, with the advantage of making the surface more inclined to react with –COOH bearing species (*e.g.* N-719 in DSCs) or with water-killed species (*e.g.* $MAPbI_3$ in PSCs).

To summarize, TiO_2 micro-flowers films with special micro- and nanoscale surface structures have been prepared. A remarkable, controllable surface wettability that shows reversible hydrophobicity/super-hydrophilicity is observed on this inorganic oxide layer. The cooperation of the surface microstructures, and the surface photosensitivity are considered to be mainly responsible for this behavior.

All those properties prospect a certain degree of applicability of the structures for surface functionalization after having faced some issues mainly related to the material uniformity and up-scalability.

4.2. *Gig-lox TiO₂ for gas-sensing*

Going back to the gig-lox processes, in this paragraph, we aim at demonstrating that the gig-lox TiO₂ layer is a versatile material that can be applied in a field different from PV, e.g. for gas sensing. This experiment demonstrates the transversal empowering gained by the uniformity of the spongy structure and by its bimodal porosity.

4.2.1. *TiO₂ gig-lox integrated in sensing device*

TiO₂ gig-lox layers were used as active material for gas sensing in resistive state-of-the-art read-out devices made by STMicroelectronics in the context of a scientific collaboration (Dr. Antonello Santangelo R&D group).
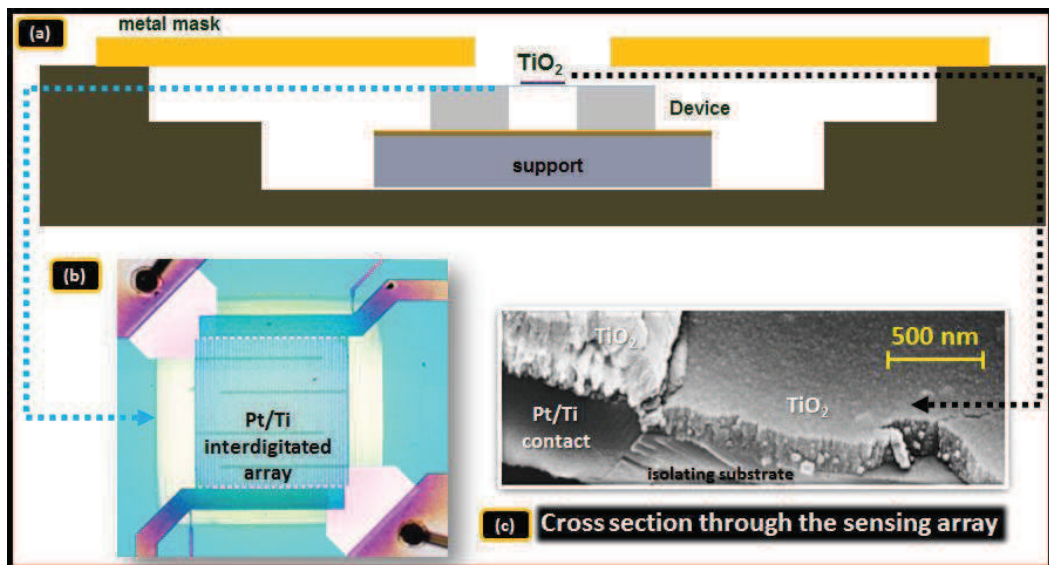
Figure 4.10: (a) Schematic showing the package cavity, the device and the metallic shadow mask for confined deposition of the spongy TiO₂ layer; **(b)** Optical image of a suspended micro hot plate, showing the interdigital electrodes and heater made of Pt/Ti films; **(c)** FE-SEM image of the device cross section taken through the sensing array.

The deposition process follows the procedure discussed in Chapter 2; the integration of the TiO₂ gig-lox into the device is done with the simple application of a shadow mask to confine it into the sensing area (**Figure 4.10(a)**). The layer thickness is 350 nm and the porosity ~50% volume; the layer is deposited at room temperature over the interdigitated Pt fingers shown in **Figure 4.10(b)**. The Pt fingers have the role of collectors and transporters of the electrical signal coming from the active TiO₂ layer during operation in a

gas ambient. The choice of the layer thickness relates to the morphology of the Pt fingers (200 nm in height); nonetheless, it can be eventually scaled-up or down to be integrated over fingers with different geometries (Figure 2.11(b)). The TiO$_2$ layer distributes along and in between the metallic fingers array through a conformal coverage that allows collecting the injected current during sensing (**Figure 4.10(c)**).

The sensing material does not require any sintering/firing process after deposition. We additionally exploit the value-added of a porosity unaffected by temperature and humidity, main parameters during operation of the sensing device. Underneath the sensing structure, a micro-hot-plate is used to set the working temperature, needed to activate surface reactions, directly on the active material. The material integration in all is 1) extremely simple and 2) implementable over any device architecture.

Note that this technology, since it applies thin active layers instead of thick layers for sensing,[235] is convenient in terms of saving materials/costs and reducing waste. As a further value added, the TiO$_2$ layer is locally heated over the integrated free-standing temperature source to avoid unwanted temperature-related effects on the overall structure during operation.

We are going to demonstrate the high sensitivity, response time and stability of such sensing structure to ethanol, and the relationship between the sensing parameters with the branched nanostructure and surface reactivity of the material. Also in this application, a special empowering is offered by the multi-dimensional pore structure and pore interconnection that promote gas infiltration and reaction deeply into the layer.

The use of this approach would represent a step forward in the sensing field to the extent that it combines, on one side, an easy technological transfer to large areas and, on the other side, a severe positive down-scaling of the active layer thickness without compromising the sensing performances.

4.2.2. *Characterizations*

The paragraph aims at investigating the properties of the material in conditions which mimics the operation in a device, with special regards to the working temperature settled through the integrated micro-hot plate. We consistently explored a temperature range between 250°C and 500°C.

4.2.2.1. *Structural properties*

In situ X-Ray diffraction analyses were collected over a 350 nm-thick layer during isothermal annealing at 300°C in air conditions to reproduce the material operation in a low-temperature-working sensor. The analyses were repeated after a heating time of 50 minutes in order to eventually follow the material transformation over time. The annealing time was prolonged for 36 hours without any visible lattice long-range restructuration-giving rise to diffraction peaks.

To force a long-range restructuration of the material, a fresh sample was annealed at 500°C in air. The lattice structure was investigated by combining the information coming from symmetric and grazing incidence analyses. The estimated penetration depth in grazing at 0.4°is ~100nm. The resulting diffraction patterns (see **Figure 4.11**) account for a body-centered tetragonal arrangement of TiO₂ in the anatase lattice. The comparison with a reference powder[161,180,236] (randomly oriented by definition) allows concluding that the anatase domains are preferentially oriented with the [001] direction being the preferred one for growth. Similar footprint in grazing incidence implies that the preferred growth axis opens in fan shape for a reason linked to the growth procedure (source in grazing + sample rotation under flux).
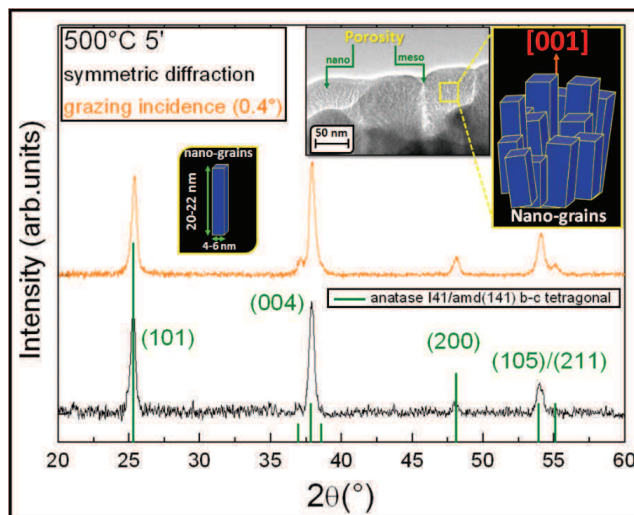
Figure 4.11: Diffraction patterns in — symmetric and — grazing incidence geometries of a 350nm-thick TiO₂ layer annealed at 500°C for 5' being restructured in the anatase lattice; the — green bars are related to a reference anatase powder having body centered (b-c) tetragonal structure with a=b=3.785; c=9.514. Note that the (101) peak is expected as the most intense one in a randomly oriented poly-layer. In the inset: the average dimensions of the nano-grains, in full agreement to what locally shown by TEM cross-section image. This latter showing the material arrangement by nano-grains in a matrix of pores.

This finding is agreement with the TEM cross-section image given in inset of Figure 4.11 to recall the fine structure of the layer. The nanograins have dimensions in the range of 5-30 nm, as confirmed on average by XRD results (hereafter); the nanopores are in the range of 1-5 nm. They are well interconnected and large enough to be deeply infiltrated by gas species. The larger pores between the spongy grains, arising from the shadowing effect.[65] during growth, are potential pipelines for gas infiltration. The pores matrix originates from the early stages of the material growth as testified by their crossing the whole thickness.

The preferred orientation of the anatase domains along the [001] direction produces a (004)/(101) ratio above 1 whilst in a randomly oriented poly-crystal a value of 0.2 is expected (see **Table 4.3**). The use of a double acquisition geometry has provided the complete scenario about not only the domains orientation but also about their size and aspect ratio. The numbers are in Table 4.3. A picture of the grain shape, that results elongated in the [001] direction by Scherrer-type calculations, is shown in the inset of figure 4.11.

Table 4.3: XRD parameters and calculations.

Scan Type	Planes	FWHM (deg)	domain size (nm)	In plane domain size (nm)	Obs. Max (deg)	d-spacing (Å)	net Area (Cps×2θ)	experimental area ratio	expected area ratio
								(004)/(101)	
symmetric	(101)	0.390	21.7		25.22	3.53	39.43	1.1	0.2
grazing incidence	(101)	0.418	20.2	4.4	25.38	3.51	94.66	1.3	0.2
symmetric	(004)	0.433	20.1		37.85	2.38	43.02		
grazing incidence	(004)	0.448	19.4	6.3	37.91	2.37	123.4		

4.2.2.2. *Optical properties*

The layer porosity was evaluated in as deposited layers and after specific thermal treatments tailored on the device operation parameters. According to what discussed in Chapter 2 (Figure 2.11(b)), the porosity of the gig-lox layer does not sensibly change with thickness and thermal treatments up to 500°C.

We also explored the optical constants n (refractive index) and k (extinction coefficient). As representative of the others, the n and k values collected in the range 1.5-4.5 eV over a 350nm-thick layer, before and after annealing at 300°C and 500°C, are represented in **Figure 4.12(a)**.

Although the porosity and the lattice structures (XRD) do not sensibly change after thermal treatment at 300°C, an effect on the bandgap is recorded, which is further enhanced by the annealing at 500°C. The figure also shows that the refractive indexes of a compact anatase layer systematically lie above those measured in our porous layers[154,160] (see Chapter 2).

To evidence the behavior close to the bandgap, **Figure 4.12(b)** shows the Tauc's plot for TiO₂ layers annealed at 300°C. The comparison with the as deposited layer highlights that, provided the thermal budget is kept low enough (annealing time within a range), the TiO₂ response remains unmodified. Prolonging the annealing time tentatively to 36h has, instead, induced modification explainable by the formation/activation of defects states; consistently, the absorption tail has moved downwards with a gap tentatively measured at ~3.5 eV (Figure 4.12(b)). Note that sample exhibits a certain absorption probability at energies lower than the 3.5 eV.

Figure 4.12(c) reports, instead, the case of a sample after a thermal treatment at relatively high temperature (HT = 500°C) for short time, which induces the complete annihilation of defects with consequent increase of the bandgap. The bandgap value measured after the HT annealing settles to 3.6 eV. Although this is more than what expected in an anatase bulk layer, it is not surprising that nanostructure TiO₂ exhibit a higher bandgap due to the low dimensionality of the system, as reported in ref [172].

Our structural findings summarize by saying that the annealing of defects is a process internal to the nano-grains, due to the TiO₂ lattice restructuration in the anatase form, which does not affect the layer porosity. We also learn that, despite the overall lattice restructuration, the branched structure of the material is preserved without grain coalescence. We are going to additionally demonstrate that the reactivity of the exposed surfaces in the gig-lox layer is not negatively affected by the annealing even if 500°C is used as working temperature for sensing.
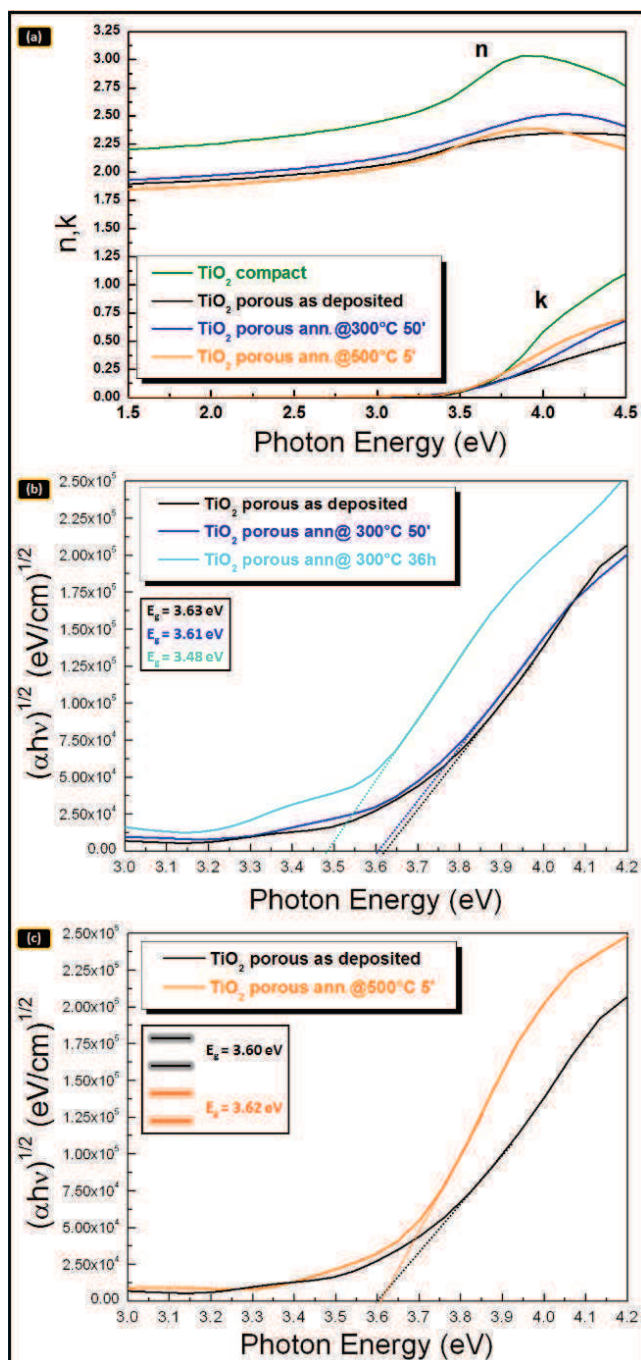
Figure 4.12: (a) refractive indexes (n) and extinction coefficients (k) of a porous 350nm-thick layer before and after annealing at 300°C and 500°C in air (40%RH) in comparison with a compact TiO₂ anatase reference material: in all cases, n and k are systematically lower than in the reference. Tauc's plots (indirect band gap) of the absorption coefficient measured in TiO₂ layers annealed at: **(b)** 300°C vs. annealing time; a prolonged annealing time drives the material through a transient state, which modifies the gap region. **(c)** 500°C for 5': the extracted energy gap (E_g) denotes a process of lattice ordering with respect to the starting point and that the material has reached a steady state.

4.2.2.3. *Sensing behaviour*

The electrical response (resistance) of the device was evaluated at two different working temperatures using ethanol as gas target. During operation, the reaction of ethanol vapour with the TiO_2 surfaces leads to a decrease of the device resistance. A well-established surface-depletion model is considered to explain the phenomenon.[237,238] Before getting in touch with the gas species, the TiO_2 surfaces spontaneously interact with the atmosphere having an inherent tendency to adsorb oxygen atoms. The atomized oxygens pick up electrons from the TiO_2 surface layer and, accordingly, the electron density is locally depleted with the formation of a surface depletion region. Note that our material is mostly surfaces and that the depletion region can occupy most of the single branch volume (see inset in Figure 4.11). When a reducing gas (*e.g.* ethyl alcohol) comes in contact with the modified TiO_2 surface it tends to react with negatively charged oxygen atoms adsorbed on the surfaces. In the process, creating CO_2 and H_2O species, electrons (6 per CH_3CH_2OH molecule) are finally injected into the conduction band of TiO_2. This causes the resistance of the material to decrease.[239,240] The response is expected to depend on the gas species concentration.

A typical figure of merit is shown in **Figure 4.13,** wherein a fast response and a high sensitivity is recorded after injection of 44 ppm of ethanol at 40% humidity and working temperature of 300°C. A high recovery time can be also observed (close reaction chamber which mimics the operative conditions).

We explain the high performances of the device according to the branched TiO_2 structure and the special pore matrix. Gases molecules are, in fact, favoured to enter the pore array through the pipelines offered by the meso-pores (coming from the shadowing strategy) to quickly imbue the structure through the interconnected fine array of nano-pores. The fast response and high sensitivity of the sensor are thus related to the high accessibility of the volume of the material (driving response and recovery time), to the high offered surface to volume ratio and to the good surface reactivity. All those strengths allow using thin active layers for sensing of low ppm of gas species at low working temperatures. Other branched TiO_2 materials have lower response to the same gas[241] probably due to lack of an effective network of electrical interconnection or to a minor surface to volume ratio instead enhanced in our gig-lox structure.
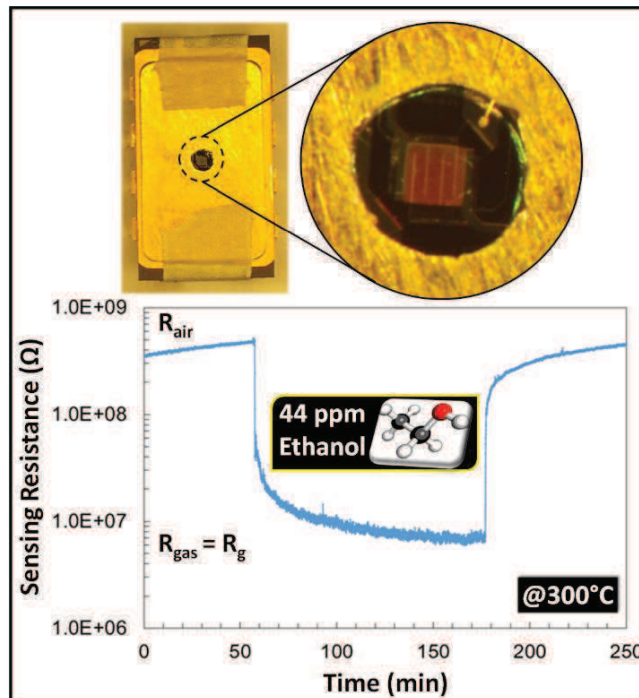
Figure 4.13: Change in the device resistance due to sensing of 44 ppm of ethanol (concentration value after calibration) at RH 40% - The working temperature is 300°C. On the top: the sensing device.

After sensor stabilization in air, the analyses were repeated changing the ambient humidity from dry condition to 60% RH at 300°C. The maximum sensitivity value, reached in dry air, is as high as 99.8. Nonetheless, the dependence on relative humidity is almost negligible (<1%) in the range explored, the response varying from 99.8 to 99.3 in dry and 60% RH condition, respectively. The response time, defined as the time for the gas response to get to 90% of the final equilibrium value when the gas is turned on, is also competitively low, being in the range of 10-16 sec. Other nanostructured materials reported in the literature[239,242] claim response times lower than 20 sec; but, among the others, in ref [239240] an unstable response is recorded at gas concentrations lower than 100 ppm or in ref [241] a stabilization process (firing) in air at 300°C is needed to allow the sensor to work properly. On the opposite, the low response time exhibited by our gig-lox layer was to just 44 ppm of ethanol and without the need of a post deposition firing. We additionally emphasize that in our devices the TiO₂ layer thickness used is competitively low (350 nm). In some other cases, *e.g.* using SnO₂-ZnO powders for sensing, the response-recovery times is high (96-400 sec[243] at 100 ppm of ethanol): or, in case of short response/recovery times

for powders (e.g. 13/8 for TiO$_2$),[172] the industrial implementation suffers from several practical constraints (e.g. implementation of powders in devices, materials consumption). We further notice that our results tightly compete with very recently published results in the literature results[244] (the section report also an interesting overview vs. the deposition method of the active layer).

A stress test at a temperature of 500°C 5min was applied to explore aging effects or the extent of the material durability. The annealing was locally done on the finite sensor directly on the membrane using the integrated heater in such a way that the architecture did not suffer from the thermal budget. We found that the gas response was not sensibly affected by the annealing, varying by about 10%. Keeping high the performances of the sensor even after annealing at 500°C testifies and further confirms that the layer porosity and the reactivity of the internal surfaces are not sensibly affected; and in that resides the strength and novelty of the gig-lox strategy applied to TiO$_2$ for sensing. For strict application purposes, the results on the applied stress test at 500°C prospect a long-time stability of the sensor operation, further expandable in a pulsed operation mode; additionally, they demonstrate the compatibility of the material with eventual additional thermal budget needed for the overall sensor architecture.

The sensor response was finally tested after further reduction of the operation temperature. In **Figure 4.14** we show the sensor response as a function of vapour concentration in a range for high sensitivity devices, and using a working temperature of 250°C compared to what found at 300°C (40% RH).

A slightly lower response is obtained at 250°C compared to what found at 44 ppm of ethanol using instead a working temperature of 300°C, likely due to a minor thermal energy that impacts on the probability of gas linking at the TiO$_2$ surface or/and due to some slight changes in the surface reactions paths or/and due to a change in the barrier to charge injection. Besides this small gap in the response by reducing the temperature, our gig-lox TiO$_2$ engineered scaffold affords a high capability of interaction with ethanol at low temperature exploiting small active volumes (hundred-nm-thick layers), with its high sensitivity mainly related to the pervasive infiltration network (the voids array), to the high surface to volume ratio and, additionally, to the finely interconnected branched nano-rods matrix. From the data in Figure 4.14 we additionally observe that the gig-lox sensitivity to ethanol settles high even reducing the gas concentration to 17 ppm.
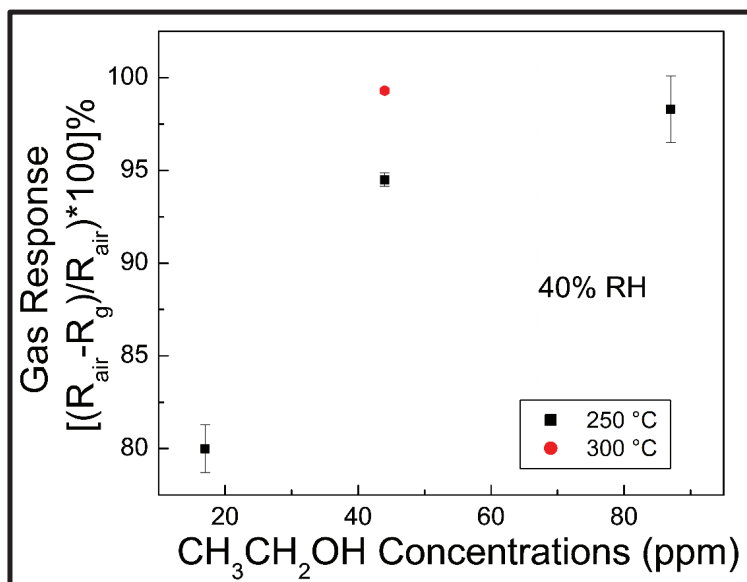
Figure 4.14: Sensor response as a function of the ethanol concentration at 40%RH. The concentration values were calibrated by the weight loss in the ethanol bubbler.

To summarize, we demonstrated that a sputtered TiO₂ layer can be raised to the level of a high sensitivity gas sensor owing to the implementation of the gig-lox growth strategy, being new in the sensing landscape. The technique is intrinsically up-scalable and therefore industrially compatible, so that it was easily applied to build-up the architecture of complete sensing devices. The novelty of the technique resides in the capability to produce spongy material in a wide range of thicknesses, here demonstrated from 350 nm to 1000 nm, with porosity being constant through the whole layer. Although the spongy TiO₂ layers do not need a firing process at high temperature to be used for sensing, we have anyhow demonstrated that its porosity is preserved in the range of 47-51% vol. by annealing up to 500°C. The annealing at 500°C has an effect on the bulk stabilization of the TiO₂ rods in reducing defects states, potentially trap-centers for the injected electrons into the depletion regions. Nonetheless, only a slight change on the responsivity of the sensors was observed after annealing. Thereby, this thermal budget, that is not strictly needed, can be eventually applied for additional production steps without negatively impacting on the sensing process.

The high surface to volume ratio, the high surface reactivity, the pervasive network of voids and the interconnected TiO₂ nano-branches offered by the spongy gig-lox TiO₂ layer allowed getting a high sensitivity to ethanol in the range of 17- 87 ppm using a layer which

is just 350nm, with the exhibited sensor response $((\Delta R/R)\times100)$ in the range of 80-100, being not sensibly affected by the ambient humidity up to 60% RH. In the branched structure of the spongy layer, the meso-pores are highways to pilot the gas through the whole thickness and nano-pores serve to finally imbue the layer such to extensively exploit the internal surfaces of the sponge. Thereby, the working temperature of the sensor can be easily reduced to 250°C.

Demonstrating high performances in sensing devices using our innovative active layer with extremely scaled thickness integrated by a simple procedure represents an important step forward both in terms of materials saving and in terms of industrial benefits. We additionally emphasize that our gig-lox method could in principle be extended to other kind of oxides and applied to detect any other gas species bearing an –OH anchoring group.

4.3. *ZnO:Al as a TCO for hybrid solar cells*

DSC[23,245,246] and PSC[24,247] both benefit from the high performances of the TCO used to collect the photo-generated charges.[65,179,180,244,248,249,250] It mainly impacts on the series resistances, and therefre it is required to be a low-resistivity material. Nowadays, Indium Tin Oxide (ITO) films are predominant as TCO in practical applications. However, Al doped ZnO (ZnO:Al = AZO) films represent a potential alternative choice to ITO mainly because of their competitive electrical and optical properties, cheap and abundant raw materials, nontoxic nature, long term environmental stability and easy fabrication. It could be even deposited at low temperature for applications on flexible substrates.[251]

We here propose ZnO:Al layers co-deposited by sputtering in the same chamber as that used for gig-lox growth.

The prospected scenario includes the sequential deposition of TCO and of active layers for PV or other applications, without breaking the vacuum in the vacuum chamber. The idea implies zero contamination at the interfaces to improve the charge transfer from one material to the other, and thus to enhance charge collection.

4.3.1. *Co-doping issues*

AZO layers can be grown by various deposition techniques including Pulsed Laser Deposition (PLD),[252] Chemical Vapor Deposition (CVD),[253,254] sol–gel[255] and magnetron sputtering.[256,257] Among those approaches, magnetron sputtering from a composite target (98%ZnO+2%Al$_2$O$_3$) has outstanding advantages such as simple apparatus, high deposition rates, low temperature and large deposition area. The method allows depositing doped ZnO films and assures contamination-free materials. Some literature works have also explored the possibility to deposit AZO conductive layers by co-sputtering using a double source (ZnO or Zn and Al or Al$_2$O$_3$).[255,258,259] This configuration would in principle allow a tuning of the Al content in the AZO matrix. In this respect, it was however observed that a thermal budget at 400°C is needed[257] in order to grow AZO layers with low resistivity. The annealing promote Al^{3+} species replacing Zn^{2+} in the ZnO lattice. Nevertheless, due to the need of high thermal budgets, this method cannot be straightforwardly transferred to plastic substrates. Some other attempts were done to deposit doped materials at nominally low temperatures,[250,258] but high power loadings, often combined with low chamber pressure,

generate energetic ad-atoms that raise the effective temperature of the substrate during deposition (intrinsic heating). To our opinion, a good compromise needs to be targeted between the sputtering rate and the intrinsic substrate heating due to ad-atoms energy, in order to render the deposition process compatible with the use of low-cost substrates (*e.g.* plastics). Effective doping by substitutional Al, rather than by oxygen vacancies or other donor lattice defects, still remains crucial.

As the pervasive dissemination of DSC/PSC technology needs to pass through a drastic cost reduction of the TCO, we focused our attention to an implementable approach able to produce ZnO:Al transparent conductive layers at low temperature by reactive co-sputtering. Moreover, the resulting material has optical-structural-electrical properties as good as those of a typical TCO film. The mutual correlation of those properties has been additionally discussed.

4.3.2. *AZO deposition by reactive co-sputtering*

Transparent Conductive Oxide (TCO) layers, to be implemented in photoanodes for hybrid Solar Cells, were prepared by co-deposition of ZnO and Al using pulsed-DC-magnetron reactive sputtering processes (see **Figure 4.15**).
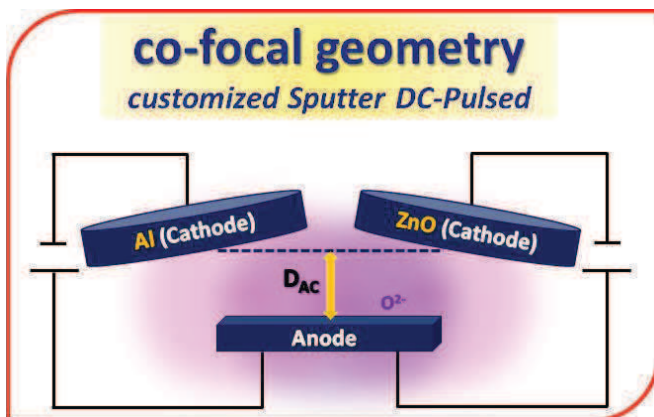
Figure 4.15: Schematic of the co-focal geometry used to obtain the ZnO:Al layer by reactive co-sputtering.

The films were deposited at low deposition temperatures (RT-188°C) and at fixed working pressure (1.4 Pa) using soft power loading conditions to avoid intrinsic extra-heating. To compensate the layer stoichiometry, O_2 was selectively injected close to the sample in a small percentage (Ar:O_2=69sccm:2sccm). The deposition temperature,

monitored directly on the sample surface by commercial thermo-strips (Racetech - Thermal Indicator Strips), was used as a parameter to incorporate an increasing amount of Al^{3+} species in the appropriate ZnO lattice position, during growth that allowed the dopant to be electrically active.

4.3.3. *Lattice engineering*

4.3.3.1. *Crystallographic properties*

The crystallographic properties of the ZnO:Al layers are investigated by XRD analyses, using a symmetric configuration (2θ-ω) (see inset on the left). The diffraction patterns of layers prepared at different deposition temperature, namely 138°C, 155°C, 188°C, are shown in **Figure 4.16**, with the maximum normalized to 1. The vertical bars refer to a random ZnO powder, with their relative scattering factors indicated by the bars height. All the patterns show a single contribution at 2θ≅34.4°, which is related to the (0002) planes of the hexagonal wurtzite lattice (see inset on the right).
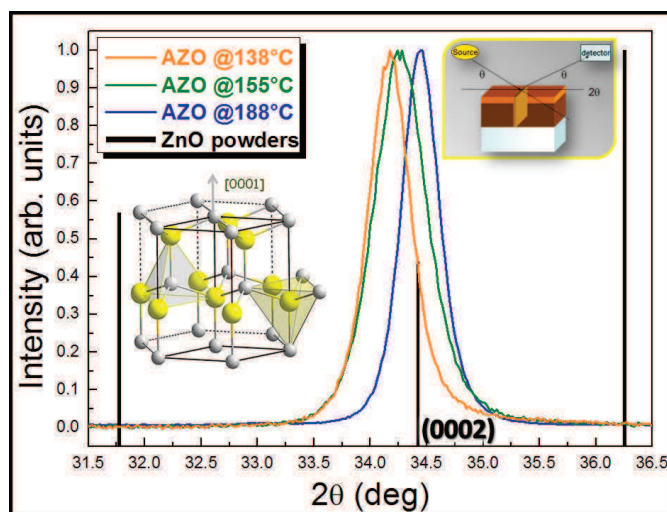
Figure 4.16: 2θ–ω XRD patterns of different AZO samples deposited at low temperature (T<200°C). In inset on the right the wurtzite structure and on the left the schematic of the diffraction geometry.

Due to the acquisition geometry (2θ-ω), those lattice planes lie parallel to the sample surface, indeed with their growth direction along the c-axis of the wurtzite structure. The lack of the other intense contributions, which are expected in a random layer (see bars in Figure 4.16), indicates a high texturing degree of all the grown layers along the c-axis. This

selectivity renders the layer structurally uniform in its extent. As a difference introduced by the deposition temperature modulation, the samples grown at temperature lower than 188°C have the (0002) peak shifted leftwards with respect to the reference bar. The corresponding $d_{spacing}$ are 0.2623 nm and 0.2616 nm for the samples deposited at 138°C and 155°C, respectively. On the contrary, the ZnO:Al layer deposited at 188°C has the peak associated to the (0002) planes at the position expected for an unstrained reference layer, whose $d_{spacing}$ is 0.2606 nm. This finding will be further discussed in what follows.

4.3.3.2. *Morphological analyses*

The morphology of all the films is investigated by FE-SEM. The average thickness of the ZnO:Al layer deposited at 188°C, measured by FE-SEM images in cross section (not shown), was ~1μm.

Element	Atomic Number	Normalized Mass Concentration [wt.%]	Atomic Concentration [at.%]	Error (1 Sigma) [wt.%]
O	8	29,09	61,71	3,61
Zn	30	68,91	35,77	2,39
Al	13	2,00	2,52	0,13
	Total	100,00	100,00	
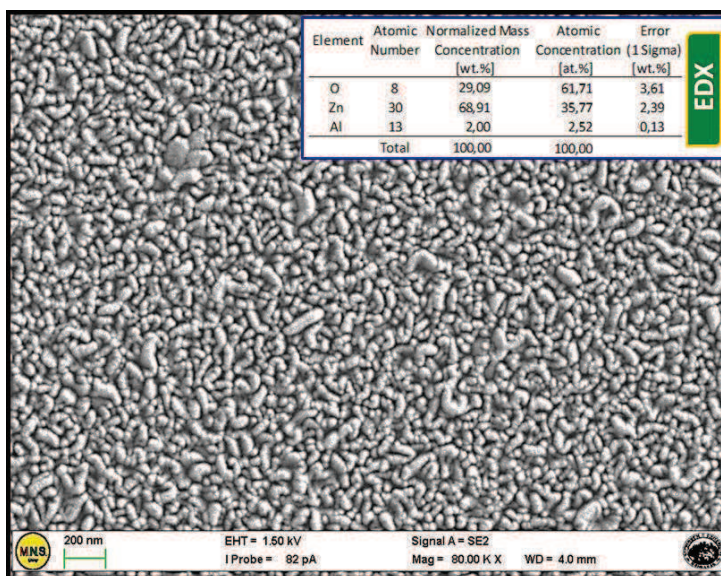
Figure 4.17: FE-SEM analysis of the AZO layer deposited by co-sputtering in co-focal geometry at 188°C. Inset: the atomic percentages of the species revealed by EDX probe.

As can be appreciated in **Figure 4.17**, the material creates a uniform coating with homogeneous morphology that is fundamental to guarantee an effective charge transfer from the scaffold towards the TCO in a DSC/PSC. Spatial disuniformities in the layer thickness or in its surface roughness, with the eventual presence of deleterious protrusions, would affect the series resistance or generate parasitic currents (respectively).[249,260,261]

In situ EDX analyses provide an average atomic percentage of Al^{3+} inside the ZnO lattice of ~2%, (see inset of Figure 4.17). Moreover, it was verified that the morphology does not significantly change from sample to sample.

4.3.3.3. *Composition of the AZO layer*

A detailed investigation on the composition of all the sputtered ZnO:Al layers is performed by XPS analyses.
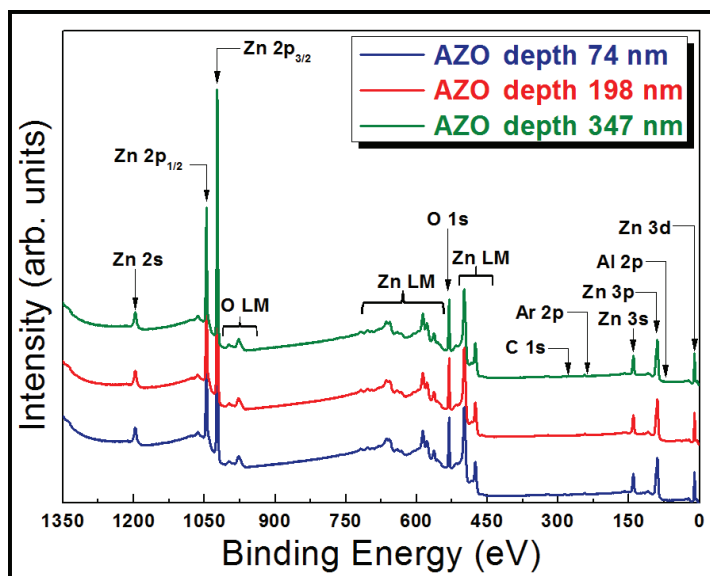
Figure 4.18: XPS wide scans of AZO layers at different depth.

In particular, we collected a depth profile of all the involved species to study the composition along the layer thickness. The erosion rate was 16.2 nm/min, with the end-point given by the silicon atoms in the glass substrate.

The representative XPS wide scans of the AZO layer prepared at 188°C, collected at different depth with respect to the film surface, are shown in **Figure 4.18**. The peaks due to C, Ar, Al, O and Zn were identified in the survey.

High-resolution spectra were acquired to investigate about the bonding fraction coordination, also along the sample depth profile and the Al content incorporate into the ZnO lattice. HR-XPS spectra for a) C 1s (at 284.7 eV); b) O 1s (at 531.4 eV); c) Zn $2p_{1/2}$ and $2p_{3/2}$ (at 1045 eV and 1022.8 eV respectively); d) Al $2p_{3/2}$ (at 74.7 eV) regions are shown in **Figure**

4.19(a-d). We note that the surface of the material has a different composition with respect to the bulk, most likely due to surface contaminations. In fact, we found the presence of both –OH groups at binding energy (BE) of 532.5eV and of carbonaceous species at about 284.7eV (see figure 4a). The atomic percentage of all the species is estimated by the HR spectra, taking into account the relative atomic Scofield's sensitivity factors.[262] The atomic composition does not vary significantly along the samples thickness. The estimated values are: Zn 52%, O 45%, Al 1.8% and C 1.2%, respectively. Thereby, as a main result, the stoichiometry of the ZnO:Al layer is constant along the layer thickness, evidencing that a uniform Al content was inserted into the ZnO lattice during growth.
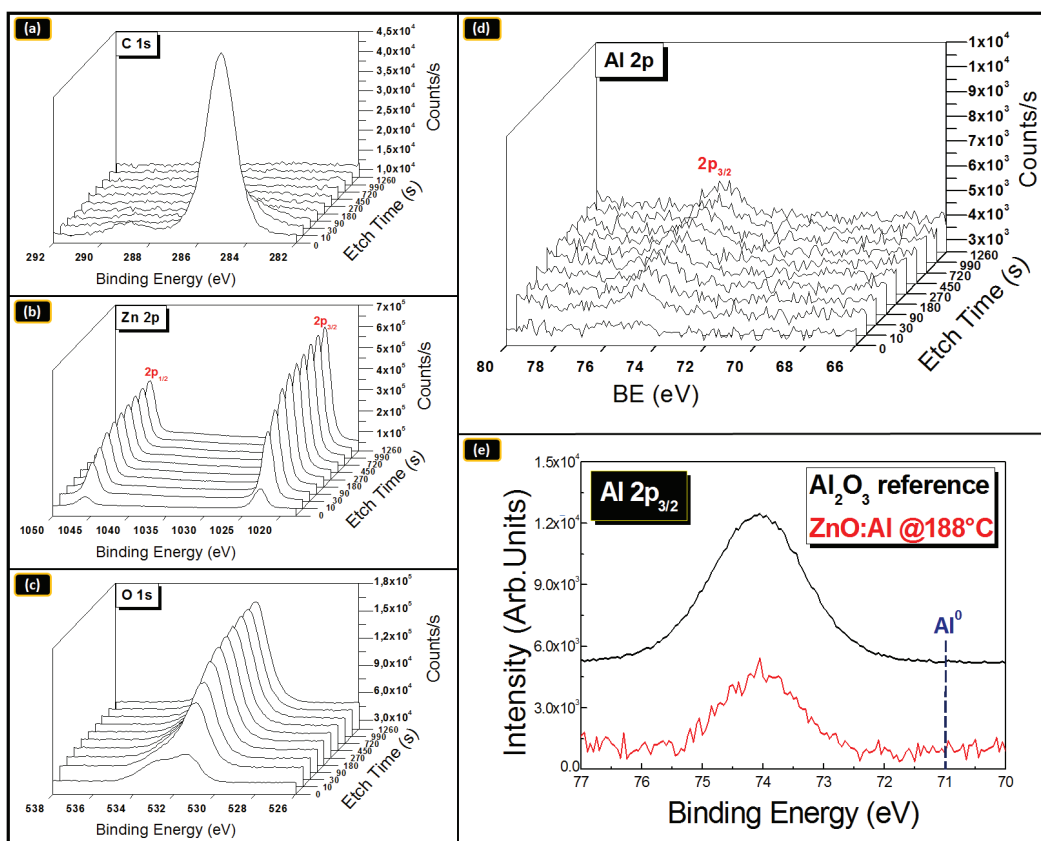
Figure 4.19: XPS in-depth profile analyses of the AZO layer deposited by co-sputtering in co-focal geometry at 188°C: **(a)** C 1s, **(b)** O 1s and **(c)** Zn 2p and **(d)** Al 2p$_{3/2}$ spectra; **(e)** Al 2p$_{3/2}$ spectrum taken on the AZO layer and on a reference Al$_2$O$_3$ material. Al^0 is the expected peak position for a metallic layer.

Figure 4.19(e) shows a detail of the XPS peak related to Al 2p$_{3/2}$ taken on the ZnO:Al layer in comparison with what found in a Al$_2$O$_3$ reference material, to emphasize that the

chemical environment of the aluminum atoms does not show a metallic character (BE = 71 eV). On the contrary, the measured binding energy depicts a typical coordination of Al species by oxygen atoms (BE = 74 eV).

4.3.4. *Conductivity and transparency optimization*

4.3.4.1. *Optical analyses*

The optical behavior of the deposited films is evaluated by investigating their transmittance response in the UV-Vis range. The mean transmittance of a 420nm-thick AZO layer, deposited at 188°C, settles around 85% in the visible range, as shown in **Figure 4.20(a)**.

The optical band gap (E_g) of the films was estimated by the Tauc plot[263] of the absorption data for direct band gap. With this procedure, the band gap is given by fitting the linear part of $(\alpha h\nu)^2$ vs. $h\nu$ at the curve onset and by extracting the intercept with the x-axis.

Figure 4.20(b) compares the Tauc plots of the ZnO:Al layers grown at different temperatures. The band gap values measured in the layer grown at 138°C and at 155°C are similar (~3.3 eV), whilst the layer grown at 188°C exhibits a higher value, namely ~3.5 eV. The band gap widening was associated to the well-known Burstein–Moss effect,[264] which derives from the electrons furnished by the dopant atoms populating states within the conduction band. This occurs at high doping level and causes the Fermi level entering the conduction band. Our findings indeed provide a first indication on the effectiveness of the doping procedure by applying a deposition temperature of 188°C.

The haze factor for the AZO samples deposited at different temperatures (in the range 400-1000nm) are reported in **Figure 4.20(c)**. We found that the haze factor of AZO layer deposited at 188°C is higher than the other samples in the whole explored range, likely due to the surface morphology. Increasing the scattering of light is a strategy to rise the probability of photon absorption in a solar cell.
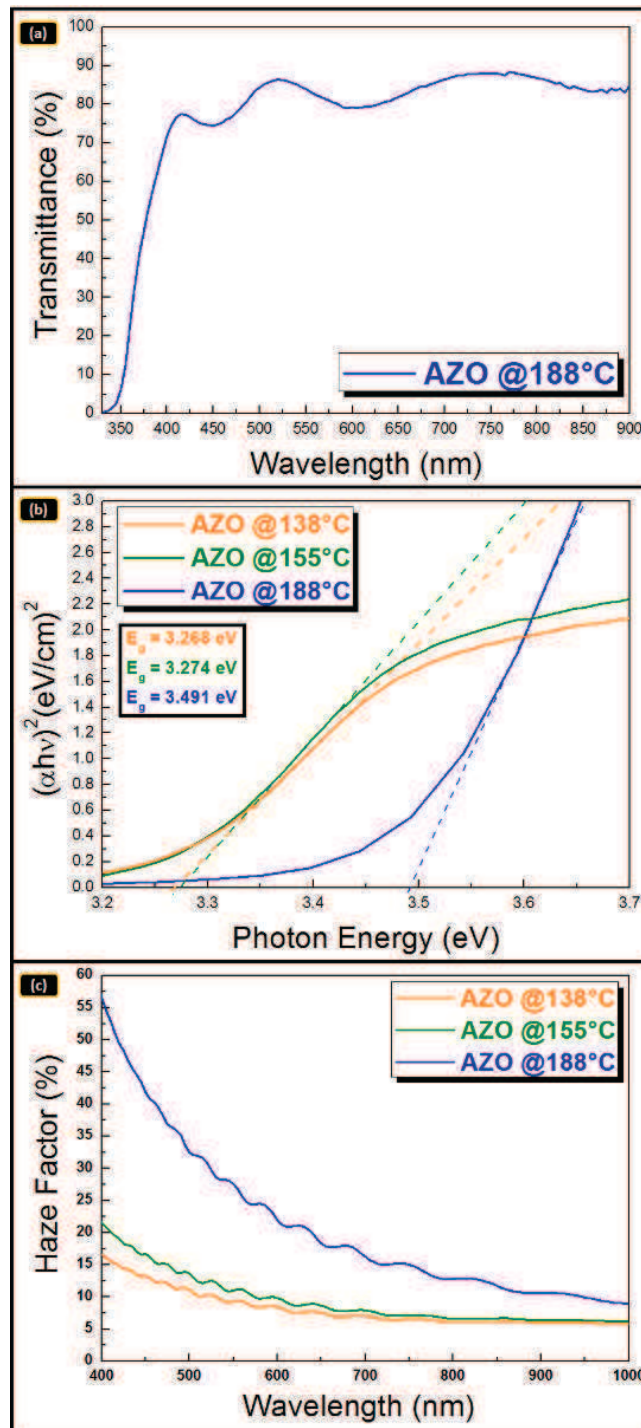
Figure 4.20: (a) Transmittance spectra of an AZO sample deposited at 188°C and **(b)** Tauc plots of AZO layers deposited at different temperatures to evaluate the optical band gap. **(c)** Haze Factor values of the AZO layers calculated in the range 400-1000 nm.

4.3.4.2. *Study of the Al incorporation*

The optical results open a real perspective on the capability to replace Zn^{2+} with Al^{3+} species in the ZnO lattice by applying mild thermal budgets during co-sputtering (fixed all the other conditions). To closely enter the structure of the mixed material, micro-Raman spectroscopy offered crucial details on the Al^{3+} location. The effects of the Al incorporation on the Raman peaks are shown in **Figure 4.21(a)**.
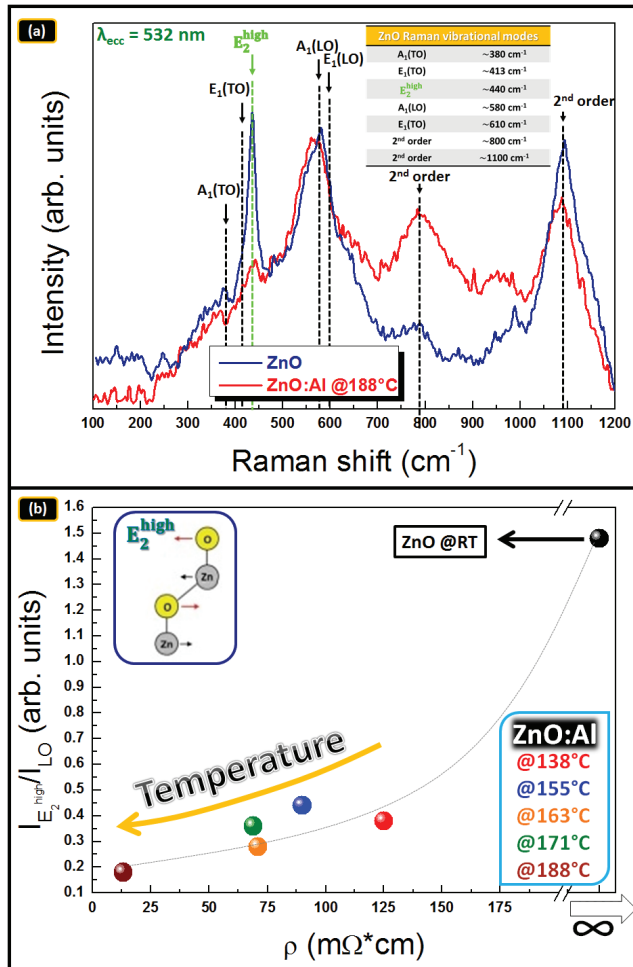
Figure 4.21: (a) typical Micro-Raman spectra of ZnO layers (—) undoped and (—) doped with Al at 188°C; in inset is reported the table with the ZnO vibrational modes. **(b)** Monotonic decrease of the $I_{E_2^{high}}/I_{LO}$ intensity ratio as a function of the layer resistivity.

The data refer to the ZnO:Al layer deposited at 188°C. For comparison, a reference spectrum collected over an undoped ZnO layer is also reported. Vibrational modes in the ZnO lattice are expected at: ~380 cm^{-1} (ascribed to A$_1$(TO) mode), ~413 cm^{-1} (ascribed to E$_1$(TO) mode), ~440 cm^{-1} (ascribed to non-polar E$_2^{high}$ mode, schematically represented in the inset of **Figure 4.21(b)**) and ~580-610 cm^{-1} (ascribed to A$_1$(LO) and E$_1$(LO)). Their positions are labeled in Figure 4.21(a). Additionally, second orders of Raman modes are visible at ~800 and 1100cm^{-1}.[265,266] All those peaks account for the wurtzite C$_{6v}$ space group with four atoms per unit cell: among the 12 possible vibrational modes, only the A$_1$, E$_1$ and E$_2$ are Raman-active. Furthermore, due to the ionic character of Zn-O bonds, polar modes (A$_1$ and E$_1$) exhibit a large splitting and second order modes.[267]

According to the UV-Vis optical transmittance values, being in all samples > 70% at 532 nm (the excitation wavelength used to carry out the Raman measurements), we assess that the Raman beam has always probed the entire thickness of the ZnO:Al films. Moreover, to avoid specific thickness effects, the $I_{E_2^{high}}/I_{LO}$ ratio (*i.e.* I$_{LO}$ indicated the longitudinal modes A$_1$(LO) and E$_1$(LO)) was taken as a diagnostic parameter (rather than E$_2^{high}$ alone)[265,266] and evaluated as a function of the deposition temperature. From the comparison between the spectra in Figure 4.21 it emerges that the E$_2^{high}$ mode is much stronger in the pure ZnO sample with respect to what found in the ZnO:Al layer deposited at 188°C. An analogous behavior was found in all the samples grown at the different temperatures. The reduction of the $I_{E_2^{high}}/I_{LO}$ ratio by increasing the deposition temperature, as shown in Figure 4.21(b), was related to structural changes in the lattice arrangement associated to the Al introduction into the ZnO matrix, compatible with Al^{3+} ions substituting Zn^{2+} species into the ZnO lattice.[265] Additional effects can be provided by the generation of oxygen-defects in the lattice.[268,269] Nevertheless, in this respect, an adjustment of the lattice structure is expected by increasing the deposition temperature rather than a progressive generation of oxygen defects, since the oxygen pressure in the chamber during sputtering was constant (as well as all the other deposition parameters except for the temperature).

On the basis of our findings, we reasoned that the Al introduction into ZnO lattice is assisted by a controlled (external heating) slight increase of the temperature during deposition.

4.3.4.3. *Electrical characterizations*

A monotonic reduction of the $I_{E_2^{high}}/I_{LO}$ ratio was recorded as a function of the deposition temperature (RT<T<200°C), as shown in Figure 4.21(b) and **Table 4.4**. The data, correlated to the layer resistivity, elucidate that a progressive inhibition of the E_2^{high} Raman mode corresponds to a progressive improvement of the AZO layer conductivity.[265,270] We are inclined to exclude that the observed reduction of the $I_{E_2^{high}}/I_{LO}$ parameter is due to an increase of residual lattice strain, as a possibility prospected in ref. [265].

This observation is based on our independent strain analyses done by XRD (see the following section). Thereby, we associate our findings to a progressive incorporation of Al^{3+} species in Zn^{2+} position, as an effect of increasing the deposition temperature. This structural property renders the incorporated species electrically active and thus able to increment the density of free carriers in the conduction band (CB). As a matter of fact, the lowest resistivity value was measured in the AZO layer grown at 188°C. The data are summarized in Table 4.4.

Table 4.4: Micro-Raman and resistivity data.

Sample	E_2^{high}/LO Intensity ratio	Resistivity (mΩ×cm)	Conductivity (S/cm)
AZO @138°C	0.38	125	8.00
AZO @155°C	0.44	90	11.11
AZO @163°C	0.36	69	14.49
AZO @171°C	0.28	71	14.08
AZO @188°C	0.18	13	76.92

Since the resistivity value is affected not only by the carrier density but also by their scattering time (due to grain boundaries, aggregates, other defects, etc), we additionally provide a correlation with the lattice strain and grain size. The average (crystallographic) domain size is measured by applying the Scherrer's equation[159] to the full width at half maximum of the (0002) peak [28] and represented in the right panel of **Figure 4.22** (right axis, pink curve). In addition to the grain size (related to the density of grain boundaries), the evaluation of the residual strain in the ZnO:Al lattice is provided as an indirect measure

of the average effect of the presence of extended defects on the ZnO:Al lattice. The residual strain is evaluated by measuring the (0002) lattice planes distances (XRD, see Figure 4.16) and was compared to reference values (unstrained ZnO lattice).[265] It is expressed as $\Delta d/d$ (%) and plotted as a function of the layer resistivity in **Figure 4.22** (left axis, blue curve). We note a decreasing trend of the strain measured along the c-axis with the resistivity reduction (and therefore with the deposition temperature), towards a zero-strain condition (unstrained: $\Delta d/d$ (%) = 0) corresponding to the most conductive layer (188°C).

This result gives evidence of a progressive reduction of the defects inside the wurtzite lattice, likely associated to less severe Al-based clustering (*e.g.* Al₂O₃) and/or to atomic disorder. Since oxygen vacancies and substitutional Al can both affect the intensity of the E_2^{high} Raman mode, it was crucial to establish that the temperature (at fixed oxygen pressure) causes a reduction of the residual strain in the film. This observed behavior argues in favor of Al^{3+} substituting Zn^{2+}, with direct positive impact on the layer resistivity.
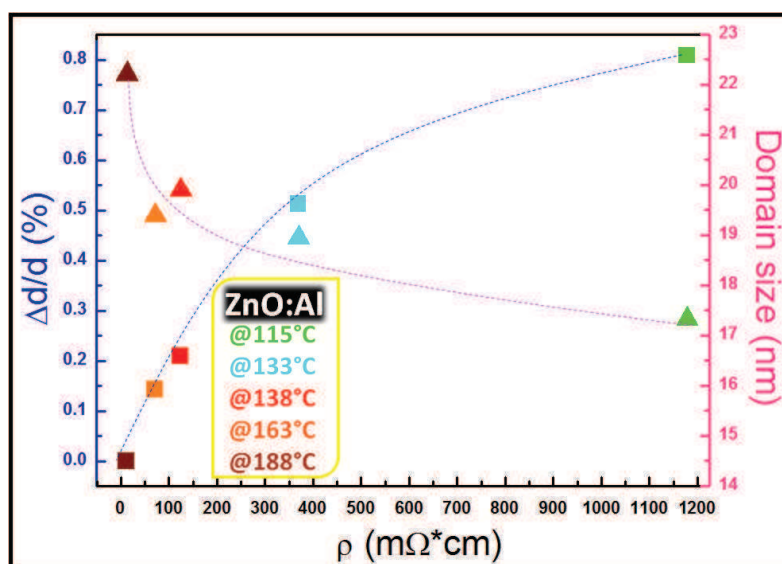
Figure 4.22: Structural properties evaluated by XRD analysis correlated to the electrical behavior of the AZO layers. On the left side (blue curve): strain along the c-axis; on the right side (pink curve): crystallographic domain size. The different colors of the data points correspond to different deposition temperatures.

On the other hand, the eventual formation of charged V_0^{2+} states (under non equilibrium conditions), with the consequent injection of electrons into the ZnO conduction band,[267,271] would imply that the Zn-Zn bonding distances around the defect would experience an outwards stretching.[267] If this relaxation was extended in average to the entire lattice, this

should cause a shift of the diffraction peaks towards lower angles. This is the opposite of what experimentally found, since the peak systematically moves upwards in the direction of the unstrained reference if the deposition temperature is increased (<200°C). A major defective material when increasing the deposition temperature is also counterintuitive. Moreover, in all the deposition process, a slight supply of oxygen was used to avoid growth condition under deficiency of oxygen.[268] All those consideration are in favor of Al atoms rather replacing Zn in a certain (even partial with respect to the 2at.% introduced) amount.

To further reinforce our conclusions, we performed mild *ex situ* annealing (at 200°C) on the as deposited sample, using dry air (N₂:O₂=78sccm:22sccm) *vs.* vacuum conditions (1.33 Pa). The presence of oxygen in the annealing ambient is expected to impact on the concentration of oxygen vacancies. Nonetheless, in both cases the sample experienced an improvement of the electrical performances, with the resistivity reducing to 8.5 and 7mΩ×cm in air and vacuum, respectively (**Figure 4.23**). This finding was thus correlated to a further adjustment of the lattice structure, including better positioning of substitutional Al species.
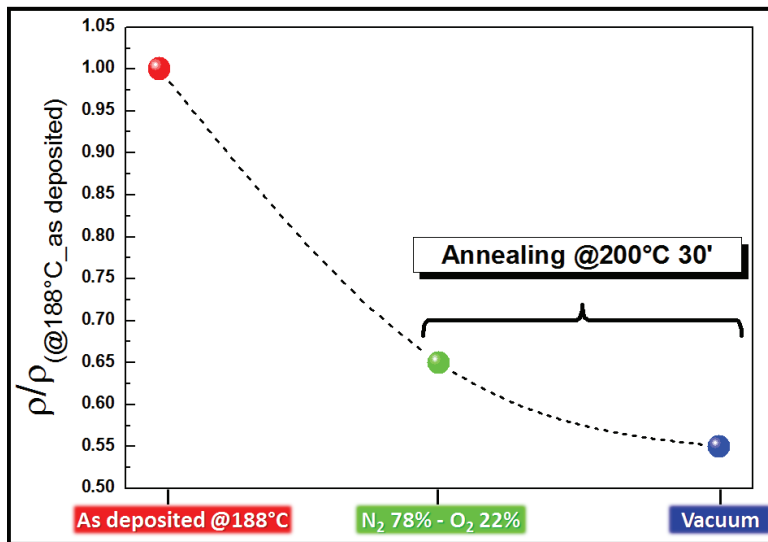
Figure 4.23: The effect of adding ex situ heating on the layer resistivity. Note that the presence of oxygen species in the annealing ambient does not negatively affect the layer conductivity.

Figure 4.22 additionally shows (pink curve) an increase of the ZnO:Al domain size, which consistently goes in the direction of a better carrier transport. We indeed argue that

the resistivity reduction also benefits from less severe carrier scattering events from grain boundary or extended defects.

4.3.4.4.   *Ellipsometric measurements*
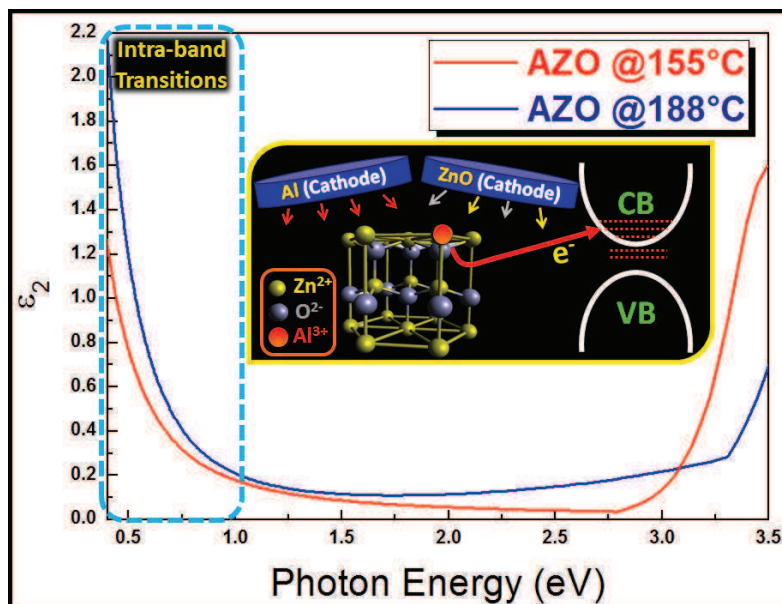
Figure 4.24: SE measurements giving the dielectric constants ε_2 as a function of the photon energy. Note the absorption in the IR region enhanced in the AZO layer deposited at 188°C, which represents a marker for intra-band transitions as a consequence of the Fermi level entering the CB (inset).

Figure 4.24 shows the imaginary part of the dielectric constant, ε_2, for two samples grown at 155°C and 188°C. It is of particular interest the behavior of ε_2 in the infrared region (<1 eV). In particular, we observe that the material deposited at 188°C shows a typical behavior from intra-band transitions experienced by the electrical carriers.[272] This is associated to the electrons, provided by the dopant atoms, which enter in the conduction band with their energetic levels and in total behave as a free electron gas, as translated in the applied Drude's model to fit the raw data. Although high doping levels tend to affect the transmittance of the material, we emphasize that the average transmittance measured on this sample stays as high as 85% (see Figure 4.20(a)). On the other hand, the ZnO:Al deposited at 155°C exhibits a lower absorption in that region, depicting a material with a lower amount of free electrons charges. The analysis gives a further clear evidence of the effectiveness of our methodology on the capability to tune the Al^{3+} species incorporation in

the ZnO lattice as substitutional dopant. Consistently with the Tauc's plot results (Figure 4.20(b)), the onset of the absorption behavior over the band gap is clearly triggered at higher energies in the sample deposited at 188°C (right part of the curves in Figure 4.24).

4.3.5. *Perspectives on AZO/gig-lox TiO₂ sequential sputtering deposition for DSC or PSC photoanodes*
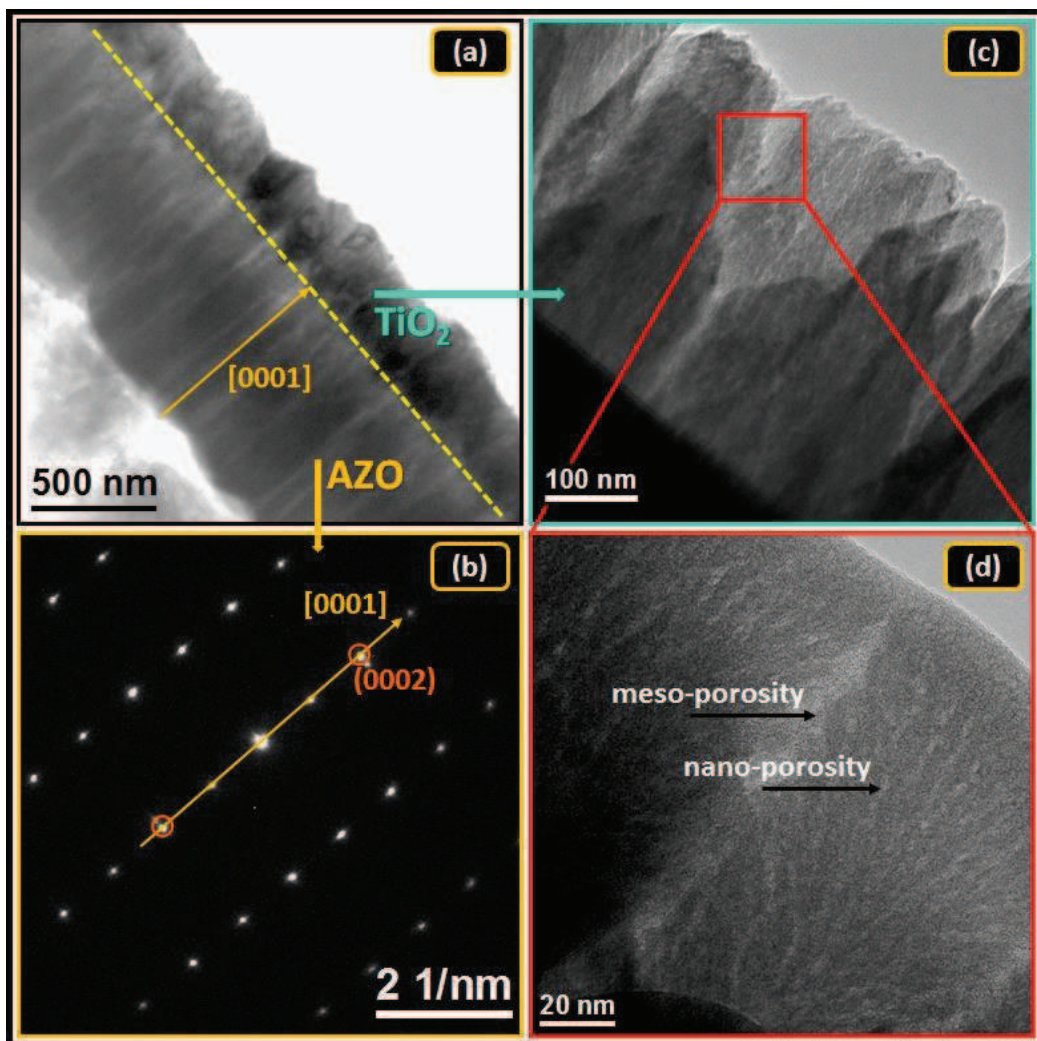
Figure 4.25: (a) TEM cross-section image of the AZO/TiO₂ bi-layer sequentially deposited by reactive magnetron sputtering in co-focal (@188°C) and grazing incidence geometries (RT), respectively. **(b)** SAED of the AZO layer; **(c)** TEM cross-section image of TiO₂ gig-lox layer and **(d)** its magnification to highlight its multi-scale-porosity.

We explored a strategy consisting of the sequential deposition of gig-lox-TiO$_2$ and AZO layers by exploiting the same deposition chamber, thus without any break of vacuum. The main concern is about the interface and the material adhesion for future integration in photoanodes of DSCs or PSCs. Preliminary results may positively catch the industrial mood.

To investigate the adhesion between AZO and TiO$_2$ gig-lox layers, we realized a bi-layer as shown in **Figure 4.25(a)**. The AZO layer was deposited in co-focal geometry at T<200°C (as seen before) whilst the TiO$_2$ gig-lox layer with the same approach discussed in Chapter 2 (at RT). Through the not troubling preparation of the TEM cross-section we infer a good adhesion between the two layers (see Figure 4.25(a)), being the interface resistant to mechanical solicitations. We also observe that the TiO$_2$ layer follows the morphological path of the AZO columns which are textured along the expected [0002] direction (see diffraction pattern in **Figure 4.25(b))**. **Figure 4.25(c)** testifies that the TiO$_2$ gig-lox structure is not modified by the use of AZO as substrate. This finding dispels all doubts on one main concern. Details of the gig-lox porosity are shown in **Figure 4.25(d)**.

In summary, we have explored a sputtering approach at low temperature and at soft power loading in compensated oxygen ambient to effectively dope ZnO layers with Aluminum atoms such to gain convenient optical and electrical responses. The approach is based on the co-deposition of the component materials (ZnO and Al) at T<200°C by using a co-focal geometry. The deposition conditions settled a compromise between power loading and working pressure in order to provide relatively high deposition rate coupled with low intrinsic substrate heating. We currently pushed the deposition process at a level of maturity that provides the material with: 1) Al^{3+} species effectively incorporated in the ZnO structure with negligible residual strain; 2) uniform ZnO:Al stoichiometry at least over 1 μm of grown thickness; 3) optical bandgap of ~3.5eV; 4) ~85% transmittance in the visible range; 5) deposition rate as high as ~7nm/min. The overall structural optimization, as achieved at a real deposition temperature of 188°C (measured on the sample surface), allowed producing a material with resistivity as low as ~13mΩ×cm, namely 13Ω/sq in 1μm. The large potentiality of our approach, in summary, resides in: 1) avoiding intrinsic overheating and instead using a mild controlled extrinsic heating; 2) compensating oxygen deficiency to limit the formation of oxygen defects; 3) guaranteeing a uniform incorporation of Al during growth. All those advantages add up with the availability of an independent Al source for

complementary stacked materials (*e.g.* Al or Al_2O_3). They represent a progress in the material reliability and stability for application on low cost substrates.

The preliminary results on the sequential deposition of AZO and gig-lox TiO_2 prospect the advent of a new methodology for the growth of the complete architecture of the inorganic component of DSC and PSC photo-anodes for high throughput and low-cost devices.

Conclusions

In the framework of the engineering of nano-materials for energy conversion, we illustrated the empowering offered by the newly-designed spongy TiO$_2$ layers deposited by a reactive sputtering method based on Grazing-Incidence Geometry coupled with Local OXidation (gig-lox) we initiated in the landscape of the nanostructured materials growth. It represents a viable way to force sputtering methods, naturally addressed to compact layers, to arrange spongy materials via a progressive bottom-up oxidation of building blocks. The technique is intrinsically up-scalable and therefore industrially compatible, and can be, in principle, extended to any reactive metallic source to produce porous oxides.

The spongy layers deposited by the gig-lox methods were investigated from different perspectives and used as scaffold in DSC's and PSC's photoanodes for photon-to-current conversion.

The spongy gig-lox TiO$_2$ is unique in its twofold structure. It consists of a regular array of rods, separated by meso-pores (tens of nanometers) as the result of applying the grazing geometry. The rods, on their side, have an internal branched structure that give rise to an interconnected network of nano-pores (a few nanometers) related to the proper partial pressure of Ar used for sputtering. Moreover, the confinement of the oxygen species at the substrate side during growth assures a homogeneous localized self-assembly of TiO$_6$ chains and also prevents the Ti source from oxidation. The overall bimodal porosity of the layer amounts to ~50% of the volume for thicknesses tunable up to (at least) 1000nm. It represents the cornerstone to allow matters of different size and nature intimately entering into the TiO$_2$ scaffold and forming active interacting (chemically and physically) blends.

In this respect, we demonstrated that the engineered fine structure of the material allows N-719 photo-active molecules deeply entering the layer via the interconnected array of pores, with the Ru atoms detected even at the bottom-side of the scaffold. The measured average density of molecules infiltrated into the gig-lox TiO$_2$ layer is ~1-2×10^{20} molecules/cm^3. As a second empowering, the pore size, being similar to the typical steric hindrance of dye molecules, promotes a multi-branch (we define "octopus-like") linking configuration with multiple anchoring groups chemisorbed to the pore walls. In the

anchoring process, the role of the solvent was also exploited to rise the injection probability of the photo-generated carriers into the conduction band of TiO₂. We demonstrated the internal branched structure of the TiO₂ nanorods as a further empowering that influence the charge collection efficiency. As an overall effect (injection + collection efficiency), we measured that the density of electrons in the conduction band of the gig-lox TiO₂ layer is raised by 4 orders of magnitude under 1 sun illumination with respect to the intrinsic carrier level. The result was obtained by disentangling the bare effects related to the dye/TiO₂ blend from many other parasitic/additional effects occurring in a complete device.

We disclosed a similar tendency of the spongy TiO₂ scaffolds to establish tight structural relationships and effective interactions with photo-active hybrid perovskites layers. In this case, we reasoned on the way the CH₃NH₃PbI₃ enters the differently sized pores of the TiO₂ architecture and on the structural stability of the blend under simulated operation conditions. The capability of the scaffold to accept and transport the carriers, photo-generated into the perovskite layer, was proved by integrating the gig-lox TiO₂ scaffold in PSCs.

Differently form gig-lox based DSCs, the thickness of the gig-lox TiO₂ scaffold in PSCs was scaled down to 150-200 nm owing to the wide absorption range and light harvesting behaviour of CH₃NH₃PbI₃ compared to the molar extinction coefficient of the N719 dye. We especially mention the efficiency we have got in PSCs (11.7%) using a standard device architecture. Upgrading the device architecture on the basis of the recent literature results can further improve this value.

As an overall comment, the demonstrated aptitude of the gig-lox TiO₂ scaffolds to establish finely interconnected blends with photo-active dyes and perovskites unveiled the outperforming behaviour of this newly-designed material with respect to TiO₂ layers sputtered in conventional ways. Its competition level with chemically synthesized commercial counterparts was, at the same time, afforded by the comparison with the reference devices we produced in the laboratory.

A third proof-of-concept on the convenience of the use of gig-lox TiO₂ layers in devices was provided in a filed different from PV, namely for gas sensing. The high surface to volume ratio, the high surface reactivity, the pervasive network of voids and the interconnected TiO₂ nano-branches offered by the spongy gig-lox TiO₂ layer allowed getting a high sensitivity to ethanol in the range of 17- 87 ppm using layers scaled to 350nm, with the exhibited sensor

response ((ΔR/R)×100) in the range of 80-100, being not sensibly affected by the ambient humidity up to 60% RH. The working temperature of the sensors was lowered to 250°C

The provided proofs-of-concept crossing different fields prospect a gig-lox platform to be shared by different functionalities in low-cost multi-functional devices. We expect that the applicative window can be further extended to other kind of devices.

At the boundary of the main core of the thesis, we explored alternative materials to be proposed as scaffold or transparent conductive oxides (TCO) for low-cost PV architectures.

During a 3-monts stage at the LMGP in Grenoble, a first attempt to compare the TiO₂ gig-lox meso/nanostructures with TiO₂ micro-flowers grown by a chemical method (AA-MOCVD) was set up. They present a remarkable, controllable surface wettability that shows reversible hydrophobicity/super-hydrophilicity. The cooperation of the surface microstructures, and the surface photosensitivity are considered to be mainly responsible for this behavior. All those properties prospect a certain degree of applicability of the structures for surface functionalization after having faced some issues mainly related to the material uniformity and up-scalability.

At the TCO side, we have explored a sputtering approach at low temperature and at soft power loading in compensated oxygen ambient to effectively dope ZnO layers with Aluminum atoms such to gain convenient optical and electrical responses. The approach is based on the co-deposition of the component materials (ZnO and Al) at T<200°C by using a co-focal geometry. As a main empowering, the AZO layer was deposited in the same sputtering chamber as the gig-lox TiO₂. This allowed performing the sequential deposition of AZO and gig-lox TiO₂ layers without vacuum break. The results provided a demonstration on the capability to grow the complete architecture of the inorganic part of DSC and PSC photoanodes keeping the mainstays of the gig-lox TiO₂ recipe for high throughput and low-cost devices.

To conclude, the results of the Ph.D. Thesis afford good practical perspectives around the full-building of photo-anodes in a sputtering chamber for DSC and similar applications, comprising dye-sensitized photo electrochemical cells and perovskite solar cells. The material empowering can be successfully moved to gas sensing.

A gig-lox TiO$_2$ scaffold is also expected to effectively interact with any species (gas or dye or others) bearing –OH or –COOH anchoring groups, as well as with hybrid perovskites having different composition from MAPbI$_3$.

We additionally emphasize that our gig-lox method could in principle be extended to other kind of oxides. There is also plenty of room to apply the gig-lox materials for different applications such as water splitting, Li-batteries, photo-cleaning.

Appendix

A1. *TiO₂ and AZO layers deposition in the customized Sputtering equipment*

In the thesis, we described the TiO$_2$ gig-lox properties and its applications. We deposited our TiO$_2$ gig-lox layer using a customized sputtering equipment. The same equipment, but a different deposition geometry, is used to grow AZO layers that represent a potential TCO for solar cells. Moreover, we explored a chemical approach (AA-MOCVD) to deposit TiO$_2$ nanostructures to be compared to gig-lox layers

Our customized DC-pulsed sputtering equipment (**Figure A1(a))** made by Kenosistec and located at the CNR-IMM laboratories (National Council of Research (CNR-IMM)- Institute for Microelectronics and Microsystems, Catania, Italy) offers two different deposition configurations, namely, the co-focal geometry for the deposition of AZO from ZnO and Al targets, and a grazing incidence geometry assisted by local oxidation for TiO$_2$ layer depsoition (see **Figure A1(b)**).
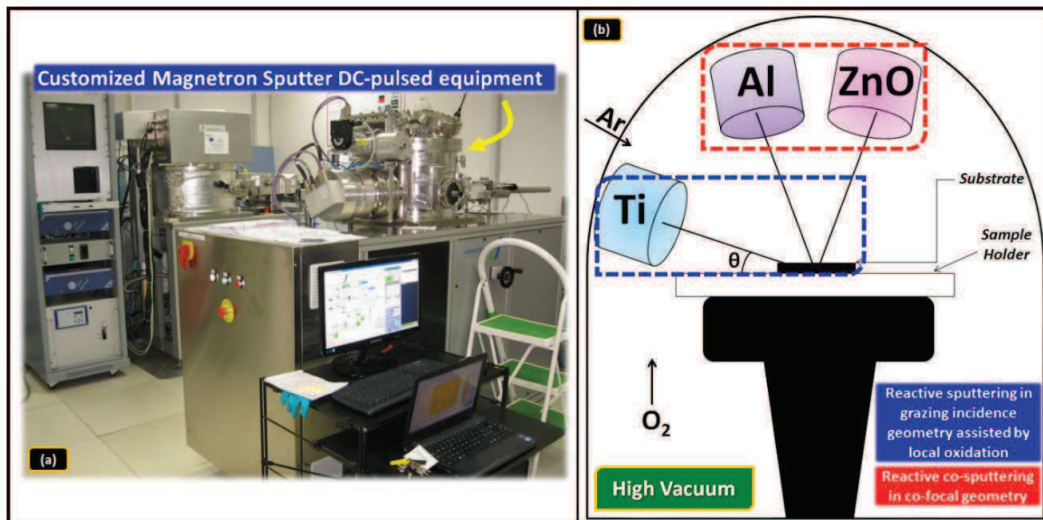
Figure A1: (a) Customized Magnetron Sputter DC-Pulsed equipment located at CNR-IMM in Catania, Italy. **(b)** Schematic section of the deposition chamber.

Different parameters were explored in order to find out the best procedure to deposit both layers, namely: the anode-cathode distance, the flow rate of both the carrier gas (Ar)

and reactive gas (O_2), the power applied to the cathodes and the temperature on the substrate. In fact, before proceeding with the deposition, we have preliminary optimized the process. We collected in **Table A1** the parameters after optimization for both deposition processes.

Table A1: Optimized sputtering parameters used for TiO₂ gig-lox and ZnO:Al depositions.

	TiO₂ gig-lox	ZnO:Al	
		Al	ZnO
Vacuum Pre-Deposition (µbar)	2.0×10^{-4}	2.0×10^{-4}	
Working Pressure (µbar)	13.0	13.0	
Flow rate Ar (sccm)	69.0	69.0	
Flow rate O₂ (sccm)	2.0	2.0	
Rotation Speed (rpm)	20.0	5.0	
Power (W)	140	20	40
Voltage (V)	295 - 298	244 - 248	327 - 332
Current (mA)	472 - 475	77 - 82	106 - 111
Power Loading (W/cm²)	6.9	1.0	2.0
Cathodes Diameter (inch)	2.0	2.0	
Anode-Cathode Distance (cm)	1.2	2.0	
Deposition Temperature (°C)	25	188	
Deposition Rate (nm/min)	4.0	7.0	
Thickness (nm)	800±10	1250±10	

A2. *DSC and PSC photoanodes preparation*

DSC architecture (see **Figure A2(a)**). The cell architecture was realised in the framework of the project EFOR, in collaboration with Dr. Luisa De Marco, IIT and CNR-Nanotec (Lecce, Italy). Fluorine-doped tin oxide (FTO, 15 Ω/sq, provided by Solaronix S.A.) glass plates were first cleaned in a detergent solution using an ultrasonic bath for 15 min, and then rinsed with water and ethanol. Compact TiO₂ layers were prepared as follows: FTO glasses were coated with 0.15M titanium diisopropoxide bis(acetylacetonate) (75% Aldrich) in 1-butanol (Aldrich) solution by the spin-coating method, which was heated at 125°C for 5 min. After the coated film was cooled down to the room temperature, the same process was repeated and the two times coated FTO glasses were finally heated at 500°C for 30 min. The prepared dense TiO₂ blocking layer were thus covered by: 1) mesoporous TiO₂ gig-lox layers deposited by sputtering at RT; or 2) standard nanocrystalline TiO₂ pastes (reference) deposited by a doctor-blading technique using a commercial diluted colloidal titania paste

(Dyesol 18NR-T). The reference samples were heated in air at 150°C for 15 min. To compensate the limitations associated to the poor light harvesting capability of the sensitizer and to reinforce the potentiality of the new material, we associated to the gig-lox scaffold to a commercial scattering layer by doctor blading a commercial scattering paste (Solaronix D/SP colloidal paste) onto the above described transparent layers and sintering the double-layer photoanode at 500°C for 30 min. The same was done for the reference photoanode. For all the samples, the dye sensitization was performed by keeping the electrodes for 14 h and under dark in 0.2 mM solutions of bis(tetrabutylammonium)-cis-di(thiocyanato)-N,N′-bis(4-carboxylato-4′-carboxylic acid-2,2′-bipyridine) ruthenium(II) (N-719, purchased by Solaronix S.A.) in a mixture of acetonitrile and tert-butyl alcohol (1:1 v/v). The counter-electrodes were prepared by sputtering a 50 nm Pt layer on a hole-drilled cleaned FTO plate. The photo-anode and the counter-electrode were faced and assembled using a suitably cut 50 μm thick Surlyn® hot-melt gasket for sealing. The iodine redox electrolyte (0.1 M LiI, 0.03 M I_2, 0.6 M 1-methyl-3-propylimidazolium iodide, and 0.5 M tert-butylpyridine in dry acetonitrile) was vacuum-injected into the space between the electrodes through pre-drilled holes on the back of the counter electrode. The holes were eventually sealed using Surlyn® hot melt film and a cover glass. Photocurrent-voltage measurements were performed using a Keithley unit (Model 2400 Source Meter). A Newport AM 1.5 Solar Simulator (Model 91160A equipped with a 1000 W Xenon arc lamp) serving as a light source.
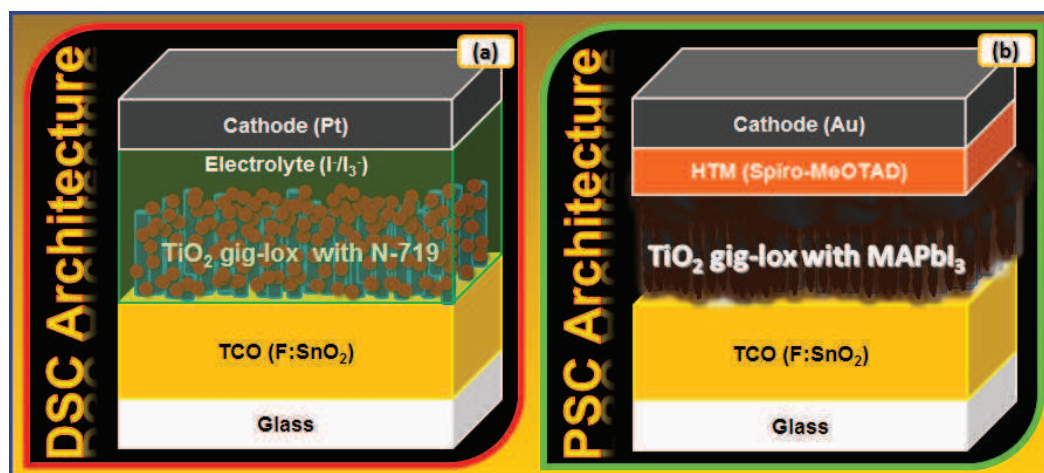
Figure A2: (a) Dye Solar Cells and **(b)** Perovskite Solar Cells architectures produced at National Research Council-Institute of Nanotechnology (CNR-Nanotec) in Lecce, Italy.

PSC architecture (see **Figure A2(b)**). Fluorine-doped tin oxide (FTO, 15 Ω/sq, provided by Solaronix S.A.) glass plates were first etched with zinc powder and HCl 2 M to form the desired electrode pattern, then cleaned in a detergent solution using an ultrasonic bath for 15 min, and rinsed with water and ethanol. A hole blocking layer of TiO_2 (40 nm) was deposited on the cleaned FTO substrates by sputtering. The TiO_2 blocking layers were covered by: 1) mesoporous TiO_2 gig-lox layers deposited by sputtering at RT; or 2) standard nanocrystalline TiO_2 pastes (reference) deposited by spin coating a commercial diluted colloidal titania paste (Dyesol 30NR-T). The samples were heated in air at 450°C for 1 h. The annealing is equivalent to 500°C 30s. The perovskite films were deposited from a precursor solution containing 461 mg of PbI_2, 159 mg of CH_3NH_3I, and 78 mg of DMSO (molar ratio 1:1:1) in 600 mg of DMF. The completely dissolved solution was spin-coated on the TiO_2 layer at 4000 rpm for 25 sec and 100 μL of toluene were poured on the spinning substrate 15 s prior to the end of the program. The film were heated at 65 °C for 1 min and 100 °C for 2 min in order to obtain a dense $CH_3NH_3PbI_3$ film.[273] The hole transporting material solution, Spiro-MeOTAD, 50 mM in chlorobenzene containing 25 mM bis(trifluoromethylsulfonyl)-imide lithium salt (Li-TFSI) and 200 mM 4tert-butylpyridine (TBP) was spun at 3000 rpm for 30 s. As a last step, 60 nm of gold top electrode were thermally evaporated under high vacuum. Photocurrent-voltage measurements were performed using a Keithley unit (Model 2400 Source Meter). A Newport AM 1.5 Solar Simulator (Model 91160A equipped with a 1000 W Xenon arc lamp) serving as a light source.

A3. *Characterization techniques*

A3.1. *Micro-Raman*

Micro-Raman measurements were carried at room temperature using a Horiba XploRA spectrometer (see **Figure A3**) equipped with a confocal microscope and a Peltier-cooled charge-coupled detector (CCD). The samples were excited using the 532 nm line from a solid state laser and integrated for 80 s, using a 100x microscope objective. To check the uniformity of the deposited films, the measurements were acquired on some different portions of the samples. The penetration depth is 1.32 μm according to the formula[155] reported in chapter 2.

Figure A3: Micro-Raman equipment located in the laboratories of the University of Messina, Italy.

A3.2. *Attenuated Total Reflectance – Fourier Transform Infra-Red*

Fourier Transform Infrared (FTIR, Perkin Elmer Spectrum 100) spectra were collected, in Attenuated Total Reflectance (ATR) configuration (see **Figure A4**), from 4000-600 cm^{-1}. The penetration depth is 1.32 μm according to the formula[187] reported in chapter 2.

Figure A4: ATR-FTIR equipment located in the laboratories of the University of Messina, Italy.

A3.3. *UV-VIS optical spectroscopy*

UV–Vis measurements were carried on the dyes in solutions using a UV–Vis V-650 JASCO spectrophotometer (see **Figure A5**), and the spectra were recorded with a ±0.2 nm resolution.

Figure A5: UV-VIS spectrophotometer located in the laboratories of the University of Messina, Italy.

A3.4. *X-Ray Photoelectron Spectroscopy*
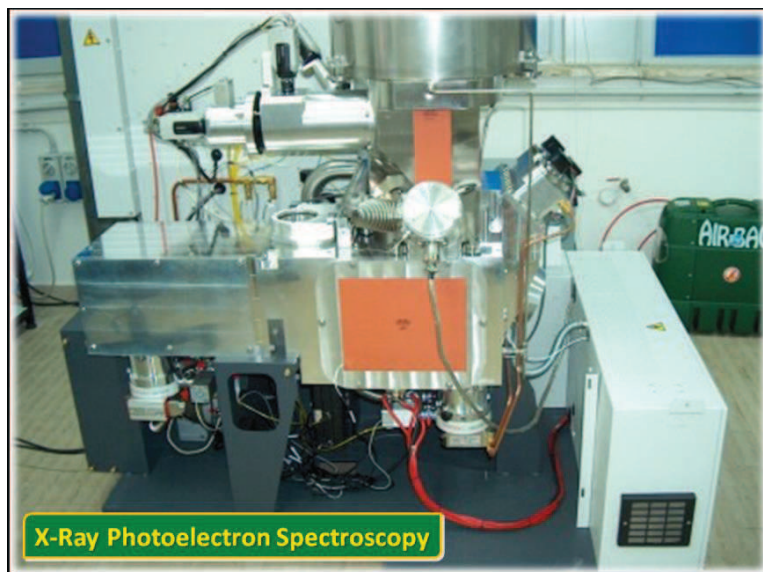
Figure A6: XPS equipment located in the laboratories of the University of Messina, Italy.

X-ray Photoelectron Spectroscopy (XPS) was carried out in ultra-high-vacuum condition (about 1.33×10^{-7} Pa) using a Thermo Scientific Instrument (see **Figure A6**) equipped with a monochromatic Al K_α source (hν = 1486.6 eV) and a hemispherical analyzer (spherical sector 180°). The constant-pass energy was set at 200 eV for survey scans and at 50 eV for the XPS high resolution spectra. Being a surface technique, XPS is able to probe only a few monolayers. Hence, to estimate the composition of the layers in depth, it was necessary to progressively remove the surface layer using a scanning 3 KeV Ar^+ ion gun, with a raster area of about 4mm×2mm.

A3.5. *Field Emission – Scanning Electron Microscopy/Energy Dispersive X-Ray*

Field emission scanning electron microscopy (FE-SEM) images were collected with a Zeiss-Gemini 2 electron microscope (see **Figure A7**) operating at an accelerating voltage of 1.50 kV. To carry out energy dispersive X-ray (EDX) analysis, FE-apparatus is coupled with a Quantax-EDX-spectrometer (Bruker AXS Advanced X-ray Solutions GmbH). The EDX detected pear-shaped dimension is about 0.7 micron.
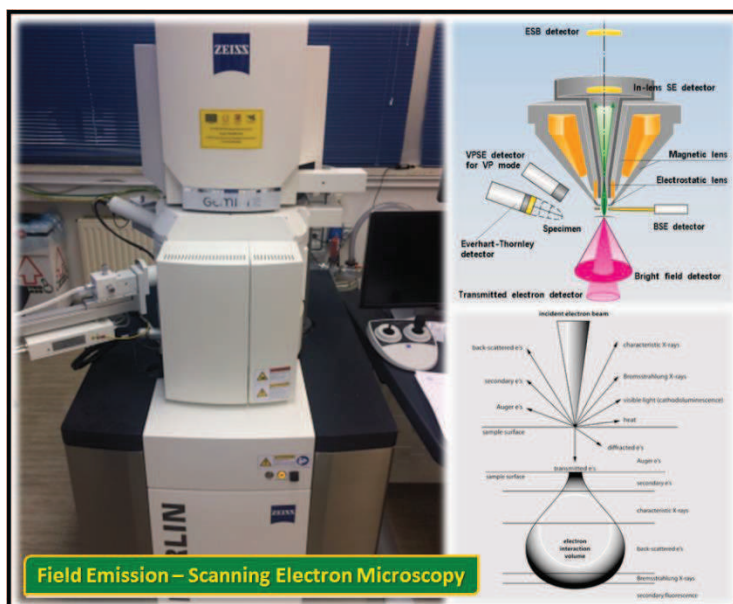
Figure A7: FE-SEM/EDX equipment located in the laboratories of the University of Messina, Italy.

A3.6. *X-Ray Diffraction*

X-Ray Diffraction (XRD) analyses were done using a D8-Discover Bruker AXS diffractometer located in Catania at CNR-IMM (see **Figure A8**), equipped with a Cu-Kα source/Goebel mirror/axial soller slits at the primary beam, and with long soller slits/detector at the secondary path.
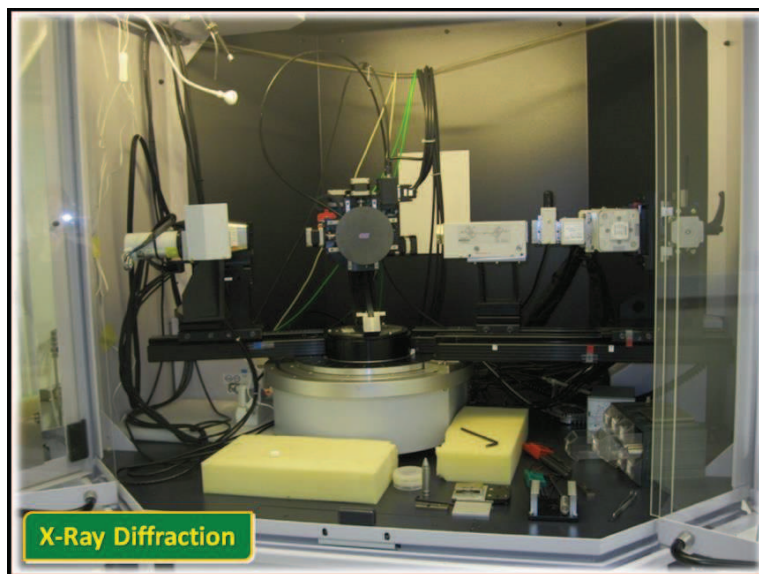
Figure A8: X-Ray Diffractometer located at CNR-IMM in Catania, Italy.

A3.7. *Transmission (and Scanning) Electron Microscopy/Energy Dispersive X-ray*

Transmission Electron Microscopy (TEM) and Selected Area Electron Diffraction analyses (SAED) were done using a JEOL JEM 2010 microscope operating at 200 kV.

STEM images are acquired in scanning mode using a high angle annular dark field detector in Z-contrast configuration. STEM and EDX analyses are performed using a Jeol ARM200 (see **Figure A9**) equipped with a cold FEG electron source, CEOS condenser aberration corrector and 100 mm² Jeol EDXS detector. EDXS profiles are extracted by a 730×180 nm spectrum image across the whole thickness, with 7 nm pixel size, and 0.1 s pixel time. The scanned area was selected in a thicker region of the sample in order to increase and average the signal.
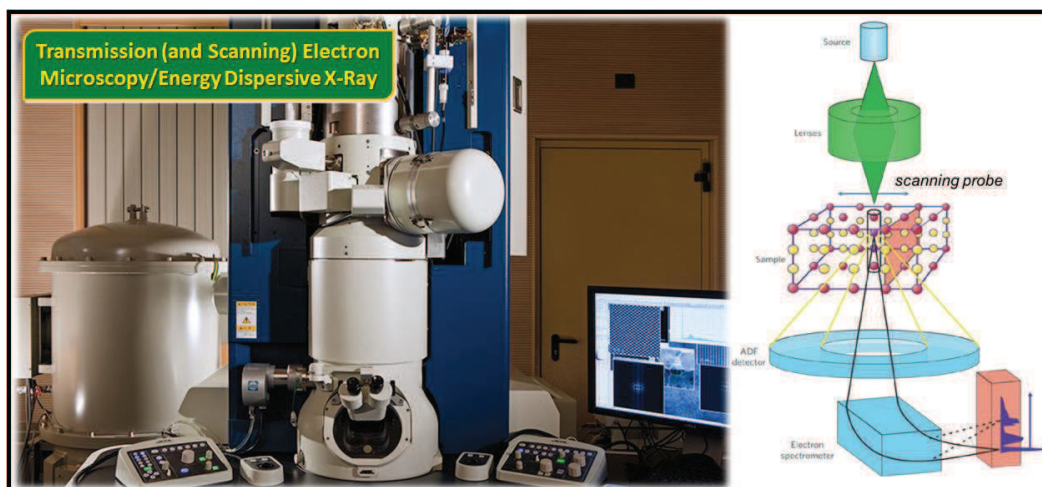
Figure A9: TEM/STEM/EDX equipment located at CNR-IMM in Catania, Italy.

A3.8. *Spectroscopic Ellipsometry*
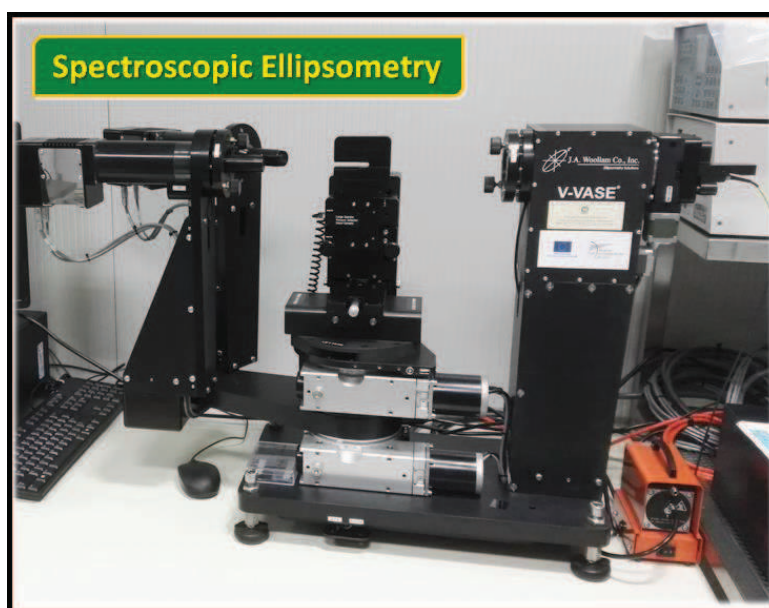
Figure A10: SE equipment located at CNR-IMM in Catania, Italy.

Spectroscopic Ellipsometry (SE) data were collected using a J.A.Woollam VASE instrument (see **Figure A10**). Measurements were performed in a vertical configuration, which is better suited for transparent samples in order to measure on the same point

ellipsometric and transmittance data. Optical spectra were recorded from 300 to 2100 nm (step 5 nm) at 55°, 60° and 65°. An initial model of the optical transitions was built for each layer constituting the sample. The TiO_2 layer was modelled by using a single Tauc-Lorentz oscillator and the surface roughness by the Bruggeman effective medium approximation (EMA). The technique was mainly used to measure the average porosity of the layer.

A3.9. *Four Point Probe with Solar Simulator*

The TiO_2 layer resistivity was measured by using a Four Point Probe,[274,275,276] in a probe station equipped with a Keithley K237, an electrometer K6512 and four micromanipulators, with positioning accuracy of about 10 μm (see **Figure A11**). The collinear configuration, with equal probe-to-probe spacing of 100 μm, was used. The measurements were carried out in dark and under illumination obtained through a Solar Simulator based on a 150 W Xenon lamp, equipped with rear reflector, collimating optics, and an American Society for Testing and Materials (ASTM) filter producing an AM1.5 G solar spectrum. The solar simulator provides a 35mm-diameter beam with irradiance controllable between 10 and 200mW/cm². The light power density was measured by using a Newport power meter with a power accuracy of 5 μW equipped with a National Institute of Standards and Technology (NIST)-traceable calibrated thermopile sensor. Some of the measurements were performed under a blow of air at 20 °C directed onto the surface of the samples.
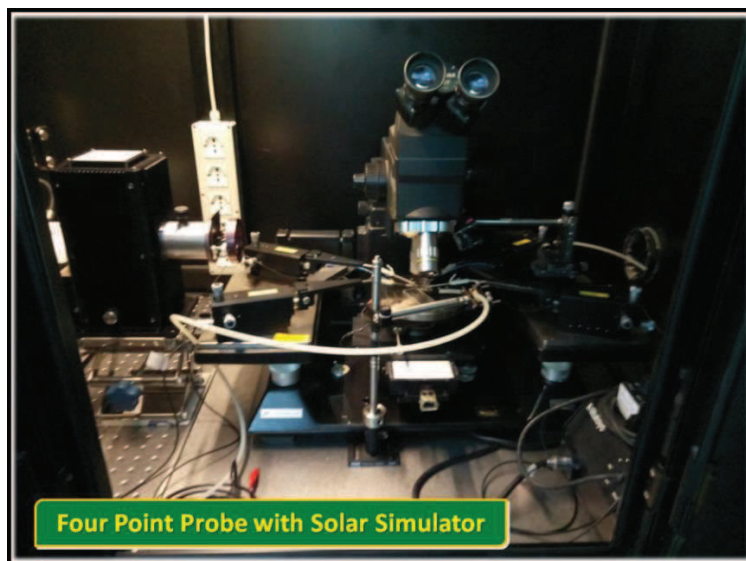
Figure A11: FPP with SS equipment located at CNR-IMM in Catania, Italy.

A3.10. *Coherent X-Ray Diffraction Imaging*

The equipment is located at the European Synchrotron Radiation Facilities in Grenoble, France, beamline ID10 (see **Figure A12**) with the supervision of Dr. Federico Zontone.

The principal attractiveness of the CXDI technique is the ability of high-resolution imaging, in principle limited by the highest q-vector where speckles are measurable. The resolution is ultimately limited by the detector active area, the quality of the diffraction pattern and finally the beam damage in the sample. For a known object, the resolution of the reconstructed image is determined from the line scan through a sharp feature. CXDI relies on a numerical algorithm that allows to phase the Fourier space to the real space when speckles are over-sampled.[145,149,150] CXDI represents a powerful tool for visualizing the outer and the inner structures of micro particles with a resolution of a few tens of nanometers.[147,148] This technique has the great advantage of providing a 3D image in real space, thus giving access to a full description of the morphology of the particles including the porosity and the specific surface area.
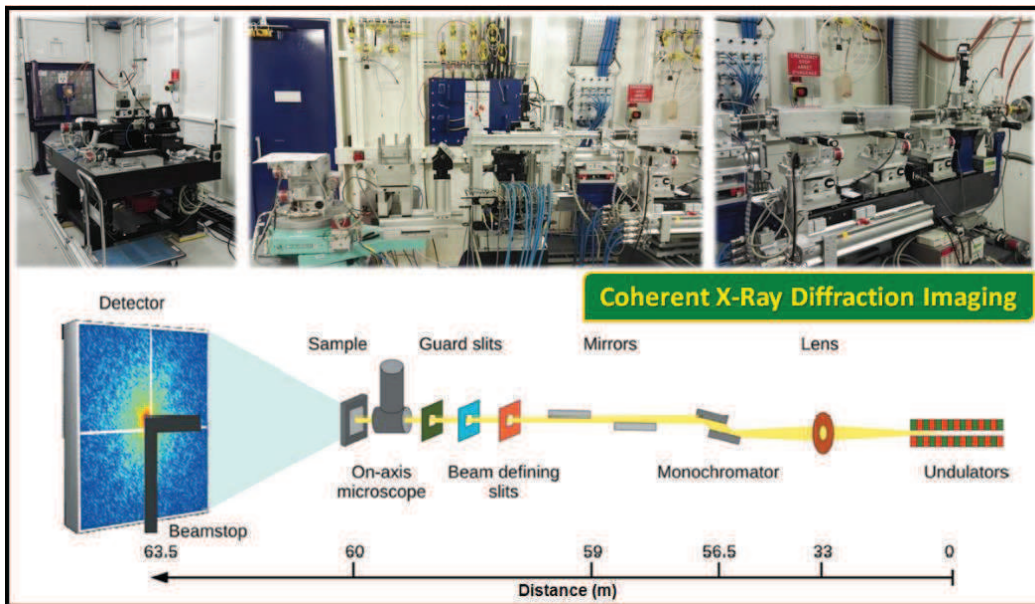
Figure A12: CXDI equipment located at ESRF in the beamline ID10, Grenoble, France.

To retrieve a 3D image of the object we assembled the 3D Fourier space from the tomographic scan of the sample and then we applied the hybrid input–output phase-retrieval algorithm (Fienup, 1982) to the 3D Fourier matrix $512 \times 512 \times 512$ resolution

elements. The 3D scattering data set contains several regions with missing intensities. The information in the central area is obstructed by the beamstop protecting the detector from the direct beam. In addition, the tomographic scan does not cover the full–range due to the support (the "missing wedge"). The optimal speckle sampling up to high q vectors usually requires an angular increment of 0.2° when the sample size is few μm. Finally, several reconstructions are averaged to account for high frequency variations in the convergence due to the noise.

A3.11 *Enviromental Ellipsometric Porosimetry*

The EEP setup used is represented in **Figure A13** and is located at the Institut Matériaux Microélectronique Nanosciences de Provence (IM2NP) Aix-Marseille Université, France.
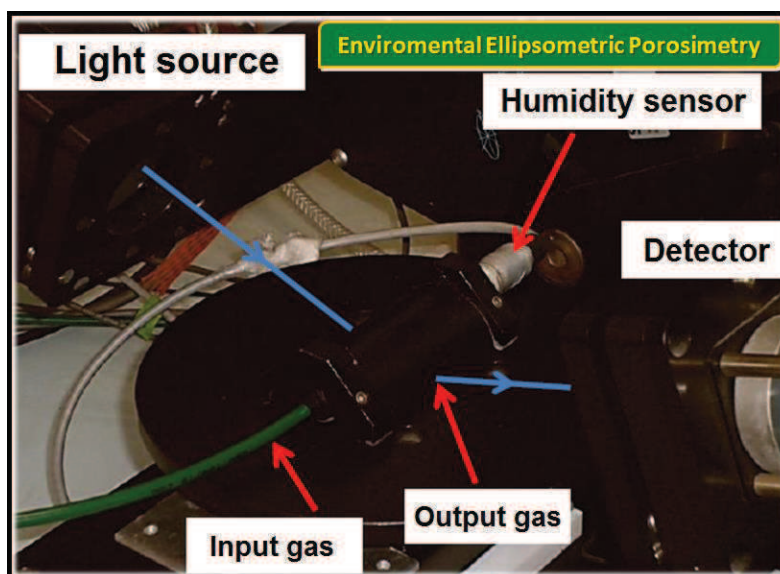
Figure A13: EEP equipment located in the laboratories of the Institut Matériaux Microélectronique Nanosciences de Provence (IM2NP) Aix-Marseille Université, Marseille, France.

It is made of an Ellipsometer equipped with a cell for environmental control containing the film to analyze. In laboratories, gas volumetry analyses are usually time-consuming, mainly because of long pressure equilibration time within the analysis chamber. In the experimental setup of these experiments, they replaced the pressure equilibration system by a continuous flux of air containing a fixed partial pressure of adsorbate directly in contact

with the mesoporous film to analyze. This procedure eliminates the dead volume effect of the analysis chamber always encountered with pressurized techniques. In addition, the flux in itself helps the rapid equilibration at low relative pressure by enhanced gas convection.[277] Though, working at atmospheric pressure limits the choice of efficient adsorbates for EEP measurements. For the analyses, the cell temperature was fixed at 23°C and was continuously filled by 2.5 L/min flux of air with a controlled water partial pressure.

References

[1] E. G. Snyder, T. H. Watkins, P. A. Solomon, E. D. Thoma, R. W. Williams, G. S. W. Hagler, D. Shelow, D. A. Hindin, V. J. Kilaru and P. W. Preuss: The Changing Paradigm of Air Pollution Monitoring. *Environ. Sci. Technol.*, **2013**, *47*, 11369–11377.

[2] J. S. Kim, H. S. Han, S. Shin, G. S. Han, H. S. Jung, K. S. Hong and J. H. Noh: $In_2O_3Sn/TiO_2/CdS$ heterojuction nanowire array photoanode in photoelectrochemical cells. *Int. J. Hydrogen Energy*, **2014**, *39*, 17473–17480.

[3] G. C. Xie, K. Zhang, B. D. Guo, Q. Liu, L. Fang and J. R. Gong: Graphene-based materials for hydrogen generation from light-driven water splitting. *Adv. Mater.*, **2013**, *25*, 3820–3839.

[4] Intergovernmental Panel on Climate Change. Climate Change: the Scientific Bas Cambridge University Press. Summary for Policymakers and Technical Summary at: www.ippc.ch/pub/reports.htm; **2001** [accessed 18.11.09].

[5] NOAA global analysis for **2017**.

[6] NASA global analysis for **2017**.

[7]https://www.ipcc.ch/publications_and_data/ar4/wg1/en/spmsspm-projectionsof.html.

[8] M. Green: Recent developments in PV and ACAP's role, **2013** Annual conference, Australian Centre for Advanced Photovoltaic (ACAP).

[9] J. Twidell and A. Weir: Renewable energy resources. London: E&FN Spon; **1986**.

[10] B. Sorenson: Renewable energy. 2nd ed. Academic Press; **2000** pag. 3.

[11] L. El Chaar, L. A. lamont and N. El Zein: Review of photovoltaic technologies. Renewable and Sustainable Energy Reviews, **2011**, *15*, 2165–2175.

[12] G. Boyle: Renewable energy power for a sustainable future. 2nd ed Oxford University Press; **2004**.

[13] M. A. Green: Commercial progress and challenges for photovoltaics. *Nat. Energy,* **2016**, *1*, 15015.

[14] www.ise.fraunhofer.de, Photovoltaic Report, Fraunhofer Institute for Solar Energy Systems (ISE) Freiburg, 12 July **2017**.

[15] https://www.nrel.gov/.

[16] S. Yang, W. Fu, Z. Zhang, H. Chen and C.-Z. Li: Recent advances in perovskite solar cells: efficiency, stability and lead-free perovskite. *Journal of Materials Chemistry A*, **2017**, *5*, 11462-11482.

[17] N.S. Sariciftci, L. Smilowitz, A. J. Heeger and F. Wudl: Photoinduced electron transfer from a conducting polymer to buckminsterfullerene *Science*, **1992**, *258*, 1474.

[18] G. Yu, J. Gao, J.C. Hummelen, F. Wudl and A.J. Heeger: Polymer Photovoltaic Cells: Enhanced Efficiencies via a Network of Internal Donor-Acceptor Heterojunctions. *Science*, **1995**, *270*, 1789.

[19] S. Günes and N.S. Sariciftci: Hybrid solar cells. *Inorganica Chimica Acta*, **2008**, *361*, 581–588.

[20] E. Arici, D. Meissner, F. Schäffler and N. S. Sariciftci: Core/shell nanomaterials in photovoltaics. *Int. J. Photoenergy*, **2003**, *5*, 199.

[21] B. B. Gardas and M. V. Tendolkar: Hybrid Photovoltaic Thermal System: A State- of the-Art Literature Review, *International Journal of Mechanical and Production Engineering*, **2013**, *2*, 2315-4489.

[22] B. O'Reagan, and M. Grätzel: A low-cost, high-efficiency solar cell based on dye-sensitized colloidal TiO₂ films. *Nature*, **1991**, *353*, 737-740.

[23] M. Grätzel: Solar Energy Conversion by Dye-Sensitized Photovoltaic Cells. *Inorg. Chem.*, **2005**, *44*, 6841–6851.

[24] T. Miyasaka: Perovskite Photovoltaics: Rare Functions of Organo Lead Halide in Solar Cells and Optoelectronic Devices. *Chem. Lett.*, **2015**, *44*, 720–729.

[25] Y. Idota, T. Kubota, A. Matsufuji, Y. Maekawa, and T. Miyasaka, Tin-Based Amorphous Oxide: A High-Capacity Lithium-Ion–Storage Material. *Science*, **1997**, *276*, 1395-1397.

[26] A. Kogo, S. Iwasaki, M. Ikegami and T. Miyasaka, An Ultrathin Sputtered TiO₂ Compact Layer for Mesoporous Brookite-based Plastic CH₃NH₃PbI₃(₁-ₓ)Clₓ Solar Cells. *Chem. Lett.*, **2017**, *46*, 530–532.

[27] Y. Numata, A. Kogo, Y. Udagawa, H. Kunugita, K. Ema, Y. Sanehira and T. Miyasaka: Controlled Crystal Grain Growth in Mixed Cation-Halide Perovskite by Evaporated Solvent

Vapor Recycling Method for High Efficiency Solar Cells. *ACS Appl. Mater. Interfaces*, **2017**, *9*, 18739–18747.

[28] R. Hamaguchi, M. Yoshizawa-Fujita, T. Miyasaka, H. Kunugita, K. Ema, Y. Takeoka and M. Rikukawa: Formamidine and cesium-based quasi-two-dimensional perovskites as photovoltaic absorbers. *Chem. Commun.*, **2017**, *53*, 4366–4369.

[29] T. Singh, Y. Udagawa, M. Ikegami, H. Kunugita, K. Ema and T. Miyasaka: Tuning of perovskite solar cell performance via low-temperature brookite scaffolds surface modifications. *APL Mater.*, **2017**, *5*, 016103.

[30] N. Shibayama, H. Kanda, S. Yusa, S. Fukumoto, A. K. Baranwal, H. Segawa, T. Miyasaka and S. Ito: All-inorganic inverse perovskite solar cells using zinc oxide nanocolloids on spin coated perovskite layer. *Nano Converg.*, **2017**, *4*, 18.

[31] A. Agresti, S. Pescetelli, A. L. Palma, A. E. D. R. Castillo, D. Konios, G. Kakavelakis, S. Razza, L. Cinà, E. Kymakis, F. Bonaccorso and A. Di Carlo: Graphene interface engineering for perovskite solar module: a power conversion efficiency exceeding 12.6% over 50 cm² active area. *ACS Energy Letters*, **2017**, *2*, 279-287.

[32] A. Agresti, S. Pescetelli, B. Taheri, A. E. Del Rio Castillo, L. Cinà, F. Bonaccorso and A. Di Carlo: Graphene–Perovskite Solar Cells Exceed 18% Efficiency: A Stability Study. *ChemSusChem*, **2016**, *9*, 2609–2619.

[33] F. Matteocci, L. Cinà, F. Di Giacomo, S. Razza, A. L. Palma, A. Guidobaldi, A. D'Epifanio, S. Licoccia, T. M. Brown, A. Reale and A. Di Carlo: High efficiency photovoltaic module based on mesoscopic organometal halide perovskite. *Prog. Photovoltaics Res. Appl.*, **2014**, *20*, 6–11.

[34] G. Mincuzzi, A. L. Palma, A. Di Carlo and T. M. Brown: Laser Processing in the Manufacture of Dye-Sensitized and Perovskite Solar Cell Technologies, *ChemElectroChem*, **2016**, *3*, 9–30.

[35] G. Pellegrino, A. Alberti, G. G. Condorelli, F. Giannazzo, A. La Magna, A. M. Paoletti, G. Pennesi, G. Rossi and G. Zanotti: Study of the Anchoring Process of Tethered Unsymmetrical Zn-Phthalocyanines on TiO₂ Nanostructured Thin Films. *Journal of Phys. Chem. C*, **2013**, *117*, 11176-11185.

[36] J.-H. Im, C.-R. Lee, J.-W. Lee, S.-W. Park and N.-G. Park: 6.5% efficient perovskite quantum-dot-sensitized solar cell. *Nanoscale*, 2011, **3**, 4088–4093.

[37] M. M. Lee, J. Teuscher, T. Miyasaka, T. N. Murakami and H. J. Snaith, Efficient Hybrid Solar Cells Based on Meso-Superstructured Organometal Halide Perovskites. *Science*, **2012**, *338*, 643–647.

[38] S. Hadlington: Perovskite coat gives hybrid solar cells a boost. *RSC Chemistry world*, **2012**.

[39] H.-S. Kim, C.-R. Lee, J.-H. Im, K.-B. Lee, T. Moehl, A. Marchioro, S.-J. Moon, R. Humphry-Baker, J.-H. Yum, J. E. Moser, M. Grätzel and N.-G. Park: Lead Iodide Perovskite Sensitized All-Solid-State Submicron Thin Film Mesoscopic Solar Cell with Efficiency Exceeding 9%. *Sci. Rep.*, **2012**, *2*, 591.

[40] M. Liu, M. B. Johnston and H. J. Snaith: Efficient planar heterojunction perovskite solar cells by vapour deposition. *Nature*, **2013**, *501*, 395–398.

[41] J. M. Ball, M. M. Lee, A. Hey and H. J. Snaith: Low-temperature processed meso-superstructured to thin-film perovskite solar cells. *Energy & Environmental Science*, **2013**, *6*, 1739.

[42] G. E. Eperon, V. M. Burlakov, P. Docampo, A. Goriely and H. J. Snaith: Morphological control for high performance, solution-processed planar heterojunction perovskite solar cells. *Adv. Funct. Mater.*, **2014**, *24*, 151–157.

[43] M. Saliba, K. W. Tan, H. Sai, D. T. Moore, T. Scott, W. Zhang, L. a Estro, U. Wiesner and H. J. Snaith: In fl uence of Thermal Processing Protocol upon the Crystallization and Photovoltaic Performance of Organic – Inorganic Lead Trihalide Perovskites. *J. Phys. Chem. C*, **2014**, *118*, 17171–17177.

[44] K. W. Tan, D. T. Moore, M. Saliba, H. Sai, L. A. Estroff, T. Hanrath, H. J. Snaith and U. Wiesner: Thermally induced structural evolution and performance of mesoporous block copolymer-directed alumina perovskite solar cells. *ACS Nano*, **2014**, *8*, 4730–4739.

[45] J. Burschka, N. Pellet, S.-J. Moon, R. Humphry-Baker, P. Gao, M. K. Nazeeruddin and M. Grätzel: Sequential deposition as a route to high-performance perovskite-sensitized solar cells. *Nature*, **2013**, *499*, 316–319.

[46] O. Malinkiewicz, A. Yella, Y. H. Lee, G. M. Espallargas, M. Graetzel, M. K. Nazeeruddin and H. J. Bolink: Perovskite solar cells employing organic charge-transport layers. *Nat. Photonics*, **2013**, *8*, 128–132.

[47] M. Liu, M. B. Johnston and H. J. Snaith: Efficient planar heterojunction perovskite solar cells by vapour deposition. *Nature*, **2013**, *501*, 395–398.

[48] https://www.theguardian.com: The perovskite lightbulb moment for solar power. *The Guardian,* **2014***.*

[49] P. Docampo, J. M. Ball, M. Darwich, G. E. Eperon and H. J. Snaith: Efficient organometal trihalide perovskite planar-heterojunction solar cells on flexible polymer substrates, *Nat. Commun.*, **2017**, *4*, 2761.

[50] H. Gerischer, M. Michel-Beyerle, E. Rebentrost, and H. Tributsch: Sensitization of Charge-Injection into Semiconductors with Large Band Gap. *Electrochimica Acta*, **1968**, *13*, 1509–1515.

[51] H. Tributsch and M. Calvin: Electrochemistry of Excited Molecules: Photoelectrochemical Reactions of Chlorophylls. *Photochem. Photobiol*, **1971**, *14*, 95–112.

[52] H. Tributsch: Reaction of Excited Chorophyll Molecules at Electrodes and in Photosynthesis. *Photochem. Photobiol.*, **1972**, *16*, 261–269.

[53] M. Matsumura, S. Matsudaira, H. Tsubomura, M. Takata and H. Yanagida: Dye Sensitization and Surface Structures of Semiconductor Electrodes. *Ind. Eng. Chem. Prod. Res. Dev.*, **1980**, *19*, 415–421.

[54] F. De Angelis and P. A. Kamat: Conversation with Michael Grätzel. *ACS Energy Lett.*, **2017**, *2*, 1674–1676.

[55] J. Bisquert: Dye-sensitized solar cells. Departament de Física, Universitat Jaume I.

[56] Dye Solar Cell Assembly Instructions. Solaronix. Retrieved 22 May **2007**.

[57] H. Kohjiro and A. Hironori: Chapter 15. Dye-Sensitized Solar Cells". In A. Luque; S. Hegedus. Handbook of Photovoltaic Science and Engineering. John Wiley & Sons, **2005**.

[58] C. C. Stoumpos and M. G. Kanatzidis: Halide Perovskites: Poor Man's High-Performance Semiconductors. *Adv. Mater.*, **2016**, *28*, 5778–5793.

[59] A. Miyata, A. Mitioglu, P. Plochocka, O. Portugall, J. T.-W. Wang, S. D. Stranks, H. J. Snaith and R. J. Nicholas. Direct measurement of the exciton binding energy and effective masses for charge carriers in organic–inorganic tri-halide perovskites. *Nat. Phys.*, **2015**, *11*, 582–587.

[60] M. A. Leguy, P. Azarhoosh, M. I. Alonso, M. Campoy-Quiles, O. J. Weber, J. Yao, D. Bryant, M. T. Weller, J. Nelson, A. Walsh, M. van Schilfgaarde and P. R. F. Barnes: Experimental and theoretical optical properties of methylammonium lead halide perovskites. *Nanoscale*, **2016**, *8*, 6317–6327.

[61] A. Alberti, I. Deretzis, G. Pellegrino, C. Bongiorno, E. Smecca, G. Mannino, F. Giannazzo, G. G. Condorelli, N. Sakai, T. Miyasaka, C. Spinella and A. La Magna: Similar Structural Dynamics for the Degradation of $CH_3NH_3PbI_3$ in Air and in Vacuum. *ChemPhysChem*, **2015**, *16*, 3064–3071.

[62] K. Mahmood, B. S. Swain and A. Amassian: Highly efficient hybrid photovoltaics based on hyperbranched three-dimensional TiO$_2$ electron transporting materials. *Adv. Mater.*, **2015**, *27*, 2859–2865.

[63] J. H. Noh and S. Il Seok: Steps toward efficient inorganic–organic hybrid perovskite solar cells. *MRS Bull.*, **2015**, *40*, 648–653.

[64] M. Saliba, T. Matsui, J.-Y. Seo, K. Domanski, J.-P. Correa-Baena, M. K. Nazeeruddin, S. M. Zakeeruddin, W. Tress, A. Abate, A. Hagfeldt and M. Grätzel: Cesium-containing triple cation perovskite solar cells: improved stability, reproducibility and high efficiency. *Energy Environ. Sci.*, **2016**, *9*, 1989–1997.

[65] S. Sanzaro, E. Smecca, G. Mannino, C. Bongiorno, G. Pellegrino, F. Neri, G. Malandrino, M. R. Catalano, G. G. Condorelli, R. Iacobellis, L. De Marco, C. Spinella, A. La Magna and A. Alberti: Multi-Scale-Porosity TiO$_2$ scaffolds grown by innovative sputtering methods for high throughput hybrid photovoltaics. *Sci. Rep.*, **2016**, *6*, 39509.

[66] S. Yang, W. Fu, Z. Zhang, H. Chen and C.-Z. Li: Recent advances in perovskite solar cells: efficiency, stability and lead-free perovskite. *J. Mater. Chem. A*, **2017**, *5*, 11462–11482.

[67] S. Masi, A. Rizzo, R. Munir, A. Listorti, A. Giuri, C. Esposito Corcione, N. D. Treat, G. Gigli, A. Amassian, N. Stingelin and S. Colella: Organic Gelators as Growth Control Agents for Stable and Reproducible Hybrid Perovskite-Based Solar Cells. *Adv. Energy Mater.*, **2017**, 1602600, 1–11.

[68] G. Pellegrino, S. D'Angelo, I. Deretzis, G. G. Condorelli, E. Smecca, G. Malandrino, A. La Magna and A. Alberti: From PbI$_2$ to MAPbI$_3$ through Layered Intermediates. *J. Phys. Chem. C*, **2016**, *120*, 19768–19777.

[69] A. Ishii, Jena, A. K., Miyasaka, T. *APL Mater.* **2014**, *2*, 091102.

[70] H. W. Chen, N. Sakai, A. K. Jena, Y. Sanehira, M. Ikegami, K. C. Ho and T. Miyasaka: A switchable high-sensitivity photodetecting and photovoltaic device with perovskite absorber. *J. Phys. Chem. Lett.*, **2015**, *6*, 1773–1779.

[71] K.-L. Wu, A. Kogo, N. Sakai, M. Ikegami and T. Miyasaka: High Efficiency and Robust Performance of Organo Lead Perovskite Solar Cells with Large Grain Absorbers Prepared in Ambient Air Conditions. *Chem. Lett.*, **2015**, *44*, 321–323.

[72] J. Song, L. Liu, X.-F. Wang, G. Chen, W. Tian, and T. Miyasaka: Highly efficient and stable low-temperature processed ZnO solar cells with triple cation perovskite absorber. *J. Mater. Chem. A*, **2017**, *5*, 13439-13447.

[73] N. Sakai, S. Pathak, H. -W. Chen, A. A. Haghighirad, S. D. Stranks, T. Miyasaka, and H. J. Snaith, The mechanism of toluene-assisted crystallization of organic-inorganic perovskites for highly efficient solar cells. *J. Mater. Chem. A*, **2016**, *4*, 4464-4471.

[74] T. Singh and T. Miyasaka: High performance perovskite solar cell via multi-cycle low temperature processing of lead acetate precursor solutions. *Chem. Commun*., **2016**, *52*, 4784-4787.

[75] L. K. Ono, N.-G. Park, K. Zhu, W. Huang and Y. Qi: Perovskite Solar Cells - Towards Commercialization. *ACS Energy Lett.*, **2017**, *8*, 1749–1751.

[76] A.-N. Cho and N.-G. Park: Impact of Interfacial Layers in Perovskite Solar Cells. *ChemSusChem*, **2017**, DOI: 10.1002/cssc.201701095.

[77] N.-G. Park, M. Grätzel, T. Miyasaka, K. Zhu, and K. Emery: Towards stable and commercially available perovskite solar cells. *Nat. Energy*., **2016**, *1*, 16152.

[78] A. Cannavale, L. Ierardi, M. Hörantner, G. E. Eperon, H. J. Snaith, U. Ayr and F. Martellotta: Improving energy and visual performance in offices using building integrated perovskite-based solar cells: A case study in Southern Italy. *Appl. Energy*, **2017**, *205*, 834–846.

[79] J. S. Manser, J. A. Christians and P. V. Kamat: Intriguing Optoelectronic Properties of Metal Halide Perovskites. *Chemical Reviews*, **2016**, *116*, 12956–13008.

[80] L. Hamers: Perovskites power up the solar industry. *ScienceNews.org*, **2017**, *192*, 22.

[81] M. A. Green and S. P. Bremner: Energy conversion approaches and materials for high-effciency photovoltaics. *Nat. Mater.*, **2016**, *16*, 23-34.

[82] H. Zhang, J. Cheng, F. Lin, H. He, J. Mao, K. S. Wong, A. K. Y. Jen and W. C. H. Choy: Pinhole-free and surface-nanostructured NiO$_x$ film by room-Temperature solution process for high-performance flexible perovskite solar cells with good stability and reproducibility. *ACS Nano*, **2016**, *10*, 1503–1511.

[83] T. J. Jacobsson, W. Tress, J. P. Correa-Baena, T. Edvinsson and A. Hagfeldt: Room Temperature as a Goldilocks Environment for CH₃NH₃PbI₃ Perovskite Solar Cells: The Importance of Temperature on Device Performance. *J. Phys. Chem. C*, **2016**, *120*, 11382–11393.

[84] A. J. Pearson, G. E. Eperon, P. E. Hopkinson, S. N. Habisreutinger, J. T. W. Wang, H. J. Snaith and N. C. Greenham: Oxygen Degradation in Mesoporous Al₂O₃/CH₃NH₃PbI₃₋ₓClₓ Perovskite Solar Cells: Kinetics and Mechanisms. *Adv. Energy Mater.*, **2016**, *6*, 1600014.

[85] D. Wang, M. Wright, N. K. Elumalai and A. Uddin: Stability of perovskite solar cells. *Sol. Energy Mater. Sol. Cells*, **2016**, *147*, 255–275.

[86] G. Niu, X. Guo and L. Wang: Review of recent progress in chemical stability of perovskite solar cells. *J. Mater. Chem. A*, **2015**, *3*, 8970–8980.

[87] D. Bryant, N. Aristidou, S. Pont, I. Sanchez-Molina, T. Chotchunangatchaval, S. Wheeler, J. R. Durrant and S. A. Haque: Light and oxygen induced degradation limits the operational stability of methylammonium lead triiodide perovskite solar cells. *Energy Environ. Sci.*, **2016**, *9*, 1655–1660.

[88] I. Deretzis, A. Alberti, G. Pellegrino, E. Smecca, F. Giannazzo, N. Sakai, T. Miyasaka and A. La Magna: Atomistic origins of $CH_3NH_3PbI_3$ degradation to PbI_2 in vacuum. *Appl. Phys. Lett.*, **2015**, *106*, 131904.

[89] D. Yang, W. Ming, H. Shi, L. Zhang and M. H. Du: Fast Diffusion of Native Defects and Impurities in Perovskite Solar Cell Material $CH_3NH_3PbI_3$. *Chem. Mater.*, **2016**, *28*, 4349–4357.

[90] E. Smecca, Y. Numata, I. Deretzis, G. Pellegrino, S. Boninelli, T. Miyasaka, A. La Magna and A. Alberti: Stability of solution-processed MAPbI₃ and FAPbI₃ layeres. *Phys. Chem. Chem. Phys.*, **2016**, *18*, 13413–13422.

[91] J. M. Frost, K. T. Butler, F. Brivio, C. H. Hendon, M. Van Schilfgaarde and A. Walsh: Atomistic origins of high-performance in hybrid halide perovskite solar cells. *Nano Lett.*, **2014**, *14*, 2584–2590.

[92] Y. Han, S. Meyer, Y. Dkhissi, K. Weber, J. M. Pringle, U. Bach, L. Spiccia and Y.-B. Cheng: Degradation observations of encapsulated planar $CH_3NH_3PbI_3$ perovskite solar cells at high temperatures and humidity. *J. Mater. Chem. A*, **2015**, *3*, 8139–8147.

[93] S. N. Habisreutinger, T. Leijtens, G. E. Eperon, S. D. Stranks, R. J. Nicholas and H. J. Snaith: Carbon nanotube/polymer composites as a highly stable hole collection layer in perovskite solar cells. *Nano Lett.*, **2014**, *14*, 5561–5568.

[94] I. Deretzis, B. N. Di Mauro, A. Alberti, G. Pellegrino, E. Smecca and A. La Magna: Spontaneous bidirectional ordering of $CH_3NH_3^+$ in lead iodide perovskites at room temperature: The origins of the tetragonal phase. *Sci. Rep.*, **2016**, *6*, 24443.

[95] Y. Kawamura, H. Mashiyama and K. Hasebe: Structural Study on Cubic–Tetragonal Transition of $CH_3NH_3PbI_3$. *J. Phys. Soc. Japan*, **2002**, *71*, 1694–1697.

[96] T. Baikie, N. S. Barrow, Y. Fang, P. J. Keenan, P. R. Slater, R. O. Piltz, M. Gutmann, S. G. Mhaisalkar and T. J. White: A combined single crystal neutron/X-ray diffraction and solid-

state nuclear magnetic resonance study of the hybrid perovskites $CH_3NH_3PbX_3$ (X = I, Br and Cl). *J. Mater. Chem. A*, **2015**, *3*, 9298–9307.

[97] S. D. Stranks, G. E. Eperon, G. Grancini, C. Menelaou, M. J. P. Alcocer, T. Leijtens, L. M. Herz, A. Petrozza and H. J. Snaith: Electron-Hole Diffusion Lengths Exceeding 1 Micrometer in an Organometal Trihalide Perovskite Absorber. *Science*, **2013**, *342*, 341–344.

[98] J. You, Z. Hong, Y. M. Yang, Q. Chen, M. Cai, T. Song, C. Chen, S. Lu, Y. Liu, H. Zhou and Y. Yang: Low-temperature solution-processed perovskite solar cells with high efficiency and flexibility. *ACS Nano*, **2014**, *8*, 1674–80.

[99] A. Fujishima and K. Honda: Electrochemical photolysis of water at a semiconductor electrode. *Nature*, **1972**, *238*, 37–39.

[100] H. Liu, J. B. Joo, M. Dahl, L. Fu, Z. Zeng and Y. Yin: Crystallinity control of TiO₂ hollow shells through resin-protected calcination for enhanced photocatalytic activity. *Energy Environ. Sci.*, **2015**, *8*, 286–296.

[101] H. F. Zhuang, C. J. Lin, Y. K. Lai, L. Sun and J. Li: Some critical structure factors of titanium oxide nanotube array in its photocatalytic activity. *Environ. Sci. Technol.*, **2007**, *41*, 4735–4740.

[102] A. Alberti, C. Bongiorno, G. Pellegrino, S. Sanzaro, E. Smecca, G. G. Condorelli, A. E. Giuffrida, G. Cicala, A. Latteri, G. Ognibene, A. Cassano, A. Figoli, C. Spinella and A. La Magna: Low temperature sputtered TiO₂ nano sheaths on electrospun PES fibers as high porosity photoactive material. *RSC Adv.*, **2015**, *5*, 73444-73450.

[103] W.-J. Ong, L.-L. Tan, S.-P. Chai, S.-T. Yong and A. R. Mohamed: Crystallographic Facet-Induced Toxicological -Dependent Photocatalytic Properties of TiO₂-Based Composites for Energy Conversion and Environmental Remediation. *ChemSusChem*, **2014**, *7*, 690–719.

[104] W. J. Ong, L. L. Tan, S. P. Chai, S. T. Yong and A. R. Mohamed: Self-assembly of nitrogen-doped TiO₂ with exposed {001} facets on a graphene scaffold as photo-active hybrid nanostructures for reduction of carbon dioxide to methane. *Nano Res.*, **2014**, *7*, 1528–1547.

[105] N. Liu, K. Li, X. Li, Y. Chang, Y. Feng, X. Sun, Y. Cheng, Z. Wu and H. Zhang: Crystallographic Facet-Induced Toxicological Responses by Faceted Titanium Dioxide Nanocrystals. *ACS Nano*, **2016**, *6*, 6062-6073.

[106] P. Zhai, T.-Y. Hsieh, C.-Y. Yeh, K. S. K Reddy, C.-C. Hu, J.-H. Su, T.-C. Wei and S.-P. Feng: Trifunctional TiO₂ Nanoparticles with Exposed {001} Facets as Additives in Cobalt-Based Porphyrin-Sensitized Solar Cells. *Adv. Funct. Mater.*, **2015**, *25*, 6093-6100.

[107] B. Seger, T. Pedersen, A. B. Laursen, P. C. K. Vesborg, O. Hansen and I. Chorkendorff: Using TiO₂ as a conductive protective layer for photocathodic H₂ evolution. *J. Am. Chem. Soc.*, **2013**, *135*, 1057–1064.

[108] Q. Kang, J. Cao, Y. Zhang, L. Liu, H. Xu and J. Ye: Reduced TiO₂ nanotube arrays for photoelectrochemical water splitting. *J. Mater. Chem. A*, **2013**, *1*, 5766.

[109] I. Cho, J. Choi, K. Zhang, S. J. Kim, M. J. Jeong, L. Cai, T. Park, X. Zheng and J. H. Park: Highly Efficient Solar Water Splitting from Transferred TiO₂ Nanotube Arrays. *Nano Lett.*, **2015**, *15*, 5709-5715.

[110] Y. Ji, M. Zhang, J. Cui, K.-C. Lin, H. Zheng, J.-J. Zhu and A. C. S. Samia: Highly-ordered TiO2 nanotube arrays with double-walled and bamboo-type structures in dye-sensitized solar cells. *Nano Energy*, **2012**, *1*, 796–804.

[111] P. Roy, D. Kim, K. Lee, E. Spiecker and P. Schmuki: TiO₂ nanotubes and their application in dye-sensitized solar cells. *Nanoscale*, **2010**, *2*, 45–59.

[112] H. Li, Z. Chen, C. K. Tsang, Z. Li, X. Ran, C. Lee, B. Nie, L. Zheng, T. Hung, J. Lu, B. Pan and Y. Y. Li: Electrochemical doping of anatase TiO₂ in organic electrolytes for high-performance supercapacitors and photocatalysts. *J. Mater. Chem. A*, **2014**, *2*, 229–236.

[113] B. Chen, J. Hou and K. Lu: Formation mechanism of TiO₂ nanotubes and their applications in photoelectrochemical water splitting and supercapacitors. *Langmuir*, **2013**, *29*, 5911–5919.

[114] Y. Lai, L. Lin, F. Pan, J. Huang, R. Song, Y. Huang, C. Lin, H. Fuchs and L. Chi: Bioinspired patterning with extreme wettability contrast on TiO₂ nanotube array surface: A versatile platform for biomedical applications. *Small*, **2013**, *9*, 2945–2953.

[115] X. W. and L. P. T. Huaqiong Li, Yuekun Lai, Jianying Huang, Yuxin Tang, Lei Yang, Zhong Chen, Keqin Zhang: Multifunctional wettability patterns prepared by laser processing on superhydrophobic TiO₂ nanostructured surfaces. *J. Mater. Chem. B Mater. Biol. Med.*, **2014**, *3*, 342–347.

[116] H. Gao, M. Sun, C. Lin and S. Wang: Electrochemical DNA Biosensor Based on Graphene and TiO₂ Nanorods Composite Film for the Detection of Transgenic Soybean Gene Sequence of MON89788. *Electroanalysis*, **2012**, *24*, 2283-2290.

[117] J. S. Chen, Y. L. Tan, C. M. Li, Y. L. Cheah, D. Luan, S. Madhavi, F. Y. C. Boey, L. A. Archer and X. W. Lou: Constructing hierarchical spheres from large ultrathin anatase TiO₂ nanosheets with nearly 100% exposed (001) facets for fast reversible lithium storage. *J. Am. Chem. Soc.*, **2010**, *132*, 6124–6130.

[118] K. Wang, M. Wei, M. A. Morris, H. Zhou and J. D. Holmes: Mesoporous Titania Nanotubes: Their Preparation and Application as Electrode Materials for Rechargeable Lithium Batteries. *Adv. Mater.*, **2007**, *19*, 3016–3020.

[119] W. Guo, X. Xue, S. Wang, C. Lin and Z. L. Wang: An integrated power pack of dye-sensitized solar cell and Li battery based on double-sided TiO₂ nanotube arrays. *Nano Lett.*, **2012**, *12*, 2520-2523.

[120] U. Sulaeman and A. Z. Abdullah: The way forward for the modification of dye-sensitized solar cell towards better power conversion efficiency. *Renewable and Sustainable Energy Reviews*, **2017,** *74*, 438–452.

[121] M. Ge, C. Cao, J. Huang, S. Li, Z. Chen, K.-Q. ZHANG, S. S. Al-deyab and Y. Lai: A Review of One-dimensional TiO₂ Nanostructured Materials for Environmental and Energy Applications. *J. Mater. Chem. A*, **2016**, *4*, 6772–6801.

[122] J. Lin, Y.-U. Heo, A. Nattestad, Z. Sun, L. Wang, J. H. Kim and S. X. Dou: 3D Hierarchical Rutile TiO₂ and Metal-free Organic Sensitizer Producing Dye-sensitized Solar Cells 8.6% Conversion Efficiency. *Sci. Rep.*, **2015**, *4*, 5769.

[123] J. Lin, L. Zhao, Y. U. Heo, L. Wang, F. H. Bijarbooneh, A. J. Mozer, A. Nattestad, Y. Yamauchi, S. X. Dou and J. H. Kim: Mesoporous anatase single crystals for efficient Co$^{(2+/3+)}$-based dye-sensitized solar cells. *Nano Energy*, **2015**, *11*, 557–567.

[124] J. Lin, Y.-U. Heo, A. Nattestad, M. Shahabuddin, Y. Yamauchi and J. H. Kim: N719- and D149-sensitized 3D hierarchical rutile TiO₂ solar cells - a comparative study. *Phys. Chem. Chem. Phys.*, **2015**, *17*, 7208-7213.

[125] L. González-García, I. González-Valls, M. Lira-Cantu, A. Barranco and A. R. González-Elipe: Aligned TiO₂ nanocolumnar layers prepared by PVD-GLAD for transparent dye sensitized solar cells. *Energy Environ. Sci.*, **2011**, *4*, 3426.

[126] J. A. Thornton: The microstructure of sputter-deposited coatings. *J. Vac. Sci. Technol. A*, **1986**, *4*, 3059-3065.

[127] B. A. Movchan and A. V. Demchishin: Study of the structure and properties of thick vacuum condensates of nickel, titanium, tungsten, aluminium oxide and zirconium dioxide. *Phys. Met. Metallogr.*, **1969**, *28*, 83-90.

[128] S. H. Kang, M.-S. Kang, H.-S. Kim, J.-Y. Kim, Y.-H. Chung, W. H. Smyrl and Y.-E. Sung: Columnar rutile TiO₂ based dye-sensitized solar cells by radio-frequency magnetron sputtering. *J. Power Sources*, **2008**, *184*, 331–335.

[129] M. M. Gómez, J. Lu, E. Olsson, A. Hagfeldt and C. . Granqvist: High efficiency dye-sensitized nanocrystalline solar cells based on sputter deposited Ti oxide films. *Sol. Energy Mater. Sol. Cells*, **2000**, *64*, 385–392.

[130] Q. Zhou, Z. Li, J. Ni and Z. Zhang: A Simple Model to Describe the Rule of Glancing Angle Deposition. *Materials Transactions*, **2011**, *52*, 469-473.

[131] Z. Li, Y. Teng, L. Xing, N. Zhang and Z. Zhang: Enhancement of the photocatalytic property of TiO₂ columnar nanostructured films by changing deposition angle. *Mater. Res. Bull.*, **2014**, *50*, 68–72.

[132] Y. Motemani, C. Greulich, C. Khare, M. Lopian, P. J. S. Buenconsejo, T. A. Schildhauer, A. Ludwig and M. Köller: Adherence of human mesenchymal stem cells on Ti and TiO₂ nano-columnar surfaces fabricated by glancing angle sputter deposition. *Appl. Surf. Sci.*, **2014**, *292*, 626–631.

[133] Y. Pihosh, I. Turkevych, J. Ye, M. Goto, A. Kasahara, M. Kondo and M. Tosa: Photocatalytic Properties of TiO₂ Nanostructures Fabricated by Means of Glancing Angle Deposition and Anodization. *J. Electrochem. Soc.*, **2009**, *156*, K160-K165.

[134] O. Sanchez-Sobrado, M. J Mendes, S. Haque, T. Mateus, A. Araujo, H. Aguas, E. Fortunato and R. Martins: Colloidal-lithographed TiO₂ photonic nanostructures for solar cell light trapping. J. of Mat. Chem. C, 2017, 27, 6852-6861.

[135] D. Nunes, A. Pimentel, L. Santos, P. Barquinha, E. Fortunato and R. Martins: Photocatalytic TiO₂ Nanorod Spheres and Arrays Compatible with Flexible Applications. *Catalysts*, **2017**, *7*, 60.

[136] D. C. Iza, D. Muñoz-Rojas, K. P. Musselman, J. Weickert, A. C. Jakowetz, H. Sun, X. Ren, R. L. Z. Hoye, J. H. Lee, H. Wang, L. Schmidt-Mende and J. L. Macmanus-Driscoll: Nanostructured conformal hybrid solar cells: a promising architecture towards complete charge collection and light absorption. *Nanoscale Res. Lett.*, **2013**, *8*, 359.

[137] S. Biswas, C. Jiménez, A. Khan, S. Forissier, A. K. Kar, D. Muñoz-Rojas and J.-L. Deschanvres: Structural study of TiO₂ hierarchical microflowers grown by aerosol-assisted MOCVD. *CrystEngComm*, **2017**, *11*, 1535-1544.

[138] S. Chen, Z. Li and Z. Zhang: Anisotropic Ti_xSn_{1-x}O₂ nanostructures prepared by magnetron sputter deposition. *Nanoscale Res. Lett.*, **2011**, *6*, 326.

[139] Y. Cao, Y. Saygili, A. Ummadisingu, J. Teuscher, J. Luo, N. Pellet, F. Giordano, S. M. Zakeeruddin, J.-E. Moser, M. Freitag, A. Hagfeldt and M. Grätzel: 11% efficiency solid-state dye-sensitized solar cells with copper(II/I) hole transport materials. *Nat. Commun.*, **2017**, *8*, 15390.

[140] D. Depla; S. Mahieu and J. E. Greene: Sputter deposition processes. *Biblio UGent*, **2001**.

[141] M. M. Gòmez, N. Beermannb, J. Lua, E. Olssona, A. Hagfeldt, G. A. Niklasson and C. G. Granqvist: Dye-sensitized sputtered titanium oxide films for photovoltaic applications: influence of the O_2/Ar gas flow ratio during the deposition. *Solar Energy Materials & Solar Cells*, **2003**, *76*, 37-56.

[142] S. Sério, M. E. Melo Jorge, M. J. P. Maneira and Y. Nunes: Influence of O_2 partial pressure on the growth of nanostructured anatase phase TiO_2 thin films prepared by DC reactive magnetron sputtering. *Materials Chemistry and Physics*, **2011**, *126*, 73-81.

[143] T. Lindgren, J. M. Mwabora, E. Avendaño, J. Jonsson, A. Hoel, C. G. Granqvist and S. E. Lindquist: Photoelectrochemical and optical properties of nitrogen doped titanium dioxide films prepared by reactive DC magnetron sputtering. *J. Phys. Chem. B*, **2003**, *107*, 5709-5716.

[144] R. K. Waits: Planar Magnetron Sputtering. *J. Vac. Sci. Technol.* **1978**, *15*, 179-187.

[145] J. Miao, P. Charalambous, J. Kirz, and D. Sayre: Extending the methodology of X-ray crystallography to allow imaging of micrometre-sized non-crystalline specimens. *Nature*, **1999**, *400*, 342–344.

[146] H. N. Chapman, A. Barty, S. Marchesini, A. Noy and S. P. Hau-Riege: High-resolution *ab initio* three-dimensional X-ray diffraction microscopy. *J. Opt. Soc. Am. A*, **2006**, *23*, 1179-1200.

[147] E. T. B. Skjønsfjell, Y. Chushkin, F. Zontone, N. Patil, A. Gibaud and D. W. Breiby: Wavefront metrology for coherent hard X-rays by scanning a microsphere. *Opt. Express*, **2016**, *24*, 10710-10722.

[148] Y. Chushkin, F. Zontone, E. Lima, L. De Caro, P. Guardia, L. Manna and C. Giannini: Three-dimensional coherent diffractive imaging on non-periodic specimens at the ESRF beamline ID10. *J. Synchrotron Rad.*, **2014**, *21*, 594‑599.

[149] D. Sayre and H. N. Chapman: X-ray microscopy. *Acta Crystallogr., Sect. A: Found. Crystallogr.*, **1995**, *51*, 237–252.

[150] D. Sayre, H. N. Chapman and J. Miao: On the extendibility of x-ray crystallography to noncrystals. *Acta Crystallogr., Sect. A: Found. Crystallogr.*, **1998**, *54*, 232–239.

[151] E. M. L. D. de Jong, G. Mannino, A. Alberti, R. Ruggeri, M. Italia, F. Zontone, Y. Chushkin, A. R. Pennisi, T. Gregorkiewicz and G. Faraci: Strong infrared photoluminescence in highly porous layers of large faceted Si crystalline nanoparticles. *Sci. Rep.*, **2016**, *6*, 25664.

[152] E. F. Pettersen, T. D. Goddard, C. C. Huang, G. S. Couch, D. M. Greenblatt, E. C. Meng and T. E. Ferrin: UCSF Chimera-A visualization system for exploratory research and analysis. *J. Comput. Chem.*, **2004**, *25*, 1605-1612.

[153] C. Boissiere, D. Grosso, S. Lepoutre, L. Nicole, A. B. Bruneau, C. Sanchez: Porosity and Mechanical Properties of Mesoporous Thin Films Assessed by Environmental Ellipsometric Porosimetry. *Langmuir* **2005**, *21*, 12362-12371.

[154] B. S. Richards, N. T. P. Huong and A. Crosky: Highly Porous Nanocluster TiO₂ Films Deposited Using APCVD in an Excess of Water Vapor. *J. of the Electrochem. Soc.*, **2005**, *152*, F71-F74.

[155] S. Mamedov**,** T. Moriyama, T. Numata, N. Nabatova-Gabain, S. Yanagida, and L. Yan: Characterization of nano-crystalline structure of TiO₂ for Dye-sensitized Solar Cells by Raman Spectroscopy and spectroscopic ellipsometry. *Mater. Res. Soc. Symp. Proc.*, **2013**, *1578*.

[156] C. P. Leon, L. Kador, B. Peng and M. Thelakkat: Influence of the Solvent on the Surface-Enhanced Raman Spectra of Ruthenium(II) Bipyridyl Complexes. *J. Phys. Chem. B*, **2005**, *109,* 5783-5789.

[157] H. Zhang and J. F. Banfield: Thermodynamic analysis of phase stability of nanocrystalline titania. *J. Mater. Chem.*, **1998**, *8*, 2073-2076.

[158] T.-J. Park, A. A. Levchenko, H. Zhou, S. S. Wong and A. Navrotsky: Shape-dependent surface energetics of nanocrystalline TiO₂. *J. Mater. Chem.*, **2010**, *20*, 8639-8645.

[159] B. D. Cullity: Elements of X- ray diffraction, 2nd Edition Addison Wesley, Reading, MA, USA **1978**.

[160] C. Hanaor and C. Sorrell: Review of the anatase to rutile phase transformation. *J. Mater Sci.* **2011**, *46*, 855-874.

[161] A. Alberti, C. Bongiorno and G. Pellegrino: Anatase/Rutile nucleation and growth on (0002) and (11-20) oriented ZnO:Al/glass substrates at 150°C. *Thin Solid Films*, **2014**, *555*, 3–8.

[162] K. Fukushima and I. Yamada: Electrical properties of TiO₂ films deposited by a reactive-ionized cluster beam. *J. Appl. Phys.* **1989**, *65*, 619-623.

[163] M. H. Suhail, G. Mohan Rao and S. Mohan: DC reactive magnetron sputtering of titanium-structural and optical characterization of TiO₂ films. *J. Appl. Phys.* **1992**, *71*, 1421-1427.

[164] K. Eufinger, D. Poelman, H. Poelman, R. De Gryse and G. B. Marin, Effect of microstructure and crystallinity on the photocatalytic activity of TiO₂ thin films deposited by dc magnetron sputtering. *J. Phys. D: Appl. Phys.* **2007**, *40*, 5232-5238.

[165] B. Karunagaran, R. T. Rajendra Kumar, D. Mangalaraj, Sa. K. Narayandass, G. Mohan Rao: Influence of thermal annealing on the composition and structural parameters of DC magnetron sputtered titanium dioxide thin films. *Cryst. Res. Technol.* **2002**, *37*, 1285-1292.

[166] L.-J. Meng, M. Andritschky, M. P. dos Santos: The effect of substrate temperature on the properties of d.c. reactive magnetron sputtered titanium oxide films. *Thin Solid Films*, **1993**, *223*, 242-247.

[167] S. Schiller, G. Beister and W. Sieber: Influence of deposition parameters on the optical and structural properties of TiO₂ films produced by reactive d.c. plasmatron sputtering. *Thin Solid Films*, **1981**, *83*, 239-245.

[168] M. Pagliaro, G. Palmisano, R. Ciriminna, and V. Loddo: Nanochemistry aspects of titania in dye-sensitized solar cells. *Energy & Environ. Sci.* **2009**, *2*, 838-844.

[169] R. Buonsanti, E. Carlino, C. Giannini, D. Altamura, L. De Marco, R. Giannuzzi, M. Manca, G. Gigli and P. D. Cozzoli: Hyperbranched Anatase TiO₂ Nanocrystals: Nonaqueous Synthesis, Growth Mechanism and Exploitation in Dye-Sensitized Solar Cells. *J. Am. Chem. Soc.* **2011**, *133*, 19216-19239.

[170] M. Pagliaro, G. Palmisano, R. Ciriminna, and V. Loddo: Nanochemistry aspects of titania in dye-sensitized solar cells. *Energy & Environ. Sci.* **2009**, *2*, 838-844.

[171] R. Buonsanti, E. Carlino, C. Giannini, D. Altamura, L. De Marco, R. Giannuzzi, M. Manca, G. Gigli and P. D. Cozzoli: Hyperbranched Anatase TiO₂ Nanocrystals: Nonaqueous Synthesis, Growth Mechanism and Exploitation in Dye-Sensitized Solar Cells. *J. Am. Chem. Soc.* **2011**, *133*, 19216-19239.

[172] Y. Ma, X.L. Wang, Y.S. Jia, X.B. Chen, H.X. Han, C. Li: Titanium Dioxide-Based Nanomaterials for Photocatalytic Fuel Generations. *Chem. Rev.*, **2014**, *114* 9987–10043.

[173] G. Pellegrino, A. La Magna, G. G. Condorelli, C. Bongiorno, C. Mocuta, E. Smecca and A. Alberti: A strategy to stabilise the local structure of Ti⁴⁺ and Zn²⁺ species against aging in TiO₂/aluminium-doped ZnO bi-layers for applications in hybrid solar cells. *Journal of Applied Physics*, **2014**, *116,* 054907.

[174] A. Yella, H.-W. Lee, H. N. Tsao, C. Yi, A. K. Chandiran, M. K. Nazeeruddin, E. W.-G. Diau, C.-Y. Yeh, S. M. Zakeeruddin and M. Grätzel: Porphyrin-Sensitized Solar Cells with Cobalt (II/III)-Based Redox Electrolyte Exceed 12 Percent Efficiency. *Science*, **2011**, *334*, 629–634.

[175] L. Song, W. Wang, V. Körstgens, D. Moseguí González, Y. Yao, N. K. Minar, J. M. Feckl, K. Peters, T. Bein, D. Fattakhova-Rohlfing, G. Santoro, S. V. Roth and P. Müller-Buschbaum: Spray Deposition of Titania Films with Incorporated Crystalline Nanoparticles for All-Solid-State Dye-Sensitized Solar Cells Using P3HT. *Adv. Funct. Mater.*, **2016**, *26*, 1498–1506.

[176] H. Tian, X. Yu, J. Zhang, W. Duan, F. Tian and T. Yu: The influence of environmental factors on DSSCs for BIPV. *Int. J. Electrochem. Sci.*, **2012**, *7*, 4686–4691.

[177] S. Mathew, A. Yella, P. Gao, R. Humphry-Baker, B. F. E. Curchod, N. Ashari-Astani, I. Tavernelli, U. Rothlisberger, M. K. Nazeeruddin and M. Grätzel: Dye-sensitized solar cells with 13% efficiency achieved through the molecular engineering of porphyrin sensitizers. *Nat. Chem.*, **2014**, *6*, 242–247.

[178] A. R. Pascoe, S. Meyer, W. Huang, W. Li, I. Benesperi, N. W. Duffy, L. Spiccia, U. Bach and Y. B. Cheng: Enhancing the Optoelectronic Performance of Perovskite Solar Cells via a Textured CH₃NH₃PbI₃ Morphology. *Adv. Funct. Mater.*, **2016**, *26*, 1278–1285.

[179] A. Alberti, L. De Marco, G. Pellegrino, G. G. Condorelli, R. Giannuzzi, R. Scarfiello, M. Manca, C. Spinella, G. Gigli and A. La Magna: Combined Strategy to Realize Efficient Photoelectrodes for Low Temperature Fabrication of Dye Solar Cells. *ACS Appl. Mater. Interfaces*, **2014**, *6*, 6425-6433.

[180] A. Alberti, G. Pellegrino, G. G. Condorelli, C. Bongiorno, S. Morita, A. La Magna and T. Miyasaka: Efficiency enhancement in ZnO:Al-based dye-sensitized solar cells structured with sputtered TiO₂ blocking layers. *J. Phys. Chem. C*, **2014**, *118*, 6576–6585.

[181] H. Liu, V. Avrutin, N. Izyumskaya, Ü. Özgür and V. Morkoç: Transparent conducting oxides for electrode applications in light emitting and absorbing devices. *Superlattices Microstruct.*, **2010**, *48*, 458-484.

[182] R. Agosta, R. Grisorio, L. De Marco, G. Romanazzi, G. P. Suranna, G. Gigli and M. Manca: An engineered co-sensitization system for highly efficient dye solar cells., *Chem. Commun.*, **2014**, *50*, 9451–3.

[183] V. Gutmann: The Donor-Acceptor Approach to Molecular Interactions. New York: Plenum, **1978**.

[184] A. Alberti, L. Renna, S. Sanzaro, E. Smecca, G. Mannino, C. Bongiorno, C. Galati, L. Gervasi, A. Santangelo and A. La Magna: Innovative spongy TiO₂ layers for high sensitivity gas detection at low working temperature. *Sensors and Actuators B: Chemical*, **2017**, submitted.

[185] Q. Tai, X. Zhao and F. Yan: Hybrid solar cells based on poly(3-hexylthiophene) and electrospun TiO₂ nanofibers with effective interface modification. *J. Mater. Chem.*, **2010**, *20*, 7366–7371.

[186] K. E. Lee, M. A. Gomez, S. Elouatik and G. P. Demopoulos: Further Understanding of the Adsorption Mechanism of N719 Sensitizer on Anatase TiO₂ Films for DSSC Applications Using Vibrational Spectroscopy and Confocal Raman Imaging. *Langmuir*, **2010**, *26*, 9575–9583.

[187] S. G. Kazarian and A. K. L. Chan: Micro- and Macro-Attenuated Total Reflection Fourier Transform Infrared Spectroscopic Imaging. *Applied Spectroscopy*, **2010**, *64*, 135A-152A.

[188] V. Shklover, Y. E. Ovchinnikov, L. S. Braginsky, S. M. Zakeeruddine and M. Grätzel: Structure of Organic/Inorganic Interface in Assembled Materials Comprising Molecular Components. Crystal Structure of the Sensitizer Bis[(4,4′-carboxy-2,2′-bipyridine)(thiocyanato)]ruthenium(II). *Chem. Mater.*, **1998**, *10*, 2533–2541.

[189] F. De Angelis, S. Fantacci, A. Selloni, M. Grätzel and M. K. Nazeeruddine: Influence of the Sensitizer Adsorption Mode on the Open-Circuit Potential of Dye-Sensitized Solar Cells. *Nano Lett.*, **2007**, *7*, 3189–3195.

[190] F. Hirose, K. Kuribayashi, T. Suzuki, Y. Narita, Y. Kimura and M. Niwano: UV Treatment Effect on TiO₂ Electrodes in Dye-Sensitized Solar Cells with N719 Sensitizer Investigated by Infrared Absorption Spectroscopy. *Electrochem. Solid-State Lett.*, **2008**, *11*, A109–A111.

[191] K. Kuribayashi, H. Iwata and F. Hirose: N719 Dye Adsorption on Anatase TiO₂ Surfaces Investigated by Infrared Absorption Spectroscopy. *ECS Trans.*, **2007**, *6*, 15–19.

[192] E. M. J. Johansson, M. Hedlund, H. Siegbahn and H. Rensmo: Electronic and Molecular Surface Structure of Ru(tcterpy)(NCS)₃ and Ru(dcbpy)₂(NCS)₂ Adsorbed from Solution onto Nanostructured TiO₂: A Photoelectron Spectroscopy Study. *The J. Phys. Chem. B*, **2005**, *109*, 22256–22263.

[193] P. Falaras: Synergetic effect of carboxylic acid functional groups and fractal surface characteristics for efficient dye sensitization of titanium oxide. *Sol. Energy Mater. Sol. Cells*, **1998**, *53*, 163–175.

[194] M. K. Nazeeruddin, R. Humpry-Baker, P. Liska and M. Grätzel: Investigation of Sensitizer Adsorption and the Influence of Protons on Current and Voltage of a Dye-Sensitized Nanocrystalline TiO₂ Solar Cell. *J. Phys. Chem. B*, **2003**, *107*, 8981–8987.

[195] G. B. Deacon and R. Phillips: Relationships between the carbon-oxygen stretching frequencies of carboxylate complexes and the type of carboxylate coordination. *J. Coord. Chem. Rev.*, **1980**, *33*, 227–250.

[196] F. De Angelis, S. Fantacci, A. Selloni, M. K. Nazeeruddin and M. Grätzel: Time-Dependent Density Functional Theory Investigations on the Excited States of Ru(II)-Dye-Sensitized TiO₂ Nanoparticles: The Role of Sensitizer Protonation. *J. Am. Chem. Soc.*, **2007**, *129*, 14156–14157.

[197] T. Cai, Z. Song, Z. Chang, G. Liu, J. A. Rodriguez and J. Hrbek: Ru nanoclusters prepared by Ru₃(CO)₁₂ deposition on Au(1 1 1). *Surf. Sci.*, **2003**, *538*, 76–88.

[198] G. Liu, W. Jaegermann, J. He, V. Sundström and L. Sun: XPS and UPS characterization of the TiO₂/ZnPcGly heterointerface: Alignment of energy levels. *J. Phys. Chem. B*, **2002**, *106*, 5814–5819.

[199] G. Liu, A. Klein, A. Thissen and W. Jaegermann: Electronic properties and interface characterization of phthalocyanine and Ru-polypyridine dyes on TiO₂ surface. *Surf. Sci.*, **2003**, *539*, 37–48.

[200] J. Singh, A. Gusain, V. Saxena, A. K. Chauhan, P. Veerender, S. P. Koiry, P. Jha, A. Jain, D. K. Aswal and S. K. Gupta: XPS, UV-Vis, FTIR, and EXAFS studies to investigate the binding mechanism of N719 dye onto oxalic acid treated TiO₂ and its implication on photovoltaic properties. *J. Phys. Chem. C*, **2013**, *117*, 21096–21104.

[201] K. E. Lee, M. A. Gomez, T. Regier, Y. Hu and G. P. Demopoulos: Further Understanding of the Electronic Interactions between N719 Sensitizer and Anatase TiO₂ Films: A Combined X-ray Absorption and X-ray Photoelectron Spectroscopic Study. *J. Phys. Chem. C*, **2011**, *115*, 5692–5707.

[202] H. A. Azab, I. T. Ahmed and M. R. Mahmoud: Potentiometrie Determination of the Dissociation Constants of Some Monocarboxylic Acids in Various Hydroorganic Media. *J. Chem. Eng. Data*, **1995**, *40*, 523–525.

[203] H. Rensmo, K. Westermark, S. Södergren, O. Kohle, P. Persson, S. Lunell and H. Siegbahn: XPS studies of Ru-polypyridine complexes for solar cell applications. *J. Chem. Phys.* **1999**, *111*, 2744-2750.

[204] J. N. O'Shea, J. Schnadt, P. A. Brulhwiler, H. Hillesheimer and N. Mårtensson: Hydrogen-Bond Induced Surface Core-Level Shift in Isonicotinic Acid. *J. Phys. Chem. B,* **2001**, *105,* 1917-1920.

[205] M. K. Nazeeruddin, S. M. Zakeeruddin, R. Humphry-Baker, M. Jirousek, P. Liska, N. Vlachopoulos, V. Shklover, C.-H. Fischer and M. Grätzel: Acid–Base Equilibria of (2,2'-Bipyridyl-4,4'-dicarboxylic acid)ruthenium(II) Complexes and the Effect of Protonation on Charge-Transfer Sensitization of Nanocrystalline Titania. *Inorg. Chem.*, **1999**, *38*, 6298–6305.

[206] P. Chen and T. J. Meyer, Medium Effects on Charge Transfer in Metal Complexes, *Chem. Rev.*, **1998**, *98*, 1439–1478.

[207] P. Corio, M. L. A. Temperini, J. C. Rubim and P. S. Santos: The effects of solvent and electrolyte in the surface enhanced Raman spectrum of iron(II)bis(1,10

phenanthroline)dicyano: evidence for the formation of strong ion-pairs. *Spectrochim. Acta A: Molecular and Biomolecular Spectroscopy*, **1999**, *55*, 2411-2421.

[208] D. Li, B. I. Swanson, J. M. Robinson and M. Hoffbauer: Porphyrin Based Self-Assembled Monolayer Thin Films: Synthesis and Characterization. *J. Am. Chem. Soc.* **1195**, *115*, 6975-6980.

[209] G. Pellegrino, G. G. Condorelli, V. Privitera, B. Cafra, S. Di Marco and A. Alberti: Dye-Sensitizing of Self-Nanostructured Ti(:Zn)O₂/AZO Transparent Electrodes by Self-Assembly of 5,10,15,20-Tetrakis(4-carboxyphenyl)porphyrin. *J. Phys. Chem. C*, **2011**, *115*, 7760–7767.

[210] Z. Zhao, J. Tian, Y. Sang, A. Cabot and H. Liu: Structure, Synthesis, and Applications of TiO₂ Nanobelts. *Adv. Mater.*, **2015**, *27*, 2557-2582.

[211] R. Malone and F. Kelley: Interligand electron transfer and transition state dynamics in Ru(II)trisbipyridine. *J. Chem. Phys.* **1991**, *95*, 8970-8976.

[212] S. Fantacci, F. De Angelis and A. Selloni: Absorption Spectrum and Solvatochromism of the [Ru(4,4'-COOH-2,2'-bpy)₂(NCS)₂] Molecular Dye by Time Dependent Density Functional Theory. *J. Am. Chem. Soc.*, **2003**, *125*, 4381-4387.

[213] J. Streiff and J. L. Mchale: Resonance Raman study of the solvatochromic electronic transitions of [Ru(NH₃)₄bipyridine]²⁺ in methanol and dimethylsulfoxide. *J. Chem. Phys.*, **2000**, *112*, 841-850.

[214] G. Wypych: Handbook of solvents. Chem. Tec. Publishing, **2001**.

[215] J. Lin, X. Liu, S. Zhu and X. Chen: Anodic Nanostructures for Solar Cell Applications Green Nanotechnology - Overview and Further Prospects. Dr. Marcelo Larramendy (Ed.), InTech, **2016**.

[216] D. Kim, A. Ghicov, S. P. Albu and P. Schmuki: Bamboo-type TiO₂ nanotubes: Improved conversion efficiency in dye-sensitized solar cells. *J. Am. Chem. Soc.*, **2008**, *130*, 16454–16455.

[217] P. Persson and M. J. Lundqvist: Calculated Structural and Electronic Interactions of the Ruthenium Dye N3 with a Titanium Dioxide Nanocrystal. *J. Phys. Chem. B*, **2005**, *109*, 11918–11924.

[218] T. W. Hamann, R. A. Jensen, A. B. F. Martinson, H. Van Ryswyk and J. T. Hupp: Advancing beyond current generation dye-sensitized solar cells. *Energy Environ. Sci.*, **2008**, *1*, 66–78.

[219] E. Smecca, Y. Numata, I. Deretzis, G. Pellegrino, S. Boninelli, T. Miyasaka, A. La Magna and A. Alberti: Stability of solution-processed MAPbI₃ and FAPbI₃ layeres. *Phys. Chem. Chem. Phys.*, **2016**, *18*, 13413–13422.

[220] G. Pellegrino, S. Colella, I. Deretzis, G. G. Condorelli, E. Smecca, G. Gigli, A. La Magna and A. Alberti: Texture of MAPbI₃ Layers assisted by Chloride on Flat TiO₂ Substrates. *J. Phys. Chem. C*, 2015, *119*, 19808–19816.

[221] S. Colella, E. Mosconi, P. Fedeli, A. Listorti, F. Gazza, F. Orlandi, P. Ferro, T. Besagni, A. Rizzo, G. Calestani, G. Gigli, F. De Angelis and R. Mosca: MAPbI₃₋ₓClₓ Mixed Halide Perovskite for Hybrid Solar Cells: The Role of Chloride as Dopant on the Transport and Structural Properties. *Chem. Mater.* **2013**, *25*, 4613–4618.

[222] S. Colella, E. Mosconi, G. Pellegrino, A. Alberti, V. L. P. Guerra, S. Masi, A. Listorti, A. Rizzo, G. G. Condorelli, F. De Angelis and G. Gigli: Elusive presence of chloride in mixed halide perovskite solar cells. *J. Phys. Chem. Lett.*, **2014**, *5*, 3532–3538.

[223] A. M. A. Leguy, Y. Hu, M. Campoy-Quiles, M. I. Alonso, O. J. Weber, P. Azarhoosh, M. van Schilfgaarde, M. T. Weller, T. Bein, J. Nelson, P. Docampo and P. R. F. Barnes: The reversible hydration of CH₃NH₃PbI₃ in films, single crystals and solar cells, *Chem. Mater.*, **2015**, *27*, 3397–3407.

[224] J. Yang, B. D. Siempelkamp, D. Liu and T. L. Kelly: Investigation of CH₃NH₃PbI₃ degradation rates and mechanisms in controlled humidity environments using in situ techniques. *ACS Nano*, **2015**, *9*, 1955–1963.

[225] D. T. Moore, H. Sai, K. W. Tan, D. M. Smilgies, W. Zhang, H. J. Snaith, U. Wiesner and L. A. Estroff: Crystallization Kinetics of Organic-Inorganic Trihalide Perovskites and the Role of the Lead Anion in Crystal Growth. *J. Am. Chem. Soc.*, **2015**, *137*, 2350–2358.

[226] A. Alberti, I. Deretzis, G. Mannino, E. Smecca, S. Sanzaro, Y. Numata, T. Miyasaka and A. La Magna: Revealing a Discontinuity in the Degradation Behavior of CH₃NH₃PbI₃ during Thermal Operation. *J. Phys. Chem. C*, **2017**, *121*, 13577–13585.

[227] G. Mannino, A. Alberti, I. Deretzis, E. Smecca, S. Sanzaro, Y. Numata, T. Miyasaka and A. La Magna: First Evidence of CH₃NH₃PbI₃ Optical Constants Improvement in a N₂ Environment in the Range 40-80°C. *J. Phys. Chem. C*, **2017**, *121*, 7703–7710.

[228] R. Gago, A. Redondo-Cubero, M. Vinnichenko and L. Vázquez: Annealing of heterogeneous phase TiO₂ films: An X-ray absorption and morphological study. *Chem. Phys. Lett.*, **2011**, *511*, 367–371.

[229] P. Gondoni, M. Ghidelli, F. Di Fonzo, M. Carminati, V. Russo, A. Li Bassi and C.S. Casari: Structure-dependent optical and electrical transport properties of nanostructured Al doped ZnO. *Nanotechnology*, **2012**, *23*, 365706.

[230] X. Feng, J. Zhai and L. Jiang: The fabrication and switchable superhydrophobicity of TiO₂ nanorod films. *Angew. Chemie - Int. Ed.*, **2005**, *44*, 5115–5118.

[231] R. Wang, K. Hashimoto, A. Fujishima, M. Chikuni, E. Kojima, A. Kitamura, M. Shimohigoshi and T. Watanabe: Photogeneration of Highly Amphiphilic TiO₂ Surfaces. *Adv. Mater.*, **1998**, *10*, 135–138.

[232] R. Wang, N. Sakai, A. Fujishima, T. Watanabe and K. Hashimoto: Studies of surface wettability conversion on TiO₂ single-crystal surfaces. *J. Phys. Chem. B*, **1999**, *103*, 2188–2194.

[233] R. N. Wenzel: Resistance of solid surfaces to wetting by water. *Ind. Eng. Chem.*, **1936**, *28*, 988–994.

[234] A. B. D. Cassie and S. Baxter: Wettability of porous surfaces. *Trans. Faraday Soc.*, **1944**, *40*, 546.

[235] N. Chen, Y. Li, D. Deng, X. Liu, X. Xing, X. Xiao and Y. Wang: Acetone sensing performances based on nanoporous TiO₂ synthesized by a facile hydrothermal method. *Sensors Actuators, B Chem.*, **2017**, *238*, 491–500.

[236] G. Pellegrino, C. Bongiorno, S. Ravesi and A. Alberti: Fiber texturing in nano-crystalline TiO₂ thin films deposited at 150°C by dc-reactive sputtering on fiber-textured [0001] ZnO:Al substrates. *J. Phys. D: Appl. Phys.*, **2012**, *45*, 355301.

[237] S. Park, S. An, H. Ko, S. Lee, H. W. Kim and C. Lee: Enhanced ethanol sensing properties of TiO₂/ZnO core-shell nanorod sensors. *Appl. Phys. A Mater. Sci. Process.*, **2014**, *115*, 1223–1229.

[238] P. Feng, Q. Wan and T. H. Wang: Contact-controlled sensing properties of flowerlike ZnO nanostructures. *Appl. Phys. Lett.*, **2005**, *87*, 1–3.

[239] J. Li, H. Fan, X. Jia, W. Yang and P. Fang: Enhanced blue-green emission and ethanol sensing of Co-doped ZnO nanocrystals prepared by a solvothermal route. *Appl. Phys. A Mater. Sci. Process.*, **2010**, *98*, 537–542.

[240] Y. Kwon, H. Kim, S. Lee, I. J. Chin, T. Y. Seong, W. I. Lee and C. Lee: Enhanced ethanol sensing properties of TiO₂ nanotube sensors. *Sensors Actuators, B Chem.*, **2012**, *173*, 441–446.

[241] Y. Wang, Y. Zhou, C. Meng, Z. Gao, X. Cao, X. Li, L. Xu, W. Zhu, X. Peng, B. Zhang, Y. Lin and L. Liu: A high-response ethanol gas sensor based on one-dimensional TiO₂/V₂O₅ branched nanoheterostructures, *Nanotechnology*, **2016**, *27*, 425503.

[242] K. Hazra, P. P. Sengupta and P. Ghosh, in *2014 2ⁿᵈ International Conference on Business and Information Management (ICBIM)*, **2014**, pp. 108–112.

[243] S. Hemmati, A. A. Firoozb, A. A. Khodadadi and Y. Mortazavi, Nanostructured SnO_2–ZnO sensors: highly sensitive and selective to ethanol, *Sensors and Actuators B*, **2011**, *160*, 1298–1303.

[244] P. Dwivedi, N. Chauhan, P. Vivekanandan, S. Das, D. Sakthi Kumar and S. Dhanekar: Scalable fabrication of prototype sensor for selective and sub-ppm level ethanol sensing based on TiO2 nanotubes decorated porous silicon. *Sensors Actuators, B Chem.*, **2017**, *249*, 602–610.

[245] R. Grisorio, L. De Marco, R. Giannuzzi, G. Gigli and G. P. Suranna: Molecular engineering of largely π-extended metal-free sensitizers containing benzothiadiazole units: Approaching 10% efficiency dye-sensitized solar cells using iodine-based electrolytes. *Dyes and Pigments*, **2016**, *131*, 282–292.

[246] J. H.Noh, H. S. Han, S. Lee, D. H. Kim, J. H. Park, S. Park, J. Y. Kim, H. S. Jung, and K. S. Hong: A Newly Designed Nb-Doped TiO2/Al-Doped ZnO Transparent Conducting Oxide Multilayer for Electrochemical Photoenergy Conversion Devices. *J. Phys. Chem. C*, **2010**, *114*, 13867–13871.

[247] T. Liu, L. Zuo, T. Ye, J. Wu, G. Xue,a W. Fu and H. Chen: Low temperature processed ITO-free perovskite solar cells without a hole transport layer. *RSC Adv.*, **2015**, *5*, 94752-94758.

[248] P. Dong, Y. Zhu, J. Zhang, F. Hao, J. Wu, S. Lei, H. Lin, R. H. Hauge, J. M. Tour and J. Lou: Vertically Aligned Carbon Nanotubes/Graphene Hybrid Electrode as a TCO- and Pt-Free Flexible Cathode for application in Solar Cells. *J. Mater. Chem. A*, **2014**, *2*, 20902-20907.

[249] M. Huang, Z. Hameiri, H. Gong, W.-C. Wong, A. G. Aberle and T. Mueller: Novel hybrid electrode using transparent conductive oxide and silver nanoparticle mesh for silicon solar cell applications. *Energy Procedia*, **2014**, *55*, 670–678.

[250] G. Pellegrino, G. G. Condorelli, F. De Rossi, T. M. Brown, F. Giovenale, C. Bongiorno and A. Alberti: Thermally induced structural modifications of nano-sized anatase films and the effects on the dye-TiO₂ surface interactions. *Appl. Surf. Sci.*, **2014**, *296*, 69-78.

[251] Y. M. Chung, C. S. Moon, M. J. Jung and J. G. Han: The low temperature synthesis of Al doped ZnO films on glass and polymer using magnetron co-sputtering: Working pressure effect. *Surface & Coatings Technology*, **2005**, *200*, 936-939.

[252] Y.D. Liu, L. Zhao and J. S. Lian: Al-doped ZnO films by pulsed laser deposition at room temperature. *Vacuum*, **2006**, *81*, 18-21.

[253] J. Hu and R. G. Gordon: Textured aluminum-doped zinc oxide thin films from atmospheric pressure chemical-vapor deposition. *J. Appl. Phys.*, **1992**, *71*, 880-890.

[254] T. Shirahata, T. Kawaharamura, S. Fujita and H. Orita: Transparent conductive zinc-oxide-based films grown at low temperature by mist chemical vapor deposition. *Thin Solid Films*, **2015**, *597*, 30–38.

[255] Y. S. Kim and W. P. Tai: Electrical and optical properties of Al-doped ZnO thin films by sol–gel process, *Appl. Surf. Sci.*, **2006**, *253*, 4911-4916.

[256] Q. H. Li, D. Zhu, W. Liu, Y. Liu and X. C. Ma: Optical properties of Al-doped ZnO thin films by ellipsometry, *Appl. Surf. Sci.*, **2008**, *254*, 2922-2926.

[257] S. Sanzaro, A. La Magna, E. Smecca, G. Mannino, G. Pellegrino, E. Fazio, F. Neri and A. Alberti: Controlled Al³⁺ Incorporation in the ZnO Lattice at 188°C by Soft Reactive Co-Sputtering for Transparent Conductive Oxides. *Energies*, **2016**, 9, 433-446.

[258] Z. Deng, C. Huang, J. Huang, M. Wang, H. He, H. Wang and Y. Cao: Effects of Al content on the properties of ZnO:Al films prepared by Al₂O₃ and ZnO co-sputtering, *J. Mater. Sci. Mater. Electron*, **2010**, *21*, 1030–1035.

[259] A. Gorgulla, D. P. Ertel, M. Steyer, G. Hahn and B. Terheiden: Effect of Al concentration analyzed by ICP-OES on the structural, electrical and optical properties of co-sputtered ZnO:Al films, *Energy Procedia*, **2015**, *77*, 687–693.

[260] S. Caramori, V. Cristino, R. Boaretto, R. Argazzi, C. A. Bignozzi and A. Di Carlo: New Components for Dye-Sensitized Solar Cells. *International Journal of Photoenergy*, **2010**, *458614*, 1-16.

[261] M. Grätzel: Photoelectrochemical cells, *Nature,* **2001**, *414,* 338-344.

[262] J. H. Scofield: Hartree-Slater subshell photoionization cross-sections at 1254 and 1487 eV. *J. Electron Spectrosc. Relat. Phenom.*, **1976**, *8*, 129-137.

[263] B. Karunagaran, K. Kim, D. Mangalaraj, J. Yi and S. Velumani: Structural, optical and Raman scattering studies on DC magnetron sputtered titanium dioxide thin films. *Solar Energy Mater. Solar Cells*, **2005**, *88*, 199-208.

[264] E. Burstein: Anomalous Optical Absorption Limit in InSb. *Phys. Rev.*, **1954**, *93*, 632.

[265] Ü. Özgür, Y. I. Alivov, C. Liu, A. Teke, M. A. Reshchikov, S. Doğan, V. Avrutin, S. J. Cho and H. Morkọ: A comprehensive review of ZnO materials and devices, *J. of Appl. Phys.* **2005**, *98*, 1-103.

[266] V. Russo, M. Ghidelli, P. Gondoni, C. S. Casari and A. Li Bassi: Multi-wavelength Raman scattering of nanostructured Al-doped zinc oxide. *J. of Appl. Phys.*, **2014**, *115*, 1-10.

[267] J. S. Reparaz, L. R. Muniz, M. R. Wagner, A. R. Goñi, M. I. Alonso, A. Hoffmann and B. K. Meyer: Reduction of the transverse effective charge of optical phonons in ZnO under pressure, *Appl. Phys. Lett.*, **2010**, *96*, 231906-231906-3.

[268] S. Lany and A. Zunger: Anion vacancies as a source of persistent photoconductivity in II-VI and chalcopyrite semiconductors. *Phys. Rev. B*, **2005**, *72*, 035215.

[269] S. Lany and A. Zunger: Dopability, Intrinsic Conductivity, and Nonstoichiometry of Transparent Conducting Oxides. *Phys. Rev. Letters*, **2007**, *98*, 045501.

[270] A. El Manouni, F. J. Manjón, M. Mollar, B. Marí, R. Gómez, M. C. López and J. R. Ramos-Barrado: Effect of aluminium doping on zinc oxide thin films grown by spray pyrolysis. *Superlattices and Microstructures*, **2006**, *39*, 185–192.

[271] S. J. Clark, J. Robertson, S. Lany and A. Zunger: Intrinsic defects in ZnO calculated by screened exchange and hybrid density functionals. *Phys. Rev. B*, **2010**, *81*, 115311.

[272] C. M. Maghanga, G. A. Niklasson and C. G. Granqvist: Optical properties of sputter deposited transparent and conducting TiO₂:Nb films. *Thin Solid Films*, **2009**, *518*, 1254–1258.

[273] N. Ahn, D. Y. Son, I. H. Jang, S. M. Kang, M. Choi and N. G. Park: Highly Reproducible Perovskite Solar Cells with Average Efficiency of 18.3% and Best Efficiency of 19.7% Fabricated via Lewis Base Adduct of Lead(II) Iodide. *J. Am. Chem. Soc.*, **2015**, *137*, 8696–8699.

[274] D. K. Schroder: Semiconductor material and device characterization. 3rd ed; Wiley-Interscience Publication: Canada, **2006**.

[275] F. M. Smiths: The Bell System Technical Journal. **1958**, 37, 711.

[276] R. Hall: Minimizing errors of four point probe measurements on circular wafers. *J. Sci. Instrum.*, **1967**, *44*, 53.

[277] C. Boissiere, D. Grosso, S. Lepoutre, L. Nicole, A. B. Bruneau and C. Sanchez: Porosity and mechanical properties of mesoporous thin films assessed by environmental ellipsometric porosimetry. *Langmuir*, **2005**, *21*, 12362–12371.

Acknowledgments

Il traguardo rappresentato dal "*Dottorato di Ricerca*" costituisce non solo la fine di un percorso formativo ma la crescita da un punto di vista sia scientifico e professionale nonché di vita. In questi tre anni, infatti, il percorso è stato intenso ma soprattutto costruttivo, dandomi la possibilità di arricchire le mie conoscenze e incontrare persone fantastiche il cui ricordo rimarrà sempre nel mio cuore. Detto questo, sperando di non dimenticare nessuno vorrei, a questo punto, ringraziare tutti coloro i quali mi hanno sostenuto, seguito e guidato durante questo cammino.

Innanzi tutto voglio ringraziare i miei tutors, il Prof. Fortunato Neri e la Dr. Alessandra Alberti per avermi accolto nei loro rispettivi gruppi di ricerca, per avermi accompagnato e sostenuto in questo lavoro in maniera esemplare e per avermi aiutato a crescere non solo scientificamente ma anche umanamente.

Un ringraziamento particolare va alla Dr. Enza Fazio che, nonostante la sua investitura di tutor non ufficiale, mi ha comunque seguito, sostenuto e aiutato durante l'intero percorso di ricerca. Ringrazio il coordinatore del *Dottorato,* il Prof. Lorenzo Torrisi, per il suo costante impegno e la sua disponibilità. Un ringraziamento va anche al Dr. Antonino La Magna per il suo sempre presente supporto scientifico. Ringrazio il Dr. David Muñoz-Rojas per avermi accolto nel suo gruppo di ricerca e datomi la possibilità di ampliare sempre più le mie conoscenze durante lo stage di tre mesi fatto presso i laboratori del LMGP a Grenoble. Doveroso è anche un ringraziamento al Dr. Federico Zontone per avermi seguito durante lo stage di un mese fatto presso la beamline ID10 di ESRF a Grenoble.

Ringrazio tutti i membri del gruppo dell'Università di Messina in particolare il Dr. Francesco Barreca e tutti i miei colleghi di corso. Essendo anche associato al CNR-IMM di Catania, un grazie va a tutti i membri dell'Istituto e a tutti colleghi incontrati e conosciuti. In particolare, di essi, volevo ringraziare: il Direttore Dr. Guglielmo Fortunato, il Dr. Giovanni Mannino, il Dr. Corrado Bongiorno, il Dr. Ioannis Deretzis, la Dr. Rosaria A. Puglisi, il Dr. Salvatore Di Franco, la Dr. Simona Boninelli e, in maniera speciale, il Dr. Emanuele Smecca, non solo come collega ma anche e soprattutto come grande amico.

Inoltre, ci tenevo a dire che questa esperienza mi ha permesso anche di avere un contatto diretto con l'industria poiché i laboratori del CNR-IMM sono collocati all'interno del sito di STMicroelectronics di Catania in Zona Industriale. Questo mi ha dato la possibilità di collaborare con alcuni della suddetta industria e per l'appunto ci tenevo a ringraziare il Dr. Antonello Santangelo, il Dr. Lucio Renna, il Dr. Leonardo Gervasi e la Dr. Clelia Galati.

Ringrazio la Prof.ssa Graziella Malandrino e il Prof. Guido G. Condorelli del Dipartimento di Chimica dell'Università di Catania per il loro sempre costante sostegno, aiuto e disponibilità.

Un grazie va anche a tutti i membri dei gruppi di ricerca esteri con i quali ho condiviso parte di questo dottorato di ricerca, in particolare: la Dr. Carmen Jiménez e il Dr. Jean-Luc Deschanvres del LMGP e il Dr. Oleg Konovalov assieme al Dr. Yuriy Chushkin di ESRF.

Ringrazio anche il Prof. Tsutomu Miyasaka e a tutto il suo gruppo della Toin University of Yokohama (Giappone), il Dr. Corrado Spinella (Direttore del Dipartimento di Scienze Fisiche e Tecnologie della Materia del CNR), il Prof. Giuseppe Faraci, il Prof. Antonio Terrasi, la Dr. Maria Rita Catalano e il Prof. Gianluca Cicala (Università di Catania), la Dr. Luisa De Marco e la Dr. Rosabianca Iacobellis (dell'IIT e CNR- Nanotec, Lecce), il Prof. David Grosso insieme al Dr. Thomas Bottein (IM2NP Aix-Marseille Université, Francia) e il Dr. Stefano Perugini, Dr. Carlo Aliberti e Dr. Giovanni Barbieri del team Kenosistec S.r.l. (Milano).

Un doveroso grazie va ai progetti Plast_ics e Beyond Nano upgrade.

Andando sul personale ringrazio i miei amici e in particolare mio Amico-Cugino Salvo e l'Amico Corrado che mi hanno sempre sostenuto e hanno sempre creduto in me. Grazie Salvo e Corrado.

Un ringraziamento di Cuore va alla mia ragazza che non senza fatica, è stata sempre presente in qualsiasi momento, una figura costante che mi ha supportato e sopportato, dandomi forza, coraggio e aiuto in qualsiasi istante. Grazie Maria.

Un ringraziamento particolare va a alla famiglia mia tutta, ai miei fratelli, Vincenzo e Davide, esempi di vita e di sostegno altrui, fratelli di nome ma anche e soprattutto di fatto e ai miei genitori. A loro sono veramente grato per tutti i sacrifici fatti per me e per aver reso possibile il raggiungimento di questo traguardo, sostenendomi continuamente in tutto e per tutto.

Ringrazio anche tutti coloro che mi sono stati vicino.

Infine un ringraziamento lo voglio fare a Me stesso ricordando che i traguardi e la possibilità di crescere e arricchire sempre più le proprie conoscenze non finiscono mai nella vita e pertanto di mantenere costante l'audacia, la speranza, la pazienza e la volontà.

AD MAIORA!

My Supervisors

Prof. Fortunato Neri
Università di Messina

Dr. Alessandra Alberti
CNR-IMM

IMM Institute for Microelectronics and Microsystems

Consiglio Nazionale delle Ricerche

DISTRETTO TECNOLOGICO SICILIA MICRO E NANO SISTEMI

Collaborations

ST life.augmented

LMGP

ESRF The European Synchrotron

SICILIAE STVDIVM GENERALE · 1434 ·

CNrs

TOIN UNIVERSITY OF YOKOHAMA

Im2np

CNRNANOTEC
INSTITUTE OF NANOTECHNOLOGY

Salvatore Sanzaro

📍 Via Risorgimento, 121 – 96010 Sortino (SR)

📞 +39 0931 952565   📱 +39 3334242695   📱 +39 3277805408

✉ s.sanzaro@gmail.com, salvatore.sanzaro@imm.cnr.it, ssanzaro@unime.it, s.sanzaro@pec.it

Sex M | Date of birth 02 April 1986 | Nationality Italian

ResearchGate https://www.researchgate.net/profile/Salvatore_Sanzaro
Google Scholar http://scientificreport.edu/salvatoresanzaro
LinkedIn www.linkedin.com/in/salvatore-sanzaro-023b4b98

WORK EXPERIENCE

From 02.11.2017 to today

Teacher Natural Sciences, Chemistry and Geography, Microbiology at I.I.S. G. Giorgi

Secondary School, Institute of Higher Education (I.I.S.) Giovanni Giorgi (MIIS082004), Viale Liguria 19/21, 20143 Milano, Italy.

▪ Natural Sciences, Chemistry and Geography, Microbiology.

Business or sector Teaching.

From 01.11.2014 to 31.10.2017

Ph.D. Student in Physics – XXX Cycle

University of Messina, Department of Mathematical and Computational Sciences, Physics and Earth Sciences (MIFT), V. le F. Stagno d'Alcontres 31, Messina 98166, Italy.

Associated with National Research Council - Institute for Microelectronics and Microsystems (CNR-IMM) Zona Industriale VIII Strada, 5 – 95121 Catania (CT), Italy, from 17.07.2015

▪ Topic scholarship – Semiconductor Oxides deposited by reactive sputtering for photovoltaic and sensor applications.

Business or sector Chemistry-Physics for Nanotechnologies.

From 03.07.2017 to 31.07.2017

Stage at ESRF

European Synchrotron Radiation Facility (ESRF), 71 Avenue des Martyrs, 38000 Grenoble, France.

▪ Porous TiO_2 thin film structures for photovoltaic applications studied by Coherent X-ray Diffraction Imaging: CXDI data collection and management of software packages for analysis with Linux, ImageJ and Chimera for tomographic image reconstruction.

Business or sector Chemistry-Physics for Nanotechnologies.

From 28.03.2017 to 28.06.2017

Teacher of Polymer at CAMPLUS COLLEGE D'ARAGONA

University Camplus College D'Aragona, Via Monsignor Ventimiglia 184, Catania 95129, Italy.

▪ Science and Chemical Technology of polymer.

Business or sector Teaching.

From 11.11.2016 to 24.06.2017

Teacher Natural Sciences, Chemistry and Geography, Microbiology at I.T.C. E. Mattei (on leave for Ph.D.)

Secondary School, Commercial Technical Institute (I.T.C.) Enrico Mattei (MITD52000A), Via Padre Luigi Vaiani, 18, 20017 Rho, Milano, Italy.

▪ Natural Sciences, Chemistry and Geography, Microbiology.

Business or sector Teaching.

From 12.09.2016 to 15.12.2016

Stage at LMGP

Laboratoire des Matériaux et du Génie Physique (LMGP), Grenoble INP – Minatec, 3 parvis Louis Néel - CS 50257 - 38016 Grenoble cedex 1, France.

▪ TiO₂ micro-flowers deposited by Assisted Aerosol Metal Organic Chemical Vapor Deposition (AA-MOCVD) and structural, optical and morphological characterizations for photovoltaic applications: independent use of the equipment and analyses of the grown materials.

Business or sector Chemistry-Physics for Nanotechnologies.

From 26.01.2016 to 30.06.2016 | **Teacher Natural Sciences, Chemistry and Geography, Microbiology at I.I.S. J. C. Maxwell (on leave for Ph.D.)**

Secondary School, Institute of Higher Education (I.I.S.) James Clerk Maxwell (MIRI01701L), Via Narni, 18, 20132 Milano, Italy.

▪ Natural Sciences, Chemistry and Geography, Microbiology.

Business or sector Teaching.

From 07.06.2016 to 14.06.2016 | **User at ESRF**

European Synchrotron Radiation Facility (ESRF), 71 Avenue des Martyrs, 38000 Grenoble, France.

▪ Porous TiO₂ thin film structures for photovoltaic applications studied by Coherent X-ray Diffraction Imaging.

Business or sector Chemistry-Physics for Nanotechnologies.

From 03.06.2014 to 31.10.2014 | **Scholarship**

National Research Council - Institute for Microelectronics and Microsystems (CNR-IMM), Zona Industriale VIII Strada, 5 – 95121 Catania (CT), Italy.

▪ Research Project - PON Tecnologie per l'Energia e l'Efficienza Energetica (ENERGETIC).
▪ Topic: Study of the oxides deposited on not conventional substrates by reactive sputtering at low temperature. Mesoporous TiO₂ layers deposited on ZnO:Al (TCO = transparent conductive oxide) as a scaffold on plastic substrates for Dye Sensitized Solar Cells (DSSC).

Business or sector Chemistry-Physics for Nanotechnologies.

From 26.04.2013 to 28.02.2014 | **Thesis for Master's Degree in Chemistry of Materials**

Department of Chemical Sciences, University of Catania, V. le Andrea Doria 6, 95125 Catania, Italy.

National Research Council - Institute for Microelectronics and Microsystems (CNR-IMM) Zona Industriale VIII Strada, 5 – 95121 Catania (CT), Italy.

▪ Experimental Thesis (Master Degree), Oxides deposition for photo-anodes in Dye-Sensitized Solar Cells (DSSC).

Business or sector Chemistry-Physics for Nanotechnologies.

From 18.06.2011 to 07.05.2012 | **Town Councillor**

Council member at Sortino's Municipality – Viale Mario Giardino – 9010 Sortino (SR), Italy.

▪ Assessor to the Town Police, Civil Protection, Agriculture and Forest, Commerce and Cemetery Services.
Business or sector Administration.

From 02.11.2010 to 10.03.2011 | **Thesis for Bachelor's Degree in Chemistry**

Department of Chemical Sciences, University of Catania, Viale Andrea Doria 6, 95125 Catania, Italy.

▪ Experimental Thesis (Bachelor's Degree), on synthesis and characterization of Kalium precursors and their applications.

Business or sector Inorganic Chemistry.

From 24.05.2007 to 12.12.2007 | **Public relationships**

E.R.S.U. (Ente Regionale per il Diritto allo Studio Universitario) – Via Etnea, 570 – 95128 Catania (CT), Italy.

Business or sector Administration.

From 26.04.2004 to 30.04.2004 | **Stage in commercial sector**

Agenzia delle Entrate - Via Turchia, 2/4, Siracusa (SR), Italy.

▪ Training for work formation and work orientation.
Business or sector Commercial.

EDUCATION AND TRAINING

In progress
(Defence: 5th December 2017)

Ph.D. in Physics.

Thesis title: "*Newly-Designed Spongy TiO$_2$ Layers by Modified Sputtering Methods for Hybrid PhotoVoltaics*".

University of Messina, Department of Mathematical and Computational Sciences, Physics and Earth Sciences (MIFT), V. le F. Stagno d'Alcontres 31, Messina 98166, Italy.

Associated with National Research Council - Institute for Microelectronics and Microsystems (CNR-IMM) Zona Industriale VIII Strada, 5 – 95121 Catania (CT), Italy, from 17.07.2015.

▪ Chemistry-Physics study of the optical-electrical-structural properties of semiconductor oxides; nano-materials deposition by reactive sputtering; optical analyses (UV-Vis, Infrared, Raman Spectroscopies and Spectroscopic Ellipsometry), morphological analysis (Scanning Electrical Microscopy), structural analyses (X-Ray Diffraction and Transmission Electrical Microscopy), chemical analyses (Energy Dispersive X-Ray and X-Ray Photoelectron Spectroscopy).

In progress

Qualification to the profession of CHEMIST

Ordine dei Chimici - Via Giuffrida Vincenzo, 4, Catania (CT), Italy.

3rd December 2015

Safety course in the industries (FAD)

Prevention in the places of job, general knowledges.
National Research Council (CNR) – Servizio di Prevenzione e Protezione (SPP) – Italy.

28th March 2014

Master's Degree in CHEMISTRY OF MATERIALS

Vote: **110/110 cum Laude**.
Thesis title: "*Sequential deposition of TiO$_2$/ZnO:Al by reactive sputtering for photo-anodes in Dye Sensitized Solar Cells*".
Department of Chemical Sciences, University of Catania, V. le Andrea Doria 6, 95125 Catania, Italy.

1st December 2011

Safety in laboratories course

Department of Chemical Sciences, University of Catania, Viale Andrea Doria 6, 95125 Catania, Italy.

25th March 2011

Bachelor's Degree in CHEMISTRY

Vote: **101/110**.
Thesis title: "*Synthesis and characterization of new kalium complexes, K(hfa)polietere, and their applications for the preparation of fluoride compounds*".
Department of Chemical Sciences, University of Catania, Viale Andrea Doria 6, 95125 Catania, Italy.

18th July 2005

School-leaving Certificate of ACCOUNTANT

Vote: **95/100**.
Technical Commercial Institute, "Filadelfo Insolera", Via Modica, Siracusa (SR), Italy.

PERSONAL SKILLS

Mother tongue   Italian

Other languages

UNDERSTANDING	SPEAKING	WRITING

	Listening	Reading	Spoken interaction	Listening	Reading
English	B1	B1	B1	B1	B1
French	A2	A1	A1	A1	A2

Levels: A1/A2: Basic user - B1/B2: Independent user - C1/C2 Proficient user
Common European Framework of Reference for Languages

Communication skills Detached abilities to listen, to report and to interact with the public, it acquired during the experience of assessor and PhD student within the respective institution.

Organisational / managerial skills Ability to work in binding situations, tied up to the expirations and the relationship with the public also in autonomous way. Acquired competences thanks to the experience in the research sector.

Job-related skills Theoretical-Practices competences arising from the use of instruments and equipment in Physical and Chemical laboratories following the experiences at the Universities (Catania and Messina, Italy) and at the National Research Council (CNR-IMM, Italy) during the experimental theses (master and Ph.D.). I would like to particularly mention independent skills and direct use of: reactive sputtering deposition equipment for oxides and metallic layers; UV-vis optical measurements; IR and Raman analyses; CXDI with synchrotron radiation; SEM and EDX analyses; XPS surface analyses and contact angle measurements; XRD analyses: Sheet resistance by four-point-probe equipment. Further experience was gained during the two stages at ESRF (Grenoble) and LMGP (Grenoble) on synchrotron techniques and chemical synthesis methods, respectively
Theoretical-Practices competences in chemistry of materials for: surfaces functionalization and the related issues, especially for mesoporous oxides functionalization to be used in the Photovoltaic field (DSC) and for gas sensing; formation of oxide/hybrid perovskite blend for PSC and related issues; issues related to DSC and PSC devices, with special regards to photo-carrier transport phenomena in relationship with the material structure and the involved interfaces.

Digital competence

SELF-ASSESSMENT				
Information processing	Communication	Content creation	Safety	Problem solving
Independent user	Independent user	Proficient user	Independent user	Independent user

Levels: Basic user - Independent user - Proficient user
Digital competences - Self-assessment grid

Other skills ▪ Accounting
▪ Teaching

Driving licence B

ADDITIONAL INFORMATION ▬▬▬▬▬▬▬▬▬▬▬▬▬▬▬▬▬▬▬▬▬ ■

Publications in JCR journals Title: *Pervasive infiltration and multi-branch chemisorption of N719 molecules into spongy TiO₂ layers deposited by gig-lox sputtering processes.*
Authors: **Salvatore Sanzaro**, Enza Fazio, Fortunato Neri, Emanuele Smecca, Corrado Bongiorno, Giovanni Mannino, Rosaria Anna Puglisi, Antonino La Magna and Alessandra Alberti.
Journal: Journal of Materials Chemistry A, DOI: 10.1039/C7TA07811K. [I.F. 2016 = 8.867]
Year: 2017

Title: *Innovative spongy TiO₂ layers for high sensitivity gas detection at low working temperature.*
Authors: Alessandra Alberti, Lucio Renna, **Salvatore Sanzaro**, Emanuele Smecca, Giovanni Mannino, Corrado Bongiorno, Clelia Galati, Leonardo Gervasi, Antonello Santangelo and Antonino La

Magna.
Journal: Sensors and Actuators B: Chemical (submitted). [I.F. 2016 = 5.401]
Year: 2017.

Title: *Revealing a discontinuity in the degradation behaviour of CH₃NH₃PbI₃ during thermal operation.*
Authors: Alessandra Alberti, Ioannis Deretzis, Giovanni Mannino, Emanuele Smecca, **Salvatore Sanzaro**, Youhei Numata, Tsutomu Miyasaka and Antonino La Magna.
Journal: The Journal of Physical Chemistry C, 121, 13577−13585. [I.F. 2016 = 4.536]
Year: 2017.

Title: *First evidence of CH₃NH₃PbI₃ optical constant improvement in N₂ environment at 40-80°C.*
Authors: Giovanni Mannino, Alessandra Alberti, Ioannis Deretzis, Emanuele Smecca, **Salvatore Sanzaro**, Youhei Numata, Tsutomu Miyasaka and Antonino La Magna.
Journal: The Journal of Physical Chemistry C, 121, 7703-7710. [I.F. 2016 = 4.536]
Year: 2017.

Title: *Multi-Scale-Porosity TiO₂ scaffolds grown by innovative sputtering methods for high throughput hybrid photovoltaics.*
Authors: **Salvatore Sanzaro**, Emanuele Smecca, Giovanni Mannino, Corrado Bongiorno, Giovanna Pellegrino, Fortunato Neri, Graziella Malandrino, Maria Rita Catalano, Guglielmo Guido Condorelli, Rosabianca Iacobellis, Luisa De Marco, Corrado Spinella, Antonino La Magna and Alessandra Alberti.
Journal: Scientific Reports 2016, 9, 39509. [I.F. 2016 = 4.259]
Year: 2016.

Title: *Controlled Al³⁺ Incorporation in the ZnO Lattice at 188°C by Soft Reactive Co-Sputtering for Transparent Conductive Oxides.*
Authors: **Salvatore Sanzaro**, Antonino La Magna, Emanuele Smecca, Giovanni Mannino, Giovanna Pellegrino, Enza Fazio, Fortunato Neri and Alessandra Alberti.
Journal: Energies 2016, 9, 433-446. [I.F. 2016 = 2.262]
Year: 2016.

Title: *Low temperature sputtered TiO₂ nano sheaths on electrospun PES fibers as high porosity photoactive material.*
Authors: A. Alberti, C. Bongiorno, G. Pellegrino, **S. Sanzaro**, E. Smecca, G. G. Condorelli, A. E. Giuffrida, G. Cicala, A. Latteri, G. Ognibene, A. Cassano, A. Figoli, C. Spinella and A. La Magna.
Journal: RSC Advances, 5, 73444–73450. [I.F. 2016 = 3.108]
Year: 2015.

Chapter on books   Title: *Spongy TiO₂ gig-lox scaffold for Dye Sensitized Solar Cells and Perovskite Solar Cells.*
Authors: **S. Sanzaro**, A. Alberti, E. Fazio, E. Smecca, G. Mannino, G. Malandrino, A. La Magna and F. Neri.
Journal: Activity Report 2017 - Dottorato di Ricerca in Fisica, Università di Messina – ISSN 2838-5889.
Year: 2017.

Title: *New growth methodology to produce mesoporous TiO₂ scaffolds for Dye Sensitized Solar Cells.*
Authors: **S. Sanzaro**, A. Alberti, E. Fazio, E. Smecca, G. Mannino, G. Malandrino, A. La Magna and F. Neri.
Journal: Activity Report 2016 - Dottorato di Ricerca in Fisica, Università di Messina – ISSN 2838-5889.
Year: 2016.

Title: *Dye-Sensitized Solar Cells: ZnO:Al by reactive co-sputtering in co-focal geometry.*
Authors: **S. Sanzaro**, A. La Magna, E. Smecca, G. Mannino, G. Pellegrino, E. Fazio, F. Neri and A. Alberti.
Journal: Activity Report 2015 - Dottorato di Ricerca in Fisica, Università di Messina – ISSN 2838-5889.
Year: 2015.

Title: *Deposition of ZnO:Al/TiO₂ bi-layers at low temperature by reactive sputtering for application as photoanodes in Dye Sensitized Solar Cells.*
Authors: **S. Sanzaro**, G. Pellegrino, E. Smecca, G. Malandrino, R. Catalano, A. La Magna, A. Alberti.
Journal: Activity Report 2014 - Dottorato di Ricerca in Fisica, Università di Messina – ISSN 2838-5889.

Year: 2014.

Patent   Title: *Especially designed TiO$_2$ sputtering layer for high sensitivity gas detection.*
Authors: A. Alberti, L. Renna, L. Gervasi, **S. Sanzaro**, E. Smecca, C. Galati, A. Santangelo, A. La Magna.
ID Patent: 82681506.
Year: 2017, to be submitted on behalf of STMicroelectronics.

Conferences   Abstract: *Full-frame use of up-scalable spongy TiO$_2$ layer for deep dye chemisorption. (Oral)*
Authors: **Salvatore Sanzaro**, Enza Fazio, Fortunato Neri, Emanuele Smecca, Giovanni Mannino, Rosaria Anna Puglisi, Antonino La Magna and Alessandra Alberti.
Conference: 103° Congresso Nazionale della Società Italiana di Fisica.
Trento, Italy
11-15 September 2017

Abstract: *Demonstration of the order-disorder character of the CH$_3$NH$_3$PbI$_3$ polymorphic transition and its implications on the lattice stability. (Oral)*
Authors: Alessandra Alberti, Ioannis Deretzis, Giovanni Mannino, Emanuele Smecca, **Salvatore Sanzaro**, Corrado Bongiorno, Corrado Spinella, Youhei Numata, Tsutomu Miyasaka and Antonino La Magna.
Conference: Materials.it 2016.
Aci Castello – Catania, Italy
12-16 December 2016

Abstract: *Morphological and optical modification in CH$_3$NH$_3$PbI$_3$ planar layers at room temperature in air ambient. (Oral)*
Authors: Emanuele Smecca, Ioannis Deretzis, **Salvatore Sanzaro**, Simona Boninelli, Giovanni Mannino, Corrado Bongiorno, Tsutomu Miyasaka, Antonino La Magna and Alessandra Alberti.
Conference: Materials.it 2016.
Aci Castello – Catania, Italy
12-16 December 2016

Abstract: *Dye sensitized mesoporous thick TiO$_2$ layers deposited by grazing incidence reactive sputtering methods assisted by local oxidation. (Oral)*
Authors: **Salvatore Sanzaro**, Emanuele Smecca, Giovanna Pellegrino, Corrado Bongiorno, Fortunato Neri, Graziella Malandrino, Maria Rita Catalano, Luisa De Marco, Rosabianca Iacobellis, Giovanni Mannino, Antonino La Magna and Alessandra Alberti.
Conference: 6th International Symposium on Transparent Conductive Materials (TCM).
Platanias – Chania, Crete, Greece
09-13 October 2016

Abstract: *Multi-Scale-Porosity TiO$_2$ Platforms Grown by Grazing Sputtering Methods Assisted by Local Oxidation for Multipurpose Applications. (Oral)*
Authors: **S. Sanzaro**, E. Smecca, G. Pellegrino, C. Bongiorno, F. Neri, G. Malandrino, M.R. Catalano, L. De Marco, R. Iacobellis, G. Mannino, A. La Magna and A. Alberti.
Conference: NanoSEA 2016
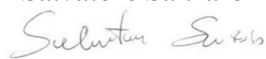Giardini Naxos - Messina, Italy
03-08 July 2016

Abstract: *Deposition of ZnO:Al/TiO$_2$ bi-layers at low temperature by reactive sputtering for applications as photoanodes in Dye Sensitized Solar Cells. (Poster)*
Authors: **S. Sanzaro**, G. Pellegrino, E. Smecca, G. Malandrino, M.R. Catalano, E. Fazio, F. Neri, A. La Magna, A. Alberti.
Conference: E-MRS Spring Meeting 2015
Lille, France
11-15 May 2015

Abstract: *Sequential deposition of ZnO:Al/TiO$_2$ films by reactive sputtering for photoanodes in Dye Sensitized Solar Cells preparation. (Poster)*
Authors: **S. Sanzaro**, E. Smecca, G. Pellegrino, A. La Magna, A. Alberti.

Conference: 5th International Symposium on Transparent Conductive Materials (TCM).
Platanias – Chania, Crete, Greece
12-17 October 2014

I declare that the information contained in this CV is accurate and truthful, according to art. 46 and 47 D.P.R. n. 445/2000.
I authorize the processing of my personal data, including sensitive ones, for the purposes and for the effects of art. 23 - Privacy Law of the Italian Legislative Decree n. 196/03 for the purposes of this notice of application.

Salvatore Sanzaro

October 8th 2017

Report on M. Salvatore Sanzaro's thesis manuscript:

In addition to discovering new material with improved properties, the development of low-cost, scalable fabrication protocols is a very important issue for the development of new or improved technologies. This is even more the case for nanomaterials, where the unique properties that going to the nanoscale offer should be harnessed at affordable costs. The thesis of M. Sanzaro has focused in these two key aspects, materials and methods, with very satisfactory results.

As a main result, he has developed a new deposition approach based on the sputtering technique (a widely used technique in industry) to fabricate mesoporous TiO_2 films in one step, without the need for templating. The so-called GIG-LOX approach is based on performing the deposition in gracing angle geometry and with a local supply of oxygen which is limited to the substrate. The characteristics of the films obtained by this new approach are very appealing and the implementation of GIG-LOX growth should be straight forward and easily transposable to sputtering systems in other laboratories and industrially.

The films obtained with the new approach have been used as anodes in hybrid solar cells in combination with dyes and hybrid perovskites and the superior results obtained demonstrate the advantages offered by the mesoporous structure obtained with the new GIG-LOX approach. The films have also been successfully tested as gas sensors.

In addition, an alternative morphology of TiO_2 think films containing microflowers with nanometric petals has been studied and compared to the GIG-LOX $TiIO_2$. This has been done during a 3 months stay in the LMGP, France. Also, the deposition of Al doped ZnO films as transparent Conductive oxide layers has been implemented, also by sputtering, allowing the fabrication of Both the TCO and anode layer in the same system.

Finally, and in addition to the characterization tools used in his home and host laboratories, M. Sanzaro has performed two stays in the ESRF synchrotron where he

has carried out advanced characterization of his TiO_2 samples, gaining insights into their structure, morphology and porosity.

As a consequence of the exhaustive and systematic work performed, the thesis has provided many results of relevance and importance for several fields, including, materials synthesis, renewable energies, sensing, etc. The conclusions derived from the experimental work are sound and supported by the characterization techniques used.

M. Sanzaro has several publications as first author and many others as coauthor, including a patent. He has also presented his work in several international and national conferences, both through poster and oral presentations. His stays in the LMGP and ESRF are also a very positive point in M. Sanzaro's thesis.

Concerning the manuscript, it is clear and well structured. I would nevertheless recommend to include a section with objectives just after the introduction.

In views of the above, I fully recommend the admission of Ms. Sanzaro to the final exam.

Dr. Muñoz-Rojas
Chargé de Recherche CNRS / CNRS Research Scientist
Laboratoire des Matériaux et du Génie Physique (LMGP)
UMR 5628 CNRS – Grenoble INP Minatec
3, Parvis Louis Néel MINATEC
CS 50257
38016 GRENOBLE Cedex 1 France

Prof. Elvira Fortunato
Materials Science Department
FCT-UNL
Campus de Caparica
2829-516 Caparica, Portugal
emf@fct.unl.pt

FACULDADE DE
CIÊNCIAS E TECNOLOGIA
UNIVERSIDADE NOVA DE LISBOA

Report on the PhD thesis from Salvatore Sanzaro from
Universita Degli Studi di Messina

General comments

The thesis is titled **Newly-designed spongy TiO2 layers by modified sputtering methods for hybrid photovoltaics** and is divided in 4 main chapters complemented by a set of 3 annexes.

The main focus as well as the innovative character of the thesis was the preparation, study and characterization of a new concept for a material based on TiO2 where by changing the sputtering parameters it was possible to achieve a spongy material (named *gig -lox TiO2*) that will be integrated as a scaffold in photovoltaic solar cells (DSC and PSC) where an efficiency of 11.7% was achieved.

Besides the use of this material as anodes in solar cells it was also demonstrated the possibility to use it as a gas sensor (ethanol), taking profit of the very high surface area. The combination of the same material based platform for producing different devices is also a positive aspect of the multifunctionality exhibit by this material.

Finally it was also study the production and characterization of AZO deposited by sputtering at low temperature using the same chamber for depositing TiO2 which is an advantage for the sequential deposition of the different layers without breaking the vacuum.

The bibliography used was adequate and updated.

As final comment I would like to highlight that the thesis has originated directly 5 original papers having Salvatore Sanzaro as first author or co-author, in ISI journals

Prof. Elvira Fortunato
Materials Science Department
FCT-UNL
Campus de Caparica
2829-516 Caparica, Portugal
emf@fct.unl.pt

FACULDADE DE
CIÊNCIAS E TECNOLOGIA
UNIVERSIDADE NOVA DE LISBOA

and the application for a patent. These results attest by them self the high quality of the work performed during the thesis.

I will accept the thesis without reserve.

FCT-UNL, 6 October 2017

Elvira Fortunato
Full Professor FCT-UNL